Semiconductor quantum plasmonics

Andrew Haky

PSL
UNIVERSITÉ PARIS

THÈSE DE DOCTORAT
DE L'UNIVERSITÉ PSL

Préparée à l'École normale supérieure
au Laboratoire de Physique de l'École normale supérieure

Semiconductor Quantum Plasmonics

Soutenue par
ANDREW HAKY
Le 19 décembre 2022

École doctorale nº 564
Physique en Île-de-France

Spécialité
Physique

Composition du jury :

Lydéric BOCQUET Director of Research, CNRS - École normale supérieure	Président
Andrea ALÙ Professor, City University of New York	Rapporteur
Frédéric TEPPE Director of Research, CNRS - Université de Montpellier	Rapporteur
Pascale ROY Director of Research, Synchrotron SOLEIL - CNRS - CEA Paris-Saclay	Examinatrice
Giorgia FUGALLO Director of Research, CNRS - Université de Nantes	Examinatrice
Carlo SIRTORI Professor, École normale supérieure	Invité
Angela VASANELLI Professor, Université Paris Cité	Directrice de thèse

ENS | PSL

Contents

Acknowledgments

I want to thank each member of the jury, Lydéric Bocquet, Andrea Alù, Frédéric Teppe, Pascale Roy, and Giorgia Fugallo, for not only agreeing to review my work, but for the interest that they showed in it. I sincerely appreciate the time and effort each member of the jury committed. Their careful reading of the manuscript was evident by the pertinent questions they asked. This made the defense rewarding for me - *it was interesting* to hear comments on my work from researchers of diverse scientific backgrounds. It is my hope that I was able to convey the subject matter was sufficient clarity so that each member of the jury came away with some new knowledge.

I want to thank my advisor, Angela Vasanelli. I learned an enormous amount over these past years, and much of it has been the result of her efforts. Her availability and open office are truly remarkable, and demonstrate her commitment to her students. I appreciate her consistent willingness to listen to and consider seriously my ideas, some more promising than others. I appreciate the independence Angela afforded me in pursuing my work - this gave me the opportunity to develop as a researcher. In that vein, I thank Angela, in particular, for her willingness to let me be a student of the subject - for not questing the time I spent reading papers, or working through calculations of which the answer has long been known. By example, Angela conveyed to me the importance of clarity in scientific communication, which I now consider a most important quality. Finally, our work cannot be completely separated from the many other elements of our lives - I thank Angela for the concern and care she showed outside of our common project.

I want to thank my co-advisor and director of the QUAD team, Carlo Sirtori. Not being my official advisor, Carlo had no formal commitment to follow my work, to share his time, to listen to my ideas, or to offer his expertise, yet he did all of the above with consistency, and above all, enthusiasm. Carlo's knowledge (*intuition*!) of the subject material may be unrivaled, and is profoundly helpful. I appreciate Carlo's scientific rigor, and his devotion to the data. He taught me that the data is never *wrong*, but rather always has a story to tell. I appreciate in particular Carlo's effort to build a *scientific community* around the QUAD team, as is evidenced by his commitment to regular group meetings and unforgettably, QUAD days. I appreciate the atmosphere of open discussion and open criticism that Carlo has established in the QUAD group.

I wish to note that I am particularly proud of the progress that I, Angela, and Carlo have made together in understanding the Berreman mode photocurrent effect. I recall that my excitement upon initially observing the effect was soon overshadowed by a sense of overwhelm in the face of a set of data and a problem which we did not understand. We have made tremendous strides in our understanding since the first experiments, and continue to do so. Some discoveries have been more mundane, others more profound, but all have contributed

to the emergence of a clearer picture, and I am proud of the progress we have made together.

I wish to thank the people who grew nearly every sample studied in this manuscript, Konstantinos Pantzas, Grégoire Beaudoin, and Isabelle Sagnes. Their collaboration makes this work possible.

I want to thank Yanko Todorov for his willingness to discuss with me the quantum theory for the collective excitations of the electron gas - it has been a privilege. I am still awed by the creativity it must have took to arrive at the $\hat{\mathbf{P}}^2$ term.

I would like to thank Djamal Gacemi for his availability to help in the lab.

I want to acknowledge the work of those who trained me in the clear room: Stéphan Suffit, Jose Palomo, and Pascal Filloux. You gave me the skills and knowledge which enabled me to pursue my work. In particular, I am thankful to Stéphan Suffit whom I could always count on for helpful advice. As it pertains to the clean room, I most also express my gratitude to Thomas Bonazzi, who willingly helped me with all things SEM.

I thank Yannick De Wilde and Jérôme Tignon for being on my thesis committee and for following my work.

I want to thank Mathieu Jeannin for welcoming me to the QUAD group, for supporting me, for teaching me skills in the lab, and for setting an inspiring example with his academic curiosity, rigor, and work ethic. I want to thank in particular Azzurra Bigioli and Thomas Bonazzi for stepping up in a difficult moment - their kindness has not been forgotten. I want to thank Sébastien Cosme for welcoming me to the group and training me as an intern, and above all, for making it a fun experience. I am glad we could share an office together - the same goes for Sofia Ribeiro. I am glad to have worked alongside Allegra Calabrese, Zahra Asghari, and Grégoire Vallet, each of whom contributed an important dynamic to the QUAD group I knew before, or just after, the move to ENS. I am likewise happy to have worked with Benjamin Rousseaux, who could always be counted on for his enthusiasm and good attitude.

The QUAD group has grown considerably since my arrival, and I would like to thank all of the members, some of whom have already gone, for contributing to a bright and fun workplace: Hamza Dely, Jiawen Liu, Baptiste Chomet, Etienne Rodriguez, Mohsen Bahrehmand, Jihye Baik, Tung Dang-Huu, Livia Del Balzo, Francesco Pisani, Joel Perez Urquizo, Marta Mastrangelo, Tituan Allain, Bruno Martin, Thomas Krieguer, Usama Iqbal, and Mohammadreza Saemian. I am glad to have worked with each of you. Thank you to Etienne for taking on the effort to organize many a social outing. Thank you to Jiawen, who I found particularly kind.

I would like to thank Marta and Jihye in particular for their friendship and support during the difficult final periods of the thesis. I anticipate a bright future for both of you. I particularly appreciate the cheerful attitude which Tituan brought during his stay with the QUAD group. Finally, a special thanks goes to Francesco and Livia for keeping me company during the lonely (and incredibly hot) period of the summer when I was writing the thesis and just about everybody else seemed to be on vacation. Though not a member of the QUAD group, I must also thank Sirine Amiri for her good attitude and for being a great office mate during the writing of the thesis.

I want to thank Luigi De Marco and Mike Reppert who first instilled in me a desire to pursue scientific research. You encouraged and supported my curiosity, which was the most important thing you could have done when I was a young intern in the lab. You both served as an inspiration.

I want to thank Julianna Stermer, who supported me in this work from the beginning through to the end. Your support was invaluable, and as I look back, I am astonished how much we have grown on this journey. I am optimistic and excited for what the future holds for each of us. I must also thank the entire Carlesimo family for warmly welcoming me to Paris, especially Anna.

I want to thank my family, Mom, Dad, Josie, Barry, and Adeline, who arrived just before the writing of this manuscript, for their unwavering and absolute support. This project could not have been accomplished without them. I thank them for their steady encouragement, and for accepting that I would pursue a project so far from home.

Introduction

Historically, the study of collective electronic motion, or *plasma oscillations*, developed without considering size confinement. The quantum theory of plasma oscillations developed by Pines and Bohm [106] is for a 3D electron gas. In the characteristic energy loss experiments which confirmed the existence of plasma oscillations [105], electrons were scattered inelastically by metal films a few tens of nanometers thick. Ferrell predicted [41], and McAlister and Stern confirmed [84], that plasma oscillations in thin metal films couple with free space radiation. In these experiments, it was not possible to resolve the effect of size confinement on the energy of the plasmon excitations.

With the advent of nanofabrication techniques and technologies enabling the nanoscale characterization of materials, the effect of size confinement on plasmonic excitations could be observed, thus beginning the study of *quantum plasmonics*. One of the pioneering works was the demonstration that the optical resonances of localized surface plasmons are strongly affected by electronic confinement for metallic nanoparticle with sizes on the order of 10 nm [115]. In this regime, the Drude model fails to correctly describe the optical response of the electron gas, and a quantum treatment or nonlocal electromagnetic models [86] must be considered. The effect of quantum size confinement on *surface plasmons* has now been investigated in many works [32, 42, 53, 125, 128].

In the case of semiconductors, the development of mature growth and nanofabrication techniques [23, 81, 82, 85] enabled the development of two separate branches of research, which have, until recently, been separated by the dimensionality of the system. On one branch is semiconductor plasmonics, which has traditionally been limited to studies of the 3D electron gas, described by the classical Drude model.

On the other branch is the study of low-dimensional structures, of which the optical properties are well described with a single particle description. The electronic transitions between bound states of a 2D electron gas, the so-called *intersubband transitions* [146], are an example of a low dimensional system in which the single particle description is usually adequate. Unipolar devices employing semiconductor quantum wells, such as quantum cascade lasers [40] and quantum well detectors [47, 71], are successfully described in the single particle picture. This description remains sufficient as long as the energy separation between confined states is large compared with the plasma energy of the electron gas.

This should not be interpreted to mean that collective effects have not been studied in low dimensional systems. As summarized in the review of Ando, Fowler, and Stern, it was not long after the first observations of intersubband transitions in Si inversion layers [64] that, "It quickly became clear that energy-level splittings could not be explained on the basis of one-electron models but could be understood if many-body effects were included in the theory" [6]. Indeed, collective effects in intersubband transitions have long been a subject of

fascination as evidenced by the many important contributions made from numerous authors toward their understanding [3, 50, 92, 145, 151]. However, these authors studied systems in which collective effects represented a correction to the description of the system. In the low dimensional systems that they analyzed, the energy level spacing was still the dominant contribution to the excitation energy.

Only recently has the regime in which the plasma energy is larger than a finite, non-negligible level spacing begun to be investigated in semiconductor quantum wells [8, 34, 100]. In this regime, the regime of quantum plasmonics, both quantum confinement and collective effects can be of equal significance in the determination of the optical response.

Collective excitations in this regime are investigated in this work in highly doped thin semiconductor layers. The excitations studied are *volume plasmons*, otherwise described as longitudinal oscillations of the electron gas. As Ferrell originally predicted for thin metal films, these modes couple with free space radiation.

A semiconductor platform offers numerous benefits for the study of quantum plasmonics. Single particle electronic states can be described in the envelope function formalism. Mature growth technologies enable the realization of carefully designed electronic potentials in which the electronic band structure can be precisely engineered. The electronic density can be tuned during the growth, and consequently, plasmons can be coupled to other oscillators over a wide spectral range, including for example, the longitudinal optical phonons. These favorable aspects enable the studies presented throughout this work.

The manuscript is organized as follows:

In Chapter 1, the plasmonic mode studied throughout this manuscript, the Berreman mode, is introduced. The semiconductor material platform and quantum well heterostructures in which the mode is studied are likewise introduced. A semiclassical description for the optical response of the electron gas, sufficiently general to describe the response for confinement regimes from a quantum well with only two bound states up to the 3D free electron gas, is established. A particular effort is made to provide a conceptually clear semiclassical description of collective effects in the excitations of the electron gas in thin films.

In Chapter 2, it is demonstrated that the Berreman mode can be excited in a single material platform in which a high density of dopants are added to a subwavelength layer. The optical modes of the system are described theoretically and investigated experimentally both above and below the light line. The same modes are studied as efficient sources of thermal emission.

In Chapter 3, the interaction between the electron plasma and optically active vibrations of the crystal lattice is studied in thin films. Coupled longitudinal optical phonon-plasmon modes are directly observed as resonances in spectroscopic measurements.

In Chapter 4, a quantum description of the collective excitations of the confined electron gas is established. The collective modes of the system are calculated from a basis of single particle excitations between confined states, considering their coupling. The model is applied to describe the dispersion of collective modes in a square quantum well. The form of the dispersion is tied to the size confinement.

In Chapter 5, it is demonstrated theoretically and experimentally that the collective modes of the electron gas can be engineered by careful design of the static confining potential. From the application of the microscopic quantum model of the previous chapter, it is demonstrated that the breaking of the square well symmetry is a key element for the

engineering of novel collective excitations. This motivates the experimental study of a step well potential, in which it is demonstrated that the oscillator strength of the system can be split into multiple collective modes.

In Chapter 6, the Berreman mode is experimentally investigated as the absorption mechanism in a photodetector and the first experimental observation of photocurrent from the Berreman mode is reported. The devices are classified as hot electron detectors. The chapter begins with a clear enunciation of the fundamental motivation for the study: to understand how a collective excitation scatters into a single particle photocurrent. The experimental results are interpreted with the simplest of theoretical descriptions, as a first attempt to understand the novel phenomenon observed.

In Chapter 7, the Berreman mode is coupled to the photonic mode of a double metal microcavity structure. A fabrication procedure to realize the microcavity devices with three contact terminals is detailed. The coupled light-matter modes, the polaritons, are investigated with optical measurments, and the system is shown to be in the ultrastrong coupling regime. The photocurrent generated from the excitation of the upper polariton mode is experimentally investigated under illumination by a tunable quantum cascade laser.

A series of Appendices complement the main text. Appendix A is intended to remind the reader under which condition the wave equation admits longitudinal solutions. In Appendices B and C, additional experimental studies of Berreman mode photodetectors which complement those described in Chapter 5 are reported. These studies are reported in appendices to improve the readability of Chapter 5, wherein they are referenced. In Appendix D, the calibration of the tunable quantum cascade laser source used to characterize the photodetectors in Chapters 5 and 7 is reported. Appendix E serves as a repository for the growth sheets of the samples investigated throughout the manuscript. Finally, in Appendix F, a French language summary of each chapter of the manuscript can be found.

Chapter 1

Optical Properties of Thin Semiconductor Layers

In this chapter, the optical properties of thin (sub-wavelength) semiconductor layers in the infrared spectral region are described. In this spectral region, the optical response of semiconductors is determined microscopically by the optically active vibrations of the crystal lattice (phonons), and in the case when the semiconductor is n-doped, by the response of an electron gas in the conduction band. In both cases, the subwavelength thickness of the film modifies the optical properties of the layer. Whereas in bulk media resonances occur at the poles of the dielectric function, in subwavelength layers, resonances occur at the zeros of the dielectric function. This phenomenon is explored in the following chapter. A particular focus is placed on describing the optical properties of highly doped semiconductor layers when the thickness of the film is sufficiently small as to impart a quantum confinement on the electrons of the conduction band.

1.1 The Berreman Mode

It is natural that the optical properties which arise as a consequence of the thin film geometry (beyond simple reflections at the boundaries) should be observed when the film is investigated with light which has an electric field component in the direction normal to the film, which we denote $\hat{\mathbf{z}}$. This is the case for p-polarized light incident at oblique angles of incidence.

In classic experiments, Berreman [11], and shortly thereafter, McAlister and Stern [84], investigated the optical spectra of thin films of LiF and silver, respectively, for light incident under such conditions. The transmission spectra from their experiments are presented in Fig. 1.1.

In the spectra Berreman measured of a 200 nm LiF film (Fig. 1.1a), a single resonant dip is observed in the s-polarized (no E_z component) spectrum at 32.6 µm and is attributed to the transverse optical (TO) phonon, which is also observed in bulk crystals. In the p-polarized spectrum (the light has an E_z component), there are two resonances: one at the same wavelength of the TO phonon resonance in the s-polarized spectrum, and a second at a shorter wavelength corresponding to the excitation frequency of the longitudinal optical (LO) phonon. For a bulk crystal, no optical resonance is observed at the LO phonon frequency.

Similar to Berreman's observation of an LO phonon resonance in a thin film, McAlister

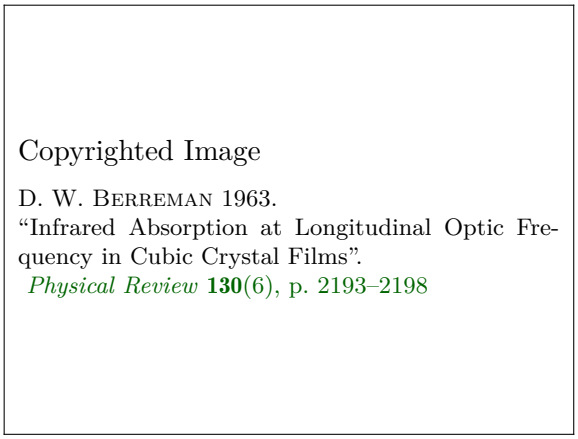

(a) Berreman's study of 200 nm LiF film

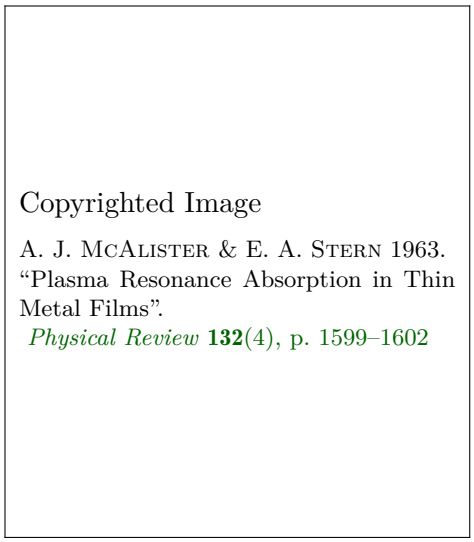

(b) McAlister and Stern's study of 15 nm silver film

Fig. 1.1 The transmission spectra of p- and s-polarized light, incident in a cone from 26° to 34° in (a) and for the various angles indicated in (b), are plotted. Figures reproduced from [11, 84].

and Stern observed a resonance in the p-polarized transmission spectra of silver films which did not appear in the s-polarized spectra, and which is not observed in optical spectra of bulk silver. As evident in Fig. 1.1b, the resonance is only observable at off-normal angles of incidence (when the light has an E_z component). The energy at which the resonance occurs corresponds to the plasma frequency of silver.

At the frequency of the LO phonon in LiF (or any polar dielectric material), the real part of the dielectric function[1] crosses zero. At the plasma frequency of silver (or any material with the optical response of an electron gas), the real part of the dielectric function crosses zero. The modes observed by Berreman and McAlister and Stern are therefore resonant for the same optical condition, namely that $\varepsilon' = 0$, regardless of the microscopic origin of the matter polarization.

In an infinite homogeneous dielectric medium, longitudinal modes are solutions to the wave equation under the condition that $\varepsilon' = 0$. This is demonstrated in Appendix A. It is a general fact that *transverse* light from free space cannot couple to *longitudinal* modes in an infinite medium. It is for this reason that no optical resonance is observed at the LO phonon frequency in bulk crystals or at the plasma frequency in metals.

Let us consider a physical picture which describes the modes observed by Berreman and McAlister and Stern. The experiment is sketched in Fig. 1.2. Light incident with an E_z component is assumed to induce a uniform polarization P_z in the medium. Due to the discontinuity of the polarization at the film boundaries, a surface charge density $\sigma = -P_z \cdot \hat{\mathbf{n}}$

[1] Throughout this manuscript, the real quantities ε' and ε'' are used to describe the real and complex components of the frequency-dependent dielectric function $\varepsilon = \varepsilon' + i\varepsilon''$.

arises at both surfaces of the film. Here, $\hat{\mathbf{n}}$ is the unit vector facing out from either surface. This results in a density of opposite surface charge $\pm\sigma$ on either side of the film.

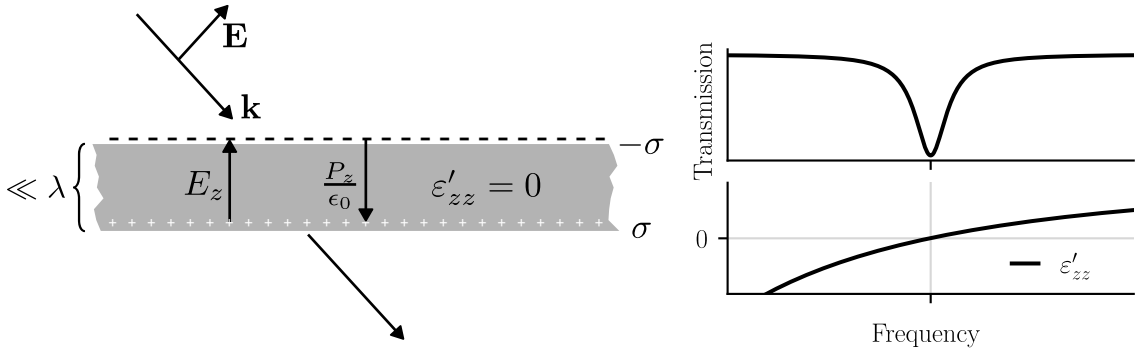

Fig. 1.2 The condition to observe a resonance in a thin polarizable film is sketched.

For a film thin enough that electronic screening may be neglected, the surface charges give rise to a homogeneous electric field inside the film which is opposite in direction and equal to the polarization up to the factor ϵ_0:

$$E_z = \frac{-\sigma}{\epsilon_0} = \frac{-P_z}{\epsilon_0} \tag{1.1}$$

The electric field E_z results in a force on the oscillators in the film opposite to their displacement. In the absence of damping, this results in a sustained oscillation, which describes a mode [148].

Equation (1.1) implies that the displacement field D_z vanishes inside the film since:

$$\mathbf{D} = \epsilon_0 \mathbf{E} + \mathbf{P} \tag{1.2}$$

The dielectric constant ε and the relative dielectric constant ε_r, are defined through:

$$\mathbf{D} = \varepsilon \mathbf{E} = \epsilon_0 \varepsilon_\mathrm{r} \mathbf{E} \tag{1.3}$$

where ϵ_0 is the vacuum permittivity. Consequently, the vanishing displacement field implies that $\varepsilon = 0$ inside the film, exactly the condition for which the resonance is observed.

In this picture, which describes the resonances observed in the experiments of both Berreman and McAlister and Stern, the microscopic origin of the polarization was not specified to highlight the common electromagnetic origin of the modes. Consequently, it is common practice to refer to the mode excited in a thin film by p-polarized light at oblique incidence at the frequency for which $\varepsilon' = 0$ as the Berreman mode, regardless of the microscopic origin of the matter polarization [8, 138]. The coupling of plasma oscillations in the normal direction of a thin film to light was first predicted by Ferrell [41], and thus some authors refer to the mode as the Ferrell-Berreman mode when the microscopic origin is the motion of electrons [93]. Throughout this manuscript, we shall refer to the mode simply as the Berreman mode, regardless of the microscopic origin.

1.1.1 Plasma Oscillations in Thin Films

In this section, we explicitly demonstrate that the resonant behavior of a Berreman mode excited in a thin metallic layer is a consequence of the thin film geometry by considering a classical microscopic description of the electrons. We consider that the metal can be described as a gas of free electrons with effective mass m^*.

We first describe the optical response of the free electron gas in the bulk (homogeneous and without boundaries). We begin with the equation of motion for an electron of effective mass m^* subject to an electric field $E_z(t) = E_0 \mathrm{e}^{-\mathrm{i}\omega t}$ in the absence of damping:

$$m^* \frac{\mathrm{d}^2 z(t)}{\mathrm{d}t^2} = -eE_0 \mathrm{e}^{-\mathrm{i}\omega t} \tag{1.4}$$

The solution is found as:

$$z(t) = z_0 \mathrm{e}^{-\mathrm{i}\omega t} \quad \text{with} \quad z_0 = \frac{eE_0}{m^*\omega^2} \tag{1.5}$$

For an electron gas of density N, the polarization density is defined as:

$$P_z(t) = -Nez(t) \tag{1.6}$$

Inserting Eq. (1.5) into Eq. (1.6), we find:

$$P_z(t) = -Nez_0 \mathrm{e}^{-\mathrm{i}\omega t} = P_0 \mathrm{e}^{-\mathrm{i}\omega t} \tag{1.7}$$

From the definition of the displacement field in Eq. (1.2), it follows that:

$$D_0 = \epsilon_0 E_0 + P_0 = \epsilon_0 E_0 \left(1 - \frac{Ne^2}{m^*\omega^2 \varepsilon}\right) = \epsilon_0 E_0 \left(1 - \frac{\omega_\mathrm{p}^2}{\omega^2}\right) \tag{1.8}$$

The plasma frequency has been introduced in the final expression as:

$$\omega_\mathrm{p}^2 = \frac{Ne^2}{m^*\epsilon_0} \tag{1.9}$$

From Eq. (1.3) and Eq. (1.8), the relative dielectric function describing the free electron gas is found as:

$$\varepsilon_\mathrm{r}(\omega) = 1 - \frac{\omega_\mathrm{p}^2}{\omega^2} \tag{1.10}$$

This expression is plotted in Fig. 1.2, and is evidently equal to zero for $\omega = \omega_\mathrm{p}$.

The dielectric function of Eq. (1.10) does not describe any resonant behavior, yet as demonstrated by the experiment of McAlister and Stern, resonances are observed in the spectra of thin metallic films described by this dielectric function. We turn now to consider how the thin film geometry modifies the electronic response to the incident radiation and leads to a resonance phenomenon. The physical picture we describe was introduced by McAlister and Stern [84].

As in the previous section, let us consider that light with an E_z component induces a uniform polarization density P_z in the thin film. With the polarization density of the free electron gas as defined in Eq. (1.6), the surface charge density at the film boundaries is

$\sigma = \pm Nez$. This results in an electric field and thus a force on each electron opposite in direction to its displacement. Consequently, there is a new equation of motion for the system:

$$m^* \frac{\mathrm{d}^2 z(t)}{\mathrm{d}t^2} = \frac{-Ne^2}{\epsilon_0} z(t) + eE_0 \mathrm{e}^{-\mathrm{i}\omega t} \tag{1.11}$$

The added term, linear in z, describes a restoring force on each electron. The solution to the new equation of motion is:

$$z(t) = \frac{eE_0}{m^* \left(\omega^2 - \omega_\mathrm{p}^2\right)} \mathrm{e}^{-\mathrm{i}\omega t} \tag{1.12}$$

The solution describes plasma oscillations. In the absence of damping, when $\omega = \omega_\mathrm{p}$, $z(t) \to \infty$ and a resonance is observed. We recall that at ω_p, the dielectric function Eq. (1.10) for an electron gas is equal to zero. The model thus links the optical condition at which the mode is observed, namely that $\varepsilon = 0$, with a microscopic description of the resonance.

The resonant behavior is a direct consequence of the restoring force introduced in Eq. (1.11), which exists only because of the thin film geometry. The restoring force, which acts on a single electron in Eq. (1.11), is proportional to the electronic density and thus arises as a collective effect. Later in this chapter, it will be shown that the same collective effect is responsible for renormalizing the resonance frequencies of bound electrons.

1.2 Semiconductor Platform for Quantum Plasmonics

1.2.1 Semiconductor Plasmonics

When the microscopic origin of the thin film polarization which gives rise to the Berreman mode is due to the collective oscillation of an electron gas, the Berreman mode is a plasmonic mode. The Berreman mode is a volume plasmon and should not be confused with the well-known surface plasmon polariton [80].

In this work, Berreman modes hosted in thin, highly doped semiconductor layers will be investigated. This work thus falls under the domain of semiconductor plasmonics [126], which is concerned with the interaction of light with the collective oscillations of the electron gas of highly doped semiconductors. An electron gas is realized in the semiconductor by doping the crystal into the degenerate regime, in which the Fermi level lies above the conduction band minimum. To describe an electron gas in a semiconductor, the effective mass m^* is introduced to account for the periodic potential of the crystal lattice. The plasma frequency ω_p, which is the natural oscillation frequency of the electron gas, can then be defined as:

$$\omega_\mathrm{p}^2 = \frac{N_\mathrm{v} e^2}{m^* \epsilon_0 \varepsilon_\infty} \tag{1.13}$$

where N_v is the electronic density, e is the electron charge, ε is the vacuum permittivity, and ε_∞ is the high frequency dielectric constant, introduced to account for the nonresonant contributions to the polarization which originate from interband transitions at frequencies much greater than ω_p.[2] Defined as above, ω_p is sometimes called the screened plasma frequency since ε_∞ has been (arbitrarily) included in the definition [126].

[2]The ∞ subscript is used to denote that this dielectric constant is valid at frequencies much greater than ω_p. It is not intended to suggest that it is valid towards infinite frequency, since we are using it to describe the approximately static response *below* interband excitation frequencies [149].

In semiconductor plasmonics, ω_p is in the infrared region of the spectrum. Unlike the case for metal plasmonics, in semiconductors, the electronic density N_v can be controlled, which allows ω_p to be tuned.

In the present work, highly doped layers of $In_{0.53}Ga_{0.47}As$ will be studied, for which a density $N_\mathrm{v} \sim 10^{19}\,\mathrm{cm}^{-3}$ of electron-donating Si impurities are added. The Si impurities have a sufficiently small ionization energy such that at room temperature the conduction band electron density can be assumed equal to the impurity density. In $In_{0.53}Ga_{0.47}As$, $\varepsilon_\infty = 11.6108$, and at the conduction band minimum, the effective mass has the value $m^* = 0.043m_e$ where m_e is the electron mass [142]. Then, for $N_\mathrm{v} \sim 10^{19}\,\mathrm{cm}^{-3}$, the plasma frequency lies in the mid-infrared.

1.2.2 Confined Electron Gases in Semiconductor Quantum Wells

In Section 1.1.1, the Berreman mode was considered classically: a *free* electron gas in a subwavelength layer was considered, and the resonance was found to occur at the plasma frequency. In this work, collective electronic excitations will be studied in semiconductor layers thin enough that the electron gas is quantum confined. The collective response of the confined electron gas will be calculated beginning from the single particle electronic states, which we now introduce.

The electron gas is confined in an $In_{0.53}Ga_{0.47}As/Al_{0.48}In_{0.52}As$ quantum well heterostructure lattice-matched to InP. The subscripts indicating the composition of the InGaAs/AlInAs layers are omitted in the remainder of the text. In this system, a 0.52 eV offset in the conduction band potential at the interface of the InGaAs well and AlInAs barrier results in a confining potential $V_\mathrm{CB}(z)$ for an electron in the heavily doped InGaAs layer.

The quantized electronic states of a heterostructure can be written as a product of the Bloch function, which varies with the same periodicity of the crystal, and a so-called envelope function which varies slowly on the scale of the lattice constant [9, 111]. By introducing the effective mass m^* to account for the quickly varying potential of the crystal lattice, the problem can be simplified to a Schrödinger equation for the envelope functions.

Let us consider an InGaAs/AlInAs heterostructure like the one sketched in Fig. 1.3 in which the electron gas is confined in the $\hat{\mathbf{z}}$ direction, such that the electrons remain free to move in the $\hat{\mathbf{x}}-\hat{\mathbf{y}}$ plane. The envelope functions in the position basis $\mathbf{r} = \left(\mathbf{r}_\parallel, z\right)$ are written as:

$$\left\langle \mathbf{r} \middle| \lambda, \mathbf{k}_\parallel \right\rangle = \phi_\lambda(z) \frac{1}{\sqrt{S}} \mathrm{e}^{\mathrm{i}\mathbf{k}_\parallel \cdot \mathbf{r}_\parallel} \tag{1.14}$$

where $\mathbf{k}_\parallel$ is the wavevector in the $\hat{\mathbf{x}}-\hat{\mathbf{y}}$ plane, λ is the quantum number associated with the confinement in the $\hat{\mathbf{z}}$ direction, and S is the surface area. In the constant effective mass (parabolic band) approximation, the quantized energy levels are written:

$$E_{\lambda \mathbf{k}_\parallel} = E_\lambda + \frac{\hbar^2 k_\parallel^2}{2m^*} \tag{1.15}$$

The eigenstates of Eq. (1.14) represent plane waves in the $\hat{\mathbf{x}}-\hat{\mathbf{y}}$ plane multiplied by a wavefunction $\phi_\lambda(z)$ which depends on the confinement in the $\hat{\mathbf{z}}$ direction. Each λ indexes a subband, for which electrons may take on any value of $k_\parallel$ as illustrated in Fig. 1.3.

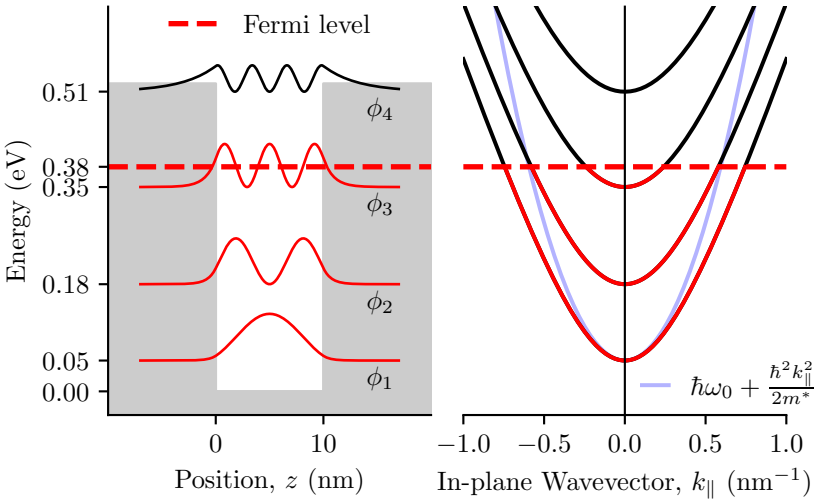

Fig. 1.3 The single particle eigenstates are presented for a 10 nm InGaAs/AlInAs well accounting for nonparabolicity. On the left, the square moduli $|\phi_\lambda(z)|^2$ are plotted at the energies $\hbar\omega_\lambda$ inside the well potential. On the right, the energy dispersion of the subbands as a function of the in-plane wavector is plotted. The dispersion for the first subband is also plotted for a constant effective mass of $0.041m_e$ to make apparent the strong nonparabolicity effects in InGaAs.

The envelope functions $\phi_\lambda(z)$ are solutions of the Schrödinger equation in the $\hat{\mathbf{z}}$ direction:

$$\left[-\frac{\hbar^2}{2}\frac{\partial}{\partial z}\frac{1}{m^*(E_\lambda,z)}\frac{\partial}{\partial z} + V_{\mathrm{CB}}(z)\right]\phi_\lambda(z) = E_\lambda\phi_\lambda(z) \tag{1.16}$$

The effective mass can be position and energy dependent. The position dependency reflects the different effective masses of the materials which constitute the heterostructure. The energy dependency is important for small band gap semiconductors.

The energy dependence of the effective mass can be calculated via the $\mathbf{k}\cdot\mathbf{p}$ method [149], in which case the nonparabolicity effect is found to originate due to the coupling between bands. Considering the coupling between the conduction, light hole, and split-off bands, the energy dependent effect mass can be written [119]:

$$m^*(E,z) = m_e\left[\frac{2}{3}\frac{E_\mathrm{p}}{E+E_\mathrm{g}(z)} + \frac{1}{3}\frac{E_\mathrm{p}}{E+E_\mathrm{g}(z)+E_\mathrm{so}(z)}\right]^{-1} \tag{1.17}$$

where E is the energy with respect to the bottom of the conduction band, E_g is the band gap energy, E_so is the split-off energy, and E_p is the Kane energy. For InGaAs lattice-matched to InP, $E_\mathrm{g}(T=0) = 0.816\,\mathrm{eV}$, $E_\mathrm{so} = 0.36\,\mathrm{eV}$, and $E_\mathrm{p} = 20.7\,\mathrm{eV}$ [2, 142, 152].

The nonparabolicity effect is significant in InGaAs. Furthermore, due to the high electronic densities investigated in this manuscript, electrons occupy and transition to states of large $k_\parallel$ well above the conduction band minimum, for which the parabolic approximation becomes increasingly inaccurate.

The electronic band structures studied in this work were calculated using either a program written within the Quantum Devices group, in which the nonparabolicity is treated according to the 3-band $\mathbf{k}\cdot\mathbf{p}$ model of Eq. (1.17); or using the commercial *nextnano* software [15] in which the nonparabolicity is treated by solving an 8-band $\mathbf{k}\cdot\mathbf{p}$ model.

With knowledge of the density of states of the system and the electron density N_{v}, the Fermi level inside the quantum well may be calculated. At zero temperature, states below the Fermi level are occupied, and states above the Fermi level are unoccupied. This is illustrated in Fig. 1.3 where red curves are used to indicate the subband states that are occupied. At nonzero temperatures, the electrons are thermally distributed across the subbands according to the Fermi-Dirac distribution.

The example InGaAs/AlInAs quantum well shown in Fig. 1.3 is only 10 nm wide and has only three occupied subbands. It was demonstrated in [8] that the Berreman mode is observed in heavily doped wide ($\sim$ 100 nm) quantum well structures where many ($\sim$ 10) subbands are occupied. In this regime, the spacing between the bound states E_λ is small ($<$ 10 meV) .

1.2.2.1 Self-Consistent Schrödinger-Poisson Solution

In heavily doped semiconductor heterostructures, inhomogeneous charge distributions may give rise to electrostatic interactions described by Poisson's equation $\nabla^2 V_\rho(z) = -\rho(z)/\varepsilon$ where $\rho(z)$ is a spatial charge distribution, $V_\rho(z)$ is its associated potential, and ε is the permittivity of the material.

Inhomogeneous charge distributions arise because positively charged ionized donors are fixed in space, while electrons can be free to move. While the volume density of the ionized donors at a given position $d(z)$ is set by the dopant impurity distribution during the sample growth, the positions of the electrons are determined by the probabilistic nature of their wavefunctions.

As an example, let us consider a narrow square quantum well with a single occupied subband ϕ_1. The volume density of electronic charge at a location z is $N\phi_1^*(z)\phi_1(z)$ where N is the total number of electrons, equal to the number of dopant impurities assuming perfect ionization. The net surface charge density in an infinitesimal sheet of width ∂z is then written [55]:

$$\sigma(z) = q\left[N\phi_1^*(z)\phi_1(z) - d(z)\right]\partial z \tag{1.18}$$

The probability amplitude given by $|\phi_1(z)|^2$ peaks in the center of the quantum well. Assuming that the donors are evenly distributed such that d does not vary with z, then the charge density $\sigma(z)$ also peaks in the center of the well. This results in a static electric field between the negatively charged center and the positively charged edges of the well. The above expression is easily generalized to the case of multiple occupied subbands by introducing a sum over the subbands of the spatial distribution of the volume charge *per subband*.

The electrostatic potential which results from an inhomogeneous charge distribution constitutes an additional potential term to be included in the Schrödinger equation: $V_{\mathrm{CB}} \rightarrow V_{\mathrm{CB}} + V_\rho$. The added term V_ρ is the Hartree potential [57]. As evident from the example of the single occupied subband, the Hartree term depends itself on the wavefunction solutions to the Schrödinger equation. The Schrödinger and Poisson equations are therefore coupled. The problem is solved by finding wavefunctions which are simultaneous solutions to both

equations. This is usually done numerically using an iterative method. The final form of the wavefunction solutions then accounts for the electrostatic Coulomb interactions.

In this manuscript, self-consistent solutions to the Schrödinger-Poission equations, when sought, were determined using either the freely available *1D Poisson* program [129] or the commercial *nextnano* software [15].

1.3 Semiclassical Description of Optical Response

Having now introduced the semiconductor material system and the discrete electronic states found when the electrons of the conduction band are confined, we turn now to describe the optical response of the system. The semi-classical Drude-Lorentz model describes all of the microscopic oscillators of the material system which respond to a time varying electric field, including free electrons, bound electrons (electron transitions), and later in Section 1.5, optical phonons.

1.3.1 Drude-Lorentz Model

To describe the motion of bound electrons, a restoring force must be added to Eq. (1.4), which was introduced to describe the free electron gas in the absence of damping. We also introduce a damping term. The resulting equation of motion constitutes the Drude-Lorentz model, and is written:

$$m^* \frac{\mathrm{d}^2 z(t)}{\mathrm{d}t^2} = -eE_0 \mathrm{e}^{-\mathrm{i}\omega t} - kz(t) - m^* \frac{\mathrm{d}z(t)}{\mathrm{d}t}\gamma \tag{1.19}$$

We look for solutions which oscillate at the frequency of the driving field such that $z(t) = z_0 \mathrm{e}^{-\mathrm{i}\omega t}$ where z_0 may be complex and find:

$$z_0 = \frac{eE_0}{m^*\omega^2 - k + \mathrm{i}m^*\gamma\omega} \tag{1.20}$$

Realizing that z_0 is maximized at the *resonance* condition where $k = m^*\omega^2$, we introduce the natural vibrational frequency $\omega_0 = \sqrt{k/m^*}$ so that z_0 may be written:

$$z_0 = \frac{eE_0}{m^*\left(\omega^2 - \omega_0^2 + \mathrm{i}\gamma\omega\right)} \tag{1.21}$$

Our solution for $z(t)$ describes the motion of a single harmonic oscillator. By considering a density N of identical harmonic oscillators, the polarization density can be defined as in Eq. (1.6). Inserting the expression for the polarization density into the definition of the displacement field (Eq. (1.2)), we find the following expression

$$D_0 = \epsilon_0 \left(1 - \frac{Ne^2}{\epsilon_0 m^*} \frac{1}{\left(\omega^2 - \omega_0^2 + \mathrm{i}\gamma\omega\right)}\right) E_0 \tag{1.22}$$

Since $\mathbf{D} = \varepsilon_\mathrm{r}\epsilon_0\mathbf{E}$, the relative dielectric function is found as:

$$\varepsilon_\mathrm{r}(\omega) = 1 - \frac{Ne^2}{\epsilon_0 m^*} \frac{1}{\left(\omega^2 - \omega_0^2 + \mathrm{i}\gamma\omega\right)} \tag{1.23}$$

Accounting for the nonresonant contributions due to the high frequency electronic transitions, the dielectric function is written:

$$\varepsilon_{\mathrm{r}}(\omega) = \varepsilon_{\infty} - \frac{Ne^2}{\epsilon_0 m^*} \frac{1}{(\omega^2 - \omega_0^2 + \mathrm{i}\gamma\omega)} \tag{1.24}$$

For $\omega \gg \omega_0$, $\varepsilon_{\mathrm{r}} \to \varepsilon_{\infty}$ implying that the oscillators with natural frequency ω_0 cannot keep up with the driving frequency. This dielectric function can be immediately generalized to describe the response of a medium with multiple resonances below the interband excitations by introducing a sum:

$$\varepsilon_{\mathrm{r}}(\omega) = \varepsilon_{\infty} - \frac{e^2}{\epsilon_0 m^*} \sum_j \frac{N_j}{\left(\omega^2 - \omega_j^2 + \mathrm{i}\gamma\omega\right)} \tag{1.25}$$

We may also define the static dielectric frequency for $\omega = 0$ as $\varepsilon_{\mathrm{s}} = \varepsilon_{\mathrm{r}}(0)$. With this definition, the dielectric function describing a medium with a single resonance takes the form:

$$\varepsilon_{\mathrm{r}}(\omega) = \varepsilon_{\infty} + \frac{(\varepsilon_{\mathrm{s}} - \varepsilon_{\infty})\,\omega_0^2}{\omega^2 - \omega_0^2 + \mathrm{i}\gamma\omega} \tag{1.26}$$

Drude Model

The Drude-Lorentz model is referred to as the Drude model when $\omega_0 = 0$. For this condition, the dielectric function of Eq. (1.24) describes a free electron gas. Introducing the screened plasma frequency as defined in Eq. (1.13), the complex dielectric function for the free electron gas in a semiconductor takes the simple form:

$$\varepsilon_{\mathrm{r}}(\omega) = \varepsilon_{\infty}\left(1 - \frac{\omega_{\mathrm{p}}^2}{\omega^2 + \mathrm{i}\gamma\omega}\right), \tag{1.27}$$

Letting $\varepsilon_{\infty} \to 1$ and $\gamma \to 0$, the dielectric function for the free electron introduced in Eq. (1.10) is recovered. In the presence of damping, the real part of the dielectric function for the free electron gas goes to zero for:

$$\omega^2 = \omega_{\mathrm{p}}^2 - \gamma^2 \tag{1.28}$$

1.3.2 Bound Electrons: Intersubband Transitions

Bound electrons are described classically by the equation of motion given by Eq. (1.19) when the restoring term is nonzero. It was demonstrated that the restoring term leads to a natural vibrational frequency for the system. This resonance frequency then appears in the dielectric function of Eq. (1.24) as ω_0. In quantum mechanics, ω_0 is a transition frequency between eigenstates of the system.

In degenerately doped semiconductor quantum wells, transitions can be induced between confined states in the conduction band. These transition are called intersubband transitions [57]. Because the momentum of the photon which induces the transition is negligible with respect to the electronic wavevector, the transitions can be described as vertical (same $k_{\|}$ for initial and final state). As sketched in the middle panel of Fig. 1.4, the transitions occur

between electronic subbands for all in-plane wavevectors $k_\parallel$ for which the initial state is occupied and the final state is unoccupied. Because the energy separation of the subbands is nearly independent of $k_\parallel$ (it is completely independent when nonparabolicty is neglected), resonances are observed in optical spectra at discrete transition frequencies ω_α.

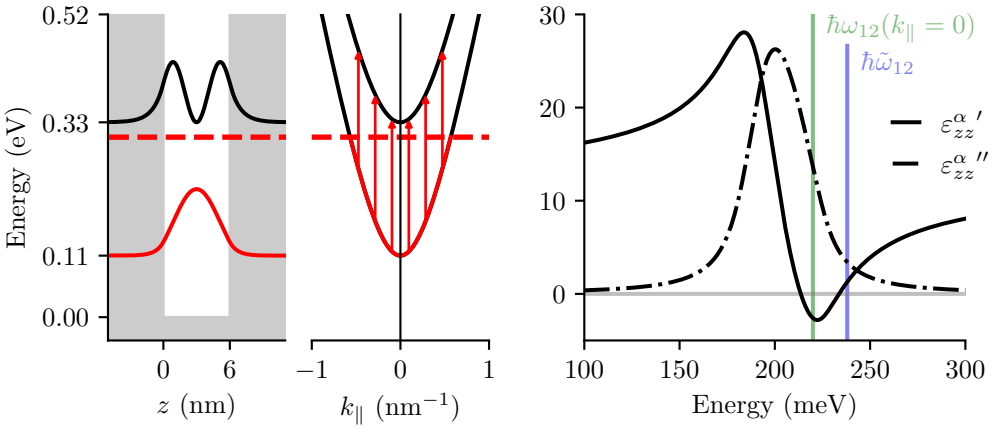

Fig. 1.4 The square-moduli of the bound state wavefunctions for a 6 nm InGaAs/AlInAs quantum well are plotted. The Fermi level is plotted as a dotted line for a volume electron density of $N_\mathrm{v} = 1 \times 10^{19}\,\mathrm{cm}^{-3}$. In the middle panel, the subband dispersion is plotted and optical transitions are sketched. On the right, the real and imaginary parts of the dielectric function Eq. (1.33) from the generalized Drude-Lorentz model are plotted.

An intersubband transition gives rise to a dipole moment between two bound states only in the confined $\hat{\mathbf{z}}$ direction. Therefore, the dielectric function which describes the quantum well is anisotropic. The in-plane components are described by the dielection function for the free electron gas found in Eq. (1.27).

In the $\hat{\mathbf{z}}$-direction, the optical response of a single intersubband transition α can be described with the dielectric function derived in Eq. (1.24) for an oscillator subject to a restoring force:

$$\varepsilon_{zz}^{\alpha}(\omega) = \varepsilon_\infty + \left(\frac{\Delta N_\alpha e^2}{L_\alpha^{\mathrm{eff}} \epsilon_0 m^*}\right) \frac{f_\alpha}{\omega_\alpha^2 - \omega^2 - \mathrm{i}\gamma\omega} \tag{1.29}$$

The volume electronic density N has been substituted with $\Delta N_\alpha \big/ L_\alpha^{\mathrm{eff}}$ where ΔN_α describes the difference in the surface density of electrons on the initial and final subbands and L_α^{eff} is an effective length, which is defined in accounting for the wave nature of the electrons [6, 101, 135]. The dimensionless oscillator strength f_α has been introduced. Classically, f_α would need to be introduced phenomenologically [45]. In quantum mechanics, f_α is determined by the dipole matrix element:

$$f_\alpha = \frac{2m^*\omega_\alpha}{\hbar} |\langle f|z|i\rangle|^2 \tag{1.30}$$

where $|i\rangle$ and $|f\rangle$ are initial and final states. Realizing that the numerator of the second term in Eq. (1.29) has units of frequency-squared, we may define a plasma frequency associated

with the transition α as [4, 135]:

$$\omega_{\mathrm{p}_\alpha}^2 = \frac{f_\alpha \Delta N_\alpha e^2}{\varepsilon_\infty L_\alpha^{\mathrm{eff}} \epsilon_0 m^*} \tag{1.31}$$

The dielectric function describing the intersubband transition α may then be written:

$$\varepsilon_{zz}^\alpha(\omega) = \varepsilon_\infty \left(1 + \frac{\omega_{\mathrm{p}_\alpha}^2}{\omega_\alpha^2 - \omega^2 - \mathrm{i}\gamma\omega}\right) \tag{1.32}$$

When nonparabolicity is considered, the subbands are not exactly parallel, and the transition energy depends on the in-plane wavevector $k_\parallel$. To account for this effect, the expression of Eq. (1.32) can be generalized [144] so that a different contribution to the permittivity is considered for each population of electrons with an in-plane wavevector in the infinitesimal interval $\mathrm{d}k_\parallel$:

$$\varepsilon_{zz}^\alpha(\omega) = \varepsilon_\infty \left(1 + \int_0^\infty \frac{\omega_{\mathrm{p}_\alpha}^2\left(k_\parallel\right)}{\omega_\alpha^2\left(k_\parallel\right) - \omega^2 - \mathrm{i}\gamma\omega} \mathrm{d}k_\parallel\right) \tag{1.33}$$

where

$$\omega_{\mathrm{p}_\alpha}^2\left(k_\parallel\right) = \frac{f_\alpha \Delta N_\alpha\left(k_\parallel\right) e^2}{\varepsilon_\infty L_\alpha^{\mathrm{eff}} \epsilon_0 m^*\left(k_\parallel\right)} \tag{1.34}$$

The real and imaginary parts of ε_{zz}^α are plotted in Fig. 1.4. They have the usual form for a Lorentz dipole oscillator: the real part oscillates once, crossing the origin twice at the *zeroes* of the dielectric function; the imaginary part peaks once at the *pole* of the dielectric function. The higher energy zero, at which the real part of ε_{zz}^α goes from negative to positive, is denoted $\hbar\tilde{\omega}_{12}$. As a consequence of nonparabolicity, the energy at which the imaginary part peaks is redshifted from the transition energy at $k_\parallel = 0$.

As the width of a quantum well is increased, the number of bound states increases. A quantum well with multiple bound states can have multiple intersubband transitions, although the transitions must occur between states of opposite parity in order to be dipole-active [57]. The dielectric function of Eq. (1.33) is easily generalized to multiple intersubband transitions by considering the additive contribution of each transition α to the permittivity:

$$\varepsilon_{zz}(\omega) = \varepsilon_\infty \left(1 + \sum_\alpha \int_0^\infty \frac{\omega_{\mathrm{p}_\alpha}^2\left(k_\parallel\right)}{\omega_\alpha^2\left(k_\parallel\right) - \omega^2 - \mathrm{i}\gamma\omega} \mathrm{d}k_\parallel\right) \tag{1.35}$$

In Fig. 1.5, a 9 nm InGaAs/AlInAs quantum well is pictured with three bound states, two of which are occupied. Optical transitions can take place between the first and second bound states ω_{12} and between the second and third bound states ω_{23}. The subbands of the three bound states are plotted in the center panel. Electronic transitions are sketched between occupied and unoccupied states of the subbands. As a consequence of Pauli blocking, only electrons which lie close to the Fermi level participate in optical transitions.

The real and imaginary parts of the dielectric function ε_{zz} (Eq. (1.35)) for the heavily doped 9 nm well are plotted in the right panel of Fig. 1.5. The imaginary part peaks twice, indicating two poles, as expected since ε_{zz} is determined as the sum of two Lorentzian

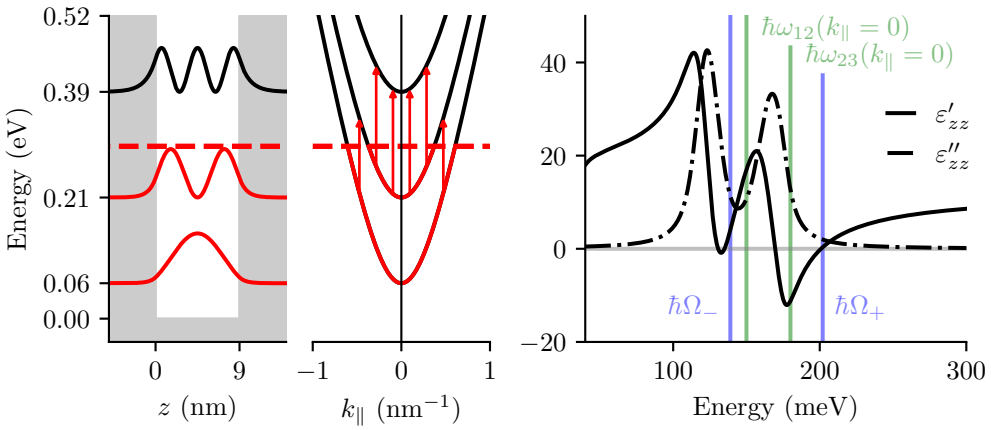

Fig. 1.5 The square moduli of the wavefunctions and the subband dispersion are shown for the three bound states of a 9 nm InGaAs/AlInAs quantum well. The Fermi level is plotted as a dotted line for a volume electron density of $N_\mathrm{v} = 1 \times 10^{19}\,\mathrm{cm}^{-3}$. On the right, the real and imaginary parts of the dielectric function calculated from Eq. (1.35) for two intersubband transitions are plotted.

contributions. The poles are redshifted with respect to the $k_\parallel = 0$ transition energies due to nonparabolicity. The real part of the dielectric function is observed to oscillate twice, crossing the origin a total of four times. The two zero crossings at which the real part goes from negative to positive are denoted $\hbar\Omega_\pm$.

1.3.3 Optical Response of Electron Gas in Wide Quantum Wells

The Drude-Lorentz model is well suited to describe the optical response of an electron gas confined in a thin semiconductor layer, since it naturally accounts for size confinement. In the previous section, the model was applied to two cases in which the size confinement was significant. In this section, we demonstrate that the model can also be used to describe the optical response of a large quantum well, in which case the size confinement is nearly negligible. In the absence of any size confinement, the classical description of the Berreman mode from Section 1.1.1 is recovered.

The band structure of a wide, heavily doped 100 nm InGaAs/AlInAs quantum well is shown in Fig. 1.6. The 100 nm well, doped with an electronic density of $N_\mathrm{v} = 1 \times 10^{19}\,\mathrm{cm}^{-3}$, has 32 bound states, 21 of which are occupied.

Just as for the case of the 9 nm well, the dielectric function is constructed by summing the contributions from all of the allowed transitions between single particle states in the quantum well, according to Eq. (1.35).

To describe the Berreman mode, only the contributions from electronic transitions between adjacent subbands need be considered. It will be demonstrated in Chapter 4 that the consideration of optically active transitions between odd numbers of states greater than one will naturally lead to a description of higher order collective modes, which are experimentally observed at energies greater than the Berreman mode [138].

Since the levels of the 100 nm quantum well are closely spaced, calculating ε_{zz} according

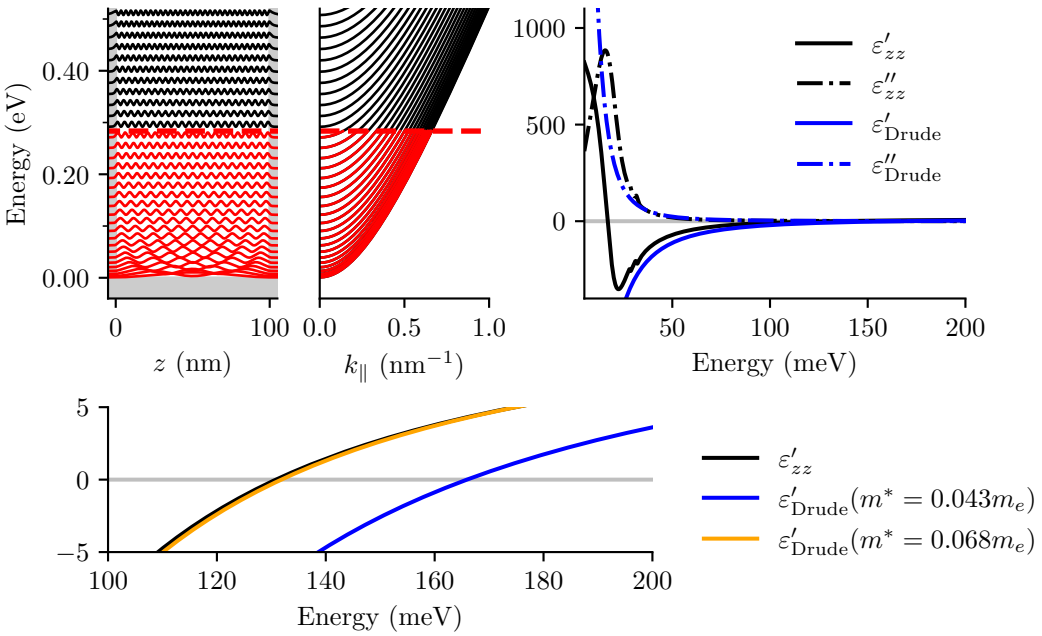

Fig. 1.6 The square moduli of the wavefunctions for a 100 nm InGaAs/AlInAs quantum well are plotted. The Fermi level is indicated with a dotted line for a volume electron density of $N_\mathrm{v} = 1 \times 10^{19}\,\mathrm{cm}^{-3}$. The subband dispersion is plotted for positive values of $k_\parallel$. Note that the subbands are symmetric for $k_\parallel \leftrightarrow -k_\parallel$. In the upper right, the dielectric function ε_{zz} calculated from Eq. (1.35) for the 100 nm well and the dielectric function from the Drude model are compared. On the bottom, the real part of ε_{zz} is plotted with the real part of $\varepsilon_\mathrm{Drude}$ for different effective masses.

to Eq. (1.35) for transitions between consecutive subbands corresponds to considering the sum of many Lorentzian oscillators at small transition frequencies. The resulting dielectric function, plotted in upper right panel of Fig. 1.6, is similar in form to the Drude dielectric function $\varepsilon_\mathrm{Drude}$ from Eq. (1.27) for energies larger than a few meV. For comparison, the real and imaginary parts of $\varepsilon_\mathrm{Drude}$ are plotted in the same panel, for an electron density of $N_\mathrm{v} = 1 \times 10^{19}\,\mathrm{cm}^{-3}$, using the value of the effective mass at the conduction band minimum of $m^* = 0.043m_e$. Whereas the real and imaginary parts of $\varepsilon_\mathrm{Drude}$ diverge toward zero, the real and imaginary parts of ε_{zz} exhibit a resonant feature at an energy on the order of the level spacing.

In the bottom panel of Fig. 1.6, ε'_{zz} and $\varepsilon'_\mathrm{Drude}$ from the upper right panel are re-plotted on a scale for which the zeros can be more easily identified. The zeros are found at 131 meV and 166 meV, respectively. In the same panel, $\varepsilon'_\mathrm{Drude}$ is plotted for a heavier effective mass of $0.068m_e$, in which case the zero crossing of ε'_{zz} is reproduced. Recall that $\varepsilon'_\mathrm{Drude}$ crosses zero at the plasma frequency (Eq. (1.13)), which scales with $1\Big/\sqrt{m^*}$.

That a heavier effective mass must be used in the Drude model to reproduce ε'_{zz} is a consequence of considering the energy dependence of the effective mass (nonparabolicity) in the calculation of ε_{zz}. The electronic transitions between adjacent subbands which contribute

to ε_{zz} must occur within the vicinity of the Fermi level, which lies 284 meV above the bottom of the conduction band. At this energy, the effective mass calculated according to Eq. (1.17) is significantly heavier than the $0.43m_e$ mass at the bottom of the conduction band.

In the Drude model, the electronic density and the constant effective mass are independent inputs. Calculating the dielectric function according to Eq. (1.35) has the advantage that the electronic density implicitly sets the effective mass.

To show that ε_{zz} calculated according to Eq. (1.35) is well suited to describe the effect of confinement on the optical response of the electron gas, ε'_{zz} is plotted in Fig. 1.7 for quantum wells of various widths, identically doped with an electronic density of $N_\mathrm{v} = 1 \times 10^{19}\,\mathrm{cm}^{-3}$. As the well width is reduced, the energy at which ε'_{zz} crosses zero, and therefore the energy at which the resonance is observed, shifts to higher energy. The blueshifting of the Berreman mode with decreasing well width was experimentally observed in [8]. In the same work, the dielectric function of Eq. (1.35) was shown to describe well the experimental results.

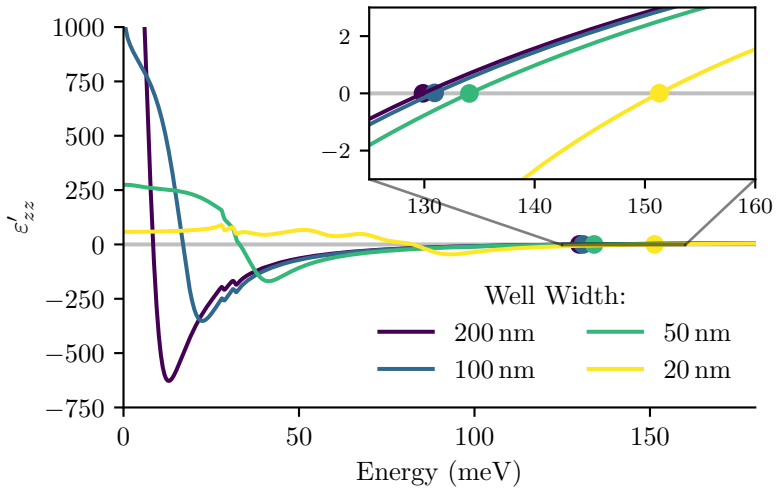

Fig. 1.7 The real part of the dielectric function calculated according to Eq. (1.35) for InGaAs/AlInAs wells of varying width but constant electronic density of $N_\mathrm{v} = 1 \times 10^{19}\,\mathrm{cm}^{-3}$.

It is important to point out that the Drude model alone cannot self-consistently describe a different resonance energy for wells of different widths: the energy of the zero crossing of $\varepsilon'_\mathrm{Drude}$ is fixed only by m^* and N_v through the plasma frequency. In the classical Drude model, neither of these quantities has any dependence on the system dimensions.

In this section and the previous, it was demonstrated that a dielectric function which describes an electron gas in the confined regime can be constructed from a proper summation of the contributions of optically active single particle intersubband transitions. There are two favorable aspects of describing the response of the electron gas in this manner which are worth remarking upon. First, the model describes in an identical manner the optical response of the electron gas across two vastly different confinement regimes. Second, and most conveniently, the model permits a semiclassical description of the optical response of the many body electron gas in term of quantities which can be easily calculated, namely the single particle bound states.

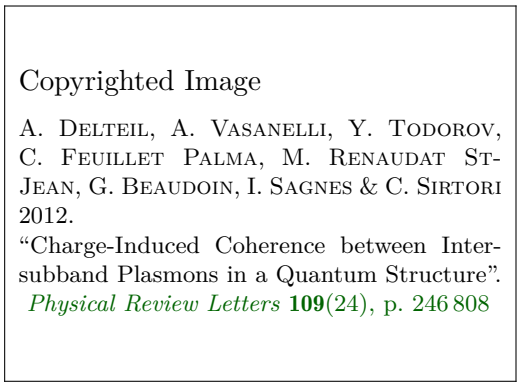

(a) Band structure of 18.5 nm well

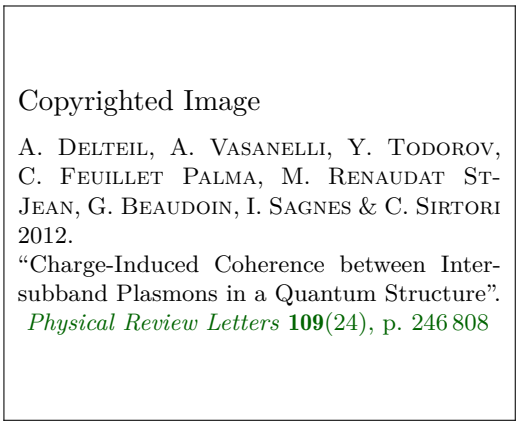

(b) Absorption Spectra

Fig. 1.8 The intersubband transitions, plotted as vertical arrows in (a), are described by the dielectric function plotted in the inset of (b), used in Eq. (1.36) to calculate the absorption spectrum plotted on the main axis of (b) in blue and shaded grey. The experimentally measured resonances are plotted in black and red. Figures reproduced from [34] with modifications.

In Chapter 4, a fully quantum model will be introduced in which the the collective response of the confined electron gas is calculated starting from the basis of single particle optical transitions in analogy to what has been demonstrated semi-classically here. The same favorable aspects of the semi-classical model are exploited in the quantum model.

1.4 Collective Effects in the Optical Spectra of Thin Films

In thin films, optical resonances are not observed at the poles of the dielectric function, but rather at the zeros. This phenomenon is dramatically demonstrated by the experimentally measured spectra of an 18.5 nm InGaAs quantum well doped with an electronic density of $1.19 \times 10^{19}\,\mathrm{cm}^{-3}$ reported in [34] and reproduced in Fig. 1.8b.

The band structure of the 18.5 nm InGaAs is plotted in Fig. 1.8a. There are four subbands populated with electrons, resulting in four intersubband transitions between adjacent levels. The real and imaginary parts of the dielectric function calculated according to Eq. (1.35) are plotted in the inset of Fig. 1.8b. The dielectric function has four poles, one for each intersubband transition, which are identifiable as the four peaks of ε''_{zz}.

For a weakly absorbing *homogeneous* medium of complex dielectric function $\varepsilon_\mathrm{r}(\omega)$, the absorption coefficient is written [45]:

$$\alpha = \frac{\omega}{c}\frac{\varepsilon''_\mathrm{r}}{\sqrt{\varepsilon'_\mathrm{r}}} \tag{1.36}$$

Apart from a small deviation due to the frequency dependence of ε'_r, the resonances in α occur where ε''_r peaks. With a blue line and a shaded area, the spectrum of Eq. (1.36) is plotted in Fig. 1.8b for the dielectric function of the 18.5 nm InGaAs quantum well. Four peaks are observed corresponding to the four intersubband transitions.

On the same axis, experimental absorption spectra of the 18.5 nm InGaAs quantum well measured at a 45° angle at T=77 K and T=300 K are plotted. In the experimental spectra, a single resonance is observed near 165 meV, which corresponds to the zero crossing of ε'_{zz}.

The fact that a single resonance is observed at the zero of the dielectric function instead of multiple resonances at the poles is due to collective effects. An electron undergoing an intersubband transition is sensitive to the electric field generated from the polarization due to the other electrons undergoing transitions. This is called the depolarization effect and formally "arises because each electron feels a field which is different from the external field by the mean Hartree field of other electrons polarized by the external field" [6].

Since each electron which undergoes a transition gives rise to an optical dipole, the collective phenomenon can be described as the dipole-dipole coupling of all the electrons participating in transitions [34]. In the case of many occupied subbands, such as the heavily doped 18.5 nm InGaAs well, this results in the dramatic effect that all of the oscillator strength is coupled into a single bright mode, giving rise to the *multisubband plasmon* [34].

In Section 1.4.1, the optical condition for which thin film resonances are observed, namely that $\varepsilon' = 0$, is tied to a microscopic description of the collective effects. A simple equation of motion model is introduced which captures the essential physics of the depolarization effect. The model is demonstrated to reproduce well-known experimentally observed phenomena in which collective effects are known to play an important role. To the best of the author's knowledge, this conceptually simple model is described here for the first time.

Then, in Section 1.4.2, an expression for the absorption coefficient is found which correctly describes the experimentally observed resonance energies in accounting for the depolarization effect.

1.4.1 Depolarization Effect in Equations of Motion

In the first section of this chapter, a restoring term of the form $eE_z \propto z$ was added to the equation of motion for free electrons to describe their motion in a thin film when driven by an oscillating external field. The restoring field E_z is the uniform electric field inside the slab due to the presence of surface charge $\sigma = \pm Nez$ resulting from the uniform polarization of the medium: $E_z = \sigma/\epsilon_0$. The restoring term describes the force on each electron from the field which arises due to the collective polarization of the medium and the thin film geometry of the problem. Consequently, the inclusion of the restoring term in the equation of motion accounts for the depolarization effect.

In the following subsections, equations of motion which describe intersubband transitions are considered when a similar restoring term is included. The solutions of the modified equations of motions are found to describe the resonance energies which are experimentally observed.

Depolarization Shift for Single Intersubband Transition

Let us consider the equation of motion for an electron in the presence of N_α intersubband oscillators per unit volume. The equation of motion has the form of Eq. (1.19) plus the additional restoring term. The volume density of charge participating in an intersubband

transition α is written $N_\alpha = \Delta N_\alpha \Big/ L_\alpha^{\text{eff}}$. The equation of motion takes the form:

$$m^* \frac{\mathrm{d}^2 z}{\mathrm{d}t^2} = \frac{-N_\alpha e^2}{\epsilon_0} z - m^* \omega_\alpha^2 z + eE_0 \mathrm{e}^{-\mathrm{i}\omega t} \tag{1.37}$$

where ω_α is the frequency of the intersubband transition. The solution to this equation of motion is written as

$$z(t) = \frac{eE_0}{m^* \left(\omega_{\mathrm{p}_\alpha}^2 + \omega_\alpha^2 - \omega^2\right)} \mathrm{e}^{-\mathrm{i}\omega t} \tag{1.38}$$

where $\omega_{\mathrm{p}_\alpha}$ is as defined in Eq. (1.31). The resonance frequency is not at the intersubband transition frequency ω_α but rather at the blueshifted frequency:

$$\tilde{\omega}_\alpha = \sqrt{\omega_{\mathrm{p}_\alpha}^2 + \omega_\alpha^2} \tag{1.39}$$

As will be seen in Section 1.4.2, it is at this frequency that a resonance is observed in the absorption spectrum.

This well-known phenomenon is referred to as the depolarization shift [6, 57], and was first described by Chen et al [22]. It is a collective effect since an electron feels a force due to the electric field resulting from the collective polarization of the electron gas.

The collective nature of the effect is underlined by its dependence on the electronic density. For a small electronic density such that $\omega_{\mathrm{p}_\alpha} \ll \omega_\alpha$, the observed transition $\tilde{\omega}_\alpha$ occurs at the bare 'single particle' transition frequency ω_α, and the depolarization shift is negligible. In the regime where $\omega_{\mathrm{p}_\alpha}$ is on the order of ω_α, the depolarization effect cannot be neglected, and the collective electronic excitation is referred to as an intersubband plasmon [137, 147].

It is found upon substituting $\tilde{\omega}_\alpha$ into Eq. (1.29) that the real part of the dielectric function for a single intersubband transition crosses zero at $\tilde{\omega}_\alpha$. This links the solutions to Eq. (1.37) with the optical condition at which the intersubband transitions are observed, namely that $\varepsilon'_{zz} = 0$.

Coupled Intersubband Oscillators

We now consider the case of two intersubband transitions α and β. Each oscillating electron is described by an equation of motion of the form of Eq. (1.19) with two added restoring terms. One restoring term originates from the displacement of the N_α charge density, while the other originates from the displacement of the N_β charge density. The equations of motion for the two intersubband transitions are coupled:

$$\begin{aligned} m^* \frac{\mathrm{d}^2 z_\alpha}{\mathrm{d}t^2} &= \frac{-N_\alpha e^2}{\epsilon_0} z_\alpha - m^* \omega_\alpha^2 z_\alpha + eE_0 \mathrm{e}^{-\mathrm{i}\omega t} - \frac{N_\beta e^2}{\epsilon_0} z_\beta \\ m^* \frac{\mathrm{d}^2 z_\beta}{\mathrm{d}t^2} &= \frac{-N_\beta e^2}{\epsilon_0} z_\beta - m^* \omega_\beta^2 z_\beta + eE_0 \mathrm{e}^{-\mathrm{i}\omega t} - \frac{N_\alpha e^2}{\epsilon_0} z_\alpha \end{aligned} \tag{1.40}$$

Each equation contains a term which describes a capacitive force originating from the polarization induced by the other oscillator. The set of coupled differential equations is simply a coupled oscillator problem.

The solutions, or *modes*, of the set of coupled differential equations are found to oscillate at the frequencies given by:

$$\Omega_{\pm}^2 = \frac{1}{2}\left(\tilde{\omega}_\alpha^2 + \tilde{\omega}_\beta^2 \pm \sqrt{\left(\tilde{\omega}_\alpha^2 - \tilde{\omega}_\beta^2\right)^2 + 4\omega_{\mathrm{p}\alpha}^2\omega_{\mathrm{p}\beta}^2}\right) \tag{1.41}$$

where the frequencies $\tilde{\omega}_\alpha$ and $\tilde{\omega}_\beta$ are as defined in Eq. (1.39). Unsurprisingly, the coupled mode solutions oscillate at frequencies different from those of the uncoupled oscillators, ω_α and ω_β. As shown in Fig. 1.5 for the case of the 9 nm quantum well with 2 occupied subbands, the real part of the dielectric function crosses zero at the energies $\hbar\Omega_\pm$. The solutions to Eq. (1.41) are thus linked with the optical condition at which the intersubband transitions are observed, namely that $\varepsilon'_{zz} = 0$.

It is interesting that a restoring term of the same form which is found to give rise to the depolarization shift for the single intersubband transition is also responsible for the coupling between multiple intersubband transitions. The two phenomena are linked because they are both collective effects which work through the Coulomb force. It is easy to see that the solutions $\Omega_\pm$ tend toward the uncoupled transition frequencies ω_α and ω_β when the electronic densities N_α and N_β are small.

The Coulombic coupling between two intersubband oscillators was experimentally studied in [35, 144]. In these works, two absorption resonances were observed at the two energies for which $\varepsilon'_{zz} = 0$, and therefore the energies $\hbar\Omega_\pm$ found in the coupled oscillator model above.

1.4.2 The Electron Energy Loss Function

Thus far, we have calculated the normal modes of bound and free charges oscillating in the normal direction of a thin film by adding to the equation of motion an additional term which describes a uniform electric field inside the medium. While this approach correctly describes the energies of the new modes of the system, it does not lend itself toward a straightforward calculation of the optical properties of the system, such as the absorption.

We wish to calculate the absorption in a thin film starting from the dielectric functions defined in Section 1.3, which were derived from an equation of motion without a depolarization term. The depolarization effect is not an inherent property of the material response, but is determined by the geometry of the electromagnetic problem, so it is not appropriate to already include the depolarization effect in the definition of a dielectric function.

The response of a medium to an electromagnetic field may be described equivalently through the electrical conductivity σ or the dielectric function, which are related through:

$$\varepsilon_{\mathrm{r}}(\omega) = \varepsilon_\infty + \frac{\mathrm{i}\sigma}{\epsilon_0\omega} \tag{1.42}$$

As before, the high frequency dielectric constant ε_∞ describes the response at frequencies just below the interband edge. Then, σ describes the response of the oscillators of interest well below interband transition frequencies.

We now consider p-polarized light incident from a medium with dielectric constant $\varepsilon^{\mathrm{out}}$ at an oblique angle to a thin film with normal direction $\hat{\mathbf{z}}$. The optical response of the film is described by Eq. (1.42). The current per unit area induced in the film in the $\hat{\mathbf{z}}$ direction is given by:

$$J_z = \sigma_{zz} E_z^{\mathrm{in}} \tag{1.43}$$

where σ_{zz} is an electrical conductivity (units of siemens/meter), and E_z^{in} is the z-component of the total electric field in the film.

Since there are no external charges in the system, the displacement field normal to the boundary, D_z, is continuous. The electric field inside the slab may then be related to the electric field outside the slab:

$$\varepsilon^{\text{out}} E_z^{\text{out}} = \varepsilon_{\text{r}}(\omega) E_z^{\text{in}} \tag{1.44}$$

The current density induced in the film may then be written in terms of the external field E_z^{out}:

$$J_z = \sigma_{zz} \frac{\varepsilon^{\text{out}}}{\varepsilon_{\text{r}}(\omega)} E_z^{\text{out}} \equiv \tilde{\sigma}_{zz} E_z^{\text{out}} \tag{1.45}$$

A modified conductivity $\tilde{\sigma}_{zz}$ has been defined which describes the response to the external field [6].

Using the expression of Eq. (1.42), the absorption coefficient α defined in Eq. (1.36) can be rewritten in terms of the conductivity as:

$$\alpha = \frac{-\operatorname{Re}\{\sigma\}}{\epsilon_0 c \sqrt{\varepsilon'}} \tag{1.46}$$

Substituting the effective conductivity $\tilde{\sigma}$ into this expression, the absorption coefficient describing the ohmic losses in the thin film induced by the external field is found as:

$$\alpha = \frac{-\operatorname{Re}\{\tilde{\sigma}\}}{\epsilon_0 c \sqrt{\varepsilon'}} = \operatorname{Im}\left\{\frac{-1}{\varepsilon_{\text{r}}}\right\} \frac{\varepsilon_\infty \varepsilon^{\text{out}} \omega}{c \sqrt{\varepsilon'}} \tag{1.47}$$

The resonances in α occur at the zeros of the dielectric function ε_{r}, and not at the poles,[3] as they do when the expression of Eq. (1.36) is used to calculate α.

The expression for α found in Eq. (1.47) takes into account the depolarization effect, unlike the expression of Eq. (1.36). Since the depolarization effect is a collective effect, calculating α via Eq. (1.47) is equivalent to considering *collective* effects. Then, Eq. (1.36) is said to describe the *single particle* absorption spectrum.

The expression $\operatorname{Im}\{\varepsilon^{-1}\}$ is used in electron energy loss spectroscopy (EELS) to describe characteristic energy loss spectra, and is sometimes called the electron energy loss function [30, 54, 109, 148]. In these experiments, a beam of mono-energetic electrons is sent through a solid. After passing through the solid, the energy of the electrons is measured. The quantities of energy lost by the electrons correspond to the excitation energies of single particle and collective excitations in the solid [105, 110]. Because the impinging beam of electrons carries a longitudinal wave, it can excite longitudinal oscillations in bulk material, including plasma oscillations, which cannot be excited by a transverse wave.

In the following sections, the expression for the absorption found in Eq. (1.47) is used to calculate the absorption coefficient for the cases already introduced in this chapter: the free electron gas in a thin film, a quantum well with a single intersubband transition, and a quantum well with multiple intersubband transitions.

[3] This is easy to see: Let $\varepsilon = a + ib$, then, $\operatorname{Im}\left\{\frac{-1}{\varepsilon}\right\} = \frac{b}{a^2 + b^2}$ which peaks when $a = 0$

Absorption of Free Electron Gas in a Thin Film

The resonant absorption feature (Berreman mode) which arises for a free electron gas in a thin film is easily found upon substituting the dielectric function of Eq. (1.27) for the free electron gas into Eq. (1.47):

$$\alpha = \frac{\varepsilon^{\text{out}}}{c\sqrt{\varepsilon'}} \frac{\omega^2 \omega_{\text{p}}^2 \gamma}{\left(\omega^2 - \omega_{\text{p}}^2\right)^2 + \gamma^2 \omega^2} \tag{1.48}$$

This function peaks at the plasma frequency ω_{p}. The resonant behavior at ω_{p} is exactly what is predicted from the solution of the equation of motion describing the free electron gas in a thin film in the presence of the depolarization field found in Eq. (1.12).

Absorption of a Single Intersubband Transition

Let us show that the expression of Eq. (1.47) describes the depolarization shift for a single intersubband transition in a quantum well. Since the absorption is proportional to $\text{Im}\{\varepsilon^{-1}\}$, we invert the dielectric function of Eq. (1.32) describing an intersubband transition α to find:

$$\frac{\varepsilon_\infty}{\epsilon_r(\omega)} = 1 + \frac{\omega_{\text{p}_\alpha}^2}{\omega^2 - \tilde{\omega}_\alpha^2 + \text{i}\gamma\omega} \tag{1.49}$$

where $\tilde{\omega}_\alpha$ is as defined in Eq. (1.39). From Eq. (1.47), the shape of the absorption spectrum is given by:

$$\alpha = \frac{\varepsilon^{\text{out}}}{c\sqrt{\varepsilon'}} \frac{\omega^2 \omega_{\text{p}_\alpha}^2 \gamma}{\left(\omega^2 - \tilde{\omega}_\alpha^2\right)^2 + \gamma^2 \omega^2} \tag{1.50}$$

This function peaks at the depolarization shifted frequency $\tilde{\omega}_\alpha$. For $\omega \approx \tilde{\omega}_\alpha$, the function simplifies to a Lorentzian centered at the frequency $\tilde{\omega}_\alpha$.

In Fig. 1.9, the collective and single particle absorption spectra are plotted for the 6 nm InGaAs/AlInAs quantum well considered in Fig. 1.4. The spectra are calculated from the dielectric function determined in accounting for nonparabolicity. The collective effects not only blueshift the resonance from the bare transition frequency, but also narrow the linewidth which is broadened by nonparabolicity in the single particle spectrum.

Absorption of Two Coupled Intersubband Transitions

Let us show that the expression of Eq. (1.47) applied to a quantum well with two intersubband transitions results in two resonant absorption peaks shifted from the bare transition frequencies. From Eq. (1.25), the dielectric function describing two intersubband transitions α and β neglecting nonparabolicity is written:

$$\varepsilon_{\text{r}}(\omega) = \varepsilon_\infty \left(1 + \frac{\omega_{\text{p}_\alpha}^2}{\omega_\alpha^2 - \omega^2 - \text{i}\gamma\omega} + \frac{\omega_{\text{p}_\beta}^2}{\omega_\beta^2 - \omega^2 - \text{i}\gamma\omega}\right) \tag{1.51}$$

After a great deal of manipulation [36, 101], the inverse of the dielectric function can be written as:

$$\frac{\varepsilon_\infty}{\varepsilon(\omega)} = 1 + \frac{A_{\text{p}_+}^2}{\omega^2 - \Omega_+^2 + \text{i}\gamma\omega} + \frac{A_{\text{p}_-}^2}{\omega^2 - \Omega_-^2 + \text{i}\gamma\omega} \tag{1.52}$$

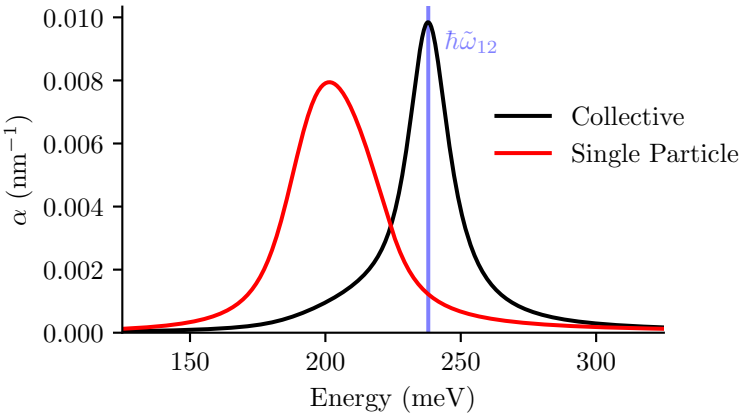

Fig. 1.9 The absorption coefficient is plotted for 6 nm InGaAs/AlInAs quantum well doped with electronic density of $N_{\mathrm{v}} = 1 \times 10^{19}\,\mathrm{cm}^{-3}$, with and without the consideration of collective effects.

where the coupled mode resonances $\Omega_{\pm}$ are given as:

$$\Omega_{\pm}^2 = \frac{1}{2}\left(\tilde{\omega}_{\alpha}^2 + \tilde{\omega}_{\beta}^2 \pm \sqrt{\left(\tilde{\omega}_{\alpha}^2 - \tilde{\omega}_{\beta}^2\right)^2 + 4\omega_{\mathrm{p}_{\alpha}}^2 \omega_{\mathrm{p}_{\beta}}^2}\right) \tag{1.53}$$

and the amplitudes $A_{\mathrm{p}_{\pm}}$:

$$A_{\mathrm{p}_{\pm}} = K_{\pm}\left(\omega_{\mathrm{p}_{\alpha}}^2 + \omega_{\mathrm{p}_{\beta}}^2\right) \tag{1.54}$$

with:

$$K_{\pm} = \frac{1}{2} \pm \frac{\left(\tilde{\omega}_{\alpha}^2 - \tilde{\omega}_{\beta}^2\right)\left(\omega_{\mathrm{p}_{\alpha}}^2 - \omega_{\mathrm{p}_{\beta}}^2\right) + 4\omega_{\mathrm{p}_{\alpha}}^2 \omega_{\mathrm{p}_{\beta}}^2}{2\left(\omega_{\mathrm{p}_{\alpha}}^2 + \omega_{\mathrm{p}_{\beta}}^2\right)\sqrt{\left(\tilde{\omega}_{\alpha}^2 - \tilde{\omega}_{\beta}^2\right)^2 + 4\omega_{\mathrm{p}_{\alpha}}^2 \omega_{\mathrm{p}_{\beta}}^2}} \tag{1.55}$$

Taking the imaginary part of Eq. (1.52), Eq. (1.47) yields:

$$\alpha = \frac{\varepsilon^{\mathrm{out}}}{c\sqrt{\varepsilon'}}\left(\frac{\omega^2 A_{\mathrm{p}_+}^2 \gamma}{\left(\omega^2 - \Omega_+^2\right)^2 + \gamma^2\omega^2} + \frac{\omega^2 A_{\mathrm{p}_-}^2 \gamma}{\left(\omega^2 - \Omega_-^2\right)^2 + \gamma^2\omega^2}\right) \tag{1.56}$$

This function peaks at the coupled mode frequencies $\Omega_{\pm}$. For $\omega \approx \Omega_{\pm}$ the two terms simplify to Lorentzian lineshapes with amplitudes of $A_{\mathrm{p}_{\pm}}$.

The amplitudes $A_{\mathrm{p}_{\pm}}$ of the coupled modes appear as effective plasma frequencies, which through Eq. (1.54) are related to the plasma frequencies of the α and β transitions. Through the form of $A_{\mathrm{p}_{\pm}}$, the oscillator strength of the α and β transitions is renormalized into the two normal modes.

The frequencies $\Omega_{\pm}$ are identical to the solutions found in Eq. (1.41) for the coupled equations of motion describing two intersubband oscillators subjected to restoring terms arising from collective charge oscillations.

In Fig. 1.10, the collective and single particle absorption spectra are plotted for the 9 nm InGaAs/AlInAs quantum well considered in Fig. 1.5 accounting for nonparabolicity. The collective effects blueshift both of the single particle resonances, redistribute the oscillator strength, and counteract the broadening effect nonparabolicity has on the single particle linewidths.

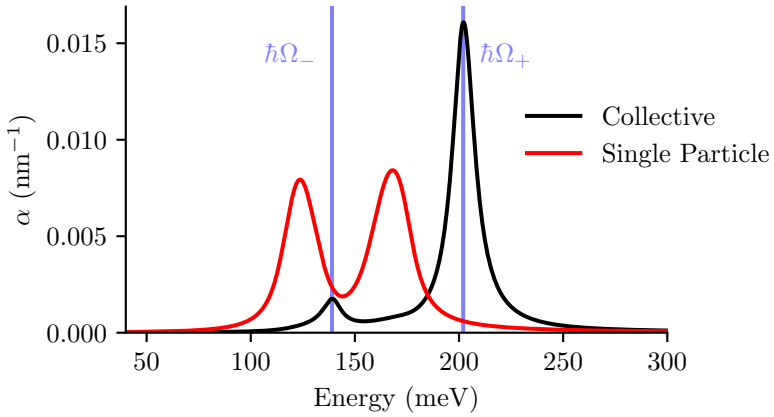

Fig. 1.10 The absorption coefficient is plotted for a 9 nm InGaAs/AlInAs quantum well doped with electronic density of $N_{\mathrm{v}} = 1 \times 10^{19}\,\mathrm{cm}^{-3}$, with and without the consideration of collective effects.

Absorption of Berreman Modes of Confined Electron Gas

In Fig. 1.11, the absorption spectra calculated from Eq. (1.47) are plotted in solid lines for the wide heavily doped quantum wells of varying width for which ε'_{zz} was plotted in Fig. 1.7. As expected, the Berreman mode resonances occur at the energies for which $\varepsilon'_{zz} = 0$ and blueshift as the electron gas is increasingly confined.

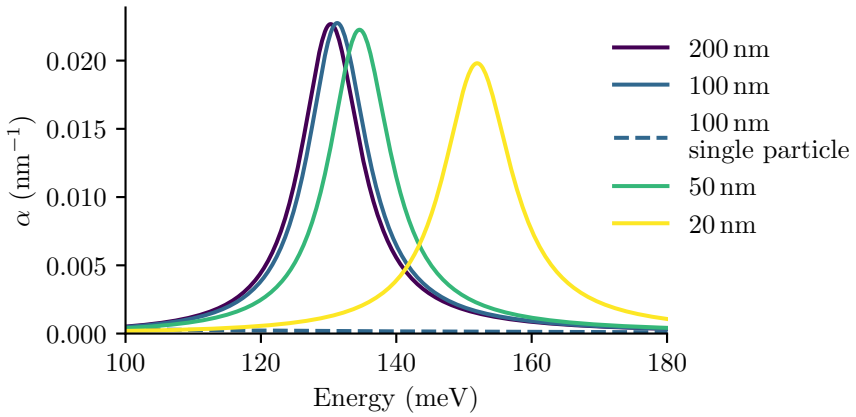

Fig. 1.11 The absorption coefficient is plotted for InGaAs/AlInAs quantum wells of various widths doped with electronic density of $N_{\mathrm{v}} = 1 \times 10^{19}\,\mathrm{cm}^{-3}$.

The single particle absorption spectrum is plotted for the 100 nm well, and shows no feature over the energy range plotted.

1.5 Optical Phonons

Throughout most of this manuscript, the Berreman modes studied are plasmonic. Microscopically, they constitute oscillations of fluctuations in the charge density of the electron gas. Berreman modes can also be observed when the microscopic source of the polarization in the thin film is due to the excitation of optically active vibrational modes of the crystal lattice, the longitudinal optical (LO) phonons. As mentioned in the beginning of this chapter, it was for this case that Berreman first observed the mode named after him.

In Chapter 3, the coupling between Berreman modes originating from these different microscopic mechanisms will be investigated. In this section, the dielectric function which describes the response of the longitudinal optical phonons is derived starting from the results of the Drude-Lorentz oscillator model introduced in Section 1.3.1.

Phonons can be described as simple harmonic oscillators [149] with charge Q and mass M. The dielectric function of the Drude-Lorentz model can thus be applied to describe their optical response, upon making the substitutions $-e \to Q$ and $m^* \to M$ in Eq. (1.24). To avoid the difficult task of defining values for Q and M, we instead immediately define a frequency ω_{LO} for which $\varepsilon_{\mathrm{r}}(\omega) = 0$ and for which phonons support longitudinal electromagnetic waves. Setting Eq. (1.24) equal to zero and solving for the frequency in the absence of damping, ω_{LO} is found:

$$\omega_{\mathrm{LO}}^2 = \frac{NQ^2}{\epsilon_0 \epsilon_\infty M} + \omega_{\mathrm{TO}}^2 \tag{1.57}$$

The frequency ω_0 in Eq. (1.24) has been renamed ω_{TO} since this frequency describes the transverse optical (TO) phonons.

With this definition for the LO phonon frequency, the dielectric function describing the optical response of the phonons is written:

$$\varepsilon_{\mathrm{r}}(\omega) = \varepsilon_\infty \left(1 + \frac{\omega_{\mathrm{LO}}^2 - \omega_{\mathrm{TO}}^2}{\omega_{\mathrm{TO}}^2 - \omega^2 - \mathrm{i}\gamma\omega}\right) \tag{1.58}$$

Introducing the static dielectric frequency $\varepsilon_{\mathrm{s}} = \varepsilon_{\mathrm{r}}(0)$, the dielectric function can be written as:

$$\varepsilon_{\mathrm{r}}(\omega) = \varepsilon_\infty + \frac{(\varepsilon_{\mathrm{s}} - \varepsilon_\infty)\,\omega_{\mathrm{TO}}^2}{\omega_{\mathrm{TO}}^2 - \omega^2 - \mathrm{i}\gamma\omega} \tag{1.59}$$

The pole of the dielectric function occurs at ω_{TO}, and the zero occurs at ω_{LO} as defined. Materials described by Eq. (1.58) are highly reflective in the region between ω_{TO} and ω_{LO}, which is known as the Reststrahlen band.

In the top panel of Fig. 1.12, the real and imaginary parts of Eq. (1.59) are plotted for the case of GaAs. The pole of ε_{r}, corresponding to the peak of $\varepsilon_{\mathrm{r}}''$, occurs at $\hbar\omega_{\mathrm{TO}} = 33.25\,\mathrm{meV}$. It is at this frequency that bulk GaAs resonantly absorbs incident radiation.

In the lower panel of the same figure, the thin film absorption coefficient (Eq. (1.47)), which describes the losses for the E_z component of the incident radiation, is plotted for the GaAs dielectric function. A resonance is found at $\hbar\omega_{\mathrm{LO}}$, which is the energy at which $\varepsilon' = 0$. This is directly analogous to the depolarization shift for intersubband transitions, in which the observed resonance occurs at $\tilde{\omega}_\alpha$ (the zero of ε_{r}) which is blueshifted from the bare transition frequency ω_α (the pole of ε_{r}).

Experimentally, the resonance at ω_{LO} is only observed for p-polarized light arriving at an oblique angle of incidence, since an electric field component E_z is needed to excite the

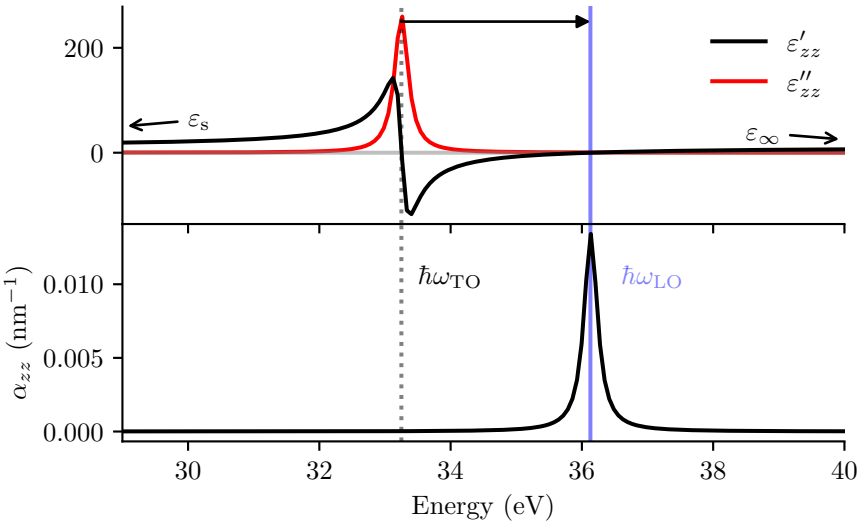

Fig. 1.12 The real and imaginary parts of Eq. (1.59) are plotted for GaAs in the Reststrahlen band, using $\varepsilon_s = 10.88$, $\varepsilon_\infty = 12.85$, $\hbar\omega_{TO} = 33.25\,\text{meV}$, and $\gamma = 0.25\,\text{meV}$ [16]. The absorption coefficient is plotted for a thin film of GaAs, calculated according to Eq. (1.47).

mode. Since the angle of incidence will always be less than 90° by definition, the incident light will always have a nonzero in-plane electric field component. The in-plane electric field component will excite resonances at ω_{TO}, since there is no depolarization effect acting in this direction. Consequently, in an absorption spectrum, resonances will be observed at both ω_{TO} and ω_{LO}. This is observed in Berreman's *p*-polarized spectrum of LiF in Fig. 1.1a.

Note that this is not analogous to the *anisotropic* quantum well case, in which case the natural frequency ω_α appears only in the z-component of the dielectric function. For *p*-polarized light incident on a quantum well at off-normal angles, a resonance is only observed at $\tilde{\omega}_\alpha$.

1.5.1 Optical Phonons of Ternary Alloys

The dielectric function of Eq. (1.58) describes the response of crystals with one longitudinal phonon mode and one transverse phonon mode. This is the case for binary semiconductors, such as GaAs. However, the experiments described in this manuscript involve the ternary alloy materials InGaAs and AlInAs. For ternary alloys, there are two Reststrahlen bands, each with a TO phonon mode and an LO phonon mode.

The frequency of the *four* optical phonon modes depends on the composition of the alloy [1, 62]. As an example, the frequencies of the optical phonons for $Ga_{1-x}Al_xAs$ are plotted in Fig. 1.13 as function of the alloy content. The LO_1 and TO_1 phonons at higher frequency are said to be "AlAs-like", while the LO_2 and TO_2 phonons at lower frequency are said to be "GaAs-like", in relation to the Reststrahlen bands of the binary crystals.

The dielectric function for the phonons in a ternary material can be written in an additive

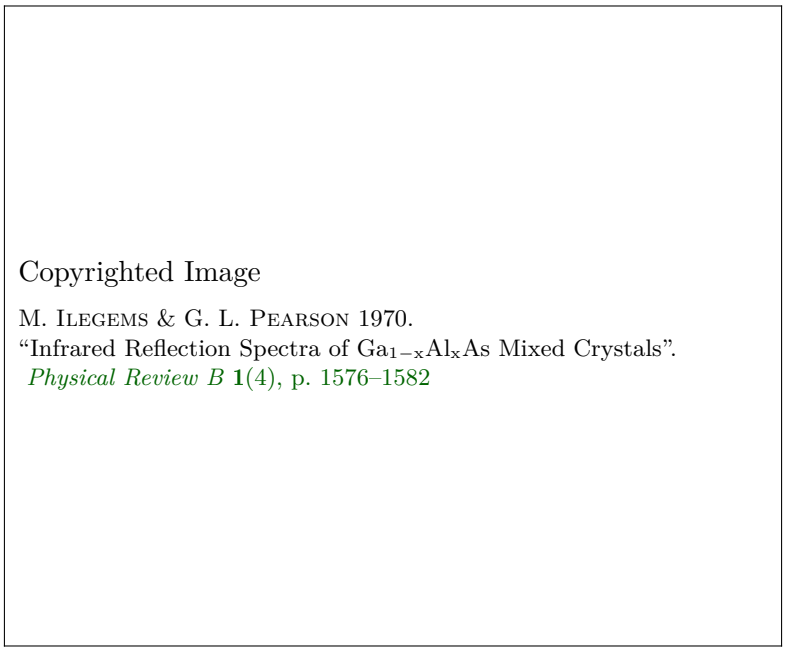

Fig. 1.13 The frequencies of the longitudinal optical (LO) and transverse optical (TO) phonons of $Ga_{1-x}Al_xAs$ are plotted as a function of the aluminum content x. Figure reproduced from [62] with annotations added.

form:

$$\varepsilon_r(\omega) = \varepsilon_\infty \left(1 + \frac{\omega_{LO_1}^2 - \omega_{TO_1}^2}{\omega_{TO_1}^2 - \omega^2 - i\gamma_1\omega} + \frac{\omega_{LO_2}^2 - \omega_{TO_2}^2}{\omega_{TO_2}^2 - \omega^2 - i\gamma_2\omega} \right) \tag{1.60}$$

The dielectric function can also be written in a factored form [12, 27] as:

$$\varepsilon_r(\omega) = \varepsilon_\infty \frac{\left(\omega_{LO_1}^2 - \omega^2 - i\gamma_1\omega\right)\left(\omega_{LO_2}^2 - \omega^2 - i\gamma_2\omega\right)}{\left(\omega_{TO_1}^2 - \omega^2 - i\gamma_1\omega\right)\left(\omega_{TO_2}^2 - \omega^2 - i\gamma_2\omega\right)} \tag{1.61}$$

in which case the zeros are easily identified as ω_{LO_1} and ω_{LO_2} in the absence of damping.

Chapter 2

Single Material Plasmonic Platform

In the following, the Berreman mode is observed in a single material semiconductor structure in which a high electronic density has been added to a subwavelength layer. Electrostatic charge effects are sufficiently strong as to give rise to a confining potential for the electron gas. A dielectric function describing the response of the highly doped layer is constructed from single particle intersubband transitions. The optical properties of the mode are explored experimentally and are found to be in agreement with the theoretical description.

It is demonstrated that the highly doped slab can support a collective surface mode which lies beyond the light line when the doped layer lies close to the sample surface and near a dielectric, such as air. The mode is resonant near the plasma frequency, and is thus not equivalent to the surface plasmon polariton mode supported at the boundary between half-infinite metal and dielectric regions.

Thermal emission experiments are presented in which both of the modes described above are used as sources of infrared radiation.

2.1 Berreman Mode in Single Material Structure

In Chapter 1, the Berreman mode was introduced as the resonance observed in subwavelength films at the zero of the dielectric function under illumination by p-polarized light at oblique incidence. When the microscopic source of the polarization is due to the motion of electrons, the mode is a collective electronic excitation.

The Berreman mode has been observed over a wide frequency range for various materials either at the longitudinal optical phonon frequency or the plasma frequency: GaN [39], AlN [94, 99], SiO_2 [117], Si_3N_4 [117], n-doped InAsSb [127], and n-doped InGaAs [8] in the mid-infrared; doped ITO in the near-infrared [19]; and silver [13, 84, 93] in the near-UV. In all cases, the media surrounding the thin layer which hosts the mode has been of a different material. For the n-doped InGaAs case, the Berreman mode was observed for an electron gas confined in a quantum well heterostructure with AlInAs barriers.

In the following, we demonstrate that a Berreman mode is supported in a structure consisting entirely of InGaAs, in which a high density of dopants has been added to a single layer of subwavelength thickness. In such a structure, there is no potential to localize the electrons other than the electrostatic potential between the mobile electrons and their ionized donors.

2.1.1 Experimental Observation

The sample studied (InP1716) consists of a 150 nm layer of InGaAs doped with a nominal electronic density of $N_v = 2 \times 10^{19}\,\mathrm{cm}^{-3}$ grown between two not-intentionally-doped InGaAs layers. The sample was grown via Metal Organic Chemical Vapor Deposition (MOCVD) on an InP substrate by the team of Grégoire Beaudoin, Konstantinos Pantzas, and Isabelle Sagnes at the Centre de Nanosciences et Nanotechnologies (C2N) in Palaiseau, France.

Transmission spectra of the sample were measured using a Fourier Transform Interferometer (FTIR), a blackbody light source, and a liquid nitrogen-cooled mercury cadmium telluride (MCT) detector. Transmission spectra were measured for p- and s-polarized light incident on the highly doped InGaAs layer, and separately, incident on a region of the sample where the highly doped layer was etched away from the substrate, as sketched in Fig. 2.1.

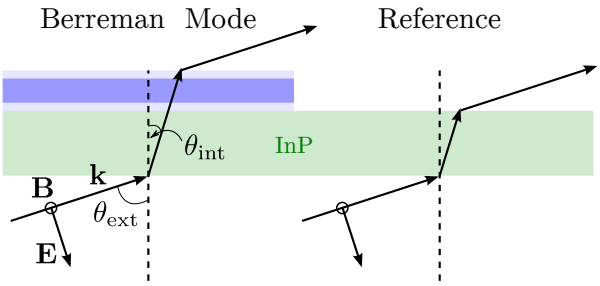

Fig. 2.1 Transmission measurements sketched for p-polarized radiation, for light incident on the plasmonic mode and, separately, the substrate reference. The external angle θ_{ext} and the internal angle θ_{int} are defined.

Since the Berreman mode is not excited by s-polarized light, the s-polarized spectrum can be used to normalize the p-polarized spectrum. The resulting transmission spectrum does not have a baseline of one, since the Fresnel coefficients differ depending on the polarization of the incident light. To have a baseline near one and to eliminate spectral artifacts which result from the polarization dependency of the optical elements, the spectrum is further normalized by the ratio of the p- and s-polarized spectra of the substrate reference. Altogether, the transmission spectrum of the Berreman mode is found as:

$$\text{Transmission} = \frac{\mathrm{T}_p^{\mathrm{plas}}}{\mathrm{T}_s^{\mathrm{plas}}} \Big/ \frac{\mathrm{T}_p^{\mathrm{sub}}}{\mathrm{T}_s^{\mathrm{sub}}} \tag{2.1}$$

At the Brewster's angle of the air/InP interface ($\theta_{ext} = 72°$ for $n_{InP} = 3.1$), no p-polarized light is reflected, and the absorptivity may be conveniently calculated as $1 -$ Transmission. Note that the angle of incidence inside the semiconductor θ_{int} is much smaller than θ_{ext} due to the large refractive index mismatch at the air/InP interface.

The experimental transmission spectrum of the InP1716 sample measured at the Brewster's angle, normalized according to Eq. (2.1), is plotted in Fig. 2.2 with a black line. A resonant dip attributed to the Berreman mode is observed at 153 meV.

The absorptivity, plotted in blue, is extracted from the experimental data as $1 -$ Transmission, after the baseline of the transmission spectrum has been corrected. In red, an absorptivity spectrum calculated with the transfer matrix method (TMM) is shown to be in good

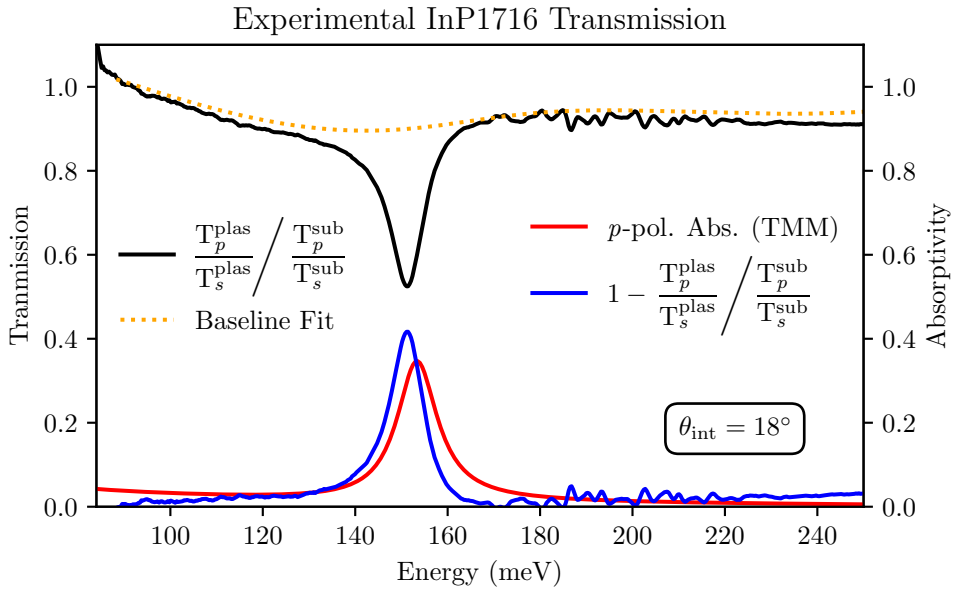

Fig. 2.2 In black, the normalized transmission of the InP1716 sample is plotted. A baseline fit (dotted orange curve) is found for the transmission spectrum. After correcting for the baseline, the experimental absorptivity (blue) is determined as 1 − Transmission and compared with the absorptivity calculated with the transfer matrix method (TMM) (red).

agreement with the experimental curve. This calculation is the subject of the following section.

The simple transmission experiment permits the determination of the electronic density of the highly doped layer without any additional processing of the sample [127], since in the case of a negligible confinement of the electron gas, the Berreman mode occurs at the plasma frequency as seen in the previous chapter. From the above experiment and taking into account nonparabolicity, the electronic density of the highly doped InGaAs layer is determined to be $N_v = 1.5 \times 10^{19}\,\mathrm{cm}^{-3}$.

2.1.2 Optical Modeling

In all the cases cited at the beginning of Section 2.1, the material structure in which the Berreman mode was observed consisted of three distinct optical layers, describable with three dielectric functions. In the present study, the electrons added to the 150 nm InGaAs layer are free to diffuse into the undoped layers, and it is not a priori apparent that the system can be described as three distinct homogeneous optical media.

Electrons which diffuse from the highly doped layer carry a net negative charge and leave behind a net positive charge. This results in an electrostatic potential, which at equilibrium, exactly balances the diffusion potential. In the following, we find that the electrostatic potential is sufficiently strong as to localize the electron gas. This justifies the description of three distinct optical media, in which the doped-layer has the response of an electron gas, and the undoped InGaAs layers are described by a frequency-independent dielectric

permittivity.

Classically, the electrostatic potential felt by an electron in the heavily doped layer is the potential which self-consistently satisfies the coupled drift-diffusion and Poisson equations at equilibrium. The Poisson equation describes the electrostatic potential which results from the displacement of charges away from their donors. The electrostatic potential enters the drift-diffusion equation and creates a current which cancels the drift current at equilibrium.

Quantum mechanically, the electrostatic potential felt by an electron in the heavily doped layer is found as the self-consistent solution to the Schrödinger and Poisson equations, as described in Section 1.2.2.1. The solution is found by solving the problem iteratively according to the following physical picture: At first, the electrons introduced into the heavily doped InGaAs layer are not bound and have an equal probability to be anywhere. They are described by completely delocalized wave functions. This implies that the electronic density goes to zero everywhere since a finite amount of charge is distributed in all space. The positive charge of the fixed ionized donors is no longer compensated, and an electrostatic potential arises. The Schrödinger equation is then solved again for the new electrostatic potential. The loop continues until a self-consistent solution is found.

The band structure of the InP1716 sample was calculated quantum mechanically using the commercially available nextnano software [15, 136] using a single band approximation for the effective mass (neglecting band nonparabolicity). The electronic density used for the 150 nm doped InGaAs region in the simulation is the experimentally extracted value of $N_\mathrm{v} = 1.5 \times 10^{19}\,\mathrm{cm}^{-3}$.

The InP1716 sample was originally designed to study the possibility of resonantly exciting the Berreman mode via an electrical current through a thin barrier [28]. Consequently, moderately doped InGaAs layers were grown on either side of the structure to serve as contacts, along with a narrow 10 nm AlInAs barrier.[1] The entire structure, detailed on Page 190, is considered in the band structure calculation presented in Fig. 2.3.

Boundary conditions must be specified for a solution to Poisson's equation. For the modeling of the InP1716 sample, the electrostatic potential $V_\rho(z)$ is fixed to a large negative value at the sample surface (Dirichlet boundary condition) as to impose a large work function to remove an electron from the structure. This is approximate, as no attempt is made to model surface states. For the other boundary, the derivative of the electrostatic potential is set to zero at the far edge of the undoped InP substrate (Neumann boundary condition).

The large electronic density introduced to the 150 nm layer of the InGaAs results in a significant band bending effect. Remarkably, a nearly square confining potential is realized for the electrons in this region, with a depth almost identical to the 0.52 eV conduction band offset of an InGaAs/AlInAs heterostructure lattice-matched to InP. The electron gas is almost totally localized to the 150 nm doped region. The abrupt change in charge density at the layer boundaries between the doped and undoped regions justifies the description of three distinct optical media.

It is important to consider nonparabolicity in describing the optical response of InGaAs. As an approximate treatment, the Schrödinger equation for the envelope functions is solved

[1] The presence of the thin AlInAs barrier hardly detracts from our claim of observing the Berreman mode in a single material structure. It is sufficiently thin as to offer little confinement to the electronic states. The electrostatic potential resulting from charge separation is clearly the dominant effect responsible for the localization of the electronic wavefunctions. Later in the chapter, the Berreman mode is observed for another sample (V0211) which consists of exclusively InGaAs layers.

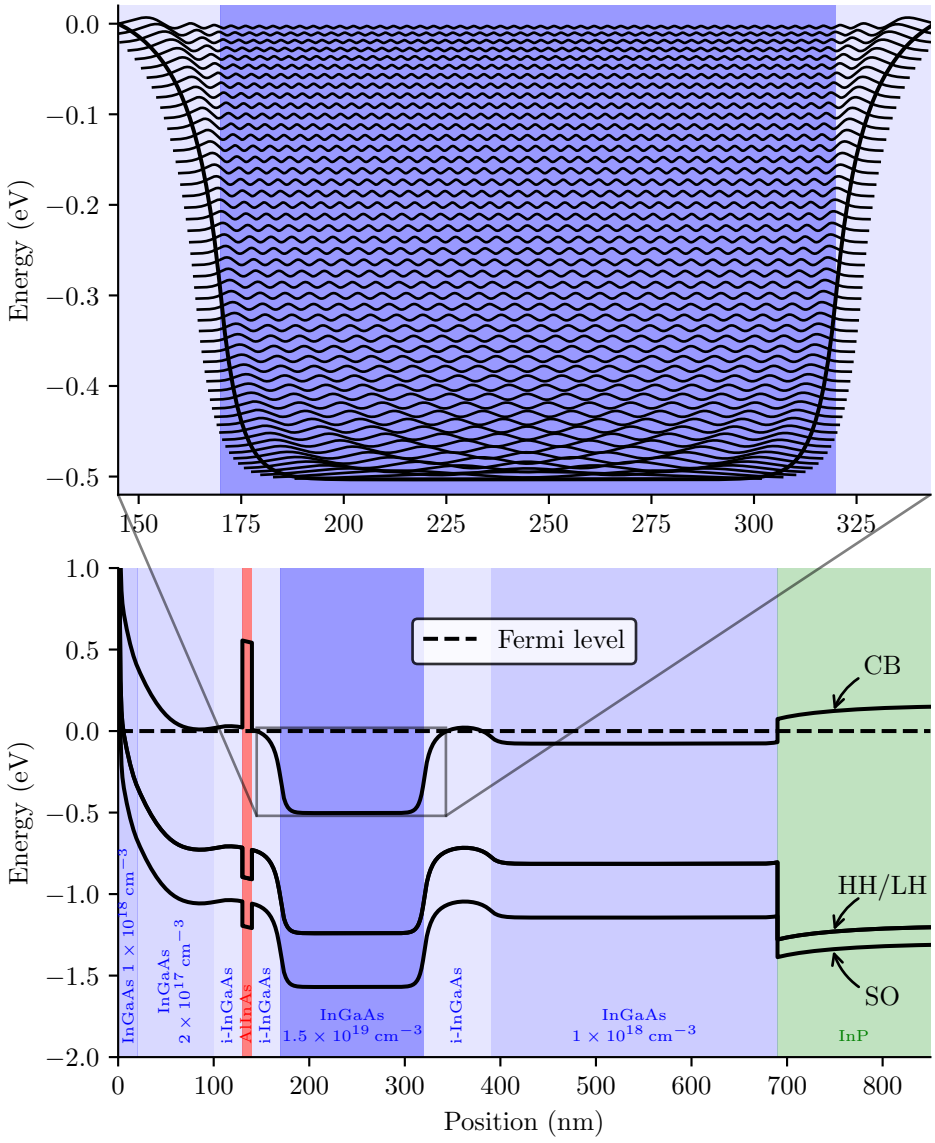

Fig. 2.3 In the lower panel, the electronic band structure found as a solution to the coupled Schrödinger-Poisson equations is plotted a function of position for the InP1716 sample. The conduction band (CB), the degenerate heavy hole (HH) and light hole (LH) bands, and the split-off (SO) band are indicated. In the upper panel, the square moduli of the bound electronic states calculated with a 3-band $\mathbf{k} \cdot \mathbf{p}$ model are plotted at their respective energies inside the potential.

for a final time, considering nonparabolicity, for the potential found as the self-consistent solution to the coupled Schrödinger-Poisson equations in the constant effective mass approximation. The square moduli of the resulting envelope functions are plotted in the top panel of Fig. 2.3. For a fully proper treatment, the band nonparabolicity should be considered for every iteration of the Schrödinger-Poisson solver.

The z-component of the uniaxially anisotropic dielectric function for the electron gas effectively confined to the 150 nm InGaAs layer, ε_{zz}, is determined from the generalized Drude-Lorentz model introduced Section 1.3.3. We recall that in this description, the dielectric function is constructed as the summation of contributions from single particle intersubband transitions to the matter polarization according to Eq. (1.35).

The real and imaginary parts of ε_{zz} are plotted in Fig. 2.4. Due to the large width of the quantum well, the dielectric function has a similar form to that of the Drude model for a free electron gas. As discussed in Section 1.3.3, our approach for calculating ε_{zz} has the two-fold advantage that it naturally accounts for confinement, and that the electronic density implicitly sets the effective mass.

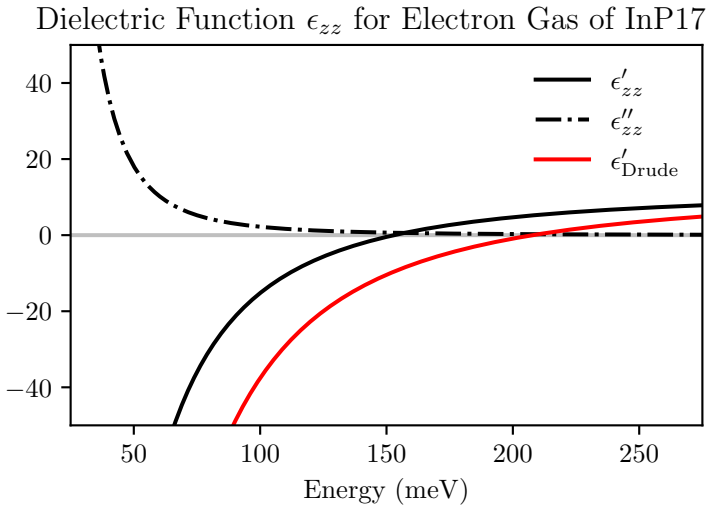

Fig. 2.4 The real and imaginary parts of ε_{zz}, calculated to describe the response of the electron gas in the potential shown in the top panel of Fig. 2.3, are plotted. The real part of the dielectric function calculated with the Drude mode for the same electronic density and using the effective mass at the bottom of the conduction band is plotted for comparison.

To model the propagation of electromagnetic fields across the structure and calculate the experimentally measurable transmission, reflection, and absorptivity, either a transfer matrix method [98] or a finite element solver can be employed. The transfer matrix (TMM) method is computationally less resource intensive, and is the method used for the numerical calculations presented throughout this chapter.

In either method, the optical response of each region of the structure is defined with a dielectric function, and the polarization and angle of the incident field is set. Apart from the highly doped 150 nm layer, the layers of the InP1716 sample are described with isotropic dielectric functions. The less-doped InGaAs layers are described with the Drude

model, whereas the intrinsic InGaAs layers and the InP substrate are described by their respective high frequency dielectric constants, ε_∞, introduced in Section 1.3.1. The in-plane components of the dielectric function for the 150 nm highly doped layer are described with the Drude model.

The absorptivity spectrum calculated with the TMM for p-polarized light at Brewster's angle, plotted in Fig. 2.2, was calculated using the dielectric function ε_{zz} as determined above, using phenomenological values for the linewidth broadening. With this approach, the amplitude of the calculated absorptivity spectra agrees well with the experimental spectrum.

2.1.3 Subtleties of Transmission Spectra Normalization

The divergence of the baseline of the (black) transmission curve in Fig. 2.2 to increasingly large values above one at low energies is a consequence of the normalization procedure described by Eq. (2.1). To demonstrate this, the four transmission spectra (T_p^{plas}, T_s^{plas}, T_p^{sub}, T_s^{sub}) which enter into Eq. (2.1) are calculated with the TMM at Brewster's angle and plotted in Fig. 2.5. A normalized transmission spectrum, determined from the series of simulated transmission spectra according to Eq. (2.1), is also plotted. As in the experiment, the baseline of the spectrum determined via the normalization procedure diverges above one at low energies.

The transmission of the highly doped layer actually decreases for energies below the Berreman mode (plasma energy), as evident in the p- and s-polarized transmission spectra (solid and dashed blue lines) of Fig. 2.5. This is due to an increase in the reflectivity below the plasma energy. For bulk metals described with the Drude dielectric function, the reflectivity sharply approaches one and the transmission sharply drops to zero below the plasma energy [45]. The highly doped thin layer behaves analogously, but since its thickness is less than the skin depth, the transmission does not completely go to zero below the plasma energy. If the thickness of the highly doped layer is increased, the transmission below the plasma energy is found to decrease until the bulk case is recovered, in which case the Berreman mode is no longer observed.

Above the plasma energy, the baseline of the transmission spectrum (black) is still not unity, despite the normalization procedure. The amplitude of the Berreman mode resonance should be determined with respect to this baseline, as was done in extracting the absorptivity in Fig. 2.2.

2.2 Coupling of Berreman Mode with Free Space

2.2.1 Theoretical Description

The Berreman mode interacts strongly with the free space electromagnetic field. This property can manifest itself in the total absorption of incident light by the mode under certain conditions. The strength of the interaction is quantified by the radiative decay rate Γ_{rad}, which determines the coupling between plasmon excitations and the radiation field. In most solid state systems, the radiative decay rate is so small compared to the nonradiative decay rate γ_{NR} that the observed linewidths are determined solely by the lifetimes of nonradiative processes. In these systems, the rate at which excited electronic states dissipate energy is much greater than the rate at which they are excited. In the case of the Berreman mode,

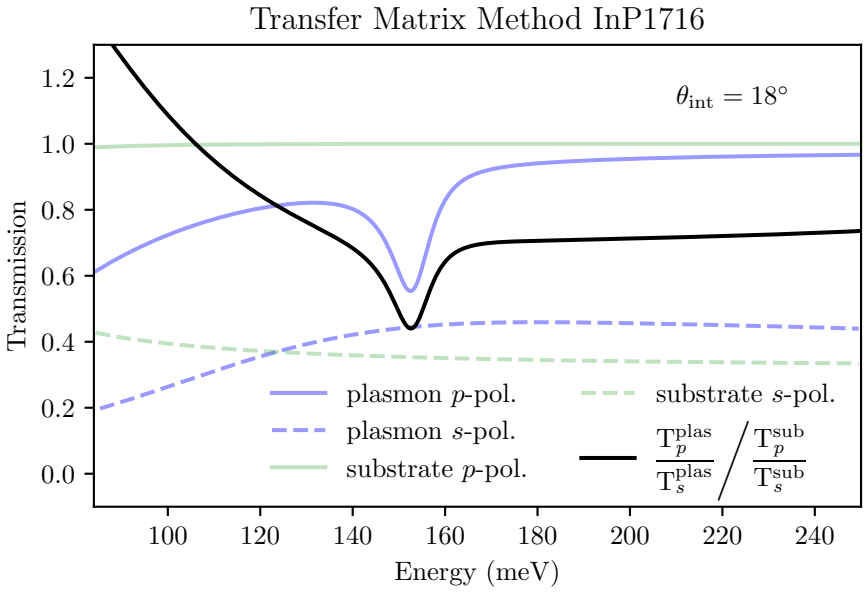

Fig. 2.5 Transmission spectra calculated via the transfer matrix method are plotted for p- and s-polarized light incident from inside the InP substrate, for light passing through the heavily doped 150 nm layer and then into air (denoted plasmon), and for light passing from the substrate directly into air (denoted substrate). The initial air/substrate interface encountered by light entering the sample in the experiment is not considered.

the interaction with the electromagnetic field can be so significant that Γ_{rad} is larger than γ_{NR} [69]. This has profound consequences on the optical properties.

The reflectivity and absorptivity spectra of a thin layer supporting a Berreman mode are highly angular-dependent. This is a consequence of the angular dependency of Γ_{rad} and the large values it can reach. Let us introduce the total decay rate, or linewidth, of the Berreman mode:

$$\Gamma_{\text{tot}} = \gamma_{\text{NR}} + \Gamma_{\text{rad}}(\theta, \omega) \tag{2.2}$$

In this expression, and for the remainder of this section, the angle θ describes the angle inside the semiconductor (we omit the subscript used elsewhere in the chapter). We see that when Γ_{rad} is of the same order of magnitude of γ_{NR}, the linewidth is no longer determined solely by the decay rate of nonradiative scattering processes.

The angular dependency of Γ_{rad} is due to the thin layer geometry of the Berreman mode and the fact that the mode only interacts with p-polarized radiation. The form of the dependency is easy to establish: the Berreman mode only interacts with the electric field in the $\hat{\mathbf{z}}$ direction, written as $E_z = E_0 \sin\theta$, and the effective interaction length of radiation with the mode goes as $(\cos\theta)^{-1}$. These two considerations suggest a factor of $\sin^2\theta/\cos\theta$ should appear in the definition of $\Gamma_{\text{rad}}(\theta, \omega)$ (the squared sinusoidal dependence appears because absorption is related to an attenuated *intensity*). A rigorous evaluation of Γ_{rad} [60] indeed

leads to the following formula:

$$\Gamma_{\mathrm{rad}}(\theta,\omega) = \Gamma_0 \frac{\omega}{\omega_0} \frac{\sin^2\theta}{\cos\theta} \tag{2.3}$$

This expression results from solving the quantum Langevin equations in the input-output formalism. The angle-independent spontaneous emission rate Γ_0 can be calculated using perturbation theory (Fermi's Golden Rule) [60, 69, 100] in which case Γ_0 is found to be proportional to the surfacic density of electrons, N_{s}. The frequency dependence of $\Gamma_{\mathrm{rad}}(\theta,\omega)$, however, can only be found in a nonperturbative, non-Markovian description [60]. We note that the dependency of the radiative decay rate $\Gamma_{\mathrm{rad}}(\theta,\omega)$ on the electronic density is evidence of the superradiant nature of the plasmonic excitation [69]. In Section 4.2.3, an expression for Γ_0 will be found from a quantum description of the ac current density associated with the excitation of the plasmon mode.

In the input-output formalism [60], the plasmon mode is described as being coupled to two bosonic baths: the free electromagnetic field in the dielectric medium, and a bath of electronic excitations. The coupling with each bath is described by $\Gamma_{\mathrm{rad}}(\theta,\omega)$ and γ_{NR}, respectively. Whereas Γ_{rad} is determined by the quantum model described above, γ_{NR} is introduced phenomenologically. Each bath represents one of two competing decay channels for the excited plasmons. When $\gamma_{\mathrm{NR}} \gg \Gamma_{\mathrm{rad}}(\theta,\omega)$, plasmon excitations relax into the electronic bath at a faster rate than they are excited. When $\Gamma_{\mathrm{rad}}(\theta,\omega) \gg \gamma_{\mathrm{NR}}$, plasmons are excited at a rate faster than they can relax into the electronic bath and the dominant relaxation pathway is radiative decay. When the two rates are equal (the critical coupling condition), plasmons decays into the electronic bath at the same rate that they are excited. For plasmons excited by an incident radiation field, this is the condition for perfect absorption.

The $\sin^2\theta/\cos\theta$ dependence of Γ_{rad} means that each of the regimes discussed above is fulfilled at a different angle. For small angles, $\sin^2\theta/\cos\theta$ is small, reaching about 0.1 only at $\theta = 18°$. This implies that for small incidence angles, the linewidth is almost entirely determined by γ_{NR}. For large angles, $\sin^2\theta/\cos\theta$ exceeds unity, which is reached around 50°. Experimentally, this is observed as a clear broadening of the resonance.

The complete expression for the absorptivity of the plasmon mode calculated in the input-output formalism is written [60]:

$$\alpha(\theta,\omega) = \frac{\dfrac{4\omega_0^2}{(\omega_0+\omega)^2}\dfrac{\gamma_{\mathrm{NR}}\Gamma_{\mathrm{rad}}(\theta,\omega)}{2}}{(\omega-\omega_0)^2 + \dfrac{4\omega_0^2}{(\omega_0+\omega)^2}\left[\dfrac{\gamma_{\mathrm{NR}}}{2} + \dfrac{\Gamma_{\mathrm{rad}}(\theta,\omega)}{2}\right]^2} \tag{2.4}$$

The expression can be simplified for certain cases. For $\gamma_{\mathrm{NR}} \gg \Gamma_{\mathrm{rad}}(\theta,\omega)$, the expression reduces to:

$$\alpha(\theta,\omega) = \frac{2}{\gamma_{\mathrm{NR}}} \frac{2\Gamma_{\mathrm{rad}}}{1+\left(\dfrac{\omega-\omega_0}{\gamma_{\mathrm{NR}}/2}\right)^2} \tag{2.5}$$

which is a Lorentzian with a full-width at half-maximum given by γ_{NR}. At the critical coupling angle θ_{crit} where $\Gamma_{\mathrm{rad}} = \gamma_{\mathrm{NR}}$, the expression reduces to a Lorentzian which peaks at 1/2:

$$\alpha(\theta_{\mathrm{crit}},\omega) = \frac{1}{2} \frac{1}{1+\dfrac{\omega-\omega_0{}^2}{\gamma_{\mathrm{NR}}}} \tag{2.6}$$

For $\Gamma_{\mathrm{rad}}(\theta,\omega) \gg \gamma_{\mathrm{NR}}$, the linewidth of the resonance determined by Eq. (2.4) is radiatively broadened.

When the Berreman mode is next to a metallic mirror, a factor of two must be included in Eq. (2.4). Under these circumstances, the Berreman mode can act as a perfect absorber. Equation (2.4) is plotted including the factor of 2 for three angles covering the three regimes in Fig. 2.6.

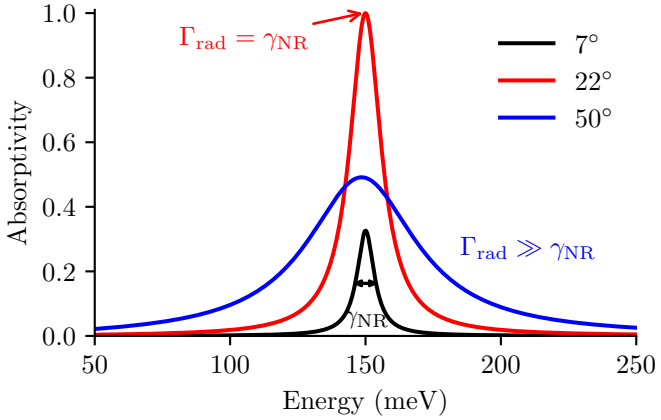

Fig. 2.6 Equation (2.4) is plotted after multiplication by a factor of 2 for $\omega = 150\,\mathrm{meV}$, $\Gamma_0 = 46\,\mathrm{meV}$, and $\gamma_{\mathrm{NR}} = 7\,\mathrm{meV}$. For a small angle, the linewidth is determined by γ_{NR}. At the critical coupling angle, the absorptivity reaches one. At large angle, the linewidth is radiatively broadened.

Finally, it must be remarked that for $\Gamma_{\mathrm{rad}}(\theta,\omega) \gg \gamma_{\mathrm{NR}}$, the expression given by Eq. (2.4) deviates from a Lorentzian lineshape. The non-Lorentzian behavior results from the anti-rotating terms in the light-matter interaction Hamiltonian. These terms ensure that the absorptivity goes to zero at zero energy, as is physically required. A Lorentzian lineshape would become unphysical in the limit of extreme radiative broadening (very large Γ_{rad}), since the low energy tail can take on a finite value below zero energy.

2.2.2 Experimental Observations

In this section, the optical properties of the Berreman mode for the single material InP1716 sample are experimentally investigated as a function of the angle of incidence. First, transmission spectra measured up to the maximum internal angle achievable for light incident from free space are presented. Afterwards, absorptivity spectra, determined from reflectivity measurements in which a gold layer has been deposited on the sample surface, are presented. Using a Ge hemisherical lens, absorptivity spectra are measured beyond the light line [31]. The regime in which $\Gamma_{\mathrm{rad}}(\theta,\omega) \geq \gamma_{\mathrm{NR}}$ is experimentally investigated and perfect absorption is demonstrated.

Transmission Measurements

As was the case for the Brewster's angle measurement reported in Section 2.1.1, the transmission measurements are performed with the light incident from free space onto the InP

substrate (350 µm thick) of refractive index $n_{\mathrm{InP}} = 3.1$. From free space, the maximum internal angle which can be reached is 18.8° for light arriving on the substrate at near-grazing incidence.

A series of experimental transmission spectra measured up to an internal angle of 17.9° are presented in the left panel of Fig. 2.7. The specular reflection was not measured in the experiment, and as a result, the absorptivity cannot be determined.

Transmission spectra calculated with the TMM for angles up to 18°, normalized in the same way as the experiment, are plotted in the right panel of Fig. 2.7. There is good agreement between the experimental spectra and the TMM simulations. The contrast of the resonant transmission dip varies approximately the same in both as a function of angle. In both sets of spectra, as the angle is increased, the value of the baseline decreases and the divergence of the baseline below the plasma energy becomes more rapid. Both of the trends are more pronounced in the TMM simulation.

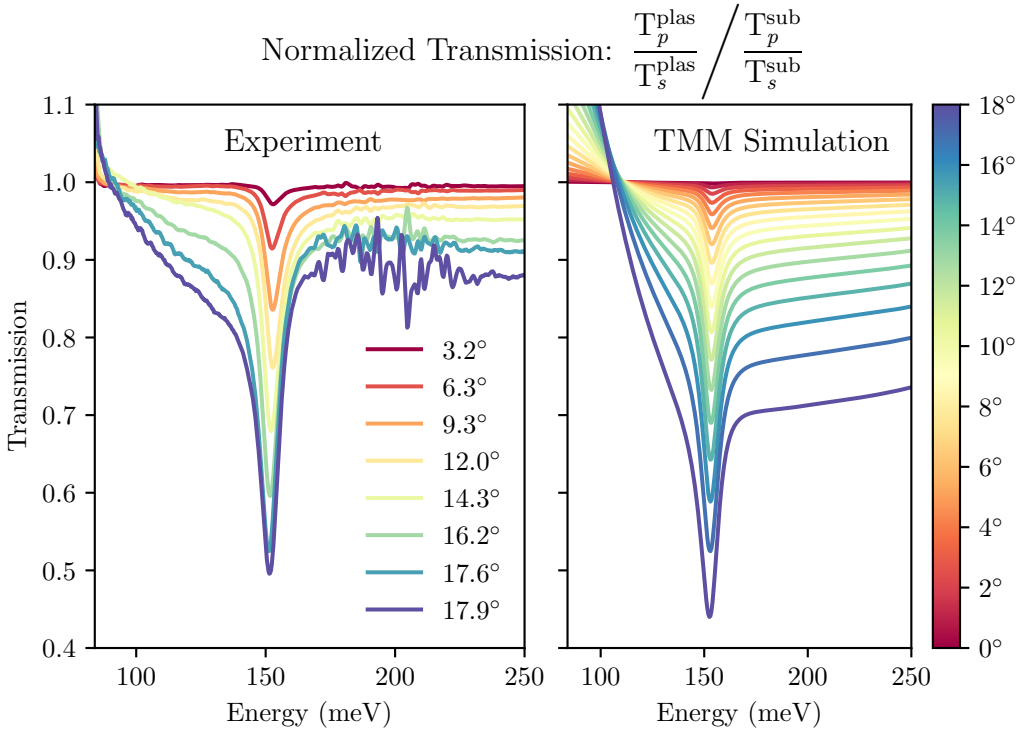

Fig. 2.7 The normalized transmission is compared for the experimentally measured spectra and transfer matrix method (TMM) calculations for internal angles up to the total internal reflection angle.

Reflectivity Measurements with Gold Mirror

In this section, the optical properties of the Berreman mode of the InP1716 sample with a deposited gold mirror are studied as a function of angle. The results of these studies were reported in a publication [139] of which I was a coauthor.

Two configurations for the reflectivity measurements are sketched in Fig. 2.8. In both cases, a gold mirror is deposited on the sample surface, close to the highly doped layer. As in the transmission experiments, light is incident onto the InP substrate. Assuming a perfectly reflective gold layer, the absorptivity of the sample can be determined as 1 − Reflectivity.

Spectra can be measured up to an internal angle of approximately 18.8° directly from free space. To access larger internal angles, a germanium hemispherical lens is used. Germanium has a refractive index of $n_{\mathrm{Ge}} \approx 4$ over the spectral range investigated. The hemispherical geometry of the germanium lens permits incident light to cross the interface of large refractive index mismatch at normal incidence, thus permitting access to large internal angles inside the InP substrate.

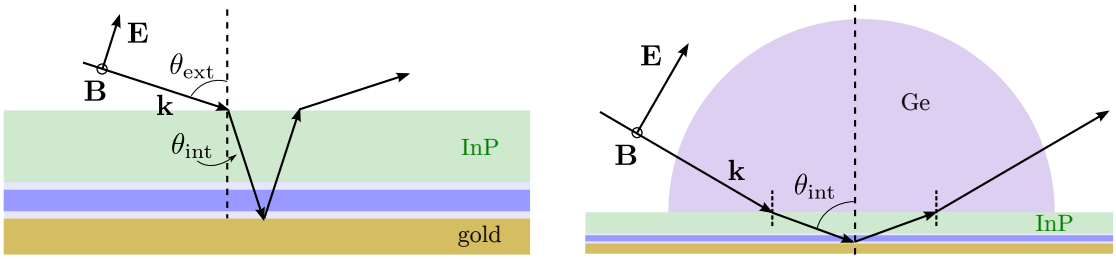

(a) Above free space light line (b) Below free space light line

Fig. 2.8 The reflectivity configurations used to probe the Berreman mode across a wide range of angles are sketched. The use of a hemispherical lens allows for light incident from free space to enter the first high refractive index material (the Ge lens) at normal incidence, avoiding refraction.

For the reflectivity experiments, reference spectra are measured over a deposited gold film. Since the Berreman mode is only excited by p-polarized radiation, and the light is assumed to be completely reflected by the gold layer, absorptivity spectra are determined as:

$$\text{Absorptivity} = 1 - \frac{\mathrm{R}_p^{\mathrm{plas}}}{\mathrm{R}_s^{\mathrm{plas}}} \Big/ \frac{\mathrm{R}_p^{\mathrm{gold}}}{\mathrm{R}_s^{\mathrm{gold}}} \tag{2.7}$$

With this procedure, the baselines of the absorptivity spectra are not equal to zero, since at non-normal incidence angles, the incident beam is reflected from the InP substrate differently depending on the polarization. The baselines of the spectra given by Eq. (2.4) are manually normalized to one far from the optical resonance, in a flat non-absorptive region.

Experimental reflectivity measurements are presented in Panel (a) of Fig. 2.9 for the gold-backed InP1716 sample. The low angle spectra, in which light was incident onto the sample directly from free space, were measured by the author. The spectra for angles larger than 18.8° (below the free space light line), were measured by Baptiste Dailly using a Ge hemispherical lens [31]. The two data sets overlap for some angles and show complete agreement.

The peak absorptivity is small at low angles, but increases quickly as the angle is enlarged. It continues to increase until an angle of approximately 22°, at which it reaches a maximum value of one, indicating a total absorption of the incident light field. This angle is identified as the critical coupling angle. Beyond this angle, the peak absorptivity begins to decrease,

and a marked broadening of the resonance linewidth is observed. The center of the resonance is observed to shift towards higher energy.

In Panel (d) of Fig. 2.9, the experimental linewidth is plotted as a function of the internal angle. At low incidence angles, the full-width at half-maximum (FWHM) is at its narrowest. As described in Section 2.2.1, the radiative linewidth Γ_{rad} is proportional to $\sin^2\theta/\cos\theta$. For small angles, this quantity is negligible and thus the total linewidth is equivalent to the nonradiative linewidth γ_{NR}. The total linewidth of the experimental resonance at low angle permits the determination of the nonradiative linewidth as $\gamma_{\text{NR}} = 8\,\text{meV}$. As the angle is increased in the experiment, the linewidth is found to broaden as $\sin^2\theta/\cos\theta$, as predicted by the theory. The theoretical curve closely models the experimental data.

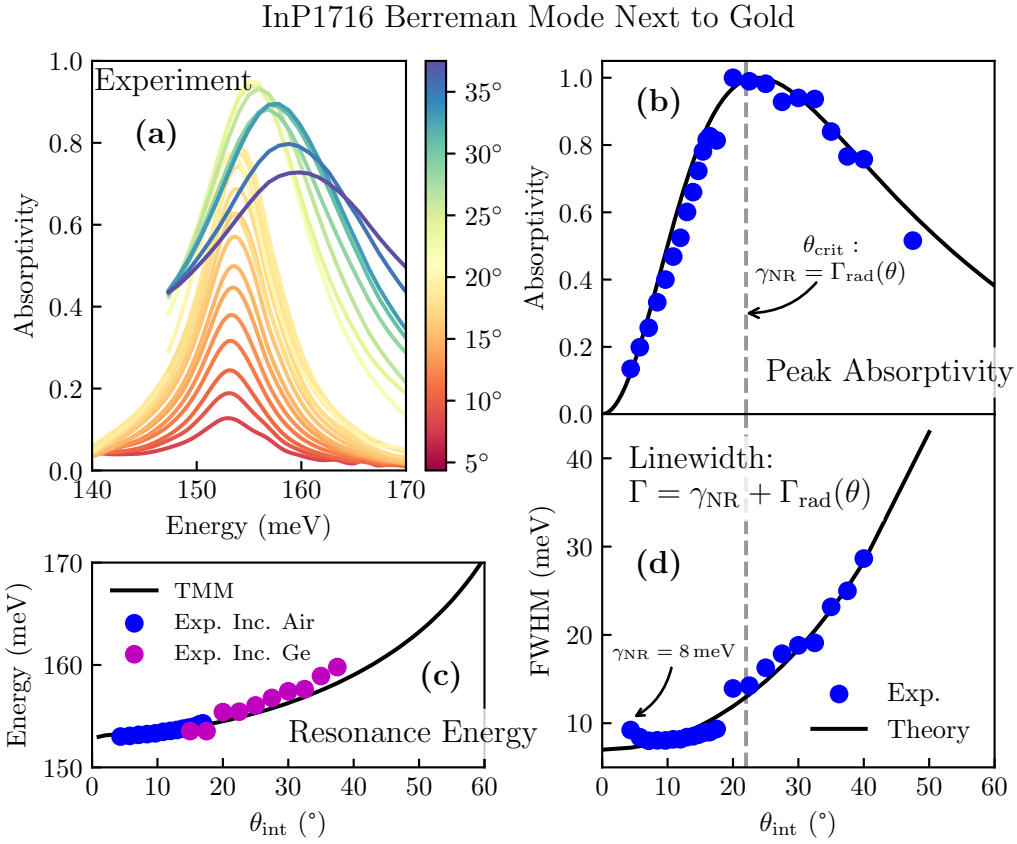

Fig. 2.9 In Panel (a), the experimental absorptivity spectra are plotted for the InP1716 sample for which a gold mirror has been deposited on the surface. In Panels (b) and (d), experimental and theoretical curves are plotted for the peak absorptivity and the total linewidth (FWHM) as a function of the internal angle. In Panel (c), the dispersion of the resonance energy with incidence angle is plotted, and is modeled with transfer matrix method (TMM) calculations.

In Panel (b) of Fig. 2.9, the experimentally measured peak absorptivity is plotted as a function of angle. The theoretical absorptivity, calculated according to Eq. (2.4), is plotted alongside the experimental data, and a close agreement is observed. Note that no free pa-

rameters are used in the theoretical calculation, as γ_{NR} has been determined experimentally, and the value for Γ_{rad} is calculated quantum mechanically beginning from the single particle electronic wavefunctions.

For increasing but still small angles, the absorptivity gets larger at an increasingly rapid rate. For low angles, it can be approximated that $\gamma_{\mathrm{NR}} \gg \Gamma_{\mathrm{rad}}$, and thus the form of the absorptivity is described by Eq. (2.5) as a Lorentzian function with amplitude proportional to the radiative linewidth Γ_{rad}, which increases as $\sin^2\theta/\cos\theta$.

The critical coupling angle is the condition for which $\Gamma_{\mathrm{rad}} = \gamma_{\mathrm{NR}}$. The phenomenon of perfect absorption can thus be understood to occur when the rate of decay of the plasmonic excitation into the electronic bath (dissipation) is the same as the rate at which plasmon is optically excited. In the case when Γ_{rad} is larger than γ_{NR}, the plasmon is optically excited at a rate faster than that which it can dissipate energy at. As a result, the plasmon must re-radiate some of its energy. In this regime, the resonance broadens, and the plasmon becomes increasingly reflective, as the radiative decay pathway is faster than the nonradiative decay pathway.

In Panel (c) of Fig. 2.9, the experimental resonance energy of the Berreman mode is plotted as a function of angle. The experimental resonance blueshifts continuously with increasing angle. This behavior is well-reproduced with the transfer matrix method calculations. The behavior is consistent with calculation for the dispersion of the Berreman mode, described in the following section.

2.3 Nonradiative (ENZ) Mode of Highly-Doped Thin Layer

2.3.1 Mode Dispersion of Thin Layer Near Zero of Dielectric Function

The mode that we have investigated up to this point, which we have called the Berreman mode, is a *radiative* mode, meaning it lies above the light line. The thin highly doped layer also supports transverse magnetic (TM) *nonradiative* modes which lie below the light line. As we shall find, whether the light line in question is that of free space, $\omega = cq_{\parallel}$, or that inside the semiconductor, $\omega = cq_{\parallel}\Big/\sqrt{\varepsilon_\infty}$, depends on the nature of the media adjacent to the highly doped layer.

In the previous expressions, $q_{\parallel}$ is the in-plane wavevector, which is related to the angle of incidence inside the semiconductor θ_{int} according to:

$$q_{\parallel} = 2\pi\frac{E}{hc}\sqrt{\varepsilon_\infty}\sin\theta_{\mathrm{int}} \tag{2.8}$$

The in-plane wavevector is a conserved quantity as light propagates through a stack of layers, due to translational invariance in the planar direction.

Thus far, we have studied the InP1716 sample with and without a deposited gold layer. In the following, to simplify the description, we neglect the thin undoped layers between the highly doped thin layer and the sample surface. Then we can describe the two cases considering only three media, with the highly doped slab directly adjacent to either gold or air. The two cases are pictured in Fig. 2.10.

We wish to consider the *dispersion* of modes supported by the thin highly doped layer for each case. The dispersion is found by solving for the modes of the three layer structure for each $\mathbf{q}$. A mode is defined as a solution to Maxwell's equations in the absence of an

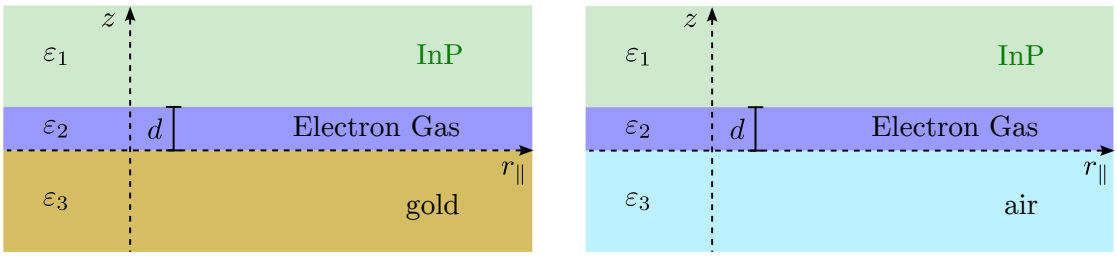

(a) Deposited gold layer (b) Interface with air

Fig. 2.10 Three layer model of InP1716 experiments. The structure with air models transmission experiments, like those reported in Section 2.2.2. The structure with gold models the reflectivity experiments reported in Section 2.2.2.

excitation [18]. The dispersion of the TM modes supported by a highly doped slab (ε_2) of width d surrounded by two half-infinite media (ε_1 and ε_3) is determined by the following expression [18, 141]:

$$\left(1+\frac{\varepsilon_1 q_{z,1}}{\varepsilon_3 q_{z,3}}\right) = \mathrm{i}\tan\left(q_{z,2}d\right)\left(\frac{\varepsilon_2 q_{z,3}}{\varepsilon_3 q_{z,2}}+\frac{\varepsilon_1 q_{z,2}}{\varepsilon_2 q_{z,1}}\right) \tag{2.9}$$

in which $q_{z,n} = \sqrt{\varepsilon_n \omega^2/c^2 - q_\parallel^2}$ is the wavevector in the $\hat{\mathbf{z}}$ direction inside medium n. No solutions exist for real $q_\parallel$ and real ω, but solutions can be found for real $q_\parallel$ and complex ω. In Fig. 2.11b, the dispersion for the semiconductor/highly doped thin layer/air case is plotted, reproduced from [18, 141].

The mode dispersion can also be calculated with a semiclassical nonlocal theory [4] and via the input-output formalism detailed in [60]. In Fig. 2.11a, the dispersion describing the semiconductor/highly doped thin layer/gold case is plotted, reproduced from [60].

In the dispersion plotted in Fig. 2.11a, for the case of the highly doped layer sandwiched between undoped semiconductor described by ε_∞ and gold (sketched in Fig. 2.10a), the Berreman mode exists above *the light line in the semiconductor*, $\omega = cq_\parallel \big/ \sqrt{\varepsilon_\infty}$. In the dispersion plotted in Fig. 2.11b, for the case of the highly doped layer sandwiched between undoped semiconductor and air (sketched in Fig. 2.10b), the Berreman mode exists above *the free space light line*, $\omega = cq_\parallel$. In the reflectivity measurements of Section 2.2.2, it was due to the presence of the gold layer that the Berreman mode could be excited beyond the free space light line using the Ge hemispherical lens.

In both dispersion plots of Fig. 2.11, the energy of the Berreman mode slightly blueshifts as $q_\parallel$ is increased up to the light line. The blueshifting of the Berreman mode was observed in the reflectivity experiment with the gold mirror, for which the results were reported in Fig. 2.9. The effect was also reproduced with transfer matrix method simulations. While the dispersion of the Berreman mode is described classically through Eq. (2.9), the blueshifting of the mode can also be explained from a quantum electrodynamics point of view as a manifestation of the cooperative Lamb shift [46].

We now turn to consider the nonradiative modes which lie below the light line in the semiconductor for the case of the highly doped layer sandwiched between undoped semiconductor and gold, and below the free space light for the case of the highly doped layer sandwiched between undoped semiconductor and air.

Copyrighted Image

S. Huppert, A. Vasanelli, G. Pegolotti, Y. Todorov & C. Sirtori 2016.
"Strong and ultrastrong coupling with free-space radiation".
Physical Review B **94**(15), p. 155 418

(a) Electron gas between layers of ε_∞

Copyrighted Image

Thierry Taliercio, Vilianne Ntsame Guilengui, Laurent Cerutti, Eric Tournié & Jean-Jacques Greffet 2014.
"Brewster "mode" in highly doped semiconductor layers: an all-optical technique to monitor doping concentration".
Optics Express **22**(20), p. 24 294

(b) Electron gas next to air

Fig. 2.11 The dispersion of modes supported in a thin highly doped semiconductor layer is calculated for two cases. (a) The dispersion is calculated for a highly doped slab surrounded by high index media. The Berreman mode branch extends to *the light line in the media described by* ε_∞, below which lies the nonradiative ENZ mode. Figure reproduced from [60] with modifications. (b) The dispersion is calculated for a highly doped thin layer bordered by air and semiconductor. The Berreman mode extends to *the light line in free space*, below which lie two branches of nonradiative modes. The higher energy branch is the so-called ENZ mode. Figure reproduced from [127] with modifications.

Let us focus on the dispersion plotted in Fig. 2.11b for the case in which there is an interface with air. There are two modes which lie below the light line, labeled **II** and **III**. These modes originate from the coupling of surface plasmon polariton modes on opposite interfaces of the doped slab, when the slab thickness is less than the decay length of the surface modes. The behavior of these modes has been extensively studied [80, 113] and is well known. The higher energy mode is traditionally known as the long-range surface plasmon polariton, while the lower energy mode is known as the short-range surface plasmon polariton.

For sufficiently thin metal-like films, the dispersion of the long range surface plasmon mode (**II** in Fig. 2.11b) becomes increasingly flat at the (plasma) frequency at which the real part of the dielectric function goes to zero. In this regime, this mode is now commonly referred to as the epsilon-near-zero (ENZ) mode [18, 140, 141]. A characteristic of the ENZ mode is that the electric field in the $\hat{\mathbf{z}}$ direction of the thin layer becomes constant within the thin layer.

In the following section, we experimentally investigate the ENZ mode for the InP1716 sample, in which the highly doped layer is close to the air interface. Unlike in the simple three medium geometry considered in the present section, in the InP1716 sample, there are some semiconductor layers between the highly doped thin layer and the interface with air. The entire thickness of these layers is still much smaller than the wavelength, and consequently, the structure is found to support the type of ENZ mode just beyond the free space light line as found in the three medium study with air.

2.3.2 Experimental Study of Nonradiative (ENZ) Mode

In the following, the optical response of the heavily doped 150 nm layer next to a boundary with air is investigated below the free space light line. This is achieved with the multipass geometry sketched in Fig. 2.12. Two facets are mechanically polished onto the substrate at 45°, allowing light to be coupled into the substrate for high internal angles.

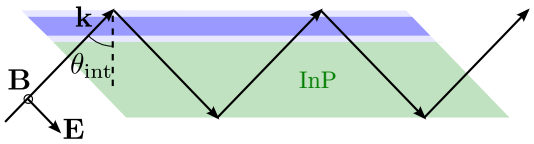

Fig. 2.12 The multipass geometry is sketched. This geometry permits experimental access to large angles of incidence inside the semiconductor medium, and thus in-plane wavevectors which lie beyond the free space light line.

This geometry is equivalent to the well-known Kretschman configuration used to excite surface plasmon polaritons [68, 80]. It is mechanically difficult to polish two facets close enough to one other that the light only reflects once inside the semiconductor (the InP substrate is 350 µm thick). As a consequence, the light passes through the highly doped slab many times. This would be favorable if the absorption was small (this effect is used to great advantage to observe resonances of low doped samples). In the present study, however, there is zero transmission over an energy range around the resonance, indicating a saturation of the absorption. This is seen in the *p*-polarized transmission spectrum shown in Fig. 2.13. Due to this effect, the linewidth of the experimental spectra cannot be properly characterized. The peak position can still be extracted, however.

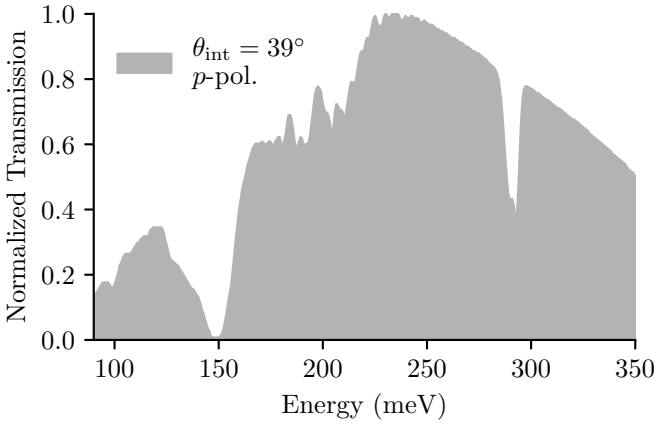

Fig. 2.13 The multipass transmisson spectrum is saturated around 150 meV. The shape of the blackbody light source is recognizable.

In Panel (a) of Fig. 2.14, resonance energies extracted from experimental transmission spectra are plotted as a function of θ_{int}. The resonance energies at low angles (above the free space light line) are extracted from the transmission spectra of Fig. 2.7, while the resonance energies for angles between 40° to 60° (below the free space light line) are extracted from multipass measurements. Over small angles, the energy of the resonances varies little. At larger

angles, the resonance significantly and continuously redshifts. Resonance energies extracted from the absorptivity spectra shown in Panel (b), calculated with the TMM, are plotted as blue scatter points. Their dispersion reproduces well the experimental observations.

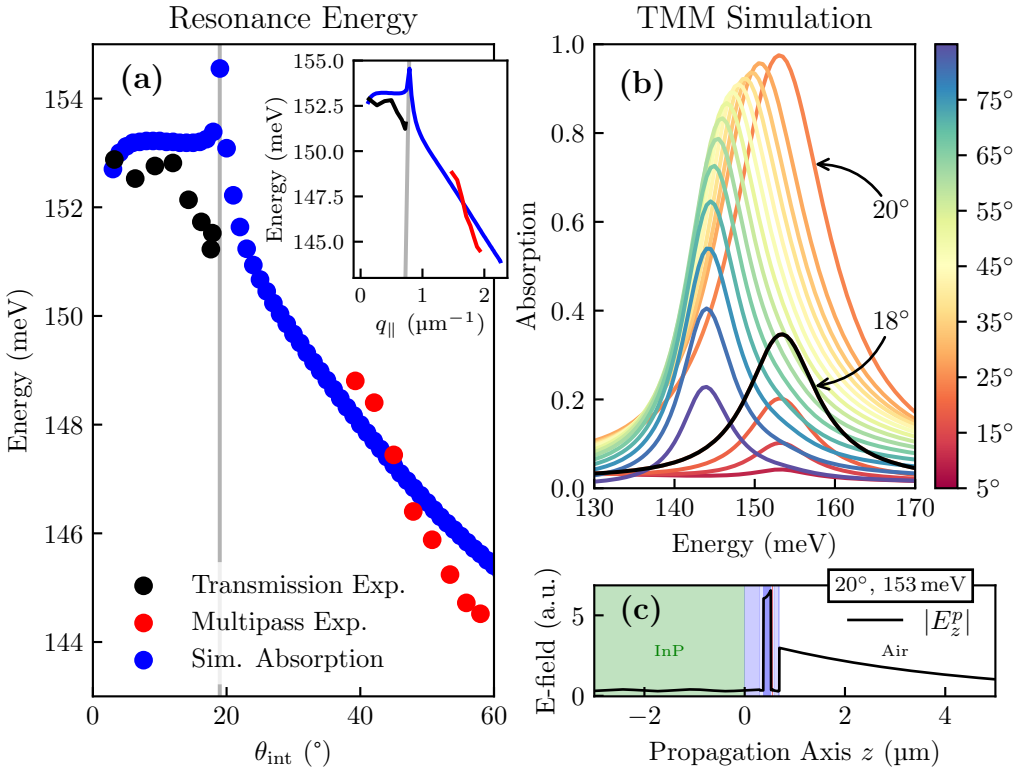

Fig. 2.14 In Panel (a), the experimental and simulated resonances energies are plotted as a function of the internal angle. The same data is plotted in the inset as a function of the in-plane wavevector $q_{\parallel}$. The grey lines indicate the light lines of free space. In Panel (b) simulated absorptivity spectra calculated via the TMM are plotted. The series of spectra are spaced at 5°, with an additional spectrum included at 18° to show the behavior just below the light line. In Panel (c), the absolute value of the electric field in the confined direction is plotted over the propagation axis of an incident p-polarized wave.

In the dispersion of the resonance energies extracted from the simulated spectra, an anomalous behavior is observed near the free space light line at 18.98°. There is a divergence between the radiative modes above the light line, and the nonradiative modes below the light line. This effect is less evident in the experiment. In the inset of the left panel of Fig. 2.14, the same data are plotted as a function of the in-plane wavevector instead of the angle.

The simulated absorptivity spectra shown in the right panel likewise exhibit noteworthy behavior near the light line. For small angles (above the light line), the amplitude of the absorptivity increases, as expected according to Eq. (2.5), and as suggested by the transmission data shown in Fig. 2.7. Then, over just the next 2°, as the light line is crossed, the peak value of the absorptivity jumps from less than 0.4 to 1. It is remarkable that the

absorptivity can reach a value of unity despite the deeply subwavelength width of the thin film, and without any surface patterning or reflective metallic layers to enhance the light matter interaction. In the case of a highly doped layer between two half-infinite semiconductor media, the absorptivity of the radiative Berreman mode, given by Eq. (2.4), never exceeds 1/2. In stark contrast to the Berreman mode, the linewidth of the nonradiative mode in the simulated spectra of a Panel (b) does not broaden with angle.

The modes below the light line are bound surface modes, and therefore the electric field of these modes decays away from the semiconductor surface. This behavior is observed for the E_z component of the electric field in Panel (c) of Fig. 2.14, calculated for an energy of 153 meV and for an internal angle of 20°, just below the light line. Inside the heavily doped thin layer, there is an enhancement of the electric field E_z. This enhancement can be attributed to an epsilon-near-zero effect [18, 141]. In [140], the authors exploit this effect in an optoelectronic device.

A nearly identical study to the one presented here of the nonradiative modes of a deeply subwavelength thin film is found in [19]. This study was performed with indium tin oxide (ITO) thin films deposited on a glass substrate. Light incident from the glass substrate can excite the surface modes of the thin film on the ITO/air interface, as the geometry resembles the Kretschmann configuration. In this study, the zero crossing of the real part of the ITO dielectric function was near 0.955 meV, giving rise to modes at much greater frequency than those studied here.

2.3.3 Summary of Optical Studies

The experiments of Section 2.2.2 and the previous section demonstrate that the nature of the medium next to the sample surface, close to the heavily doped slab, determines the nature of the mode excited. Above the free space light line, the Berreman mode is excited whether the media bordering the surface of the heavily doped layer is air or gold. Below the free space light line, the nature of the mode excited depends on the media on the surface side of the heavily doped layer. When the adjacent medium is gold, the Berreman mode is excited up to the semiconductor light line. When the adjacent medium is air, the Berreman mode is only excited up to the air light line, below which, a bound nonradiative mode is excited. The optical properties of the nonradiative mode are fundamentally different than those of Berreman mode.

2.4 Thermal Emission from Thin Layer Plasmon Modes

Up to this point, the optical properties of the plasmonic modes supported by a highly doped thin layer in a single material InGaAs platform were investigated through spectroscopy measurements. Particular attention was paid to the absorptivity α of the modes. In this section, the same modes are studied as sources of thermal emission in experiments performed at room temperature. The optical properties of the modes are investigated through the emissivity ϵ, which is extracted from the spectral distribution of the emitted thermal radiation.

It is observed once more in the emission experiments that the presence of gold or air next to the sample surface dramatically changes the nature of the collective mode supported by the heavily doped thin layer.

2.4.1 Background and Description of the Experiment

The spectral power distribution of thermal radiation emitted by an object is described by the Planck law for the thermal emission of a perfect blackbody $B(\omega, T)$ times the emissivity $\epsilon(\omega)$ of the object:

$$B(\omega, T)\epsilon(\omega) = \frac{2h\omega^3}{(2\pi)^3 c^2} n_{\mathrm{B}}(\omega, T)\epsilon(\omega) \tag{2.10}$$

where $n_{\mathrm{B}}(\omega, T) = (\exp(\hbar\omega/kT) - 1)^{-1}$ is the Bose-Einstein occupation factor. The emissivity is simply defined as the ratio of the power of thermal radiation emitted from an object at a given temperature to that of a perfect blackbody at the same temperature. It is thus a property of the object and cannot exceed 1.

According to Kirchhoff's law, for a body in thermodynamic equilibrium, the absorptivity α and the emissivity ϵ must be equivalent at a given frequency. Since in the previous section, it was demonstrated that the absorptivity of the plasmon modes supported by the heavily doped slab can reach unity under certain conditions, Kirchhoff's law dictates that these modes, at least for a certain critical coupling angle, behave as ideal ($\epsilon = 1$) thermal emitters at their resonant frequency.

At room temperature, the curve of $B(\omega, T)$, which describes the spectral radiance emitted from a blackbody, peaks in the mid-infrared where the plasmonic modes studied in this chapter are resonant. Consequently, even in the absence of a driving force, a significant number of electrons are already involved in plasmon excitations when the system is in equilibrium at room temperature. The fraction of excited plasmons is determined precisely by the Bose-Einstein occupation factor. It is the radiative decay of these excitations which is responsible for the incandescent (or thermal) emission.

To experimentally study thermal radiation emitted by the plasmon modes, devices are fabricated in which plasmons can be thermally excited with an electrical current. The device is sketched in Fig. 2.15. The semiconductor layers grown on the InP substrate are patterned into mesa structures. Then, gold electrical contacts are deposited permitting an in-plane current to be applied.

Plasmon modes between the contacts are thermally excited by square electrical pulses repeated at a 1 kHz frequency. The pulses drive a current parallel to the surface which heats the electron gas via the Joule effect. An optional gold mirror layer can be deposited above the region where the plasmons are excited. The emitted thermal radiation is coupled out to free space through a facet polished onto the substrate. The radiation emitted at a given angle inside the semiconductor is selectively detected once the radiation passes into free space, accounting for refraction at the facet interface. To study the radiation emitted over a wide range of angles, multiple facets at different angles with respect to the sample surface are polished on different devices.

Since the electron gas reaches internal equilibrium orders of magnitude faster than the inverse of the pulse frequency at 1 kHz, the temperature of the electron gas is defined as $T + \Delta T$ where T is the ambient temperature and ΔT is the temperature increase resulting from the dissipation of electrical power. Note that for fast modulation schemes, the electron gas may be out of equilibrium with respect to the lattice, and the dynamics of the heat transfer in the system must be more carefully considered to properly model the excess electronic temperature (see [139] for additional details).

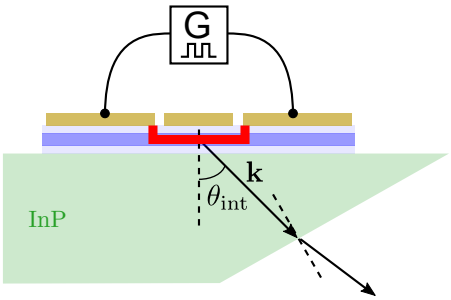

Fig. 2.15 The device used to thermally excite plasmon modes with an electrical current is sketched. A side profile of the mesa structure is shown with gold contacts and a gold mirror above the region where the plasmons are excited. In the experiment, the channel of the mesa is 55 µm wide (in the dimension out of the page), and two gold contacts are separated by 55 µm, fixing the area of the excited plasmons.

The modulation of the injected electrical power results in a modulaton of the electronic temperature, permitting a lock-in detection technique to be used to selectively detect the infrared emission only from the excited sample under study and not the ambient environment. The change in temperature of the electron gas during an electrical pulse results in a change in the Bose–Einstein occupation factor of the plasmon modes, resulting in a net increase in the total optical power emitted as well as a change in the spectral radiance distribution of this power. This is illustrated in the left panel of Fig. 2.16, where the curves $B(T)$ are plotted for a blackbody at 300 K, and a blackbody at a temperature ΔT greater than 300 K.

The signal measured by the lock-in technique is not the total optical power emitted from the plasmon modes, but is instead proportional to the difference in the optical power emitted with and without the electrical excitation. The signal is sketched in Fig. 2.16 as the shaded areas between the two blackbody curves, and at a frequency ω, is proportional to [70]:

$$\epsilon(\omega)\left(n_{\text{B}}(\omega, T+\Delta T) - n_{\text{B}}(\omega, T)\right) \tag{2.11}$$

A Fourier Transform Interferometer (FTIR) is used to spectrally resolve the detected signal into an an emission spectrum, the shape of which is described by Eq. (2.11). The frequency dependence of the spectrum depends on the emissivity and a factor determined as the difference in occupation number at two temperatures separated by ΔT. The spectrum of the emissivity at a given angle can thus be extracted provided one has knowledge of ΔT.

The shape of the factor dependent on ΔT is shown in the right panel of Fig. 2.16 for various temperatures. It is evidently not flat over the spectral region in which the plasmon modes are resonant. Thus, to properly extract the emissivity from the emission spectrum of the plasmon modes, especially when the linewidth of the emitting mode is large, requires that the energy dependence of this factor be considered.

From experiment, ΔT may be determined by establishing a relationship between the injected electrical power and the detected optical power. The optical power emitted in a solid angle $d\Omega$ may be written [70]:

$$\delta P_{\text{opt}}(\theta) = \Gamma_{\text{rad}}(\theta)\Delta U \delta N(\theta, d\Omega) \tag{2.12}$$

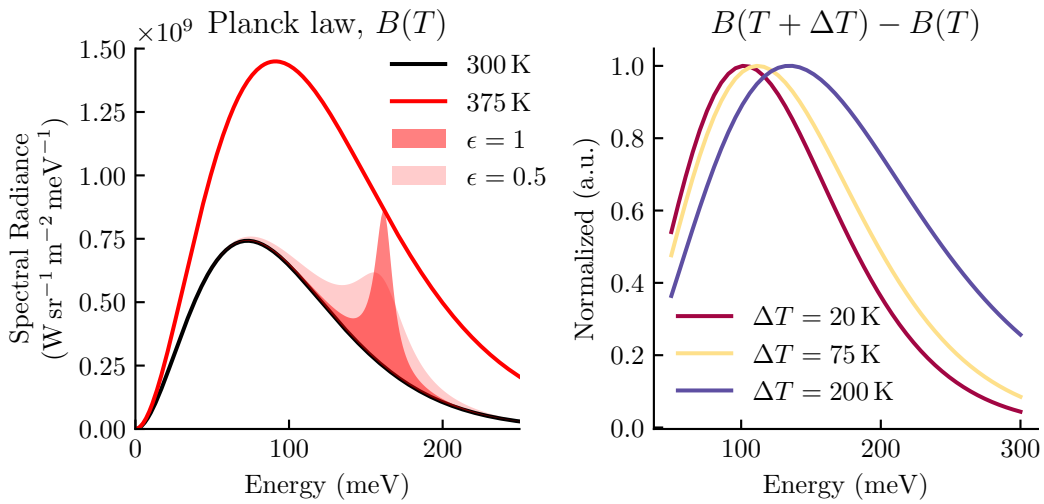

Fig. 2.16 On the left, the curves describing the spectral radiance of a blackbody (Planck's law) are plotted at temperatures T and $T+\Delta T$. The shaded areas between the curves are given by $\epsilon(\omega)\,(B(T+\Delta T)-B(T))$ in accordance with Eq. (2.11) and represent the optical power detected by the lock-in measurement. On the right, the difference between two Bose-Einstein factors at temperatures $T+\Delta T$ and T is plotted for various ΔT and normalized to one.

where $\Gamma_{\mathrm{rad}}(\theta)$ is the spontaneous emission rate, $\Delta U = \hbar\omega_0\,(n_{\mathrm{B}}\,(\omega, T+\Delta T) - n_{\mathrm{B}}\,(\omega, T))$, and $\delta N(\theta, d\Omega) = \omega_0^2 n^2 S\,(2\pi)^{-2}\,c^{-2}\cos\theta d\Omega$ describes the number of plasmons emitting in a direction θ from the area S. Equation (2.12) describes a relationship between the optical power detected and the temperature rise ΔT of the electron gas. In the simplest description, $\Delta T = R_{\mathrm{th}} P_{\mathrm{elec}}$ where P_{elec} is the current times the voltage of the injected pulse, and R_{th} is understood to be a constant electronic thermal resistance. The curve of δP_{opt} as a function of P_{elec} can be experimentally measured. By fitting the experimental curve with Eq. (2.12), the relationship between P_{elec} and ΔT can be determined. Note that in general, ΔT is dependent on the modulation frequency [139].

2.4.2 Results of the Thermal Emission Experiments

To study the thermal emission from the plasmonic modes of a highly doped thin layer, and specifically, to investigate how the medium adjacent to the sample surface (whether air or gold) influences the nature of the collective mode supported in the structure, devices like those sketched in Fig. 2.15 were processed in two forms: with and without a gold mirror centered between the contacts above the thermally excited region.

For these studies, sample V0211 was grown[2] to consist of just three InGaAs layers of thickness 100 nm, 150 nm, and 100 nm on an Fe-doped InP substrate. The middle 150 nm layer was intentionally doped with a very large electronic density. As was described for the InP1716 sample in Section 2.1.2, despite the lack of intrinsic barriers (conduction band

[2]Sample V0211 was also grown via MOCVD by the team of Grégoire Beaudoin, Konstantinos Pantzas, and Isabelle Sagnes at the Centre de Nanosciences et Nanotechnologies (C2N).

offsets) in the single-material system, electronic charge is bound in the highly doped region due to a significant band bending effect, resulting in a system which resembles that of a highly doped wide quantum well in an InGaAs/AlInAs system.

To model the optical response of the electron gas in the thin layer, a dielectric function is constructed as described in Section 2.1.2. To determine the electronic density of the highly doped layer, transmission measurements of the V0211 sample were performed at Brewster's angle. The Berreman mode was observed at 161 meV, allowing the electronic density to be determined as $N_{\mathrm{v}} = 1.7 \times 10^{19}\,\mathrm{cm}^{-3}$.

In prior thermal emission experiments [70] similar to those described here, the metallic contacts were diffused down to the highly doped layer to directly contact the electron gas. In the present experiment, the contacts were not diffused, as it was anticipated that an increase in resistivity from the not-intentionally-doped InGaAs top layer would result in an increased ΔT for the electron gas, thereby resulting in an increase in the emitted optical power. However, even without diffusing the metallic contacts, the devices were found to have a near linear current-voltage response with a small resistance of approximately $12\,\Omega$. It is very likely that some dopants are unintentionally incorporated into the top InGaAs layer, rendering it more conductive. It is difficult during the MOCVD growth to abruptly halt the incorporation of dopants in the layers grown just after the very highly doped layer, as the dopant density of this layer pushes the growth process to an extreme.

In the experiments which follow, multiple devices with and without a gold layer deposited above the region where plasmons are thermally excited were fabricated with facet angles of 20°, 30°, and 45° in order to couple radiation emitted at a wide range of angles into free space. The current-voltage characteristics of the different devices were highly consistent. All of the thermal emission spectra presented in the following sections were measured with the electron gas thermally excited by 500 ms, 2.5 V square pulses repeated at a rate of 1 kHz, during which a current of 190 mA passed through the sample, resulting in an injected peak electrical power of 475 mW.

In order to study the amplitude of the plasmon emission lineshape as a function of angle, each spectrum is multiplied by an angle-dependent factor to correct for the angle-dependent transmission across the InP/air boundary of the facet (determined by the Fresnel coefficients). The spectra are also corrected for the the responsivity of the MCT detector. Then, to extract the form of the emissivity from the emission spectra, the experimental spectra are divided by the factor $n_{\mathrm{B}}(\omega, T + \Delta T) - n_{\mathrm{B}}(\omega, T)$, appearing in Eq. (2.11). While as described in the previous section, ΔT can be extracted from experiment, in what follows ΔT was fixed to 75 K in order to find the best agreement between the extracted emissivity and the model for the absorptivity, described in Section 2.3.[3] Note that if the factor describing the difference in occupation number is neglected in extracting the form of the emissivity, then the determined emissivity will be largely underestimated at higher energies. This becomes particularly relevant when the emitting mode has a large linewidth.

Finally, note that only the spectral form of the emissivity is extracted from the experiment, meaning the emissivity is determined only up to a constant factor. To extract the

[3] Unfortunately, at the time of the experimental study, the experiment described in the previous section to extract ΔT was not performed. The value of ΔT mentioned in the text used to extract the form of the emissivity from the experimental spectra is reasonable with the values reported in [70]. Furthermore, it is evident in the right panel of Eq. (2.11) that small variations of ΔT on the order of even 50 K have little influence on the form of the factor $(n_{\mathrm{B}}(\omega, T + \Delta T) - n_{\mathrm{B}}(\omega, T))$.

absolute emissivity, fixed between 0 and 1 would require the perfect collection of all the emitted power from the device, and the precise determination of ΔT. Practically, this is difficult.

2.4.2.1 Thermal Emission with Gold Mirror

The modulated injection of electrical power to the devices at the low frequencies studied here increases the temperature not only of the electron gas, but also of the crystal lattice, which is described by its own emissivity. The spectrum of the emitted radiation detected in the lock-in measurements thus includes a background contribution. Assuming this contribution is not polarization dependent, the strict polarization dependence of the plasmon mode permits the plasmon contribution to be separated from the background. At each emission angle, spectra are measured selectively for each polarization. The s-polarized spectra S_s^{exp} can then be subtracted from the p-polarized spectra S_p^{exp}, to extract the plasmonic contribution to the emission.

Practically, this procedure does not eliminate all of the background contribution, and it is necessary to multiply S_s^{exp} by a factor f before subtracting it from the p-polarized spectrum. To determine f, a least-squares regression algorithm is used to fit the experimental p-polarized spectrum with a function of the form:

$$S_p^{\text{exp}} = f S_s^{\text{exp}} + \mathcal{F}(\omega, \ldots) \tag{2.13}$$

The expression $\mathcal{F}(\omega, \ldots)$ describes the expected lineshape of the plasmon emission. When a gold layer is present above the highly doped layer, the plasmon emissivity (absorptivity) is described by the expression of Eq. (2.4). Then, for a fixed angle and using $\gamma_{\text{NR}} = 7\,\text{meV}$ extracted from a spectrum measured at low angle where the radiative broadening contribution is absent, the emission from the plasmon is modeled as:

$$\mathcal{F}(\omega, A, \omega_0, \Gamma_{\text{rad}}) = A\alpha(\omega, \omega_0, \Gamma_{\text{rad}}) \tag{2.14}$$

The resonance frequency ω_0, the radiative linewidth Γ_{rad}, and a factor A accounting for the non-normalized amplitude of the emission are left as fit parameters. Including f above, there are a total of four free parameters in the fit.

Experimentally measured thermal emission spectra for the V0211 devices with the gold mirror measured for three emission angles are presented in Fig. 2.17. In each panel of the figure, the experimentally measured p- and s-polarized spectra are plotted. The extracted plasmon contribution, found as:

$$S_p^{\text{exp}} - f S_s^{\text{exp}} \tag{2.15}$$

is plotted, with f determined from the fit procedure described above. The values of f, $E_0 = \hbar\omega_0$, and Γ_{rad}, extracted from the fitting procedure for each angle, are reported in the figure. Finally, the model of the plasmon emission, described by $\mathcal{F}$, is plotted (gold dashed lines) using the parameters extracted from the fit. For each of the angles shown, there is a strong agreement between the extracted plasmon contribution and the form of $\mathcal{F}$, suggesting the background contribution has been effectively removed. The factors f are found to be of order 1, as expected.

The width of the emission feature is found to broaden dramatically for increasing angle, as described theoretically by Eqs. (2.2) and (2.3) and as experimentally observed in the

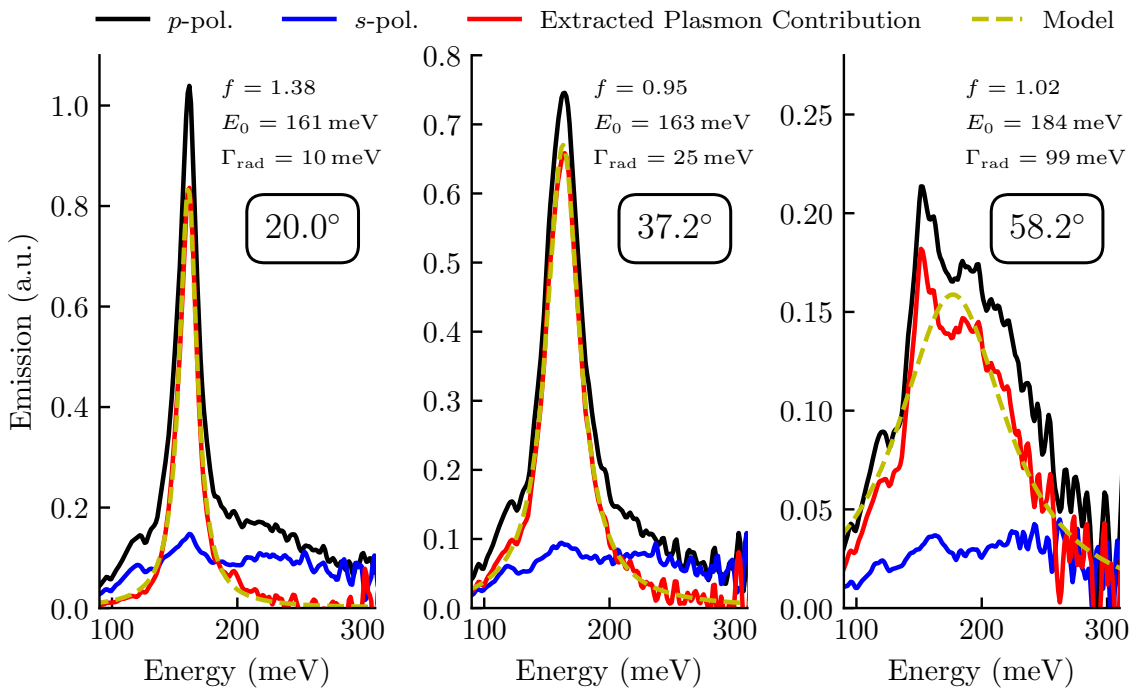

Fig. 2.17 The experimentally measured p- and s-polarized emission spectra are shown after being corrected for the factor of $n_{\mathrm{B}}(\omega, T + \Delta T) - n_{\mathrm{B}}(\omega, T)$ assuming $\Delta T = 75\,\mathrm{K}$. The function determined by Eqs. (2.13) and (2.14) in the text is fit to the p-polarized spectra, allowing the extracted plasmon contribution to be determined according to Eq. (2.15). The model $\mathcal{F}$ is plotted for the extracted parameters.

absorptivity measured reported in Fig. 2.9 for the InP1716 sample. Likewise, the resonance energy E_0 of the plasmon mode increases in energy like that of the InP1716 sample in the reflection measurements.

To more closely study the angular dependence of the plasmon emission, emission spectra were measured for angles between 18° and 58°, from devices with facets of 20°, 30°, and 45°. The plasmon contribution was extracted from each spectra using the same procedure described above and demonstrated in Fig. 2.17. The resulting series of emission spectra is plotted in Panel (a) of Fig. 2.18.

While not shown, emission spectra were measured for each of the three devices over a range of angles which overlapped with the measurements of another facet. Spectra measured from different devices with different facets but for the same emission angle were found to be nearly identical in form.

The y-axis of the experimental plasmon emission spectra plotted in Panel (a) of Fig. 2.18 describes the emissivity. While the emissivity is only determined experimentally up to a factor, modeling of the absorptivity of the Berreman mode with the TMM (shown in Panel (b) of the same figure) indicates that the emissivity peaks at one for a given angle. The series of experimental spectra are normalized such that the maximum emission value is set

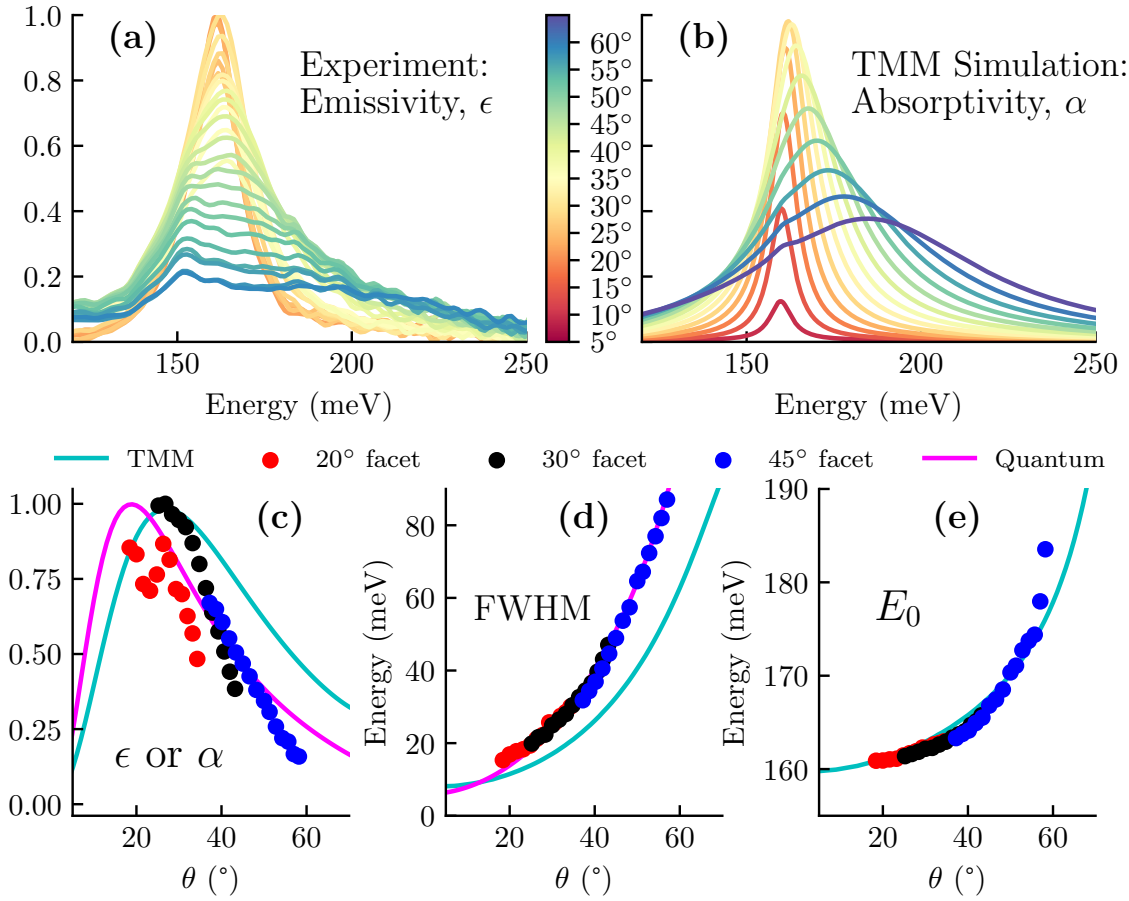

Fig. 2.18 The extracted plasmon contribution from the experimental thermal emission spectra of V0211 devices fabricated with a deposited gold layer are plotted in Panel (a). Simulated absorptivity spectra calculated with the TMM are plotted in Panel (b). Note the angle-color key set with the color bar applies to Panels (a) and (b). In the bottom panels, the experimental peak emissivity, FWHM, and resonance energy are plotted, compared with curves determined from TMM calculations, and curves determined by fitting expressions from the quantum model, as described in the text.

to one, permitting the spectra to be interpreted as the emissivity.

In the bottom panels of Fig. 2.18, the maximum of the experimental emissivity, the total linewidth, and the resonance energy, extracted from spectra measured from three devices with different facets, are plotted as scatter points as a function of the emission angle. The same quantities extracted from the TMM modeling are plotted with continuous cyan-colored lines. The trends observed in the experiment are found to be well-modeled by the simulations: the emissivity is found to peak at one between 20° and 30°, and thereafter continually decline; the linewidth broadens with angle; and the resonance energy blueshifts with increasing angle.

The total linewidth of the plasmon mode is $\Gamma_{\mathrm{FWHM}} = \gamma_{\mathrm{NR}} + \Gamma_0 \sin^2\theta/\cos\theta$. Leaving Γ_0 and γ_{NR} as free parameters, this expression can be fit to the extracted linewidth Γ_{tot} of the experimental emission spectra as a function of angle. The result of the fit is plotted in the bottom middle panel of Fig. 2.18 with a continuous pink line. From the fit, it is determined that $\Gamma_0 = 64\,\mathrm{meV}$ and $\gamma_{\mathrm{NR}} = 5.9\,\mathrm{meV}$. These values for the radiative and nonradiative linewidth can then be used to plot a curve of the peak absorptivity as a function of angle, where the peak absorptivity is found according to Eq. (2.4) for $\hbar\omega = E_0$. This curve is plotted in the bottom left panel of Fig. 2.18 as a continuous pink line. The curve is found to agree slightly better with the experimental data than the TMM prediction.

2.4.2.2 Thermal Emission with Air Next to Sample Surface

When no gold mirror is deposited, the surface of the area where the electron gas is thermally excited has a boundary with air, and the structure support a nonradiative plasmonic epsilon-near-zero mode which lies below the free space light line. In the following, we investigate the thermal emission from this mode.

As in the previous section, the plasmon contribution to the emission spectrum is extracted by fitting a function of the form described by Eq. (2.13) to the measured p-polarized emission spectrum. In the thermal emission experiments with the gold mirror, the form of the plasmon contribution $\mathcal{F}(\omega,\ldots)$ used in the fit was determined by the expression for the absorptivity (Eq. (2.4)) of the Berreman mode. In the case of the nonradiative mode, an analytic expression for the absorptivity is lacking, and we therefore assume a Lorentzian form for $\mathcal{F}$, leaving the amplitude A, the resonance energy E_0, and the FWHM Γ_{tot} as free parameters: $\mathcal{F} = \mathcal{F}(\omega,A,E_0,\Gamma_{\mathrm{tot}})$. As before, including f, there are four free parameters to fit Eq. (2.13) to the experimental p-polarized emission spectra.

Emission spectra were measured for angles between 18° and 58° from V0211 devices with facets of 20°, 30°, and 45°, in the absence of a deposited gold layer. The spectra of the extracted plasmon contributions are plotted in Panel (a) of Fig. 2.19. Simulated absorptivity spectra of the highly doped layer next to air, calculated with the TMM, are plotted in Panel (b). As observed in Fig. 2.14, the absorptivity of the modes in the simulation is found to jump to one just below the light line around 18°. The extracted plasmon contribution from the experimental spectra is therefore normalized to the maximum emission amplitude which is found to occur around 20°, permitting the experimental plasmon emission to be identified as the emissivity.

In the experiment, as in the TMM simulations, the emissivity increases with angle below 20° until reaching a maximum at one. Beyond 20°, the emissivity decreases continuously. This behavior is observed in Panel (c) of Fig. 2.19, where the experimental emissivity and calculated absorptivity are plotted as a function of angle, and are found to be in good

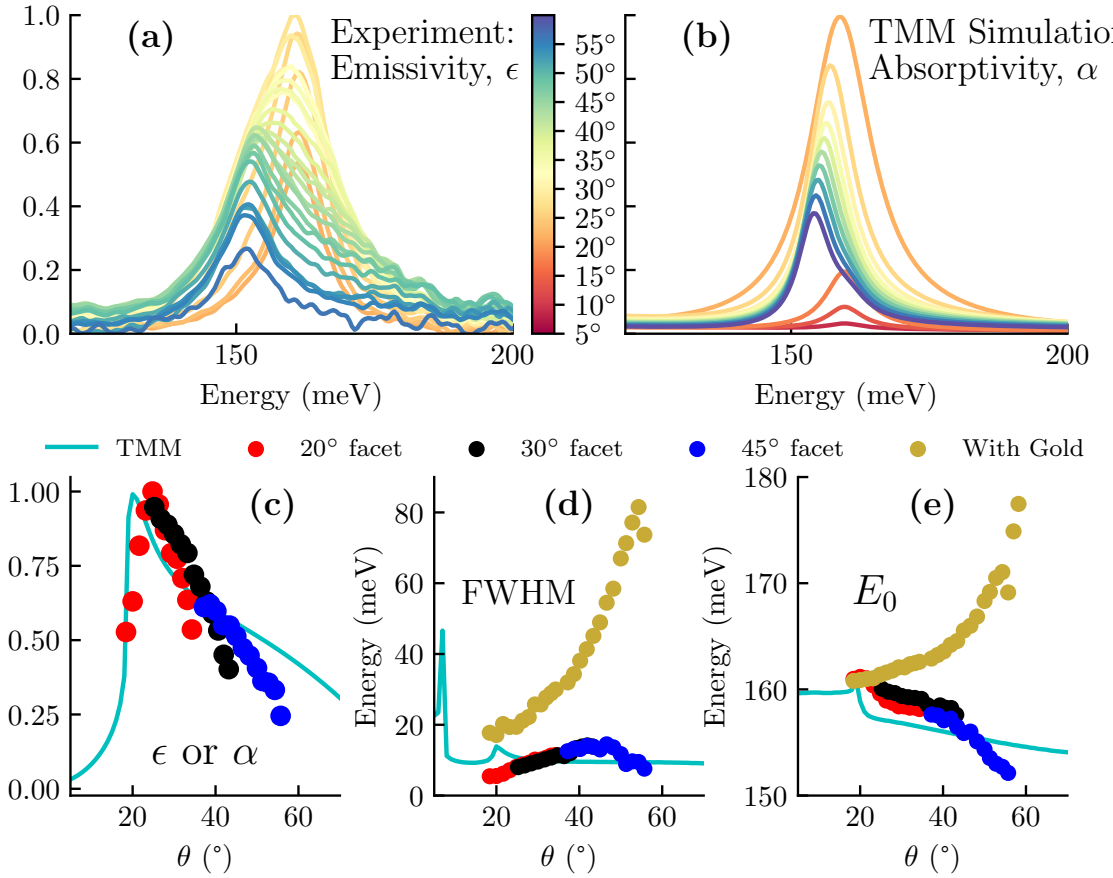

Fig. 2.19 Emission spectra of the extracted plasmon contribution of V0211 devices fabricated *without* a gold layer on the sample surface are plotted in Panel (a). Simulated absorptivity spectra, calculated with the TMM, are plotted in Panel (b). Note the angle-color key set with the color bar applies to Panels (a) and (b). In the bottom panels, the experimental peak emissivity, FWHM, and resonance energy are plotted and compared with TMM calculations and experimental data from the thermal emission experiments with the deposited gold layer.

agreement.

In total contrast to the behavior of the Berreman mode observed in the emission experiments with the gold mirror, the nonradiative mode observed without the gold mirror redshifts with increasing angle and does not radiatively broaden with a $\sin^2\theta/\cos\theta$ dependence. To stress this contrast, in Panels (b) and (c) of Fig. 2.19, the linewidth and the resonance energy of the emission spectra measured without a gold layer are plotted alongside the same quantities from the emission spectra measured with a gold layer. The linewidth and resonance energies determined from TMM simulations for the case without the gold layer are also plotted and found to be in good agreement with the corresponding experimental data.

2.5 Conclusion

It was demonstrated that a single material platform could host a Berreman mode. Modeling of electrostatic charge effects demonstrated that the highly doped layer in a single material structure can give rise to its own confining potential. This provides justification for modeling a single material structure as three distinct homogenous media.

The plasmon modes supported in a thin highly doped layer of a single material InGaAs structure were experimentally investigated through spectroscopy and thermal emission experiments. It was experimentally demonstrated that the dispersion of the modes supported by the heavily doped layer differs whether or not a gold layer is deposited on the sample surface. Measurements of the sample with the gold layer were well-described at all angles by the theoretical description of the Berreman mode developed in the input-output formalism [60]. In the absence of a gold layer, it was demonstrated that a nonradiative mode could be excited below the free space light line with different optical properties than the Berreman mode. This mode was identified as the epsilon-near-zero mode described in [141].

We conclude this chapter by noting that the fact that the electric field of the plasmon mode extends into free space when no gold layer is deposited immediately raises the perspective that other material resonances, such as colloidal quantum dots, graphene sheets, or perhaps even molecular vibrations (with possible applications in sensing) could be coupled to this mode. The coupled modes could then be studied in thermal emission.

A final interesting perspective concerns the propagation of the collective surface-type modes adjacent to the air interface. Could these modes be thermally excited electrically, propagate on a chip, and then be detected? Such a scheme would find use in both sensing and communication applications.

Chapter 3

Coupled Phonon-Plasmon Modes in Thin Films

It is usually assumed that the Reststrahlen band is a fixed property of a semiconductor material. In this spectral region, the optical response is determined by the optical phonons, whose resonance frequencies are fixed by the atomic composition of the crystal lattice. In contrast, there are many degrees of freedom in semiconductors to engineer electronic optical properties. As examples, the plasma frequency can be tuned with the addition of dopant impurities, and optical resonances can be engineered at desired frequencies via carefully designed heterostructures. In the following study, we use the electronic degrees of freedom to engineer the optical properties of the Reststrahlen band by exploiting the coupling between electronic motion and lattice vibrations.

The zero of the dielectric function in the Reststrahlen band normally occurs at the longitudinal optical (LO) phonon frequency. When an electron gas of comparable plasma frequency is introduced into the semiconductor, plasma oscillations couple with the LO phonons, and as a result, the zeros of the dielectric function are modified. In a thin film, due to the Berreman effect, the coupled LO phonon-plasmon modes can be directly observed as resonances in p-polarized spectra for light at oblique incidence. We experimentally investigate this phenomenon in thin doped InGaAs layers.

3.1 Plasmon-Phonon Coupling in Semiconductors

In this section, we solve for the zeros of the dielectric function which describes the optical response of bulk doped InGaAs in the Reststrahlen band.

The dielectric function describing the optical phonons of InGaAs in the absence of an electronic density is that provided in Eq. (1.61). It has two zeros at ω_{LO_1} and ω_{LO_2}. Literature values for the optical phonon resonances and ε_∞ are listed in Table 3.1 for the $\mathrm{In}_{0.53}\mathrm{Ga}_{0.47}\mathrm{As}$ ternary alloy.

In the presence of a gas of free electrons, the dielectric function describing the Reststrahlen band of InGaAs is found as the sum of Eq. (1.61) and the plasma frequency term

$In_{0.53}Ga_{0.47}As$	
ε_∞	11.61
$\hbar\omega_{LO_1}$	33.93 meV
$\hbar\omega_{TO_1}$	31.39 meV
$\hbar\omega_{LO_2}$	29.14 meV
$\hbar\omega_{TO_2}$	28.18 meV

Table 3.1: Literature values for the optical phonon energies and high frequency dielectric constant of $In_{0.53}Ga_{0.47}As$ [27].

of the Drude dielectric function (Eq. (1.27)):

$$\varepsilon_r(\omega) = \varepsilon_\infty \frac{\left(\omega_{LO_1}^2 - \omega^2 - i\gamma_1\omega\right)\left(\omega_{LO_2}^2 - \omega^2 - i\gamma_2\omega\right)}{\left(\omega_{TO_1}^2 - \omega^2 - i\gamma_1\omega\right)\left(\omega_{TO_2}^2 - \omega^2 - i\gamma_2\omega\right)} - \frac{\varepsilon_\infty\omega_p^2}{\omega^2 + i\gamma\omega} \tag{3.1}$$

The zeros of $\varepsilon_r(\omega)$ in the absence of damping are plotted in Fig. 3.1 as the plasma energy $\hbar\omega_p$ is varied. Since three longitudinal oscillations are coupled (two LO phonons and the plasma oscillations of the electron gas), there are three continuous branches of zeros. We name the branches L_-, L_0, and L_+ in concordance with [10, 89, 150]. An anticrossing is observed between L_+ and L_0 and between L_0 and L_-. The L_+ mode is bound below by ω_{LO_1}, the L_0 mode is bound between ω_{LO_1} and ω_{LO_2}, and the L_- mode is bound above by ω_{LO_2}. When the plasma frequency is well detuned from the LO phonon resonances, two of the branches converge to the bare LO phonon energies. The three zeros, arising from the coupling of optical phonons and plasma oscillations, are the energies at which the medium can support longitudinal electromagnetic waves.

The strength of the interaction between two coupled oscillators is usually quantified with a coupling constant. For example, in coupled light-matter systems, the Rabi energy quantifies the coupling strength [43]. When the coupled modes lie on two anticrossing branches, the coupling strength can be extracted as half of the minimal energy separation between the branches [135].

The coupled mode solutions plotted in Fig. 3.1 result from the coupling of three oscillators, and therefore three coupling constants are required to exactly describe the system. However, by setting one LO phonon and its corresponding TO phonon to zero energy, the coupling between the plasma oscillations with each LO phonon can be considered separately. In Fig. 3.2, the zeros of Eq. (3.1) are plotted for $\omega_{TO_2} = \omega_{LO_2} = 0$ (left) and $\omega_{TO_1} = \omega_{LO_1} = 0$ (right). The strength of the interaction between the LO_1 phonon and the plasma oscillations is extracted as $\Omega_1 = 6.44\,\text{meV}$ or approximately 19.0 % of the LO_1 phonon excitation energy. The strength of the interaction between the LO_2 phonon and the plasma oscillations is extracted as 3.71 meV or approximately $\Omega_2 = 12.7\,\%$ of the LO_1 phonon excitation energy. In both cases, the LO phonons are said to be ultrastrongly coupled with the plasma oscillations. Two hallmarks of the ultrastrong coupling regime are observed in either panel of Fig. 3.2: the opening of a photonic gap (shaded in gray) between the branches of coupled modes, and the redshifting of the minimal energy separation away from the crossing of the two uncoupled modes [135].

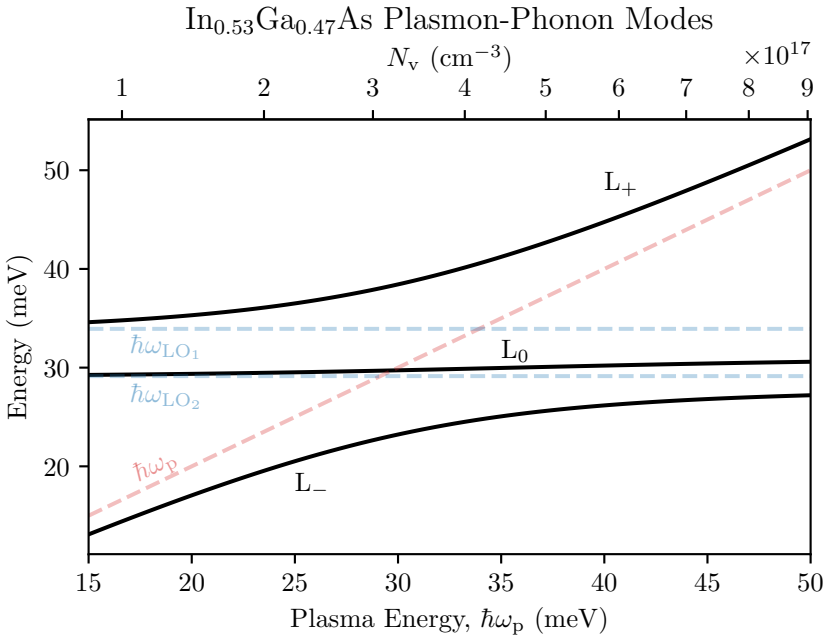

Fig. 3.1 The coupled longitudinal optical phonon-plasmon modes are found as the zeros of Eq. (3.1) and named L_-, L_0, and L_+. A constant effective mass of $0.043m_e$ is used to link the electronic density axis with the plasma energy axis.

The coupling between LO phonons and a plasma of electrons has been extensively studied with Raman spectroscopy. In this technique, inelastic light scattering is used to investigate the modes. Mooradian and Wright were the first to observe the interaction of the electron plasma with an LO phonon in the Raman spectra of bulk GaAs, for which they experimentally demonstrated an anti-crossing behavior [88]. Their work was followed by additional studies, still of n-doped GaAs [87, 130]. Later studies used Raman spectroscopy to investigate the coupling of longitudinal phonon modes with confined electronic transitions in heterostructures [104], specifically GaAs/AlGaAs heterostructures [103]. Raman scattering has also been used to investigate the coupling of the longitudinal optical phonons of ternary alloys with an electron plasma, for example in GaAlAs films [10, 150] and in GaInAs-InP quantum wells [89]. In these studies, the behavior of the coupled modes predicted in Fig. 3.1 for a ternary material was verified.

The coupling between LO phonons and an electron plasma was investigated optically in [66]. The authors measured infrared reflectivity spectra of bulk Te-doped GaAlAs, and then relied on a careful modeling of the spectra to extract the anticrossings of the coupled plasmon-phonon modes. In such optical studies of bulk materials, it is not possible to directly observe coupled LO phonon-plasmon resonances.

In the following, we study thin doped InGaAs layers in InGaAs/AlInAs heterostructures with *p*-polarized light at oblique angles of incidence and attempt to use the Berreman effect to directly observe resonances of the LO phonon-plasmon modes. We note that after the completion of our own investigation, a similar study, reported in [61], came to our attention. In the referenced study, the authors extract electronic densities from analyses of thin film

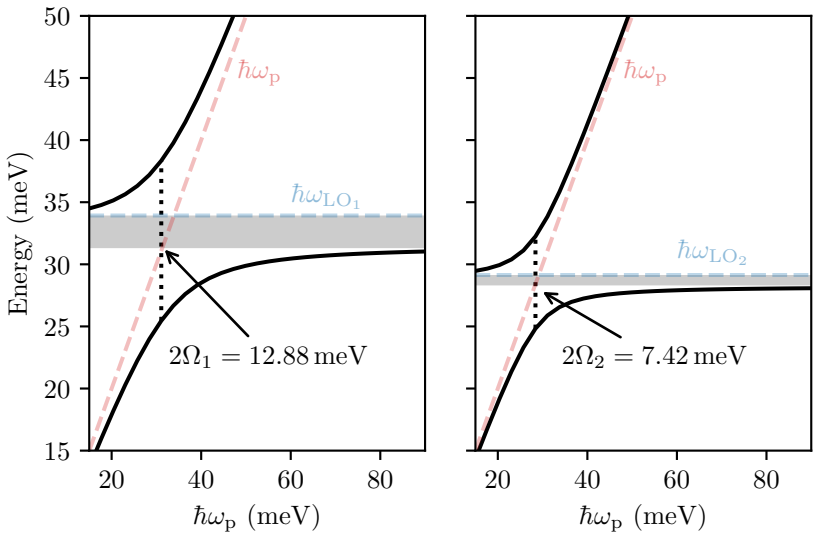

Fig. 3.2 The zeros of Eq. (3.1) in the absence of damping are plotted setting $\omega_{TO_2} = \omega_{LO_2} = 0$ on the left, and setting $\omega_{TO_1} = \omega_{LO_1} = 0$ on the right. The minimal energy separation between the branches of coupled modes is indicated.

Reststrahlen band spectra.

3.2 Description of the Experiment

Heterostructures of InGaAs/AlInAs layers, grown on an InP substrate, are studied in the reflectivity experiment sketched in Fig. 3.3. Reflectivity spectra are measured for *p*-polarized (TM) and *s*-polarized (TE) light incident from a blackbody source inside a Fourier Transform Interferometer (FTIR). The light is focused onto the sample with gold parabolic mirrors at a 45° angle. The specular reflection is collimated via another gold parabolic mirror, and finally, the beam is focused onto a liquid He-cooled bolometer. Spectra are normalized with reference spectra obtained by replacing the sample with a gold mirror.

To be able to identify dips in the reflectivity spectra as absorptivity, a 5 nm layer of titanium and a 150 nm layer of gold were deposited on the sample surface to act as a mirror. Without additional processing, incident and reflected light would need to pass through the 300 nm thick Fe-doped InP substrate before reaching the InGaAs/AlInAs layers. The InP substrate is opaque in the Reststrahlen region of InGaAs and AlInAs due to its own Reststrahlen band [5]. To avoid this difficulty, after the metal deposition, the samples are bonded mirror-side down to a host GaAs wafer using an epoxy. The entire InP substrate is then removed using an HCl solution, which is very selective against an InGaAs etch-stop layer.

Samples

The three samples summarized in Table 3.1 are studied in the following sections. Sample V0296 was grown as a control sample, and was not-intentionally-doped (n.i.d.). Sample

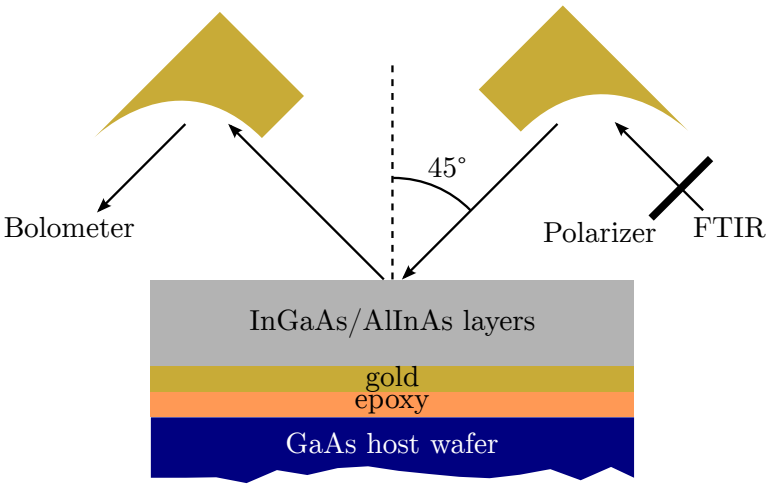

Fig. 3.3 A sketch of the experiment.

V0300 was designed identically to V0296 but with an added electronic density. The 45 nm width of the well and the nominal electron density were chosen so that, in the absence of plasmon-phonon coupling, the well would support a Berreman mode close in energy to the InGaAs optical phonons ~ 30 meV.

	Period	N_v		
Sample	InGaAs/AlInAs	Nominal	Experimental	Repetition
V0296	45 nm/10 nm	n.i.d.		30
V0300	45 nm/10 nm	1.7×10^{17} cm^{-3}	3.75×10^{17} cm^{-3}	30
V0301	35 nm/10 nm	8×10^{16} cm^{-3}	2.2×10^{17} cm^{-3}	50

Table 3.2: The samples studied in this chapter. The samples were grown via Metal Organic Chemical Vapor Deposition (MOCVD) on an InP substrate by the team of Grégoire Beaudoin, Konstantinos Pantzas, and Isabelle Sagnes at the Centre de Nanosciences et Nanotechnologies (C2N) in Palaiseau, France.

At the outset of our study, to the best of our knowledge, an electronic Berreman mode had never been observed at such low energies (in the THz). To observe a Berreman mode in this spectral range, the electronic density required is ~ 25 times less than that for which the Berreman mode is usually observed in the mid-IR (~ 150 meV). It was uncertain whether there would be sufficient charge-induced coherence to observe the *collective* mode, or if the mode would be too overdamped.

On the contrary, intersubband transitions are frequently studied in the THz [29, 132]. For this reason, we also chose to study the coupling between an intersubband transition and the optical phonons. To realize an intersubband transition around 30 meV in the InGaAs/AlInAs system, a wide quantum well is needed so that the subband spacing is sufficiently small. Sample V0301 was designed with 35 nm InGaAs/AlInAs quantum wells nominally doped with an electronic density of $N_v = 8 \times 10^{16}$ cm^{-3}. For these parameters, a single intersubband transition was expected at 26 meV.

Experimental values for the electronic density are reported in Table 3.1. These values are deduced from the modeling of experimental spectra, described in the following sections. The experimental values for the electronic density for both V0300 and V0301 are nearly a factor of two greater than the nominal values. Consequently, our studies are limited to the regime in which the 'bare' plasmon resonance is always at greater energy that the GaInAs phonons. We shall observe a coupling nonetheless.

The samples are designed with many repetitions of the well/barrier period in order that absorption features can be observed with a good contrast. This is especially important as the electronic density is reduced, since the absorption coefficient scales with the electronic density.

Though we shall not dwell on it further, we note that the V0296 structure is a hyperbolic metamaterial over certain frequency bands, meaning that structure can be described with an effective anisotropic dielectric function for which $\varepsilon_{\parallel}^{\text{eff}}$ and $\varepsilon_{\perp}^{\text{eff}}$ are of opposite sign [107]. This condition is often realized in periodic metal-dielectric structures. In the present case, the zero crossing at the LO phonon frequency fulfills the role of the metallic layers.

3.3 Optical Phonons in i-InGaAs/AlInAs Heterostructure

We begin with the study of the not-intentionally-doped InGaAs/AlInAs heterostructure, sample V0296. Resonances from the optical phonons of both the InGaAs layer and the AlInAs layer are observed in the experimental spectra. Since each material is a ternary alloy with four optical phonons, there are a total of eight optical phonon resonances which can be excited in the heterostructure. In order to more easily identify the resonances in the experimental spectra, we first examine the dielectric functions of the ternary alloys.

3.3.1 Dielectric Functions of InGaAs and AlInAs Reststrahlen Bands

Each ternary alloy is described by the dielectric function of Eq. (3.1) when the plasma frequency is set to zero. The real and imaginary parts of the dielectric function are plotted for InGaAs and AlInAs in Fig. 3.4 using parameters for the energies and linewidths determined from modeling of the V0296 experimental spectra, described in the following section. The parameters are reported in Table 3.3 under 'Values for ε'. They are found to be in good agreement with values from the literature, also reported in the table.

For each ternary alloy, two peaks are observed in the imaginary part of the dielectric function, plotted in red, at the energies of the transverse optical (TO) phonons, ω_{TO_1} and ω_{TO_2}. In the absence of damping, the real part of the dielectric function describing the ternary alloys crosses zero at ω_{LO_1} and ω_{LO_2}. However, using the linewidths from Table 3.3, the real part of the dielectric function misses the zero crossing at the frequency of the ω_{LO_2} phonon for both ternary alloys.

The absorption coefficients for thin InGaAs and AlInAs layers are calculated using the expression given in Eq. (1.47), and are plotted in the bottom panel of Fig. 3.4. Absorption peaks are observed at the two LO phonon energies of each material. However, for both materials, the amplitude of the LO_2 peak is nearly two orders of magnitude less than that of the LO_1 peak.

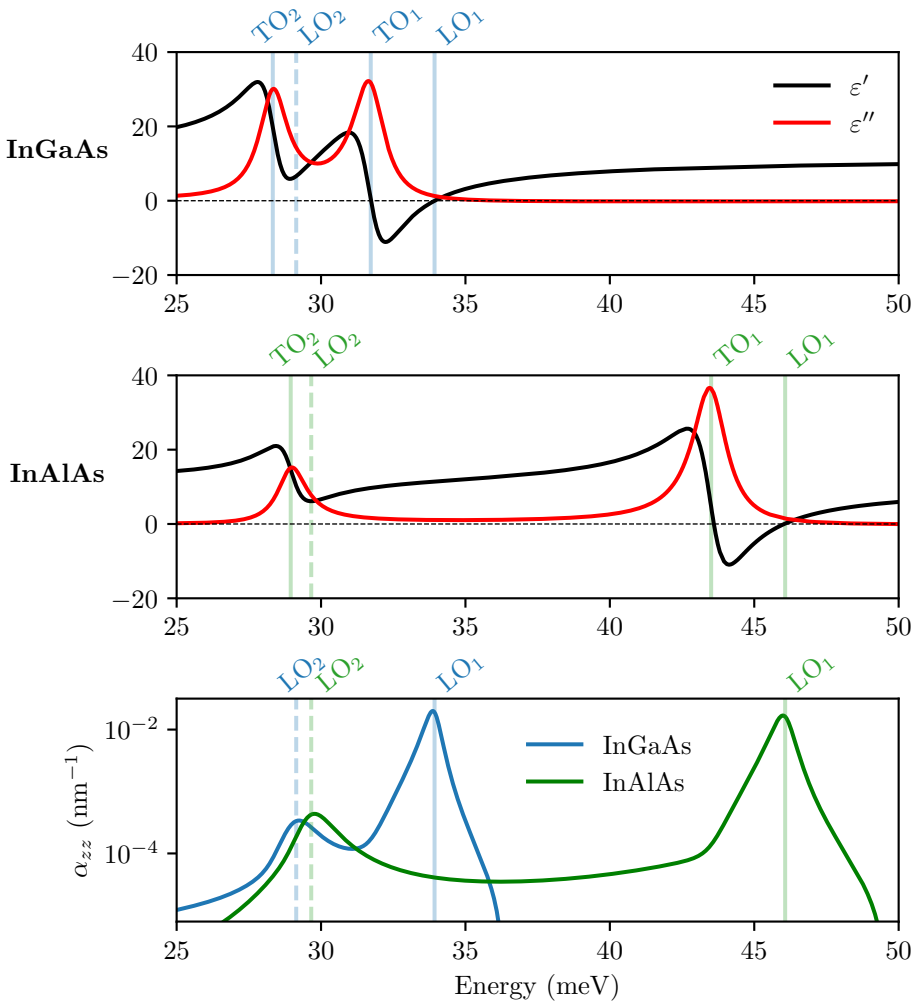

Fig. 3.4 In the top two panels, the real ε' and imaginary ε'' parts of the dielectric functions for $In_{0.53}Ga_{0.47}As$ and $Al_{0.48}In_{0.52}As$ for $\omega_p = 0$ are plotted using the values indicated in Table 3.3. In the bottom panel, the thin film absorption is plotted in logarithmic scale for each ternary material. Dashed vertical lines indicate a missed zero-crossing due to finite damping.

3.3.2 Direct Observation of InGaAs/AlInAs Optical Phonons

The experimental spectra of sample V0296 measured at T=5 K are plotted in the top panel of Fig. 3.5. In the TM spectrum, there are six phonon resonances which can be identified. The resonances at 33.9 meV and 46.1 meV appear only in the TM spectrum and are absent in the TE spectrum, and can thus be identified as LO phonons, observed due to the Berreman effect. From comparison with the literature values reported in Table 3.3, they are identified as the ω_{LO_1} phonons for InGaAs and AlInAs, respectively. In agreement with the absorbance calculated in Fig. 3.4, the ω_{LO_2} resonances are not observed in the experimental TM spectrum.

The remaining four phonons are assigned to the TO phonons of the ternary materials based on their proximity to the literature values. Note that the close proximity between the experimental resonances and the literature values for the InGaAs TO_1 and the AlInAs TO_2 phonons render the assignment of these resonances somewhat ambiguous. A summary of the observed resonance energies and their assignments is reported in Table 3.3 under 'Experiment'.

The reflectivity of the TM spectrum is less than that of the TE spectrum across the spectral range from 25 meV to 50 meV. This is due to a difference in Fresnel coefficients for the TM and TE polarizations. The TE polarized light is more strongly reflected at the semiconductor-air interface than the TM polarized light, and consequently less of the TE polarized light is coupled into the semiconductor layers where the absorption takes place.

Broad dips in the reflectivity spectra are observed for both TM and TE polarizations at energies above the phonon resonances. The dip in the TE spectrum is of slightly greater amplitude than that in the TM spectrum. These features are thin film interferences, resulting from the destructive interference between light reflected from the air/semiconductor interface and light reflected from the semiconductor/gold interface. They are analyzed in further detail below.

In the bottom panel of Fig. 3.5, simulated spectra for the V0296 reflectivity experiment are plotted. The simulations are performed with a commercial finite element software (COMSOL). The propagation of light through the InGaAs/AlInAs heterostructure is modeled in 2D for a planar slice of the heterostructure, using periodic boundary conditions for the translationally invariant directions in the layer plane. Each material layer is modeled in the simulation as a spatial domain described by its respective dielectric function. To simulate the reflectivity experiments, a gold domain is defined after the heterostructure layers, and the angle of incidence is set to 45°, as in the experiment.

The parameters used for the dielectric functions of the ternaries, reported in Table 3.3, were adapted so that the simulated spectra reproduce as closely as possible the experimental spectra. Likely due to the periodicity of the structure, there is a small discrepancy between the resonance energies used in the definition of the dielectric functions, and the energies at which resonances are observed in the simulated spectra.

With this approach, the simulated spectra closely model nearly all of the essential features of the experimental spectra: there are just two LO phonon resonances observed, one from each ternary material, present only for TM polarization; the reflectivity of the TM spectrum is less than that of the TE spectrum across the spectral range from 25 meV to 50 meV; and the relative amplitudes of the various peaks are in good agreement with the experimental spectra. The only significant disagreement between the simulated and experimental spectra

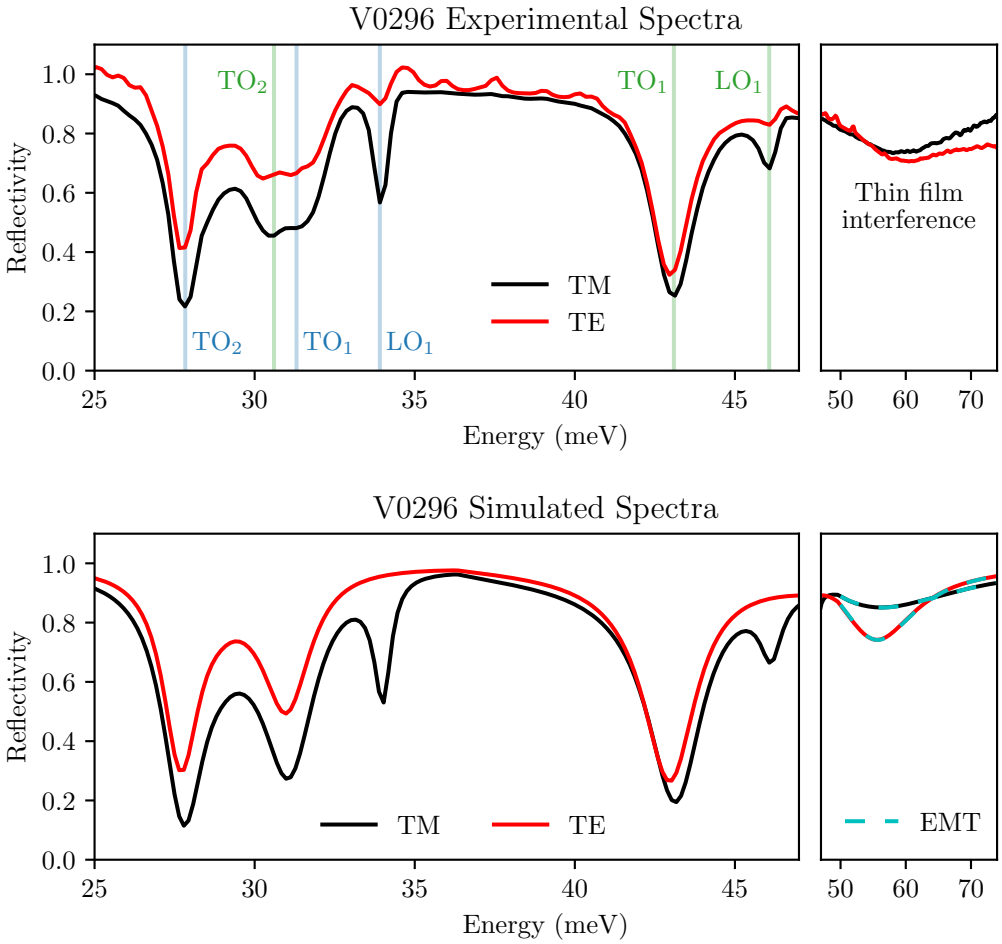

Fig. 3.5 Experimental and simulated spectra for sample V0296, consisting of 30 periods of not-intentionally-doped 45 nm InGaAs wells and 10 nm AlInAs barriers. The experimental spectra were measured at T= 5 K. The resonances attributed to GaInAs are labeled in blue, and those attributed to AlInAs are labeled in green. Simulated reflectivity spectra using Effective Medium Theory (EMT) are overlayed on top of the full structure simulations for the region between around 50 meV to 70 meV.

is the presence of only a single peak around 31 meV in the simulation in contrast to two closely spaced peaks in the experimental spectrum around the same energy.

		Literature	Experiment	Values for ε
$In_{0.53}Ga_{0.47}As$	$\hbar\omega_{LO_1}$	33.4 (0.4)	33.9	33.90 (0.6)
	$\hbar\omega_{TO_1}$	31.7 (1.3)	31.3	31.72 (1.3)
	$\hbar\omega_{LO_2}$	28.8 (2.6)		29.14 (1.5)
	$\hbar\omega_{TO_2}$	27.7 (1.5)	27.8	28.33 (1.2)
$Al_{0.48}In_{0.52}As$	$\hbar\omega_{LO_1}$	44.7	46.1	46.07 (0.8)
	$\hbar\omega_{TO_1}$	43.2	43.1	43.51 (1.4)
	$\hbar\omega_{LO_2}$	29.7		29.66 (1.5)
	$\hbar\omega_{TO_2}$	28.0	30.6	28.95 (1.2)

Table 3.3: The parameters for the phonon resonances are tabulated for the two ternary materials. Values are reported in units of meV. Parameters for the phonon linewidths are reported in parenthesis. The literature values are reproduced from [77] for InGaAs and from [27] for AlInAs.

Effective medium theory (EMT) can be used to understand the broad features at energies above the phonon resonances in the experimental and simulated spectra. In effective medium theory, an effective dielectric function is introduced to describe homogeneously a structure which is spatially inhomogeneous.

For a structure of repeating subwavelength layers of materials 1 and 2, of thicknesses t_1 and t_2, the dielectric permittivity tensor found in the EMT is diagonal with the in-plane ($\parallel$) components and the out-of-plane component ($\perp$) given by:

$$\varepsilon_{\parallel}^{\mathrm{EMT}} = \rho\varepsilon_1 + (1-\rho)\,\varepsilon_2 \tag{3.2}$$

$$\varepsilon_{\perp}^{\mathrm{EMT}} = \left(\frac{\rho}{\varepsilon_1} + \frac{(1-\rho)}{\varepsilon_2}\right)^{-1} \tag{3.3}$$

where ρ is the filling fraction of material 1: $\rho = t_1/(t_1+t_2)$. For the V0296 structure, with material 1 as InGaAs and material 2 as AlInAs, $\rho \approx 0.818$.

In the bottom panel of Fig. 3.5, the simulated reflectivity spectrum, calculated for the InGaAs/AlInAs heterostructure described with $\varepsilon^{\mathrm{EMT}}$, is plotted with a dashed line on top of the simulated reflectivity spectrum of the exact heterostructure from 47 meV to 74 meV. There is excellent agreement between the two simulations.

The condition for the thin film interference phenomenon is determined by the optical path difference (OPD), and by accounting for the phase shifts which occur upon reflection from the interface of a medium of a higher refractive index. Considering the entire heterostructure of V0296 to be a thin film of semiconductor between air and gold, and accounting for a π phase shift at both the air/semiconductor and semiconductor/gold interfaces, the condition for destructive interferences is found:

$$\mathrm{OPD} = 2n_{\mathrm{eff}}\cos(\theta_{n_{\mathrm{eff}}})t = \frac{\lambda_0}{2} \tag{3.4}$$

In this expression, t is the total film thickness, λ_0 is the wavelength in free space, n_{eff} is an

effective *isotropic* refractive index inside the semiconductor, and $\theta_{n_{\text{eff}}}$ is the incidence angle inside the semiconductor layer.

In the EMT, the refractive index of the multilayer structure is anisotropic, but to simplify the description of the thin film interference, we may assume an isotropic effective refractive index, n_{eff}. This is well justified since the anisotropy at the energy of the interference feature is rather small: at 58 meV, $n_{\perp}^{\text{EMT}} \approx 3.145$ and $n_{\parallel}^{\text{EMT}} \approx 3.158$. For a 45° angle of incidence from air and $n_{\text{eff}} \approx 3.15$, the thickness of the film may be calculated according to the condition given by Eq. (3.4) for a destructive interference fringe at 58 meV, where $\lambda_0 = 21.38\,\mu\text{m}$. We find $t = 1.74\,\mu\text{m}$, which is not far from the nominal thickness of the heterostructure, 1.81 µm.

Since the entire thickness, t, of the InGaAs/AlInAs heterostructure studied here is sub-wavelength ($t \approx 0.1\lambda$), it might be expected that resonances should be observed in the p-polarized spectra at the zeros of the effective dielectric function. In [93], the authors studied a periodic metal/dielectric structure and found the that the Berreman modes were not observed at the zeros of the effective dielectric function, but instead at the zeros of the dielectric function of the constituent material. This is in accordance with our own observations.

3.4 Plasmon-Phonon Coupling in n-InGaAs/AlInAs

In the following sections, the experimental spectra of doped InGaAs/AlInAs heterostructures are reported. We first briefly consider how the optical description of the structure is modified in the presence of a confined electron gas.

In Section 3.1, a Drude term was added to the dielectric function for the phonons in order to describe the response of a ternary alloy in the presence of a free electron gas. The resulting dielectric function (Eq. (3.1)) was isotropic. In our study, electrons are added to thin InGaAs layers in which they are confined in the $\hat{\mathbf{z}}$-direction. Consequently, the addition of an electronic density to the thin InGaAs layers results in the previously isotropic dielectric function becoming uniaxially anisotropic:

$$\varepsilon_{\text{InGaAs}}^{V0296} = \begin{pmatrix} \varepsilon_{\text{phonon}} & 0 & 0 \\ 0 & \varepsilon_{\text{phonon}} & 0 \\ 0 & 0 & \varepsilon_{\text{phonon}} \end{pmatrix} \Longrightarrow$$

$$\varepsilon_{\text{InGaAs}}^{V0300/V0301} = \begin{pmatrix} \varepsilon_{\text{phonon}} + \varepsilon_{\text{Drude}} & 0 & 0 \\ 0 & \varepsilon_{\text{phonon}} + \varepsilon_{\text{Drude}} & 0 \\ 0 & 0 & \varepsilon_{\text{phonon}} + \varepsilon_{zz} \end{pmatrix} \tag{3.5}$$

In the confined z-direction ($\perp$), the electrons are described by ε_{zz}, defined in Eq. (1.35). In the in-plane directions ($\parallel$), the electrons are free and are described by $\varepsilon_{\text{Drude}}$. For simplicity, we have neglected the 'bookkeeping' of ε_{∞} in Eq. (3.5), although it is properly considered in all calculations.

In the wide layer limit, the anisotropy disappears as $\varepsilon_{zz} \to \varepsilon_{\text{Drude}}$. In the 35 nm and 45 nm InGaAs quantum wells of samples V0300 and V0301, the confinement effects and the anisotropy remain relevant.

In the analysis of the doped samples, the parameters extracted from the modeling of the not-intentionally-doped V0296 structure reported in Table 3.3 are used for the phonon

resonances in the dielectric function.

3.4.1 V0300: Electron Plasma-Optical Phonon Coupling

We now present the experimental study of sample V0300, which we recall has the same structure as sample V0296, but with a density of electrons added. The experimental TM reflectivity spectra of V0300, measured at T=5 K, is compared with that of V0296 in Fig. 3.6.

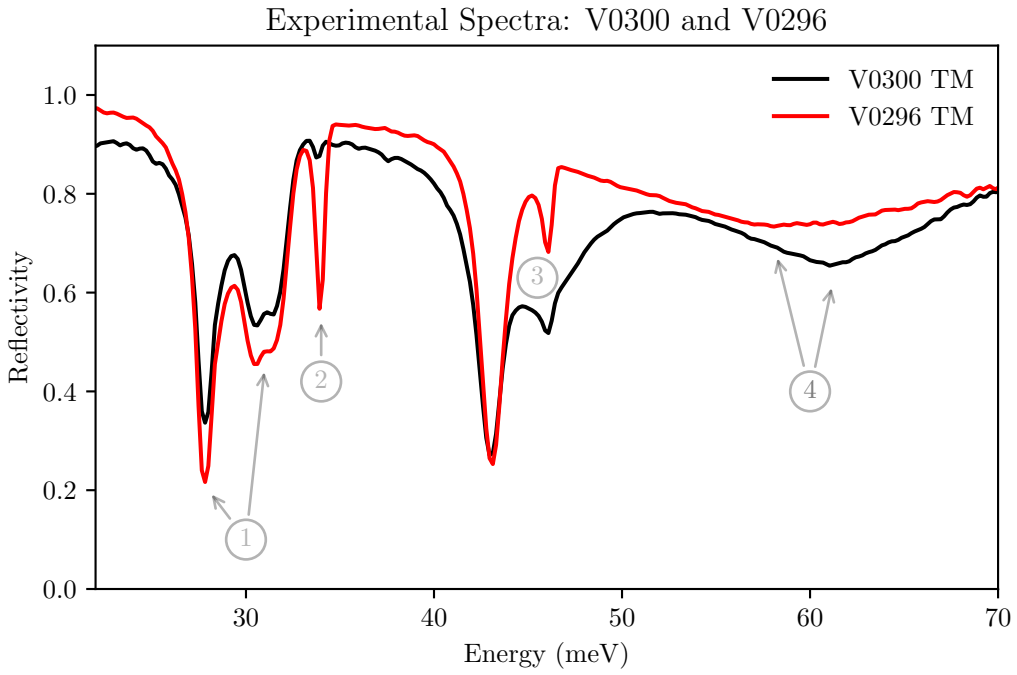

Fig. 3.6 The experimental TM reflectivity spectra at 45° and T=5 K are shown for the not-intentially-doped V0296 sample and the V0300 sample for which the InGaAs layers are nominally doped with an electronic density of $1.7 \times 10^{17}\,\mathrm{cm}^{-3}$. The four differences between the two spectra discussed in the text are annotated.

There are four primary differences between the V0300 and V0296 TM reflectivity spectra, which are numbered in Fig. 3.6:

1. The InGaAs TO_1 and TO_2 resonances (31.3 meV and 27.8 meV) and the AlInAs TO_2 resonance (30.6 meV) have a greater contrast (are more absorbing) in the V0296 spectrum.

2. The InGaAs LO_1 phonon which is sharply peaked around 34 meV in the spectrum of the undoped sample is almost completely absent in the spectrum of the doped sample.

3. There is a broad feature between about 40 meV and 50 meV present in the V0300 spectrum which is absent in the V0296 spectrum.

4. The broad thin film interference feature moves from 58 meV in the V0296 spectrum to 61 meV in the V0300 spectrum, despite the fact that the film thickness should be consistent between the samples.

Each of these differences will be demonstrated to be a consequence of the addition of an electronic density to the InGaAs layers.

We begin by discussing the second and third differences, which arise due to a coupling between plasma oscillations and the LO_1 phonon in the InGaAs layer. In the top panel of Fig. 3.7, the real part of the dielectric function in the out-of-plane (confined) direction is plotted for the not-intentionally-doped V0296 sample and for the V0300 sample doped with an electronic concentration of $N_v = 3.75 \times 10^{17}\,\mathrm{cm}^{-3}$. The addition of the electronic density shifts the energy of the zero crossing of the real part of the dielectric function from $\hbar\omega_{LO_1} = 34\,\mathrm{meV}$ to 43.9 meV.

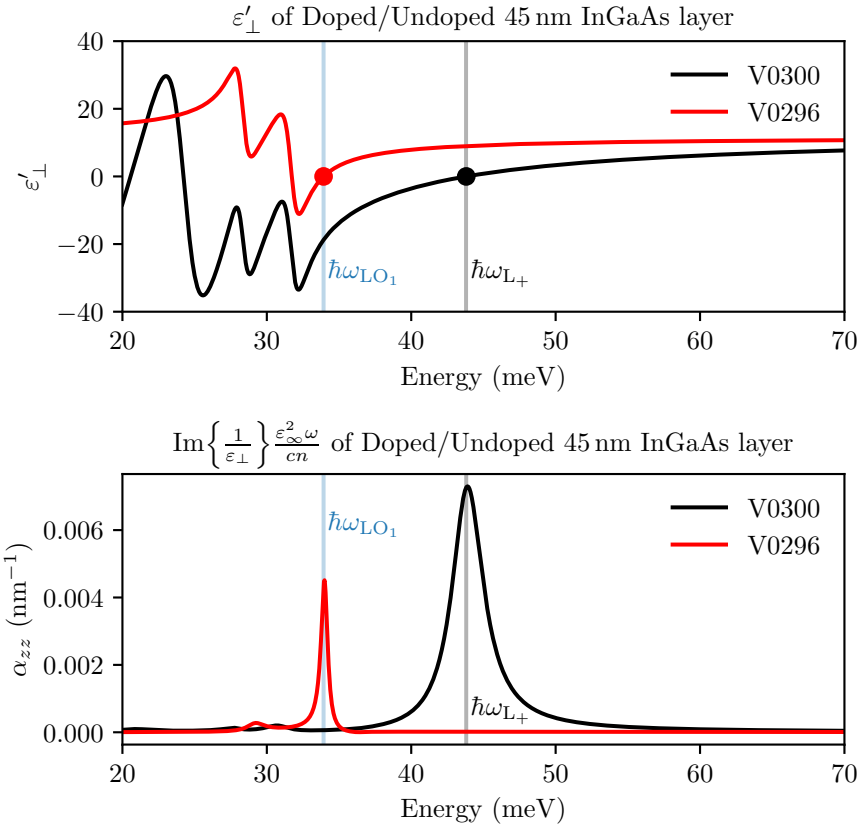

Fig. 3.7 In the top panel, the real part of the z-component of the dielectric function is plotted for the doped V0300 sample with $N_v = 3.75 \times 10^{17}\,\mathrm{cm}^{-3}$ and the undoped V0296 sample. The energy at which each dielectric function crosses zero is indicated. In the bottom panel, the thin film absorption is calculated for the doped and undoped InGaAs layers.

The thin-film absorption coefficient, calculated according to Eq. (1.47), is plotted in the bottom panel of Fig. 3.7 for the two dielectric functions describing the doped and not-doped 45 nm InGaAs layers. Due to the Berreman effect, resonances are observed at the zero crossings of $\varepsilon'_\perp$. Upon addition of the electronic density, the resonance at 34 meV disappears from the absorption spectrum and a new coupled-mode resonance appears at 43.8 meV. This exactly describes the disappearance of the LO phonon peak and the appearance of a broad

absorption feature around 45 meV in the experimental V0300 reflectivity spectrum. We identify the coupled-mode resonance at 43.8 meV as the L_+ mode of Fig. 3.1, since it lies at an energy greater than $\hbar\omega_{LO_1}$.

Note that the sharp resonances at approximately 43 meV and 46 meV observed in both the V0296 and V0300 layers originate from phonons in the AlInAs layers. For this reason, they are hardly modified between the two spectra. It is an unfortunate coincidence that the L_+ mode we wish to observe is nearly degenerate with these peaks.

We now comment on the first annotated difference between the V0296 and V0300 spectra. The decrease in the contrast of the TO resonances around 30 meV in the V0300 spectra results from an increase in the reflectivity below the energy of the L_+ mode in the InGaAs layer. Highly doped semiconductors, like metals, are usually reflective below the plasma energy, at which the real part of the dielectric function crosses zero and tends increasingly negative. When an electron gas with a plasma energy greater than the optical phonon resonances is coupled with the optical phonons, the real part of the dielectric function crosses zero and tends negative at $\hbar\omega_{L_+}$. In this case, ω_{L_+} plays the analogous role of ω_p in defining the 'plasma edge', below which the material is reflective.

In the upper panel of Fig. 3.8, the real part of the in-plane dielectric function of the doped V0300 sample is plotted. At $L_+ = 39.6$ meV, $\varepsilon'_{\parallel}$ crosses zero and tends negative (apart from the phonon oscillations). Similarly, the real part of the out-of-plane dielectric constant (top panel of Fig. 3.7) goes from positive to negative below L_+, although due to the confinement in the z-direction, L_+ occurs at 43.8 meV. At the energies where the InGaAs TO_1 and TO_2 phonons lie, below L_+, the doped InGaAs layers are increasing reflective. As a result, less light is absorbed by any single InGaAs layer, and less light is coupled into subsequent InGaAs layers where it can be absorbed. This explains the reduced contrast of the InGaAs TO_1 and TO_2 phonons in the V0300 spectrum.

Apart from the small change in contrast in the spectrum, the InGaAs TO phonon modes are otherwise not modified with the addition of an electronic density. This is in agreement with the theoretical description, as is now discussed.

In thin films, all of the absorption which gives rise to the observed TO resonances is due to losses in the in-plane direction. This is because, as described in Fig. 1.12, the TO resonances in the normal direction are depolarization-shifted to the LO resonance frequencies. To explicitly show that the TO resonances are not modified by the presence of an electronic density, $\varepsilon''_{\parallel}$ is plotted for the InGaAs layer, with (V0300) and without (V0296) an electronic density, in the bottom panel of Fig. 3.8. The peaks of $\varepsilon''_{\parallel}$, responsible for the TO phonon resonances, are found not to be modified by the electron plasma.

We now explain the fourth difference observed in Fig. 3.6: the shift of the thin film interference. In the top panel of Fig. 3.7, the real part of the dielectric function of the not-doped (V0296) layer converges to ε_∞ after crossing zero more quickly than that of the doped (V0300) layer. The same behavior occurs for the real part of the in-plane dielectric function, as seen in the top panel of Fig. 3.8. In the region where the interference dip occurs, the losses are small and $n \approx \sqrt{\varepsilon'}$. Then, from Eq. (3.4), it is evident that a decrease in ε' should move the interference dip toward higher energy as is experimentally observed.

The electronic density N_v used to model the dielectric function of the doped InGaAs layer, plotted in Figs. 3.7 and 3.8, was determined by finding the best agreement between a series of finite element simulations in which the electronic density was varied and the experimental spectrum. The best agreement was found for $N_v = 3.75 \times 10^{17}\,\mathrm{cm}^{-3}$. This value is of the

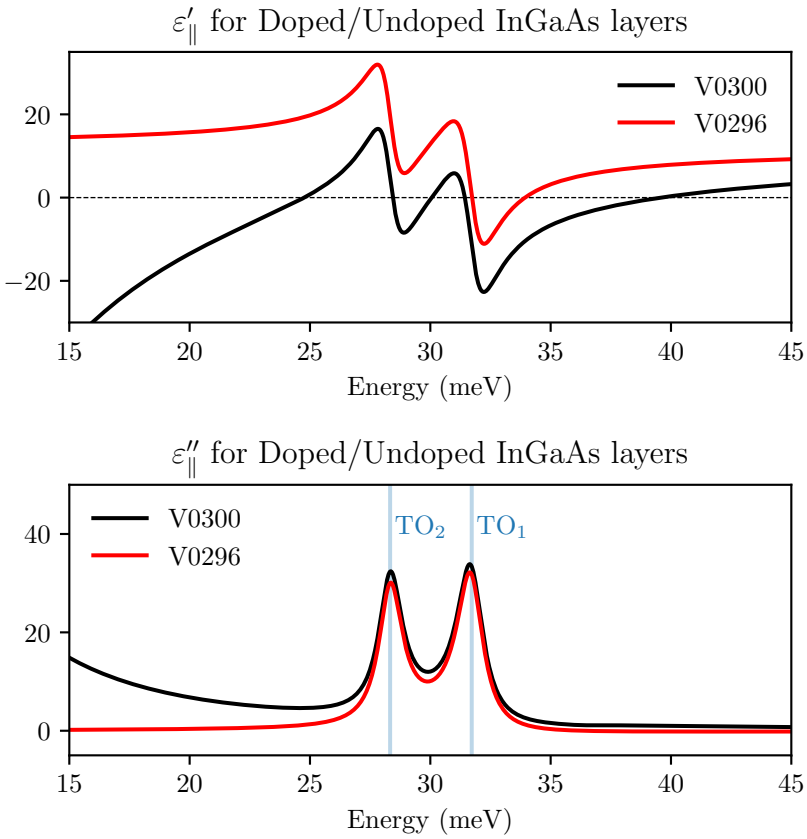

Fig. 3.8 The real and imaginary parts of the in-plane dielectric function are plotted for the doped V0300 sample with $N_v = 3.75 \times 10^{17}\,\mathrm{cm}^{-3}$ and the undoped V0296 sample.

same order of magnitude as the nominal electronic density $N_v = 1.7 \times 10^{17}\,\mathrm{cm}^{-3}$ which is assumed to have a large uncertainty.

The best parameter for the nonradiative linewidth of the electronic resonance was determined similarly. The optimal value was found as $\gamma_{NR} = 3.03\,\mathrm{meV}$ which would correspond to a quality factor of about 14.5 for the bare electronic excitation, absent coupling with the phonons. A fixed value of $\gamma = 27.57\,\mathrm{meV}$ is used to describe the damping of the free electron gas in the plane. The parameters γ_{NR} and γ are important in determining how quickly the real parts of the perpendicular and in-plane dielectric functions rise after crossing zero, and how fast they eventually converge to ε_∞.

The simulated TM 45° V0300 spectrum, for $N_v = 3.75 \times 10^{17}\,\mathrm{cm}^{-3}$ and for the values of γ_{NR} and γ provided above, is plotted with the simulated TM spectrum of the not-intentionally-doped V0296 sample in Fig. 3.9. The four differences observed between the samples in the experimental spectra (Fig. 3.6) are reproduced in the simulations. With the added electronic density, the contrast of the InGaAs TO phonons around 30 meV is reduced, the InGaAs LO_1 resonance disappears, a new broad absorption feature appears behind the AlInAs resonances around 45 meV, and the destructive interference dip shifts towards lower energy.

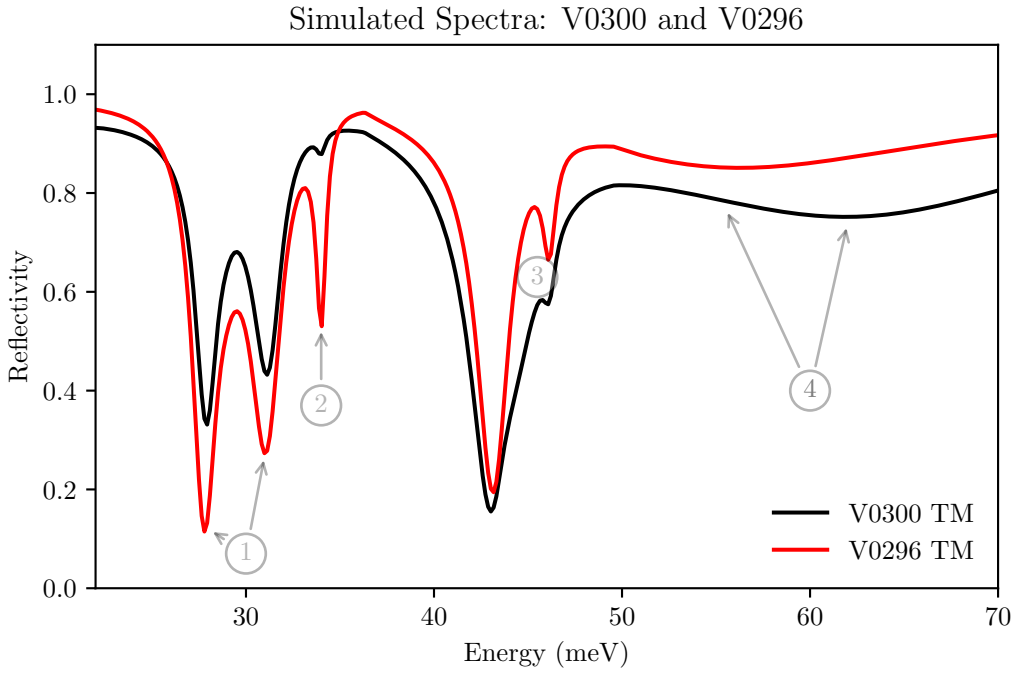

Fig. 3.9 TM reflectivity spectra simulated at 45° for the not-intentionally-doped V0296 and doped V0300 samplres are plotted. The four major differences highlighted between the experimental spectra of the two samples are reproduced in the simulated spectra.

Both in the simulated and experimental spectra of the doped V0300 sample, there is a small absorption feature which remains at the uncoupled ω_{LO_1} frequency. According to the theory, no such feature should remain at ω_{LO_1} when an electronic density has been added to the InGaAs layer. This small absorption feature is attributed to the presence of a 50 nm undoped InGaAs layer next to the gold mirror and a 100 nm undoped InGaAs layer next to the air interface. These layers were added during the growth process to serve as capping and buffer layers, respectively. They have been included in the finite element simulations. The growth sheet of sample V0300 can be found on Page 193.

To gain quantitative insight into the modification of the reflectivity spectra with the addition of an electronic density, the ratio of the V0300 and V0296 TM spectra, normalized by the ratio of the TE spectra, is plotted in Fig. 3.10. Dips in the resulting spectrum can be exclusively attributed to absorption of TM polarized light in the doped V0300 sample.

In the ratio of reflectivities, two of the four differences between the TM spectra of the not-intentionally-doped and doped samples are readily observable. First, a sharp positive feature is observed around 34 meV, which results from the absence of the InGaAs LO_1 phonon resonance in the V0300 spectrum. Second, a broad dip is observed around 45 meV, which is attributed to absorption from the coupled plasmon-phonon L_+ mode in the TM V0300 spectrum.

A Lorentzian lineshape is fit to the L_+ feature using a non-linear least squares regression, with the best fit found for a Lorentzian centered at 45.3 meV with a FWHM of $\gamma = 7.1$ meV.

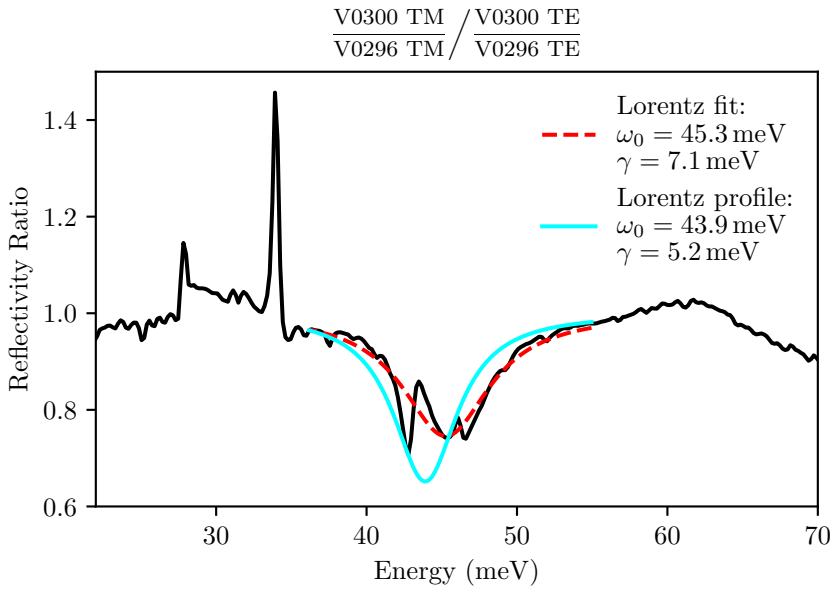

Fig. 3.10 The ratio of the experimental TM spectra of the doped V0300 sample and the undoped V0296 sample, normalized by the ratio of the respective TE spectra, is plotted. The resonant dip is fitted with a Lorentzian lineshape, with center ω_0 and FWHM γ, plotted with a dashed red line. The solid cyan-colored line shows the best Lorentzian profile found, through trial-and-error, to model the V0300 spectra in the finite element simulations.

The fitted Lorentzian is plotted in Fig. 3.10 with dashed lines. The best Lorentzian profile found through trial-and-error with finite element simulations (varying the electronic density and nonradiative linewidth of the Berreman mode), which corresponds to the Lorentzian centered at $\hbar\omega_{L_+}$ in Fig. 3.7, is plotted as a solid cyan-colored line. A reasonably good agreement is observed.

We conclude this section by highlighting that the plasmon-phonon coupled mode which we have observed is significantly shifted from the bare LO_1 resonance energy. This is a signature of the strong plasmon-phonon coupling.

3.4.2 V0301: Intersubband Excitation-Optical Phonon Coupling

In this section, the results from the study of sample V0301, designed with an intersubband transition resonant at 26 meV, are reported.

As reported in Table 3.2, the experimentally determined electronic density is significantly greater than the nominal electronic density for which the sample was designed. In the left panel of Fig. 3.11, the dispersion of the electronic subbands in the 35 nm InGaAs layers of the V0301 structure is plotted. Two Fermi levels, calculated for T=5 K, corresponding to the nominal ($N_v = 8 \times 10^{16}\,\mathrm{cm}^{-3}$) and experimental ($N_v = 2.2 \times 10^{17}\,\mathrm{cm}^{-3}$) electronic densities, are indicated.

The Fermi level for the nominal electronic density sits just below the second subband, so that the only occupied electronic states lie in the first subband. For this case, neglecting

the phonons, the thin film absorption spectrum has a single resonance, corresponding to the $1 \rightarrow 2$ intersubband transition. The absorption spectrum is plotted in the middle panel of Fig. 3.11b with a blue line. When the interaction between the optical phonons and the intersubband transition is considered, the dominant feature in the calculated absorption spectrum (red line) is a sharp resonance corresponding to the L_+ mode that is slightly blueshifted from the InGaAs LO_1 phonon resonance.

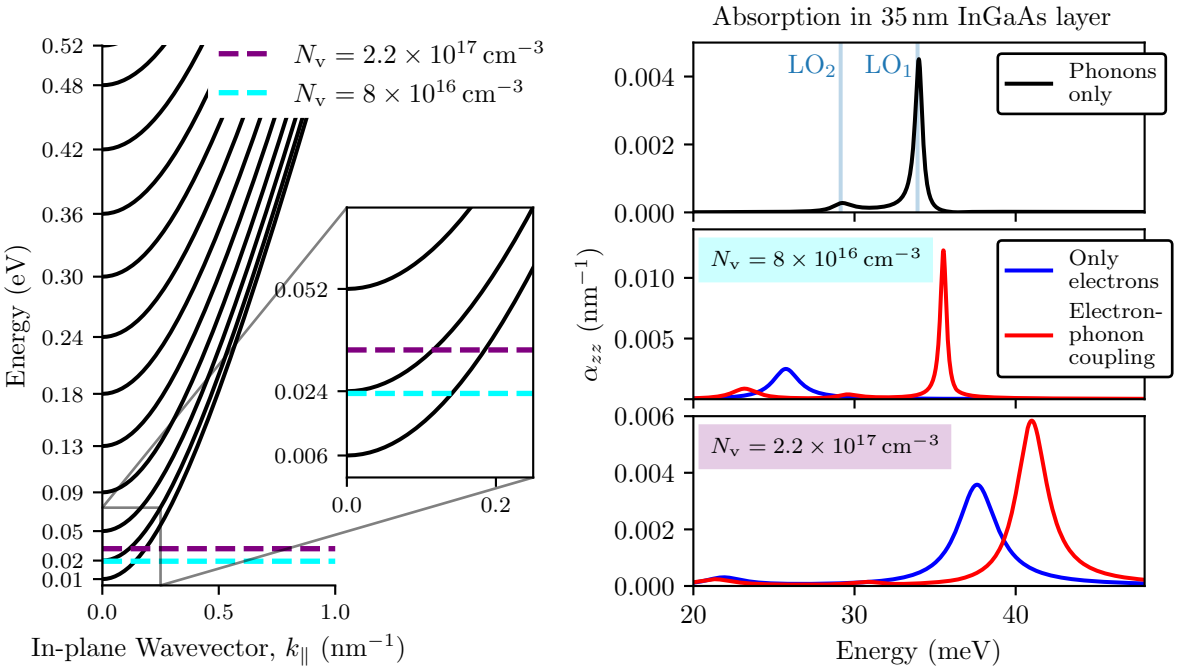

(a) Subband Dispersion (b) Thin film Absorption

Fig. 3.11 (a) The subbands are plotted for a 35 nm InGaAs/AlInAs quantum well. Two Fermi levels, calculated at T=5 K, are plotted for the two electronic densities indicated in the legend. (b) The calculated thin film absorption, $\alpha_{zz} = \mathrm{Im}\left\{-\varepsilon_\perp^{-1}\right\} \varepsilon_\infty^2 \omega/cn$ is plotted for various $\varepsilon_\perp$. In these calculations, the nonradiative linewidth γ_{NR} of the electronic mode is fixed at 7.5% of the bare resonance energy.

The Fermi level for the experimentally extracted electronic density lies almost midway between the first and second subbands. As a result, $1 \rightarrow 2$ and $2 \rightarrow 3$ intersubband transitions can occur. The two intersubband transitions are coupled through the depolarization effect, as described in Section 1.4.1. Consequently, in the absorption spectrum calculated neglecting the phonons, plotted in the bottom panel of Fig. 3.11b with a blue line, there are two resonances at 22 meV and 37.5 meV, but nearly all of the oscillator strength is coupled into the mode at 37.5 meV. When the interaction between the optical phonons and the coupled intersubband transitions is considered, the absorption spectrum (red line) is dominated by a single resonance, corresponding to the L_+ mode, at 41 meV. The resonance has a linewidth similar to the bare electronic mode.

The experimental reflectivity spectra of sample V0301, measured at T=5 K and for light incident at 45°, are plotted in the top panel of Fig. 3.12 for TM and TE polarizations. There

is a feature in the TM spectrum at 41 meV which is absent in the TE spectrum. The feature is identified as the coupled electron-phonon L_+ mode. Unfortunately, as was the case for the V0300 sample, the feature is largely obscured by the resonances of the AlInAs phonons.

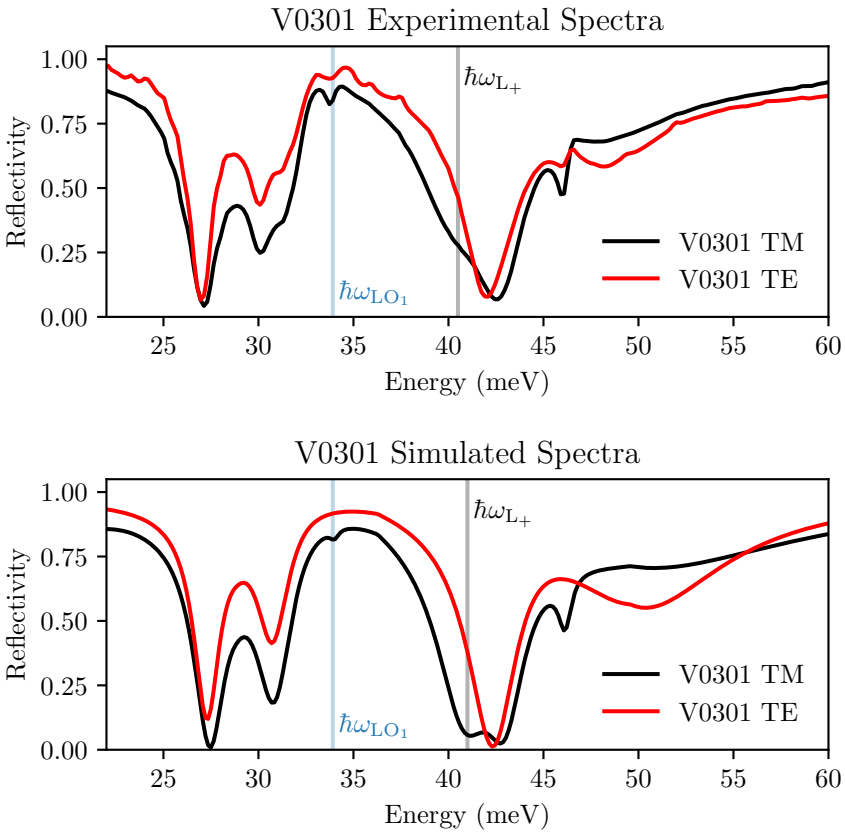

Fig. 3.12 In the top panel, experimental reflectivity spectra of sample V0301, measured at T=5 K for light incidence at 45°, are shown. Simulated reflectivity spectra are shown in the bottom panel, calculated for an electronic density of $N_v = 2.2 \times 10^{17}\,\mathrm{cm}^{-3}$ in the InGaAs layers.

There is a faint feature which can be observed at the InGaAs LO_1 phonon energy only in the TM spectrum. As was done for a similar feature in the V0300 spectrum, this feature is attributed to the excitation of the InGaAs LO_1 phonon in the not-intentionally-doped InGaAs layers bordering either side of the periodic heterostructure (see the V0301 growth sheet on Page 194).

We now comment on a few additional observations of the V0301 experimental spectra. There is broad, shallow dip just below 50 meV in both the TM and TE spectra which is attributed to a thin film destructive interference.

Below approximately 45 meV, the reflectivity of the TE spectrum is almost uniformly greater than that of the TM spectrum. This is attributed to a difference in the fraction of light reflected, depending on the polarization, at the air/semiconductor interface (the Fresnel coefficients are polarization-dependent).

In the bottom panel of Fig. 3.12, simulated reflectivity spectra for sample V0301 are

plotted. All of the essential experimental observations are reproduced: a clear feature resulting from the electron-plasmon coupling is present near 41 meV, thin film interferences are present around 50 meV, and the reflectivity is systematically less for the TM spectrum below the thin film interferences.

3.5 Conclusion and Perspectives

The Berreman effect was exploited to directly observe coupled plasmon-phonon modes in doped InGaAs. Despite the small electronic density required for the plasma energy in InGaAs to be close to the optical phonons, L_+ modes were observed which were more heavily weighted with an electronic than phononic character. For the 35 nm quantum well, the coupled mode that was observed resulted from the coupling between two intersubband transitions and the LO phonons.

The L_+ modes were observed significantly shifted from the InGaAs LO_1 phonon resonances. We conclude that the large interaction strength between LO phonons and plasma oscillations is an enabling factor for the engineering of the Reststrahlen band.

All of the essential features of the experimental spectra were well-reproduced with simulations using semiclassical dielectric functions. A fully quantum description of the interaction between the optical phonons and the electron plasma is the subject of an ongoing study within the Quantum Devices team.

In the experimental studies, there was an unfortunate overlap in the spectra between the coupled LO phonon-plasmon mode in the InGaAs layers and the phonon resonances from the AlInAs barrier layers. In future studies, samples could be designed with barrier layers of reduced width to improve the contrast between the features originating from the InGaAs layers and those originating from the barrier layers. It would also be desirable to study samples with lower electronic densities, with the hope of observing the L_0 and L_- modes. Finally, we note that the plasmon-phonon coupling phenomenon could be investigated in other material platforms.

Chapter 4

Semiconductor Quantum Plasmonics

In this chapter, a microscopic quantum model for the collective excitations of the confined electron gas is introduced. The collective excitations are calculated starting from the basis of stationary single particle electronic states, immediately implying that quantum confinement is fully considered. The microscopic matter polarization is described in space directly as a function of the single particle electronic states. Consequently, the model naturally describes the *nonlocal* response of the confined electron gas. Accounting for quantum confinement and nonlocality, the model provides a plasmonic description well beyond that of the classical Dude model.

The model was developed in the Quantum Devices team before my arrival, and I borrow heavily from the works of [100, 135] as I describe it in this chapter. I wish to state immediately that the theoretical development of the model was not my work.

The quantum model is introduced in the first part of the chapter: In Section 4.1, excitations of the electron gas are described neglecting the dynamic Coulomb interaction between electronic excitations. We qualify these non-interacting excitations as *single particle*. In Section 4.2, the *collective* excitations of the system are found by considering the interaction between the single particle excitations.

In the second part of the chapter, the model is applied to analytically describe the collective longitudinal modes of the electron gas in a wide quantum well (square static potential). The square well is shown to support a series of collective modes with different out-of-plane wavevector k_z. This dispersion of the modes with k_z is found analytically and shown to differ, due to electronic confinement, from the well-known Lindhard formula for the free electron gas. This study resulted in a publication [138] which I coauthored.

4.1 Bright Single Particle Excitations

In this section, we establish a description in the second quantization formalism for the single particle excitations of the 2D electron gas which couple with the electromagnetic field. By single particle excitations, we refer to electronic transitions between stationary electronic states which occur at the bare transition energy (not dressed through a many body Coulomb interaction). To describe the spatial distribution of oscillating charge associated with each transition, we define a polarization operator.

The section is organized as follows: In Section 4.1.1, a matter Hamiltonian describing

all the single particle excitations of the 2D electron gas is written in terms of fermionic operators. In Section 4.1.2, the Hamiltonian is rewritten in terms of bosonic operators which describe only excitations with a nonzero dipole. In Section 4.1.3, the polarization operator is defined, and the quantum description is applied to describe the single particle transitions of a 100 nm quantum well.

4.1.1 Fermionic Excitations of the 2D Electron Gas

The eigenstates $\left\langle \mathbf{r} \middle| \lambda,\mathbf{k}_\parallel \right\rangle$ of the static Hamiltonian for the electron gas confined in the $\hat{\mathbf{z}}$-direction were defined in Eq. (1.14). We recall that λ is the quantum number indexing the bound states of the confined $\hat{\mathbf{z}}$ direction, and $\mathbf{k}_\parallel$ is the in-plane wavevector describing the free motion of the electrons in the $\hat{\mathbf{x}} - \hat{\mathbf{y}}$ plane. When the $\left\langle \mathbf{r} \middle| \lambda,\mathbf{k}_\parallel \right\rangle$ states are found as self-consistent solutions to both the Schrodinger and Poisson equations, their form accounts for the static Coulomb interaction (see Section 1.2.2.1).

We introduce Fermionic creation $c^\dagger_{\lambda\mathbf{k}_\parallel}$ and annihilation $c_{\lambda\mathbf{k}_\parallel}$ operators which increase or decrease the occupation of the state $\left| \lambda,\mathbf{k}_\parallel \right\rangle$. The matter Hamiltonian describing the spectrum of single particle excitations can then be written as:

$$\hat{H}^{\mathrm{sp}}_{\mathrm{mat}} = \sum_{\lambda\mathbf{k}_\parallel} \hbar\omega_{\lambda\mathbf{k}_\parallel} c^\dagger_{\lambda\mathbf{k}_\parallel} c_{\lambda\mathbf{k}_\parallel} \tag{4.1}$$

We may immediately write the fundamental state $|f\rangle$ of the many particle system at T=0 K as the completely antisymmetric state for which all states up to the Fermi energy E_{F} are occupied:

$$|f\rangle = \prod_{\hbar\omega_{\lambda\mathbf{k}_\parallel} < E_{\mathrm{F}}} c^\dagger_{\lambda\mathbf{k}_\parallel} |0\rangle \tag{4.2}$$

where $|0\rangle$ describes the state with no particles. When $\mathrm{T} \neq 0\,\mathrm{K}$, the electrons are thermally distributed across the subbands of the system.

The basis of excited states, already necessary to describe the electron gas at finite temperature, may be spanned with:

$$\left| e_{\lambda>\mu,\mathbf{k}_\parallel} \right\rangle = c^\dagger_{\lambda\mathbf{k}_\parallel+\mathbf{q}} c_{\mu\mathbf{k}_\parallel} |f\rangle \tag{4.3}$$

The excited state on the left side of the equal sign is modified from the fundamental state in that an electron has been excited from the subband μ to the subband λ and has gained an in-plane moment contribution $\mathbf{q}$ from the photon wavevector.

The field operators [116] are found by defining raising and lowering operators in the position basis:

$$\hat{\Psi}(z,\mathbf{r}_\parallel) = \sum_{\lambda\mathbf{k}_\parallel} \frac{1}{\sqrt{S}} c_{\lambda\mathbf{k}_\parallel} \phi_\lambda(z) \mathrm{e}^{\mathrm{i}\mathbf{k}_\parallel\cdot\mathbf{r}_\parallel} \tag{4.4}$$

4.1.2 Bosonized Matter Hamiltonian

Any excited state of Eq. (4.1) may be written as a linear combination of the states defined in Eq. (4.3). However, not every excited state has a nonzero dipole matrix element with $|f\rangle$.

Excited states which do have a nonzero dipole are said to be *bright*, while those which do not are said to be *dark*. Only bright states couple with the electromagnetic field.

In this section, we will substitute the Hamiltonian of Eq. (4.1) with an effective bosonic Hamiltonian written in terms of bosonic operators which describe only bright excitations. Although the bosonic description is an approximate treatment of the problem, it will later permit us to diagonalize a Hopfield-type Hamiltonian [59] which includes interactions between electronic transitions using a Bogoliubov transformation.

We define bosonic raising and lowering operators for the single particle electronic transitions as [24]:

$$b^{\dagger}_{\lambda\mu\mathbf{q}} = \frac{1}{\sqrt{\Delta N_{\lambda\mu}}} \sum_{\mathbf{k}_{\parallel}} c^{\dagger}_{\lambda\mathbf{k}_{\parallel}+\mathbf{q}} c_{\lambda\mathbf{k}_{\parallel}} \tag{4.5}$$

where $\Delta N_{\lambda\mu} = \left\langle \hat{N}_{\mu} \right\rangle - \left\langle \hat{N}_{\lambda} \right\rangle$ is the difference in the expectation value for the number operator $\hat{N}$ of states μ and λ in thermal equilibrium at a given temperature.

The raising operator $b^{\dagger}_{\lambda\mu\mathbf{q}}$ applied to the fundamental state $|f\rangle$ has the effect of creating an excited state which is the completely symmetric superposition of states $\left|e_{\lambda>\mu,\mathbf{k}_{\parallel}}\right\rangle$ weighted with equal amplitude $\frac{1}{\sqrt{\Delta N_{\lambda\mu}}}$:

$$b^{\dagger}_{\lambda\mu\mathbf{q}} |f\rangle = \sum_{\mathbf{k}_{\parallel}} \frac{1}{\sqrt{\Delta N_{\lambda\mu}}} \left|e_{\lambda>\mu,\mathbf{k}_{\parallel}}\right\rangle \tag{4.6}$$

By construction, the completely symmetric states realized through the application of $b^{\dagger}_{\lambda\mu\mathbf{q}}$ are bright states [135]. States which are not coherent symmetric superpositions of $\left|e_{\lambda>\mu,\mathbf{k}_{\parallel}}\right\rangle$ are dark states. The bright and dark states are degenerate absent other interactions. We will find, however, that the degeneracy is lifted by the Coulomb interaction which couples the bright states to each other. From this point onward, we will not consider the dark states, other than to mention now that they must be considered in the description of electronic transport.

The factor $\frac{1}{\sqrt{\Delta N_{\lambda\mu}}}$ in the definition of $b^{\dagger}_{\lambda\mu\mathbf{q}}$ ensures that the operators satisfy the commutation relations for bosons in the weak excitation regime, as we now demonstrate. For the $b^{\dagger}_{\lambda\mu\mathbf{q}}$ operators to be bosonic, they must satisfy the following commutation relation:

$$[b_{\lambda\mu\mathbf{q}}, b^{\dagger}_{\lambda\mu\mathbf{q}'}] = \delta_{\mathbf{q}\mathbf{q}'} \tag{4.7}$$

Expanding the commutation relation using the definitions from Eq. (4.5), we find:

$$\begin{aligned} [b_{\lambda\mu\mathbf{q}}, b^{\dagger}_{\lambda\mu\mathbf{q}'}] &= \sum_{k} \frac{c^{\dagger}_{\mu\mathbf{k}_{\parallel}} c_{\mu\mathbf{k}_{\parallel}} - c^{\dagger}_{\lambda\mathbf{k}_{\parallel}+\mathbf{q}} c_{\lambda\mathbf{k}_{\parallel}+\mathbf{q}}}{\left\langle \hat{N}_{\mu} \right\rangle - \left\langle \hat{N}_{\lambda} \right\rangle} \delta_{\mathbf{q}\mathbf{q}'} \\ &= \frac{\hat{N}_{\mu} - \hat{N}_{\lambda}}{\left\langle \hat{N}_{\mu} \right\rangle - \left\langle \hat{N}_{\lambda} \right\rangle} \delta_{\mathbf{q}\mathbf{q}'} \\ &= \delta_{\mathbf{q}\mathbf{q}'} \end{aligned} \tag{4.8}$$

The last equality holds in the weak excitation regime, when the difference in occupation number $\hat{N}$ between the initial and final states is approximately equivalent to the difference in the expectation values of the number operators when the system is in thermal equilibrium.

We now replace the Hamiltonian of Eq. (4.1) with an effective bosonic Hamiltonian which describes only the single particle excitations which couple with the electromagnetic field:

$$\hat{H}^{\mathrm{sp}}_{\mathrm{mat}} = \sum_{\lambda>\mu,\mathbf{q}} \hbar\omega_{\lambda\mu} b^{\dagger}_{\lambda\mu\mathbf{q}} b_{\lambda\mu\mathbf{q}} \tag{4.9}$$

The spectrum of this Hamiltonian is determined by the level spacing of single particle electronic states (i.e. the excitations are not dressed by the Coulomb interaction). The Hamiltonian is valid only in the weak excitation regime, where the $b^{\dagger}_{\lambda\mu\mathbf{q}}$ operators satisfy the commutation relation for bosons.

4.1.3 Definiton of the Polarization Operator

In the semiclassical description of Chapter 1, we associated a spatially uniform polarization field with each intersubband transition. In this section, we introduce a polarization operator $\hat{\mathbf{P}}$ to describe *locally* the nonuniform polarization associated with each electronic excitation. The position dependence of the $\hat{\mathbf{P}}$ operator is defined directly in terms of the electronic wavefunctions ϕ_λ.

The spatial properties of the polarization operator will be shown to be related to the more familiar dipole matrix element. The definition of $\hat{\mathbf{P}}$ will be found useful later in Section 4.2 to express the Coulomb interaction between single particle excitations, the consideration of which allows the collective modes of the system to be determined.

We begin by recalling that, classically, the change in polarization density with time gives rise to a current:

$$\mathbf{j} = \frac{\mathrm{d}\mathbf{P}}{\mathrm{d}t} \tag{4.10}$$

The polarization operator $\hat{\mathbf{P}}$ is defined so that its time evolution results in a current:

$$\hat{\mathbf{j}}(\mathbf{r}) = \frac{\mathrm{d}\hat{\mathbf{P}}}{\mathrm{d}t} = -i\hbar\Big[\hat{\mathbf{P}}(\mathbf{r}), \hat{H}^{\mathrm{sp}}_{\mathrm{mat}}\Big] \tag{4.11}$$

The second equality defines the equation of motion for $\hat{\mathbf{P}}$ in the Heisenberg picture.[1]

The total current operator is written as:

$$\hat{\mathbf{j}}(\mathbf{r}) = \frac{i\hbar e}{2m^*}\left(\hat{\Psi}^{\dagger}(\mathbf{r})\boldsymbol{\nabla}_{\mathbf{r}}\hat{\Psi}(\mathbf{r}) - \boldsymbol{\nabla}_{\mathbf{r}}\hat{\Psi}^{\dagger}(\mathbf{r})\hat{\Psi}(\mathbf{r})\right) \tag{4.12}$$

where $\hat{\Psi}^{\dagger}$ and $\hat{\Psi}$ are the field operators introduced in Eq. (4.4). Intersubband transitions only carry a polarization in the z-direction, so we limit our consideration to the z-component of the current operator, which is found to take the form:

$$\hat{j}_z(\mathbf{r}) = \frac{i\hbar e}{2m^*\sqrt{S}} \sum_{\lambda>\mu,\mathbf{q}} \xi_{\lambda\mu}(z) \mathrm{e}^{i\mathbf{q}\cdot\mathbf{r}_{\parallel}} \sqrt{\Delta N_{\lambda\mu}} \left(b_{\lambda\mu\mathbf{q}} - b^{\dagger}_{\lambda\mu-\mathbf{q}}\right) \tag{4.13}$$

[1] In general, $\hat{\mathbf{P}}$ evolves under the action of the full electrodynamics Hamiltonian. When this Hamiltonian is introduced in Section 4.2.1 in the dipole representation, it will become clear that $\hat{\mathbf{P}}$ commutes with every term of the Hamiltonian except $\hat{H}^{\mathrm{sp}}_{\mathrm{mat}}$.

The spatial dependence of $\hat{j}_z(\mathbf{r})$ is determined entirely by the current distribution functions $\xi_{\lambda\mu}(z)$, defined in terms of the wavefunctions as:

$$\xi_{\lambda\mu}(z) = \phi_\lambda(z)\frac{\partial\phi_\mu(z)}{\partial z} - \phi_\mu(z)\frac{\partial\phi_\lambda(z)}{\partial z} \tag{4.14}$$

For intersubband transitions, the wavevector of the photon excitation $\mathbf{q}$ is much smaller than the electron wavevector $\mathbf{k}_\parallel$, and consequently the long wavelength approximation $\|\mathbf{q}\| = 0$ can be made. Under this approximation, the polarization operator which satisfies equation Eq. (4.11) is found as [135]:

$$\hat{P}_z(z) = \frac{\hbar e}{2\sqrt{S}m^*}\sum_{\lambda>\mu}\frac{\xi_{\lambda\mu}(z)}{\omega_{\lambda\mu}}\sqrt{\Delta N_{\lambda\mu}}\left(b^\dagger_{\lambda\mu} + b_{\lambda\mu}\right) \tag{4.15}$$

As was the case for $\hat{j}_z(\mathbf{r})$ in Eq. (4.13), the spatial dependence of the polarization operator is determined by the current distribution functions $\xi_\alpha(z)$ which are written in terms of the electronic wavefunctions. Thus, for any arbitrary potential which admits bound state solutions to the Schrödinger equation, we may calculate the dynamic polarization associated with the electronic transitions.

Up to this point, the indices μ and λ have been used to identify the initial and final subbands of an electronic transition. Instead of making reference to the subbands involved in a transition, we can index the transition itself. We define $\alpha := \mu \to \lambda$. With this notation, the polarization operator describing single particle excitations may be written in the more compact notation as:

$$\hat{P}_z(z) = \frac{\hbar e}{2\sqrt{S}m^*}\sum_{\alpha}\frac{\xi_\alpha(z)}{\omega_\alpha}\sqrt{\Delta N_\alpha}\left(b^\dagger_\alpha + b_\alpha\right) \tag{4.16}$$

Transition may also be described in terms of their initial state i and the difference in quantum number between their final and initial state, which we denote j. In this notation, a transition α is defined as $\alpha := i \to i + j$. This notation is particularly useful because it easily permits the single particle transitions to be grouped by j.

For the remainder of the chapter, greek indices will be used to index transitions, i will describe initial states, and j will describe the change in quantum number associated with a transition.

4.1.4 Single Particle Optical Properties

Since the microcurrents describe the spatial current distribution related to a polarization induced by the electromagnetic field, they must be related to the dipole matrix elements. It can be shown that the dipole matrix element z_α is related to the microcurrent ξ_α as:

$$\int_{-\infty}^{\infty}\xi_\alpha(z)\,\mathrm{d}z = \frac{2m^*\omega_\alpha}{\hbar}z_\alpha \tag{4.17}$$

This relation links the optical properties of the intersubband transition α with its associated microcurrent distribution. The link is made even more explicit by defining a quantity $\rho_\alpha(z)$ which describes the spatial distribution of charge:

$$\rho_\alpha(z) = \frac{\partial\xi_\alpha(z)}{\partial z} \tag{4.18}$$

The average displacement of the charge distribution is related to the dipole matrix element, z_α as:

$$\int_{-\infty}^{\infty} \rho_\alpha(z) z \, \mathrm{d}z = \frac{2m^*\omega_\alpha}{\hbar} z_\alpha \tag{4.19}$$

Since the oscillator strength associated with a transition is written in terms of the dipole matrix element, we may rewrite the expression for the oscillator strength in terms of the microcurrent distributions:

$$f_\alpha = \frac{2m^*\omega_\alpha}{\hbar} z_\alpha^2 = \frac{\hbar}{2\omega_\alpha m^*} \left(\int_{-\infty}^{\infty} \xi_\alpha(z) \, \mathrm{d}z \right)^2 \tag{4.20}$$

It is then straightforward to calculate the absorption spectrum for single particle transitions assuming Lorenztian lineshapes.

In Fig. 4.1, the microcurrents $\xi_\alpha(z)$ and charge distributions $\rho_\alpha(z)$ are plotted for various single particle transitions α in a 100 nm InGaAs quantum well. In the left panel, microcurrents are plotted for transitions between one, two, and three levels ($j = 1$, 2, and 3) from initial states $i = 1$, 2, and 3. Interestingly, the microcurrent distributions for transitions of identical j are similar regardless of the initial state i, and have a form approximating $\sin(j\pi z/L)$ where $L = 100\,\mathrm{nm}$ is the width of the quantum well. These properties will prove consequential later for determining the collective modes of the system.

The charge distributions $\rho_\alpha(z)$ are plotted in the right column of Fig. 4.1 for $j = 1$, 2, and 3 transitions from the lowest energy subband $i = 1$. For $j = 1$, the charge distribution has a dipolar form. The integral $\int_{-\infty}^{\infty} \rho_\alpha(z) z \, \mathrm{d}z$ is nonzero, and by Eq. (4.19), the dipole matrix element is also nonzero. For the $j = 2$ case, the charge distribution is an even function with a spatial average of zero. By Eq. (4.19), the dipole matrix element associated with this transition is zero. This confirms the selection rule for intersubband transitions which states that only odd transitions are allowed [111]. The $j = 3$ charge distribution takes the form of two dipoles aligned top to bottom. The dipole matrix element of this transition then approximately describes the length associated with the charge separation for only one of these dipoles.

4.2 Collective Excitations of the 2D Electron Gas

In Section 1.4, it was demonstrated semiclassically that the collective excitations of the confined electron gas can be described as resulting from the coupling between single particle transitions. To calculate the collective excitation spectrum of the 2D electron gas in our quantum formalism, a term must be added to the Hamiltonian to describe the interaction between the bright single particle electronic transitions.

It is the task of the following sections to: (1) establish the form of the term which must be added to Eq. (4.9) to describe the interaction between the single particle excitations; and (2) to then diagonalize the resulting Hamiltonian in order to find the collective modes. We then explore the properties of the collective modes.

4.2.1 Electrodynamics in the PZW Representation

One might postulate that the term describing the coupling between single particle transitions should describe an interaction between their associated polarizations, as this is the

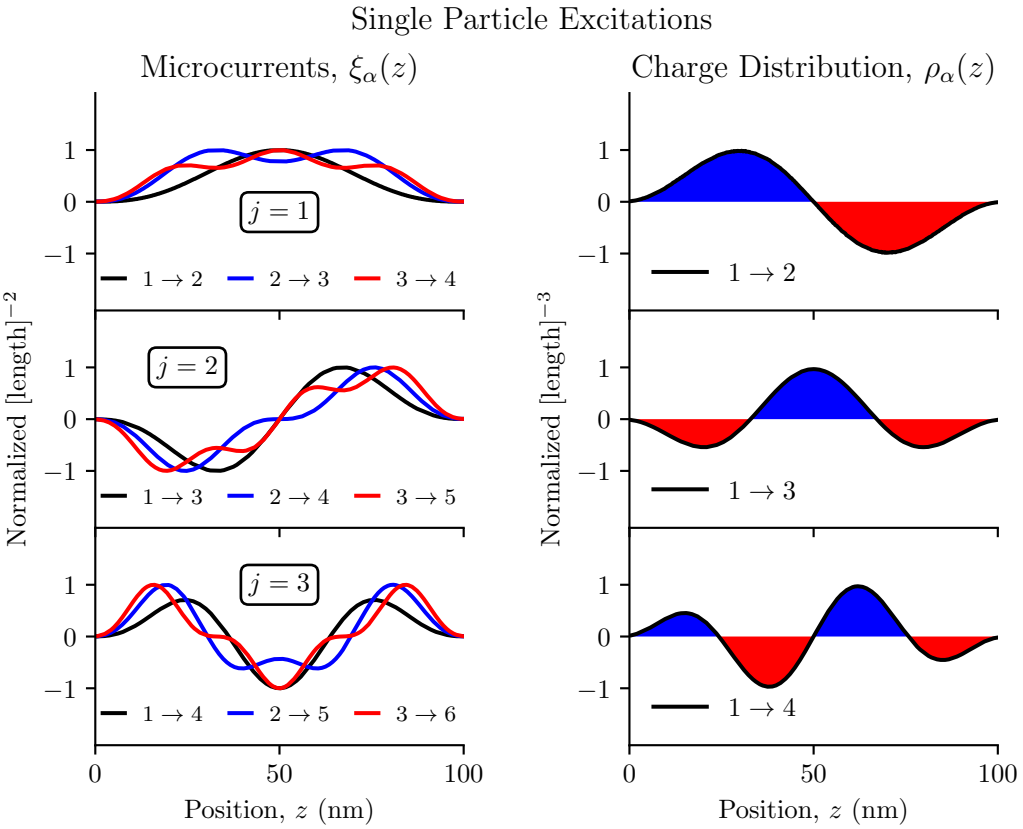

Fig. 4.1 The single particle microcurrents are plotted for transitions $\alpha := i \to i+j$ for $j = 1$, 2, and 3. The corresponding charge distributions are plotted for the $i = 1$ case.

essence of collective effects. We will not need to guess the form of the coupling term, as it appears naturally [131, 134] in the the Power, Zienau, and Woolley (PZW) representation of electrodynamics, which we now introduce.

The full PZW Hamiltonian [7, 26, 78] describing the coupled light-matter system, neglecting magnetic interactions, can be written in the following form:

$$\hat{H}_{\text{multi}} = \hat{H}_{\text{mat}} + \hat{H}_{\text{self}} + \hat{H}_{\text{phot}} + \hat{H}_{\text{l-m}} \tag{4.21}$$

The Hamiltonian has been labeled $\hat{H}_{\text{multi}}$ since this form of the Hamiltonian is sometimes called the *multipolar* Hamiltonian [91].

The matter term $\hat{H}_{\text{mat}}$ describes excitations of independent matter polarizations. For our system, $\hat{H}_{\text{mat}} = \hat{H}^{\text{sp}}_{\text{mat}}$, defined in Eq. (4.9).

The photon term $\hat{H}_{\text{phot}}$ is written in terms of operators for the displacement field $\hat{\mathbf{D}}$ and the magnetic field $\hat{\mathbf{H}}$. It is the spatial integral of the energy density of the $\hat{\mathbf{D}}$ and $\hat{\mathbf{H}}$ fields:

$$\hat{H}_{\text{phot}} = \int \left[\frac{1}{2\epsilon_0 \varepsilon(z)} \hat{\mathbf{D}}^2(\mathbf{r}) + \frac{\mu_0}{2} \hat{\mathbf{H}}^2(\mathbf{r}) \right] \mathrm{d}\mathbf{r} \tag{4.22}$$

The light-matter interaction term $\hat{H}_{\mathrm{l-m}}$ is written as an interaction between the polarization operator and the displacement field operator:

$$\hat{H}_{\mathrm{l-m}} = \int \frac{1}{\epsilon_0 \varepsilon(z)} \hat{\mathbf{D}}(\mathbf{r}) \cdot \hat{\mathbf{P}}(\mathbf{r}) \, \mathrm{d}\mathbf{r} \tag{4.23}$$

In the PZW representation, the displacement field is entire transverse: $\hat{\mathbf{D}} = \hat{\mathbf{D}}^{\perp}$ [25]. In our formulation, the displacement field is totally independent of the polarization of the electron gas [135]. It is determined by the spatially dependent dielectric response of the material system, *apart from* the polarization from the electron gas. Put otherwise, all of the polarization degrees of freedom of the matter *except* for the electron gas are already considered in $\hat{\mathbf{D}}$.

Finally, the self-interaction term $\hat{H}_{\mathrm{self}}$ describes the interaction between matter polarizations:

$$\hat{H}_{\mathrm{self}} = \int \frac{1}{2\epsilon_0 \varepsilon(z)} \hat{\mathbf{P}}^2(\mathbf{r}) \, \mathrm{d}\mathbf{r} \tag{4.24}$$

This term, quadratic in $\hat{\mathbf{P}}$, defines the form of the coupling between the single particle excitations $b^{\dagger}_{\lambda\mu\mathbf{q}}$ of the electron gas [131]. Let us define:

$$\hat{H}^{\mathrm{coll}}_{\mathrm{mat}} = \hat{H}^{\mathrm{sp}}_{\mathrm{mat}} + \hat{H}_{\mathrm{self}} \tag{4.25}$$

The collective electronic excitations, or the *collective modes* of the system, are found upon diagonalizing of this Hamiltonian, which is accomplished in the following section.

4.2.2 Diagonalization of the Collective Hamiltonian

Using the definition of the polarization operator from Section 4.1.3, the Hamiltonian of Eq. (4.25) takes the form:

$$\hat{H}^{\mathrm{coll}}_{\mathrm{mat}} = \sum_{\alpha} \hbar\omega_{\alpha} b^{\dagger}_{\alpha} b_{\alpha} + \frac{e^2}{2\epsilon_0 \varepsilon_s} \sum_{\alpha,\beta} S_{\alpha\beta} \sqrt{\Delta N_{\alpha} \Delta N_{\beta}} \left(b^{\dagger}_{\alpha} + b_{\alpha} \right) \left(b^{\dagger}_{\beta} + b_{\beta} \right) \tag{4.26}$$

with $S_{\alpha\beta}$ written as:

$$S_{\alpha\beta} = \frac{1}{\hbar\omega_{\alpha}} \frac{1}{\hbar\omega_{\beta}} \left(\frac{\hbar^2}{2m^*} \right)^2 \int_{-\infty}^{\infty} \xi_{\alpha}(z) \xi_{\beta}(z) \, \mathrm{d}z \tag{4.27}$$

$S_{\alpha\beta}$ describes the spatially dependent coupling between any two transitions α and β. It is proportional to the spatial overlap of the microcurrents associated with the transitions.

We first diagonalize the Hamiltonian found by setting $\alpha = \beta$ in Eq. (4.26). The simpler Hamiltonian which results, $H_{\alpha=\beta}$, describes the coupling between identical excitations (electronic transitions with the same i and j), and neglects the coupling between different excitations. The eigenmodes of $H_{\alpha=\beta}$ are the *intersubband plasmons* [131].

The Hamiltonian $H_{\alpha=\beta}$ can be diagonalized with a Bogoliubov procedure. We introduce bosonic operators p_{α} which describe the excitations of the intersubband plasmons, and require that they satisfy the following commutation relation:

$$[p_{\alpha}, H_{\alpha=\beta}] = \hbar\tilde{\omega}_{\alpha} p_{\alpha} \tag{4.28}$$

This equation implies that the p_α operators act on a state to shift its eigenvalue by $\hbar\tilde{\omega}_\alpha$. The new operators $p_\alpha^\dagger$ and p_α are therefore raising and lowering operators for the intersubband plasmon excitations. The diagonalization results in the following definition for the raising and lowering operators:

$$p_\alpha = \frac{\tilde{\omega}_\alpha + \omega_\alpha}{2\sqrt{\tilde{\omega}_\alpha \omega_\alpha}} b_\alpha + \frac{\tilde{\omega}_\alpha - \omega_\alpha}{2\sqrt{\tilde{\omega}_\alpha \omega_\alpha}} b_\alpha^\dagger \tag{4.29}$$

The eigenvalues $\tilde{\omega}_\alpha$ can be written as:

$$\tilde{\omega}_\alpha = \sqrt{\omega_\alpha^2 + \omega_{\mathrm{p}_\alpha}^2} \tag{4.30}$$

The collective excitation frequencies $\tilde{\omega}_\alpha$ are blueshifted from the bare (single particle) transition frequencies ω_α due to the $\omega_{\mathrm{p}_\alpha}$ term, which is the plasma frequency associated with the transition α defined in Eq. (1.31). We recall that the same expression for $\tilde{\omega}_\alpha$ was found in Eq. (1.39) from a semiclassical description. There, the blueshift was identified as the well-known depolarization shift for intersubband transitions. That the magnitude of the depolarization shift depends on the magnitude of $\omega_{\mathrm{p}_\alpha}$, which depends on the density of electrons involved in the transition, underlines the collective nature of the effect.

We are now prepared to diagonalize the full Hamiltonian of Eq. (4.26), which can be written in terms of the intersubband plasmon operators as:

$$\hat{H}_{\mathrm{mat}}^{\mathrm{coll}} = \sum_\alpha \hbar\tilde{\omega}_\alpha p_\alpha^\dagger p_\alpha + \frac{\hbar}{2} \sum_{\alpha \neq \beta} \Xi_{\alpha\beta} \left(p_\alpha + p_\alpha^\dagger\right)\left(p_\beta + p_\beta^\dagger\right) \tag{4.31}$$

This Hamiltonian describes the intersubband plasmon excitations and their coupling, the strength of which is determined by:

$$\Xi_{\alpha\beta} = \frac{\omega_{\mathrm{p}_\alpha}\omega_{\mathrm{p}_\beta}}{2\sqrt{\tilde{\omega}_\alpha \tilde{\omega}_\beta}} \frac{S_{\alpha\beta}}{\sqrt{S_{\alpha\alpha} S_{\beta\beta}}} \tag{4.32}$$

Once again, the Hamiltonian is quadratic in bosonic operators and can be diagonalized with a Bogoliubov transformation. We introduce the bosonic operators P_n which describe the collective excitations of the system, the plasmons. The number of collective modes n is equivalent to the number of unique single particle transitions.[2] This is because the Bogoliubov transformation is simply a change in basis, through which the dimensionality of the vector space is preserved.

We require that the operators satisfy:

$$\left[P_n, \hat{H}_{\mathrm{mat}}^{\mathrm{coll}}\right] = \hbar\Omega_n P_n \tag{4.33}$$

so that $P_n^\dagger$ and P_n are raising and lowering operators for the collective modes, the plasmons. In the Bogoliubov procedure, the new operators are written as linear combinations of the old operators:

$$P_n = \sum_\alpha \left(a_{n_\alpha} p_\alpha + b_{n_\alpha} p_\alpha^\dagger\right) \tag{4.34}$$

[2] For N bound states,the number of unique single particle transitions may be written as $\frac{N!}{2!(N-2)!}$.

Equations (4.33) and (4.34) lead to a system of $2N$ linear equations for a_{n_α}, b_{n_α}, and Ω_n. The problem can be recast in matrix form, where upon diagonalization, the eigenfrequencies Ω_n and their associated eigenvectors with coefficients a_{n_α} and b_{n_α} are found [101]. The problem admits 2N eigenvalues, where for each eigenvalue Ω_n there is an eigenvalue $-\Omega_n$. Only the positive frequency solutions Ω_n are physical. The normalization condition $\sum_i \left(|a_{n_i}|^2 - |b_{n_i}|^2\right) = 1$ ensures the bosonicity of the operators P_n. After diagonalization, the Hamiltonian takes the form:

$$\hat{H}^{\text{coll}}_{\text{mat}} = \sum_n \hbar\Omega_n P_n^\dagger P_n \tag{4.35}$$

4.2.3 Optical Properties of the Collective Modes

The optical properties of the collective modes are found through the polarization operator $\hat{P}_z$. Because it commutes with every term of the full system Hamiltonian (Eq. (4.21)) except $\hat{H}^{\text{sp}}_{\text{mat}}$, the expression for $\hat{P}_z$ found in Eq. (4.16) remains valid to describe the polarization of the collective excitations. Expressing $\hat{P}_z$ from Eq. (4.16) in terms of the operators P_n for the collective excitations, instead of the operators b_α for the single particle excitations, results in the following expression:

$$\hat{P}_z(z) = \frac{e\hbar}{2m^*\sqrt{S}} \sum_n \sum_\alpha \frac{\xi_\alpha(z)\sqrt{\Delta N_\alpha}}{\sqrt{\omega_\alpha \tilde{\omega}_\alpha}} X_{\alpha_n} \left(P_n + P_n^\dagger\right) \tag{4.36}$$

where $X_{\alpha_n} = (a_{n_\alpha} + b_{n_\alpha})^{-1}$ is the inverse of an $N \times N$ matrix.

The current density operator is found as the time evolution of $\hat{P}_z$ under the action of $\hat{H}^{\text{coll}}_{\text{mat}}$:

$$\hat{J}_z = \frac{\mathrm{i}}{\hbar}\left[\hat{P}_z, \sum_n \hbar\Omega_n P_n^\dagger P_n\right] = \mathrm{i}\sum_n J_n(z)\left(P_n - P_n^\dagger\right) \tag{4.37}$$

The spatial dependence of $\hat{J}_z$ has been fully captured in the definition of the current density functions $J_n(z)$:

$$J_n(z) = \frac{e\hbar}{2m^*\sqrt{S}} \Omega_n \sum_\alpha \frac{\xi_\alpha(z)\sqrt{\Delta N_\alpha}}{\sqrt{\omega_\alpha \tilde{\omega}_\alpha}} X_{\alpha_n} \tag{4.38}$$

The $J_n(z)$ are analogous to the single particle microcurrents $\xi_\alpha(z)$, as in the single particle case, it was the $\xi_\alpha(z)$ which fully determined the z-dependence of the single particle current operator $\hat{j}_z$ in Eq. (4.13).

It is worth remarking that the spatial dependence of the single particle microcurrents could be written only in terms of the electronic wavefunctions ϕ, whereas the same *cannot* be done for $J_n(z)$. As evident in Eq. (4.38), the factor ΔN_α, describing the density of charge involved in each single particle transition α, weighs each term of the sum over α. The fact that charge densities must be considered to establish the spatial dependence of $\hat{J}_z$ underscores the collective nature of the Ω_n modes.

Analogously to what was done in Eq. (4.18) for the single particle case, the spatial distribution of charge involved in the collective excitation n can be defined as:

$$\rho_n^{\text{coll}}(z) = \frac{\partial J_n(z)}{\partial z} \tag{4.39}$$

The charge distribution oscillates at the frequency Ω_n. This quantity can be interpreted similarly to the charge distribution $\rho_\alpha(z)$ defined for the single particle transitions,[3] which was shown to be linked to the dipole matrix element.

An effective oscillator strength for the collective mode n can be written in terms of $J_n(z)$ as [100]:

$$\Omega_n F_n = \frac{1}{\Omega_n}\left|\int_{-\infty}^{\infty} J_n(z)\,\mathrm{d}z\right|^2 \tag{4.40}$$

The angle-dependent radiative decay rate of the Ω_n mode, found by solving the quantum Langevin equations in the input-output formalism [60], is written:

$$\Gamma_{\mathrm{rad},n}(\theta,\omega) = \Gamma_n \frac{\omega}{\Omega_n}\frac{\sin^2\theta}{\cos\theta} \tag{4.41}$$

where Γ_n is found as:

$$\Gamma_n = \frac{S}{\hbar\epsilon_0\sqrt{\varepsilon_s}}\frac{|\int J_n(z)\,\mathrm{d}z|^2}{c\Omega_n} \tag{4.42}$$

The expression of Eq. (4.41) was introduced for the Berreman mode in Section 2.2.1. With the expression for $\Gamma_{\mathrm{rad},n}(\theta,\omega)$ and upon introducing a phenomenological nonradiative linewidth γ_{NR}, the angle-dependent absorptivity of the Ω_n mode can be calculated nonperturbatively as was described in Section 2.2.1.

We now examine the optical properties of the collective modes of a 100 nm InGaAs/AlInAs quantum well. Whereas the microcurrents and charge distributions could be plotted in Fig. 4.1 for the 100 nm well unambiguously without specifying the electronic density in the well, for the collective modes, the electronic density must be specified as per the discussion above. In Fig. 4.2, the current density distributions $J_n(z)$ and the charge distributions $\rho_n^{\mathrm{coll}}(z)$ for the first three collective modes of largest oscillator strength are plotted for an electronic density of $N_{\mathrm{v}} = 1.7\times10^{19}\,\mathrm{cm}^{-3}$.

In order of increasing oscillator strength, the modes are indexed with odd integers as $n = 1$, 3, and 5 because the form of the $J_n(z)$ functions can be described, upon introducing the *longitudinal* wavevector k_z, as:

$$J_n(z) \propto \sin(k_{z,n}z) \quad \text{where} \quad k_{z,n} = \frac{n\pi}{L} \tag{4.43}$$

In this expression, L is the width of the quantum well.

The wavevector k_z determines the spatial dependence of the polarization associated with the collective excitation. This highlights the fact that our quantum model provides a *nonlocal* description for the excitations of the electron gas. The nonlocal description stems from the fact that the polarization is defined as a function of the coordinate z in space. In the classical Drude description, excitations of the electron gas correspond to a uniform displacement of charge in space, i.e. a spatially uniform polarization independent of z.

Let us now consider the charge distribution of the $n = 1$, 3, and 5 modes. The largest oscillator strength mode, the $n = 1$ mode, has the form of a dipole. We conclude that this mode is the Berreman mode. The $n = 3$ and $n = 5$ modes have charge distributions which take the form of dipoles stacked top to bottom. Modes with even indices n are dark modes. Their charge distributions are not dipole active, and consequently, they have zero oscillator strength.

[3] The quantities $\rho_\alpha(z)$ and $\rho_n^{\mathrm{coll}}(z)$ are not, however, dimensionally homogeneous. See [101].

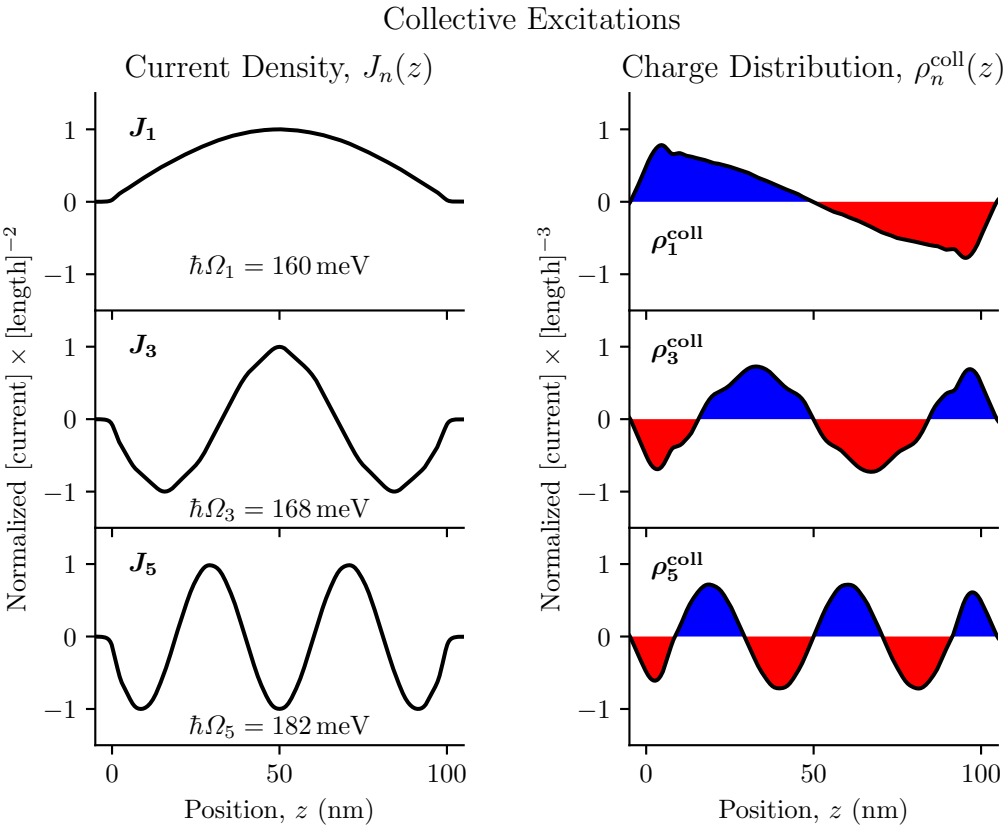

Fig. 4.2 The current densities and the corresponding charge distributions are plotted for the first three collective modes of largest oscillator strength, indexed by odd j as described in the text, for a 100 nm InGaAs/AlInAs quantum well with an electronic density of $N_{\mathrm{v}} = 1.7 \times 10^{19}\,\mathrm{cm}^{-3}$.

4.2.4 Dispersion of Plasmon Modes

The absorptivity of the electron gas confined in InGaAs/AlInAs quantum wells of 50 nm, 100 nm, and 150 nm widths, calculated with the input-output formalism for a fixed electronic density of $1.7 \times 10^{19}\,\mathrm{cm}^{-3}$, is plotted in the left panel of Fig. 4.3 for an incidence angle of 30°. The relative oscillator strengths of the collective modes which give rise to the absorption spectra are indicated by the height of the bars plotted at their respective energies.

In each of the spectra, the majority of the oscillator strength is concentrated into the lowest energy mode which is identified as the $n = 1$ (Berreman) mode, whose charge distribution was shown in Fig. 4.2 to be that of a dipole. At energies greater than this mode, there is a series of *higher order* modes of decreasing oscillator strength, which are associated with the $n = 3, 5, \ldots$ current distributions described by Eq. (4.43). Since the indices n are related to the wavevector $k_{z,n}$, we may refer to a quantized *dispersion* $\Omega_n\,(k_{z,n})$ of collective modes.

We highlight that the classical Drude description for the electron gas cannot describe a dispersion of collective modes. In the classical description, only a single collective mode,

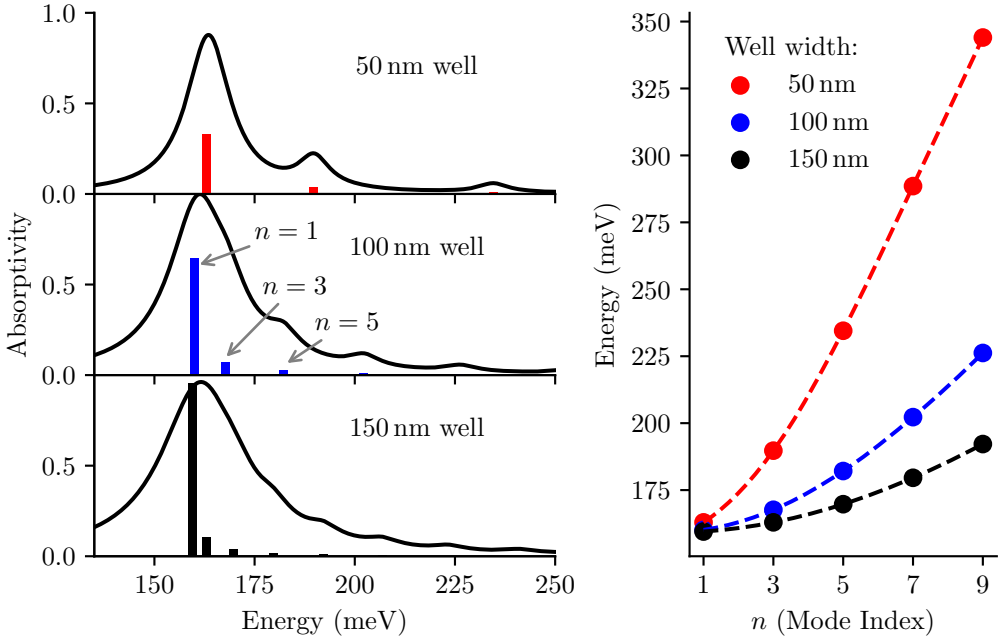

Fig. 4.3 The calculated absorptivity for a 30° angle of incidence is plotted for wide quantum wells of various widths for a fixed volume electronic density of $1.7 \times 10^{19}\,\mathrm{cm}^{-3}$ for a nonradiative linewidth of $\gamma_{\mathrm{NR}} = 7\,\mathrm{meV}$. The relative oscillator strengths of the modes are plotted, normalized to the largest oscillator strength of the 150 nm well. On the right, the energies of the collective modes are plotted as a function of the mode index (scatter points), and an interpolation function is plotted (dotted lines).

corresponding to a uniform polarization of the electron gas, can be excited exactly at the plasma energy. As described in Chapter 1, the Drude model is already insufficient to describe the Berreman mode in the presence of electronic confinement, since the mode blueshifts with increasing confinement. The blueshift of the Berreman mode is evident comparing the absorptivity spectra from the 50 nm, 100 nm, and 150 nm wells in the left panel of Fig. 4.3.

In the right panel of Fig. 4.3, the energies $\hbar\Omega_n$ of the collective modes for the three well widths are plotted as a function of the mode index, n. An interpolation function for the set of modes from each well is plotted as a dashed line to more clearly show the dispersion trend. For each of the well widths, the energy separation of the modes increases in a superlinear way with the mode index. The dispersion of modes depends strongly on the width of the quantum well, which determines the electronic confinement.

The mode dispersions plotted in the right panel of Fig. 4.3 result from numerical calculations. Other than indicating that the static electronic confinement is important in determining the dispersion, the numerical solutions do not give much physical insight. In the next section, we will derive an analytic expression for the dispersion of the collective modes assuming an infinite square well, and then show that with suitable approximations, we may even derive a dispersion relation for the collective modes arising in quantum wells of finite

potential.

4.3 Longitudinal Plasmon Modes in an Infinite Square Well

In the first sections of this chapter, the collective modes of the confined electron gas were constructed by defining a polarization for each optically active single particle transition, and then by considering the coupling of the polarizations between the single particle excitations. The collective modes, and their optical properties, were calculated numerically. In this section, we apply the same quantum formalism to analytically calculate the collective modes of the electron gas in an infinite square well, for which case, the single particle wavefunctions and bound state energies take on relatively simple forms.

Two important findings will result from our analytic approach. First, we shall establish that each collective mode $\Omega_{n=j}$ in a square well arises from the coupling of single particle transitions $i \to i+j$ with the same j. Second, we shall derive an analytic expression for the collective mode dispersion as a function of the quantized longitudinal wavevector $k_{z,j}$.

We then demonstrate that our analytic results can be extrapolated under the correct assumptions to describe the collective modes experimentally observed in a heavily doped InGaAs/AlInAs quantum well.

Consider an infinite square well of width L centered at $L/2$. The stationary states of the time-independent Schrödinger equation and their energies are found as:

$$\phi_n(z) = \sqrt{\frac{2}{L}} \sin\left(\frac{n\pi z}{L}\right) \tag{4.44}$$

$$E_n = \frac{n^2\pi^2\hbar^2}{2m^*L^2}, \quad n = 1,2,3,\ldots \tag{4.45}$$

We proceed now to derive a few quantities which will be useful in solving for the collective modes. The frequency of the $i \to i+j$ transitions can be written:

$$\omega_{i\to i+j} = \frac{\pi^2\hbar}{2m^*L^2}\left(i+j\right)^2 - i^2 = \frac{\pi^2\hbar}{2m^*L^2} j\left(2i+j\right) \tag{4.46}$$

The Fermi energy can be approximated as the energy of the highest occupied state, N_{occ}, as:

$$E_{\text{F}} \approx \frac{N_{\text{occ}}^2\pi^2\hbar^2}{2m^*L^2} \tag{4.47}$$

For a noninteracting 3D electron gas, the Fermi energy takes the usual form:

$$E_{\text{F}}^{\text{3D}} = \frac{\hbar^2}{2m^*}\left(3\pi^2 N_{\text{v}}\right)^{\frac{2}{3}} \tag{4.48}$$

where N_{v} is the number of electrons per volume. For a sufficiently wide quantum well with many occupied subbands in which the level spacing is sufficiently small, the system may be approximated as a 3D electron gas. From Eqs. (4.47) and (4.48), the volume electronic density N_{v} can be related to N_{occ}:

$$N_{\text{v}} \approx \frac{\pi N_{\text{occ}}^3}{3L^3} \tag{4.49}$$

This relation becomes increasingly exact for large L and large N_{occ}.

We now derive an expression for $\Delta N_{i\to i+j}$, the surfacic population difference between states i and $i+j$, in terms of the well width L and quantum numbers. At T=0 K, the Fermi-Dirac distribution simplifies to:

$$f_{\text{FD}}(E) = \begin{cases} 1 & \text{if } E \leq E_{\text{F}} \\ 0 & \text{if } E > E_{\text{F}} \end{cases} \tag{4.50}$$

implying that only subbands with energies below the Fermi level are populated. Supposing that the Fermi level is fixed such that the state E_{i+j} is unoccupied and the state E_i is occupied, as illustrated in Fig. 4.4, then the surfacic density of electrons on the subbands are, respectively, $N_{i+j} = 0$ and $N_i = \rho_{\text{2D}}\,(E_{\text{F}} - E_i)$, where ρ_{2D} is the 2D density of states per subband per area [111]. We may intoduce the approximation $E_{\text{F}} \approx E_{i+j}$ in order to write $N_i \approx \rho_{\text{2D}}\,(E_{i+j} - E_i)$. As illustrated in Fig. 4.4, this approximation leads to an overestimation of the initial state subband population. With this approximation, the population difference between states i and $i+j$ can be written:

$$\Delta N_{i\to i+j} \approx \hbar\omega_{i\to i+j} \cdot \rho_{\text{2D}} \tag{4.51}$$

Substituting $\rho_{\text{2D}} = m^*/\pi\hbar^2$ and $\omega_{i\to i+j}$ from Eq. (4.46), we have:

$$\Delta N_{i\to i+j} \approx \frac{\pi}{2L^2} j(2i+j) \tag{4.52}$$

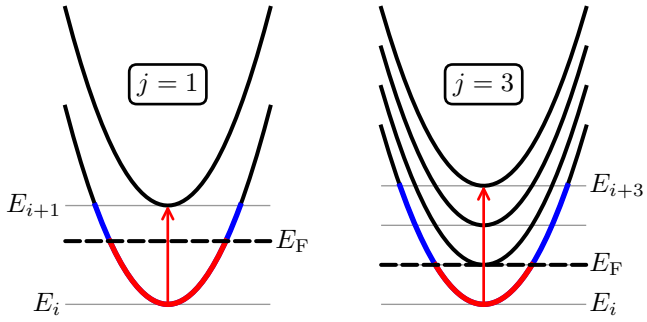

Fig. 4.4 At T=0 K, the surfacic population of the initial subband i is estimated as $N_i \approx \rho_{\text{2D}}\,(E_{i+j} - E_i)$, illustrated here with the blue shaded subbands. This approximation leads to an overestimation of the initial state subband population. The true populations for a Fermi level between the initial and final state are shown in red.

We now evaluate the coupling coefficients $S_{\alpha\beta}$ describing the coupling between optically induced single particle transitions in an infinite square well. For convenience, we reproduce $S_{\alpha\beta}$ from Eq. (4.27):

$$S_{\alpha\beta} = \frac{1}{\hbar\omega_\alpha}\frac{1}{\hbar\omega_\beta}\left(\frac{\hbar^2}{2m^*}\right)^2 \int_{-\infty}^{\infty} \xi_\alpha(z)\xi_\beta(z)\,\mathrm{d}z \tag{4.53}$$

The microcurrents describing the optical transitions in an infinite well take the form:

$$\xi_{i\to i+j}(z) = \frac{\pi}{L^2}\left[j\sin\left(\frac{2i+j}{L}\pi z\right) - (2i+j)\sin\left(\frac{j\pi z}{L}\right)\right] \tag{4.54}$$

This expression is plotted in Fig. 4.5 for $j = 1$ and $j = 3$ for various values of i. The form of $\xi_{i\to i+j}(z)$ is similar for varying i but differs for varying j. For $i \gg j$, the curves approach $\sin(j\pi z/L)$. Indeed, for $i \gg j$, only the sine term with a factor of i contributes in Eq. (4.54), and the expression for the microcurrents can be simplified to:

$$\xi_{i\to i+j}(z) \approx \frac{\pi}{L^2}\left[-2i\sin\left(\frac{j\pi z}{L}\right)\right] \tag{4.55}$$

In quantum wells with many occupied subbands, $N_{\text{occ}} \gg 1$. Because the final state involved in a transition must be initially unoccupied, it holds that $i \geq (N_{\text{occ}} - j)$. The oscillator strength of a single particle transition scales with j^{-2}, so we can neglect all but the first few j, thereby limiting the magnitude of j. Then, the condition that $i \gg j$ is satisfied for the semiconductor system we study since for a 100 nm InGaAs quantum well, $N_{\text{occ}} \approx 20$. Substituting the expressions found in Eqs. (4.46) and (4.55) into Eq. (4.53), the coupling

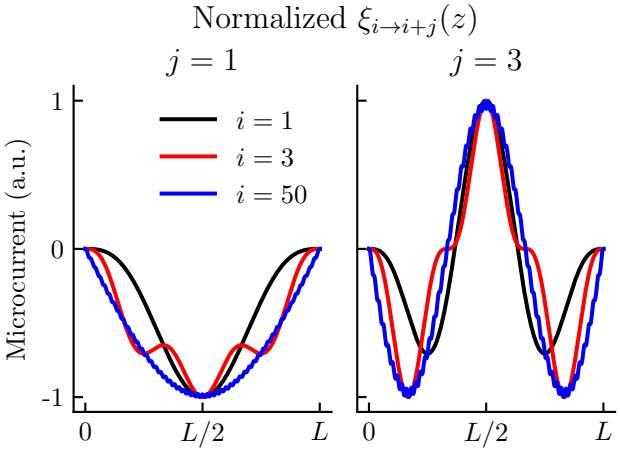

Fig. 4.5 The normalized *single particle* microcurrents $\xi_{i\to i+j}(z)$ for the infinite square well are plotted for $j = 1$ on the left and $j = 3$ on the right for various initial states i.

coefficients can be evaluated as:

$$S_{i\to i+j,i'\to i'+j'} = \frac{4ii'}{\pi^2 j(2i+j)j'(2i'+j')}\int_0^L \sin\left(\frac{j\pi z}{L}\right)\sin\left(\frac{j'\pi z}{L}\right)\mathrm{d}z \tag{4.56}$$

Noting that for $i \gg j$, $2i + j \approx 2i$ (and similarly for i' and j'), and that sine functions of different indices are orthogonal over a symmetric period:

$$\int_0^L \sin(nz)\sin(mz)\,\mathrm{d}z = \frac{L}{2}\delta_{nm}, \tag{4.57}$$

Equation (4.56) can be simplified to:

$$S_{i\to i+j,i'\to i'+j'} = \frac{L}{2\pi^2}\frac{1}{j}\frac{1}{j'}\delta_{jj'} \quad \text{for } i \gg j, i' \gg j' \tag{4.58}$$

The expression no longer depends on the initial states i or i'. The δ-function implies that only transitions with identical j couple to each other. Thus, the collective modes of the system arise from the coupling of single-particle microcurrents with the same j.

The collective modes of the system are determined by calculating the zeros of the following determinant:

$$\Delta_j(\omega) = 1 - \frac{2e^2}{\hbar\epsilon_0\varepsilon_\mathrm{s}}\sum_{i=1}^{N_\mathrm{occ}}\frac{S_{i\to i+j,i'\to i'+j'}\Delta N_{i\to i+j}\omega_{i\to i+j}}{\omega^2-\omega_{i\to i+j}^2} \tag{4.59}$$

In the sections which follow, two different approximation are introduced which permit Eq. (4.59) to be solved. In what we term the *metallic limit*, we make the approximation that $j^2/N_\mathrm{occ} \ll 1$. In this limit, we recover the Lindhard formula [76, 79, 148] which describes the dispersion of collective modes for a free electron gas. In what we term the *semiconductor limit*, we make the approximation that the level spacing in the quantum well is constant: $\omega_{i\to i+1} = \omega_0$. This is a rather good approximation for a wide InGaAs quantum well, due to the finite confinement potential and the increasing value for the effective mass with increasing energy (nonparabolicity). In this limit, we find a dispersion relation which describes the experimentally observed modes in a 100 nm InGaAs AlInAs quantum well.

4.3.1 Metallic Limit

Using Eqs. (4.46), (4.52) and (4.58) to substitute expressions for the terms in the numerator, and introducing the plasma frequency $\omega_\mathrm{p}^2 = e^2N_\mathrm{v}(m^*\epsilon_0\varepsilon_\mathrm{s})^{-1}$, the determinant may be rewritten as:

$$\Delta_j(\omega) = 1 - \frac{\pi\omega_\mathrm{p}^2}{4N_\mathrm{v}L^3}\sum_{i=1}^{N_\mathrm{occ}}\frac{(2i+j)^2}{\omega^2-\omega_{i\to i+j}^2} \tag{4.60}$$

After some manipulation, this expression may be rewritten:

$$\Delta_j(\omega) = 1 - \frac{1}{\omega^2}\frac{\pi\omega_\mathrm{p}^2}{4N_\mathrm{v}L^3}\sum_{i=1}^{N_\mathrm{occ}}\frac{(2i+j)^2\left(1+\dfrac{\omega_{i\to i+j}^2}{\omega^2}\right)}{1-\left(\dfrac{\omega_{i\to i+j}^2}{\omega^2}\right)^2} \tag{4.61}$$

The denominator in the sum is simplified to one when:

$$\frac{\omega_{i\to i+j}^2}{\omega^2} \ll 1 \tag{4.62}$$

This holds for $j^2/N_\mathrm{occ} \ll 1$, which we have defined as the metallic limit. To show this, we use the facts that $\omega_{i\to i+j} \le \omega_{N_\mathrm{occ}\to N_\mathrm{occ}+j}$ and $\omega^2 \ge \omega_\mathrm{p}^2$ (the latter because the bright modes are always at energies above the plasma frequency) to establish an upper bound for the left side of Eq. (4.62):

$$\frac{\omega_{i\to i+j}^2}{\omega^2} < \frac{3\hbar^2\pi^3\epsilon_0\varepsilon_\mathrm{s}}{m^*L}\frac{j^2}{N_\mathrm{occ}}\left(1+\frac{j}{2N_\mathrm{occ}}\right)^2 \tag{4.63}$$

The right side of Eq. (4.63) is small for $j^2/N_{\mathrm{occ}} \ll 1$. Since $j \geq 1$, this occurs for large N_{occ}, when many subbands are occupied, as in a metal.

With Eq. (4.62), the determinant takes the simpler form:

$$\Delta_j(\omega) = 1 - \frac{1}{\omega^2}\frac{\pi\omega_{\mathrm{p}}^2}{4N_{\mathrm{v}}L^3}\sum_{i=1}^{N_{\mathrm{occ}}}(2i+j)^2\left(1+\frac{\omega_{i\to i+j}^2}{\omega^2}\right) \tag{4.64}$$

Inserting closed form expressions for $\sum_{i=1}^{N_{\mathrm{occ}}} i^2$ and $\sum_{i=1}^{N_{\mathrm{occ}}} i$, we find that Ω, the zeros of the determinant, are solutions to the following equation quadratic in Ω^2:

$$A\Omega^4 + B\Omega^2 + C = 0$$

$$\begin{aligned}
A &= 1 \\
B &= -\omega_{\mathrm{p}}^2\left(1+\frac{3(i+j)}{2N_{\mathrm{occ}}}+\frac{3}{4N_{\mathrm{occ}}^2}\left(\frac{2}{3}+j(j+2)\right)\right) \\
C &= -\frac{12}{5}\omega_{\mathrm{p}}^2\frac{E_{\mathrm{F}}E_j}{\hbar^2}\left(1+\frac{5(1+j)}{2N_{\mathrm{occ}}}+\frac{5}{2N_{\mathrm{occ}}^2}\left(\frac{2}{3}+2j+j^2\right)+\frac{5j}{4N_{\mathrm{occ}}^3}\left(2+3j+j^2\right)\right. \\
&\qquad \left.+\frac{5}{16N_{\mathrm{occ}}^4}\left(-\frac{16}{30}+j^2\left(4+4j+j^2\right)\right)\right)
\end{aligned} \tag{4.65}$$

The quantities E_j and E_{F} have been introduced according to Eq. (4.45) and Eq. (4.47). Having already limited ourselves to the regime where $j^2/N_{\mathrm{occ}} \ll 1$, we may write the solution to Eq. (4.65) using only the first terms for B and C:

$$\Omega_j^2 = \frac{\omega_{\mathrm{p}}^2}{2} + \frac{\omega_{\mathrm{p}}^2}{2}\sqrt{1+\frac{48E_{\mathrm{F}}E_j}{5(\hbar\omega_{\mathrm{p}})^2}} \tag{4.66}$$

Using the approximation $\sqrt{1+x} \approx 1 + x/2$, the solutions become:

$$\Omega_j^2 \approx \omega_{\mathrm{p}}^2 + \frac{12}{5}\frac{E_{\mathrm{F}}E_j}{\hbar^2} \tag{4.67}$$

Introducing the Fermi velocity via $E_{\mathrm{F}} = m^* v_{\mathrm{F}}^2/2$ and substituting for E_j via Eq. (4.45), the solutions can be written:

$$\Omega_j^2 \approx \omega_{\mathrm{p}}^2 + \frac{3}{5}v_{\mathrm{F}}^2\left(\frac{\pi j}{L}\right)^2 \tag{4.68}$$

This dispersion relation is identical to the one derived by Lindhard for an electron gas using the rotating phase approximation [76], and experimentally investigated by Lindau et al. [75] in thin metal films. The higher order ($j \geq 3,\ 5,\ 7\ldots$) modes are known as Tonks-Dattner modes [56].

4.3.2 Semiconductor Limit

The determinant of Eq. (4.59) can be written in a simpler form by introducing the plasma frequency associated with each intersubband transition $\omega_{\mathrm{p}_{i\to i+j}}$, defined in Eq. (1.31). Making the substitution, the determinant takes the form:

$$\Delta_j(\omega) = 1 - \sum_{i=1}^{N_{\mathrm{occ}}}\frac{\omega_{\mathrm{p}_{i\to i+j}}^2}{\omega^2 - \omega_{i\to i+j}^2} \tag{4.69}$$

The zeros of Eq. (4.69) can be readily found assuming constant energy spacing ω_0 between bound states, a reasonable approximation for a semiconductor quantum well. With this assumption, $\omega^2_{i\to i+j}$ can be written as $(j\omega_0)^2$ and the zeros of the determinant are found as:

$$\Omega_j^2 = (j\omega_0)^2 + \sum_{i=1}^{N_{\mathrm{occ}}} \omega^2_{\mathrm{p}_{i\to i+j}} \tag{4.70}$$

The sum of the squared intersubband plasma frequencies is equal to the bulk plasma frequency [8], and so the solutions may be written as:

$$\Omega_j^2 = \omega_0^2 j^2 + \omega_{\mathrm{p}}^2 \tag{4.71}$$

This expression establishes a relationship between the electronic confinement and the dispersion of the plasmon modes. In the absence of confinement ($\omega_0 = 0$), the only mode excited is at the plasma frequency, and the classical description for the Berreman mode is recovered. In the presence of confinement (nonzero ω_0), the $j = 1$ Berreman mode is blueshifted from the plasma frequency ω_{p}, and the dispersion of modes is modified.

In the following section, it will be demonstrated that Eq. (4.71) correctly describes the dispersion of experimentally observed collective modes in a 100 nm InGaAs/AlInAs quantum well. In the remainder of this section, it is shown that this expression correctly describes the dispersion of collective modes calculated numerically for InGaAs/AlInAs quantum wells considering a finite barrier potential and nonparabolicity.

The analytic dispersion of Eq. (4.71) is plotted against numerically calculated plasmon energies for quantum wells of fixed electronic density but varying width in Fig. 4.6a, and for quantum wells of fixed width but varying electronic density in Fig. 4.6b. The average subband separation is calculated for each well as $\hbar\omega_0 = eV_{\mathrm{barr}}/N_{\mathrm{st}}$, where eV_{barr} is the depth of the quantum well (equal to 0.52 eV for InGaAs/AlInAs wells grown on InP), and N_{st} is the number of bound states. In all cases, the analytic expression of Eq. (4.71) well describes the dispersion of the numerically calculated modes.

In Fig. 4.6a, the dispersion curves converge at $j = 1$ and diverge for $j > 1$. The average level spacing ω_0 is increased as the width of the quantum well is reduced, resulting in a more rapid increase in the slope of the mode dispersion for thinner wells. For the wells of fixed width but varying electronic density in Fig. 4.6b, the dispersion curves for the various electronic densities are parallel but offset, indicating that the curvature of the dispersion is not affected by the electronic density.

In this section, we have linked the form of the collective mode dispersion to the electronic confinement, and in effect, have demonstrated that the electronic confinement determines the nonlocal nature, or k_z dependence, of the collective mode.

4.4 Experimental Observation of Higher Order Longitudinal Plasmon Modes

The higher order longitudinal collective modes were experimentally observed in a 100 nm InGaAs/AlInAs quantum well with an electronic density of $7.5 \times 10^{18}\,\mathrm{cm}^{-3}$ in thermal emission spectra [138]. The spectra were measured in experiments like those described in Section 2.4.1, in which the electron gas is thermally excited by Joule heating from an in-plane

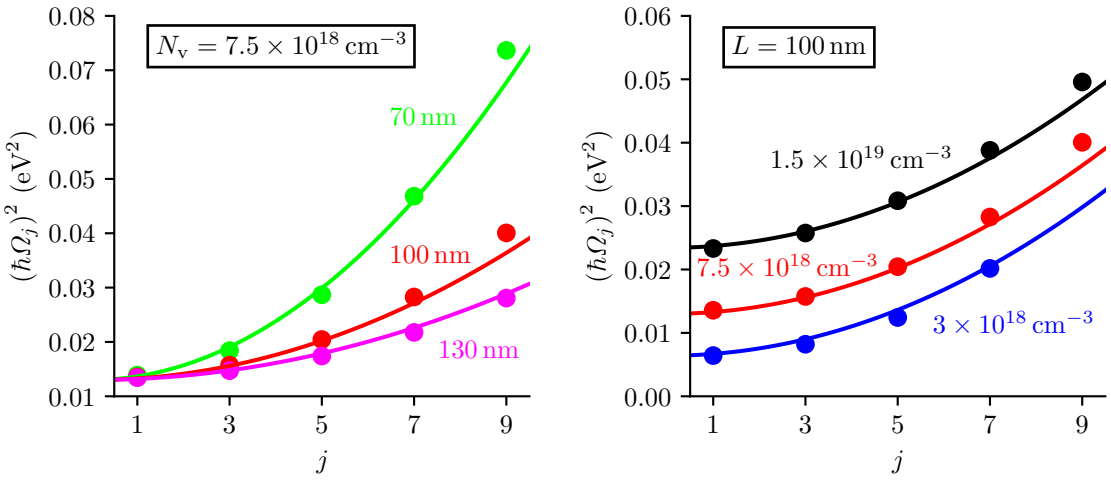

Fig. 4.6 Collective mode energies calculated from the the numerical diagonalization of $\hat{H}^{\mathrm{coll}}_{\mathrm{mat}}$ are plotted as points for varying well width L and fixed N_v in (a) and for varying N_v and fixed L in (b). Dispersion relations from the analytic formula of Eq. (4.71) are plotted as continuous curves.

current. Because the absorptivity and emissivity are equivalent at a given frequency according to Kirchhoff's law, this experiment permits a direct observation of the plasmonic modes of the system.

The thermal emission spectra from the experiment of [138] are plotted in Fig. 4.7a for four different angles in red. The emission spectra were measured at room temperature and have been normalized to one. In black, the theoretically predicted emission spectra are plotted.

Multiple resonances are clearly observed in each of the spectra at energies above the dominant (Berreman) mode. The Berreman mode radiatively broadens with increasing angle, as was described in Section 2.2.1. The radiative decay rate of the higher energy modes also increases with angle. However, these modes do not become severely overdamped like the Berreman mode because their radiative decay rates never surpass the nonradiative decay rate γ_{NR}. As a result, the emissivity of the higher order modes continuously increases with angle. For this reason, the modes are more easily observed in spectra measured at high angles. The theoretical curves well reproduce the experimental data at all angles, confirming the validity of the quantum model.

The square of the collective mode energies extracted from the spectra are plotted as a function of odd j in Fig. 4.7b and compared with the dispersion found analytically in the semiconductor limit in Eq. (4.71). The analytic dispersion is plotted with a continuous black curve using the values $\hbar\omega_0 = 17\,\mathrm{meV}$ for the average subband separation and $\hbar\omega_{\mathrm{p}} = 114\,\mathrm{meV}$ for the plasma energy and is found to closely model the experimental data.

Copyrighted Image

Angela Vasanelli, Simon Huppert, Andrew Haky, Thibault Laurent, Yanko Todorov & Carlo Sirtori 2020.
"Semiconductor Quantum Plasmonics".
Physical Review Letters **125**(18), p. 187 401

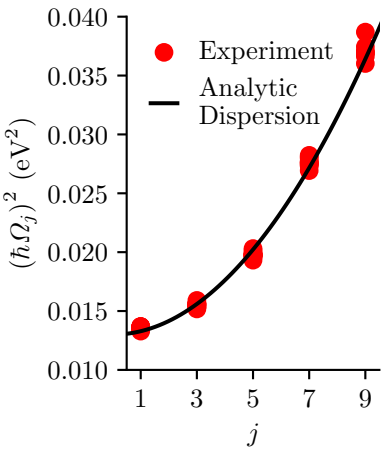

(a) (b)

Fig. 4.7 (a) Experimentally measured thermal emission spectra of a 100 nm InGaAs/AlInAs quantum well doped with electronic density of $N_v = 7.5 \times 10^{18}\,\mathrm{cm}^{-3}$ are plotted in red. Calculated emission spectra are plotted in black. Figure reproduced from [138]. (b) Energies of the plasmon modes extracted from (a) are plotted as a function of j. The analytic dispersion relation of Eq. (4.71) is plotted as a continuous black line.

4.5 Conclusion

A microscopic quantum model was introduced in the PZW formalism to describe the collective modes of the confined electron gas. The collective modes were constructed by considering the coupling between single particle transitions through the $\hat{\mathbf{P}}^2$ term of the Hamiltonian. Because the polarization associated with a single particle transition is directly expressed in terms of the electronic wavefunctions of the states involved in the transition, size confinement is naturally considered in the calculation of the collective modes.

Through the definition of a spatially dependent polarization operator, the model describes the nonlocality (or k_z-dependence) of the collective modes. This is in strong contrast to the Drude model, for which no spatial coordinate (or wavevector) enters the description of the response. By applying the quantum model to analytically study the collective modes in an infinite square well, we found expressions for the dispersion of longitudinal collective modes with quantized wavevector k_z. We demonstrated that depending on the approximations made, the Lindhard formula for the modes of a free plasma can be recovered, or the experimentally observed higher order modes in a semiconductor quantum well can be modeled.

The microscopic quantum model introduced in this chapter is general insofar as it can be used to describe the collective modes of the electron gas in any static potential once the bound electronic states are known. In the next chapter, we attempt to engineer the collective modes of the system through the careful design of the confinement potential.

Chapter 5

Collective Mode Engineering

A primary aim in nanophotonics is to leverage fundamental knowledge of the interaction of light and matter to *engineer* structures with novel optical properties. In the previous chapter, the collective modes of a highly doped square quantum well were described with a microscopic quantum model. In this chapter, we exploit our knowledge of the microscopic origin of the collective electronic response to engineer novel collective modes.

The degree of freedom available to engineer the collective modes is the electronic potential, as it determines the single particle electronic states from which the collective response is determined. The techniques of band structure engineering, including, for example, the use of tunnel-coupled quantum wells and the varying of alloy content across a heterostructure, can be used to experimentally realize designer potentials.

The collective optical response cannot be directly inferred from the band structure diagram, beyond a very limited physical intuition. The collective modes are determined only after a diagonalization of the Hamiltonian describing all of the single particle transitions and their dipole-dipole coupling. This makes the engineering of the collective modes a difficult task.

Two key findings from our study in the previous chapter of the collective modes arising in a square potential suggest points of departure for our engineering effort:

1. It was established that the coupling strength between any two single particle transitions is determined by the overlap of the microcurrents of the transitions. For the square well, a series of bright collective modes indexed with odd-j arise because the microcurrents of single particle transitions $i \to i + j$ and $i' \to i' + j'$ strongly overlap for $j = j$' and are orthogonal for $j \neq j'$. To engineer novel collective modes, we must break the strict orthogonality of the microcurrents for $j \neq j'$.

2. The collective modes are bright (have a nonzero oscillator strength) when the spatial integral of the collective microcurrent is nonzero. For the symmetric square well case, this occurs only for odd sinusoidal collective microcurrents. With the breaking of the potential symmetry, novel bright modes can be expected.

This chapter is organized as follows. In the first section, the collective modes are calculated for a tunnel coupled quantum well heterostructure, in which the strict orthogonality condition of (1) above is broken. In the second section, the collective modes are calculated for a quantum well in which the potential symmetry is broken with an applied electric field.

In the third section, the breaking of the potential symmetry is studied experimentally for step well structures.

5.1 Collective Modes from Inter-Miniband Transitions

In this section, the absorption spectrum of the 54 nm structure shown in Fig. 5.1a is calculated. The *superlattice* structure consists of alternating 7.5 nm and 5 nm quantum wells, separated by 1.5 nm barriers. The electronic band structure is dramatically different from that of a 54 nm square well, due to the formation of *minibands* of electronic states.

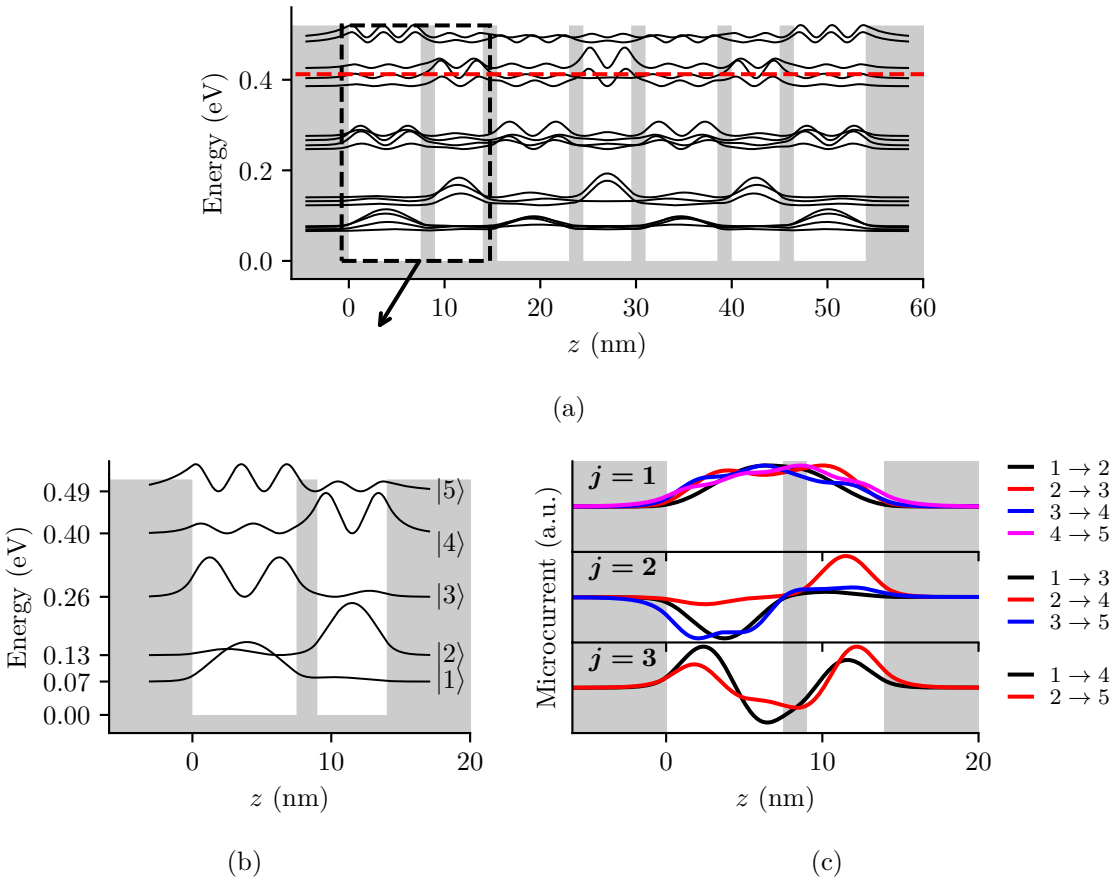

Fig. 5.1 (a) The introduction of six 1.5 nm barriers into a 54 nm square quantum well results in the formation of electronic minibands. The Fermi level calculated for an electronic density of $2 \times 10^{19}\,\mathrm{cm}^{-3}$ is indicated with the dashed red line. (b) The band structure of a single period of tunnel coupled 7.5 nm and 5 nm quantum wells is plotted. (c) The single particle microcurrents for transitions between states i and $i + j$ of the structure of two tunnel coupled wells are normalized and plotted for $j = 1$, 2, and 3.

The design of the 54 nm structure was motivated by the optical properties of asymmetric tunnel coupled quantum wells [120]. In Fig. 5.1b, the band structure of tunnel coupled 7.5 nm and 5 nm quantum wells, representing a single period of the 54 nm superlattice structure, is

plotted. In the tunnel coupled structure, unlike in a square well, the dipole matrix elements between states i and $i+j$ are nonzero for even and odd j.

The single particle microcurrents associated with transitions between states $i \to i+j$ of the tunnel coupled quantum well structure are plotted in Fig. 5.1c, up to $j=3$. For $j=1$ and $j=3$, the single particle microcurrents approximate the form of $\sin(j\pi z/L)$ for odd j, where L is the total structure length, and therefore have approximately the same form as the microcurrents associated with the $j=1$ and $j=3$ transitions of a square quantum well. On the contrary, the $j=2$ single particle microcurrents differ dramatically from the $\sin(2\pi z/L)$ form they follow in a square quantum well. As a a consequence, the microcurrents of the $j=2$ family of transitions are not strictly orthogonal to the microcurrents associated with odd j transitions, and the transitions can couple. As we have set out to do, we have broken the strict orthogonality between microcurrents associated with single particle transitions of different j.

We chose to study the collective modes of the 54 nm structure of Fig. 5.1a, in which the structure of Fig. 5.1b is repeated, in order to investigate a structure with many occupied subbands. The absorption spectrum, calculated with quantum model introduced in the previous chapter, is plotted in Fig. 5.2. The absorption spectrum of an InGaAs/AlInAs quantum well of the same total thickness with the same electronic density, is plotted on the same axis to highlight the dramatic effect of the band structure engineering on the collective response of the tunnel coupled quantum well structure. In contrast to the absorptivity spectrum of the square well, multiple peaks of similar amplitude, resulting from modes of similar oscillator strength, are present in the absorptivity spectrum of the tunnel coupled quantum well structure. Notably, the largest oscillator strength mode is not the lowest energy mode as in the square well case.

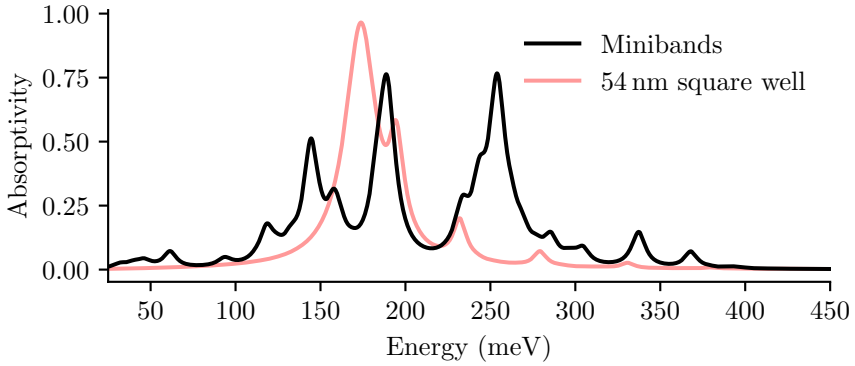

Fig. 5.2 The calculated absorptivity is plotted for the 54 nm tunnel coupled structure of Fig. 5.1a and for a single 54 nm InGaAs/InAlAs quantum well, both doped with an electronic density of $N_v = 2 \times 10^{19}\,\mathrm{cm}^{-3}$. The absorptivity is calculated considering a gold layer adjacent to each structure for 45° angle of incidence, using a nonradiative linewidth of 9 meV.

This demonstrates that the collective electronic response can be artificially modified by the engineering of the potential which confines the constituent electrons. We did not attempt an experimental study of the engineered structure, expecting that the collective modes would not survive the disorder resulting from the many interfaces and the imperfect growth of the

structure, effects which are not considered in the above modeling. Previously, a structure of two tunnel coupled quantum wells was experimentally investigated [101]. The quantum model predicted two collective modes separated by an energy larger than their linewidths, but a single broad mode was observed instead.

5.2 Symmetry Breaking with Applied Field

The conduction band profile resulting from the application of a 0.5 V bias across a structure consisting of a 50 nm AlInAs barrier, a 100 nm InGaAs quantum well doped with an electronic density of $N_v = 1.7\times10^{19}\,\mathrm{cm}^{-3}$, and a 50 nm AlInAs barrier is plotted in the inset of Fig. 5.3a. The potential is calculated as the self-consistent solution to the coupled Schrödinger-Poisson equations in the constant effective mass approximation using nextnano, considering InGaAs contact layers doped with an electronic density of $N_v = 2\times10^{18}\,\mathrm{cm}^{-3}$ on either side of the structure. The final electronic states, for which the square moduli are plotted, were calculated considering nonparabolicity using a three-band $\mathbf{k}\cdot\mathbf{p}$ model for the effective mass.

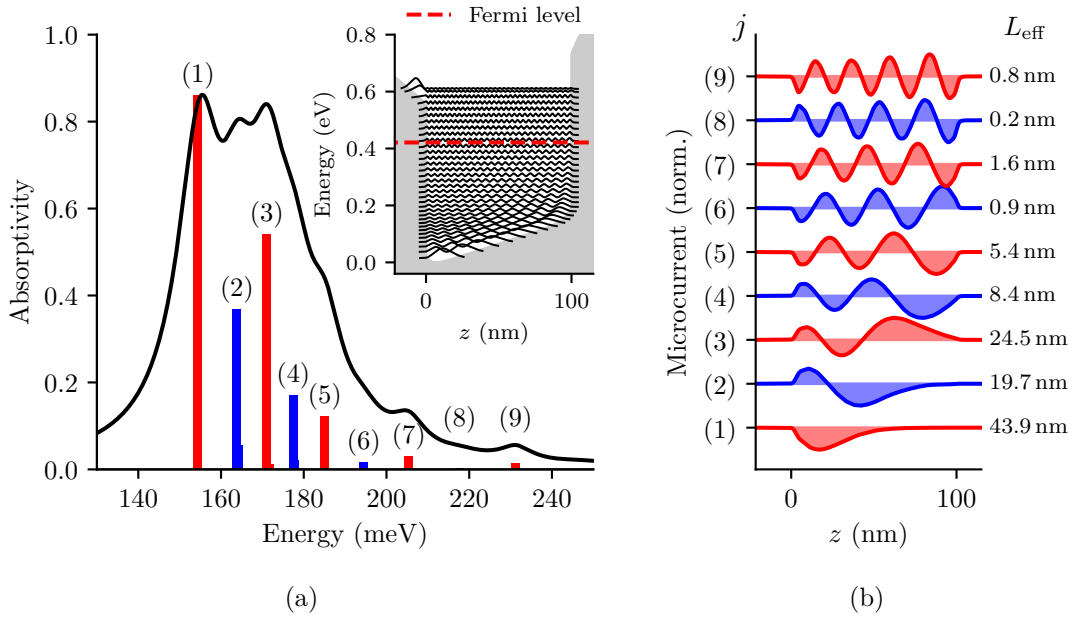

Fig. 5.3 (a) The absorptivity spectrum and the normalized oscillator strengths of the collective modes are plotted for the biased quantum well shown in the inset. (b) The collective microcurrents corresponding to the modes of (a) are plotted along the growth direction.

In the main panel of Fig. 5.3a, the absorptivity spectrum of the biased 100 nm well calculated with the quantum model is plotted. The absorptivity is calculated for a 30° angle of incidence, for a gold layer next to the structure, and for nonradiative linewidths of 9 meV. The oscillator strengths of the collective modes are plotted with bars beneath the spectrum at the energies of the modes. The modes are indexed one through nine with increasing energy. In Fig. 5.3b, the microcurrents of the collective modes are plotted along the growth direction, indexed to correspond with the modes indicated in (a).

The microcurrents plotted in red, indexed with odd-j, have an odd number of lobes and an even number of nodes, and thus resemble the microcurrents of the bright modes of a square well in the absence of a bias. The bias has the effect of distorting the sinusoidal shape of the microcurrents. As a consequence, the oscillator strength of the modes does not scale with j^{-2}, as it does for a square well without a bias. Compared to the square well without a bias, the $j = 1$ mode has a reduced oscillator strength and effective length, and $j = 3$ mode has an increased oscillator strength and effective length.

The microcurrents plotted in blue, indexed with even-j, have an even number of lobes and an odd number of nodes. In a square well without an applied bias, collective modes with this symmetry have zero oscillator strength (are dark), as the integral of the microcurrent is exactly zero. With the applied bias, the positive and negative lobes of the microcurrent no longer perfectly cancel, and these modes acquire nonzero oscillator strength, as indicated with the blue bars in (a).

This demonstrates that by breaking the square well symmetry, the oscillator strength of the collective modes can be redistributed. Most strikingly, modes which are strictly dark in a symmetric square well can be made bright with the breaking of the symmetry under an applied bias.

5.3 Plasmons in a Step Well Potential

In this section, the collective modes of step well structures, like that shown in the transmission electron microscope (TEM) image of Fig. 5.4a, are studied experimentally and theoretically. The step potential structures are realized with the growth of a 50 nm quarternary $Al_xGa_yIn_{1-x-y}As$ layer next to a 50 nm InGaAs layer, between AlInAs barriers, lattice matched to InP. Both the InGaAs and quaternary layers are doped with an electronic density N_v.

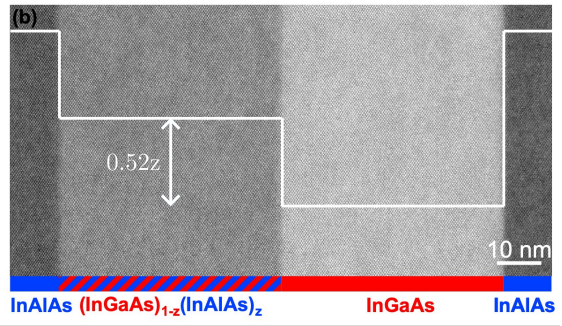

(a)

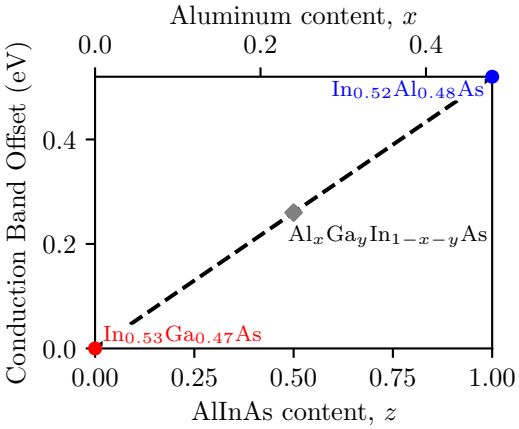

(b)

Fig. 5.4 (a) A TEM image of an epitaxially grown step structure is shown, with a sketch of the step potential. The TEM image was acquired by Konstantinos Pantzas. (b) The conduction band offset of the quaternary layer is plotted as a function of the aluminum content, x, and AlInAs content, z.

By varying the aluminum content, x, of the quaternary layer, the height of the step with respect to the bottom of the InGaAs conduction band can be varied between zero and the 0.52 eV conduction band offset of the lattice-matched InGaAs/InAlAs heterojunction, as shown in Fig. 5.4b. The quaternary may equivalently be written $(\mathrm{InGaAs})_{1-z}(\mathrm{InAlAs})_z$, in which case z determines the height of the step. The step height is plotted in Fig. 5.4b using a linear interpolation between the ternary endpoints, a good approximation considering the small bowing parameter of the quaternary [142].

The quaternary layer can be modeled with a repeating series of tunnel-coupled ternary quantum wells. A quaternary layer with InAlAs fraction z is modeled with alternating InGaAs layers of width $(1-z)p$ and InAlAs layers of width zp where p is the width of the well/barrier period. In this chapter, quaternary regions are modeled in band structure calculations with repeating 2 nm periods of ternary wells and barriers.

All of the step well structures studied in this chapter were grown by Metal Organic Chemical Vapor Deposition (MOCVD) on an InP substrate by the team of Grégoire Beaudoin, Konstantinos Pantzas, and Isabelle Sagnes at the Centre de Nanosciences et Nanotechnologies (C2N) in Palaiseau, France.

5.3.1 Experimental Study of Varying Fermi Level

Two step well structures were grown with the same InAlAs content of $z = 0.375$ in the quaternary layer but with different nominal electronic densities of $N_\mathrm{v} = 2\times10^{18}\,\mathrm{cm}^{-3}$ (sample V0388) and $N_\mathrm{v} = 2\times10^{19}\,\mathrm{cm}^{-3}$ (sample V0389). The InAlAs content was experimentally determined from high-angle annular dark-field scanning transmission electron microscopy (HAADF-STEM) images by Konstantinos Pantzas.[1]

The two different electronic densities were chosen so that the Fermi level would lie below the step in sample V0388, and above the step in sample V0389. When the Fermi level is below the step, the electrons are confined to a square-like potential and a single collective mode is expected. A dramatic change in the spectrum is observed when the Fermi level is above the step, as we now show.

Experimental transmission spectra of the two samples are shown in Fig. 5.5. The spectra were measured at room temperature for p-polarized light incident at Brewster's angle. The spectra have been normalized with only the p-polarized transmission spectra of a region of the substrate where the step well structure has been etched away.

The spectrum of the lower doped sample has a single feature around 100 meV, while the spectrum of the higher doped sample has two resonant features of similar amplitude at 140 meV and 170 meV. This demonstrates a remarkable quantum engineering of the collective electronic response which is strikingly different from the square well case, and which cannot be described with the classical Drude model of the electron gas.

The absorptivity of the lower energy mode of the V0389 sample cannot be accurately extracted from Brewster's angle transmission spectra as 1 − Transmission, because it sits below the reflective edge of the higher energy mode. The specular reflection would need to be collected to determine the experimental absorptivity of this mode.

[1] As shown in the growth sheets on Pages 195 and 196, the step region of samples V0388 and V0389 was originally intended to be realized with a digital alloy of alternating 1 nm barriers and wells. The HAADF-STEM analysis revealed a continuous quaternary region was actually grown.

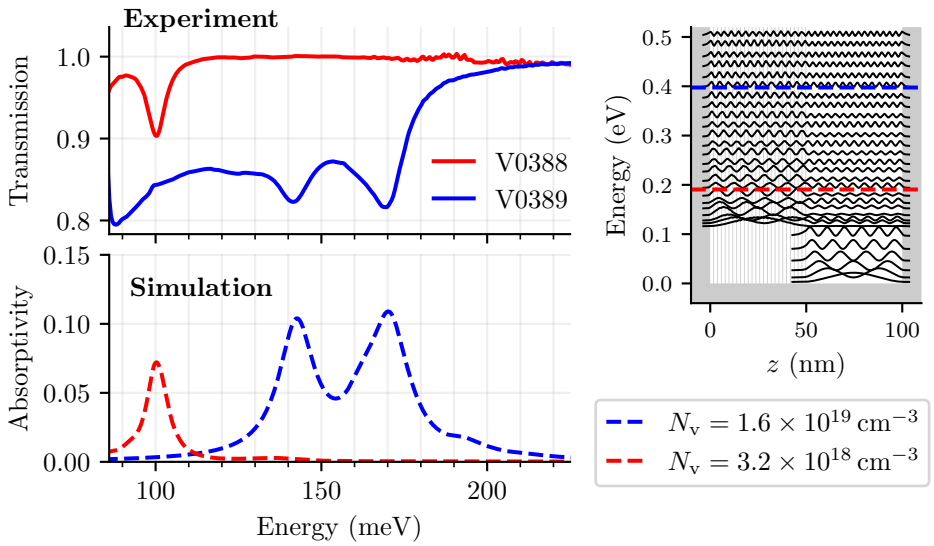

Fig. 5.5 Experimental 18° p-polarized transmission spectra measured at room temperature and normalized by a substrate reference are plotted in the upper panel. Absorptivity spectra calculated for the same conditions are plotted in the lower panel. The Fermi levels corresponding to the electronic densities used for the simulations are indicated on the step well potential.

Simulated absorptivity spectra, plotted in Fig. 5.5, were calculated for a step height fixed by $z = 0.225$, and for electronic densities of $N_v = 3.2 \times 10^{18}\,\mathrm{cm}^{-3}$ and $N_v = 1.6 \times 10^{19}\,\mathrm{cm}^{-3}$. The spectra were calculated using the quantum model for an 18° angle of incidence, with nonradiative linewidths of $\gamma_{NR} = 5\,\mathrm{meV}$ and $\gamma_{NR} = 12\,\mathrm{meV}$ for the lower and higher doped samples, respectively. The step potential, the square moduli of the calculated wavefunctions, and the two Fermi levels determined from the simulations are plotted in the right panel of Fig. 5.5. For $z = 0.225$, the step height is 116 meV.

The calculated Fermi level of the V0388 sample actually sits above the step, and consequently, two collective modes are predicted by the simulation. However, the lower energy mode (not shown) sits below the cut off of the MCT detector, and is therefore not observed in the experiment.

The energies of the plasmon modes and the nonradiative linewidths used in the modeling correspond to quality factors of $Q = 20$ for the 100 meV mode of the V0388 sample, and $Q \approx 13$ for the 140 meV and 170 meV modes of the V0389 sample. The reduction in the quality factor could be attributed to increased scattering in the quaternary region of the structure, since the collective mode of the lower doped sample is largely confined to the ternary well below the step.

The InAlAs content reported from the simulations is underestimated because the influence of static charge effects on the electronic potential has not been considered. These effects are shown in Section 5.3.3 to lower the step height. This explains the larger value of z determined from the HAADF-STEM images as compared with the value of z extracted from the simulations.

5.3.2 Experimental Study of Varying Step Height

To study the collective modes of the step well structure as a function of the step height, a series of samples was grown in which the nominal InAlAs fraction of the quaternary region was varied between $z = 0.25$ and $z = 0.60$. The step well region of each sample was nominally doped with an electronic density of $2 \times 10^{19}\,\mathrm{cm}^{-3}$. A summary of the samples is found in Table 5.1. The sample growth sheets can be found on Pages 197 to 200.

	z		N_v	
Sample	Nominal	Experimental	Nominal	Experimental
V0588	0.25	0.13	$2 \times 10^{19}\,\mathrm{cm}^{-3}$	$1.73 \times 10^{19}\,\mathrm{cm}^{-3}$
V0589	0.40	0.23	$2 \times 10^{19}\,\mathrm{cm}^{-3}$	$1.58 \times 10^{19}\,\mathrm{cm}^{-3}$
V0390	0.48*	0.30	$2 \times 10^{19}\,\mathrm{cm}^{-3}$	$1.50 \times 10^{19}\,\mathrm{cm}^{-3}$
V0590	0.60	0.35	$2 \times 10^{19}\,\mathrm{cm}^{-3}$	$1.40 \times 10^{19}\,\mathrm{cm}^{-3}$

* This value was determined from high-angle annular dark-field scanning transmission electron microscopy (HAADF-STEM) images by Konstantinos Pantzas. From the same images, the InGaAs and quaternary layers of this sample were determined to be 65 nm and 61 nm thick. These dimensions are used in the simulations of this sample.

Table 5.1: Summary of samples with varying step height. Recall z indicates the InAlAs fraction of the quaternary according to $(\mathrm{InGaAs})_{1-z}(\mathrm{InAlAs})_z$.

The samples were investigated with room temperature transmission measurements at Brewster's angle, the results of which are shown in Fig. 5.6. The values of z indicated in the legend are extracted from modeling of the experimental spectra. Two resonances can be observed in each spectrum. The higher energy resonance is hardly affected by variations in the step height. It is always centered at 169 meV with near constant amplitude. On the contrary, the lower energy resonance redshifts and decreases in amplitude with increasing step height. For convenience, we denote the higher energy mode as $\mathrm{P_T}$ and the lower energy mode as $\mathrm{P_Q}$, where T and Q refer to ternary and quaternary for reasons which will become apparent.

The experimental transmission spectra have been normalized according to the procedure described in Section 2.1.1, and are additionally normalized to one at 200 meV. The diverging baselines of the spectra at low energies are a consequence of the normalization, as detailed in Section 2.1.3.

Simulated absorption spectra are shown in the bottom panel of Fig. 5.6. The values of the InAlAs fraction in the quaternary layer and the electronic density used in the simulations to model the experimental spectra are compared with the nominal values in Table 5.1.

The electronic densities extracted from the modeling of the experimental spectra systematically decrease with increasing InAlAs fraction, z. This is attributed to an increase in the ionization energy for dopants in the quaternary layer with increasing step height, since as the step height is increased, the energy difference between the impurity band and the conduction band minimum of the quaternary layer is increased.

The InAlAs fraction extracted from the modeling of the experimental spectra is always lower than the nominal value. This is attributed to the fact that static charge effects have

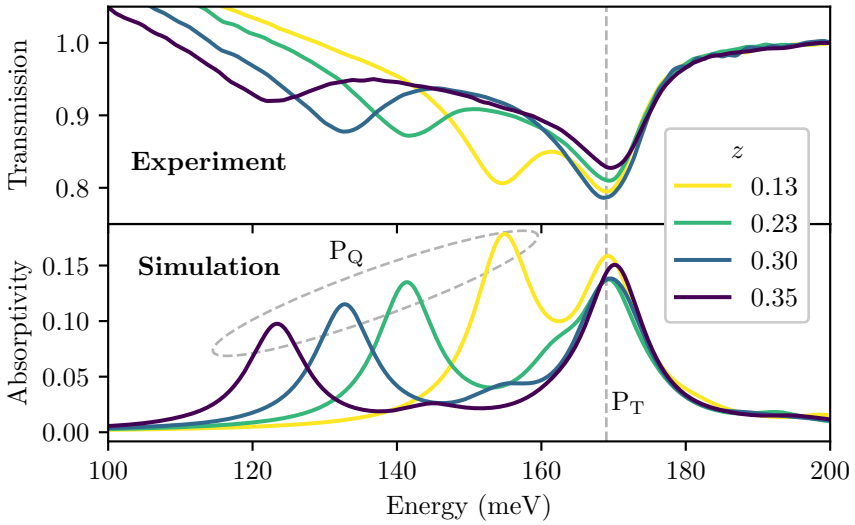

Fig. 5.6 Experimental 18° transmission spectra measured at room temperature are plotted in the upper panel. Absorptivity spectra calculated for p-polarized light incident at 18° are plotted in the lower panel using the InAlAs content indicated in the legend, the value of N_v reported in Table 5.1 under Experimental, and a nonradiative linewidth of $\gamma_{NR} = 9\,\text{meV}$.

not been taken into account in the band structure calculation. This point is considered in greater detail in Section 5.3.3.

For each pair of z and N_v for which the experimental spectra are modeled, the Fermi level is found to be at the same energy, 0.398 eV above the InGaAs conduction band minimum, in the band structure calculations. Because the electronic density of states decreases with increasing z, the electronic density must be reduced in the simulations to keep the Fermi level constant.

Let us denote the difference between the Fermi level and the InGaAs conduction band minimum as Δ_T and the difference between the Fermi level and the quaternary conduction band minimum as Δ_Q, as sketched in Fig. 5.7. The values of Δ_T and Δ_Q independently fix the energies of the P_T and P_Q modes in the step well spectra for a constant Fermi level. With varying z, Δ_T remains constant, explaining the constant energy of the P_T resonance. On the contrary, Δ_Q decreases with increasing z, resulting in the redshift of the P_Q mode.

This suggests that the lower energy mode is localized in the quaternary side of the step well, and the higher energy mode is localized in the ternary side of the step well. This is confirmed with a microscopic description of the current density of each mode in Section 5.3.4.

The P_T and P_Q modes of the step well structure can be modeled by separate 50 nm InGaAs/AlInAs and $(InGaAs)_{1-z}(InAlAs)_z$/AlInAs quantum wells, respectively, when the Fermi level in each well is set by Δ_T and Δ_Q. This is demonstrated in Fig. 5.8 for the lower energy mode of the step well structure. The experimental energies of the P_T and P_Q modes are plotted in black as a function of the InAlAs content in the quaternary layer of the step. In red, the calculated Berreman mode energies for the 50 nm quaternary well with Fermi level set by Δ_Q are plotted. The energies of the modes calculated for the 50 nm quaternary

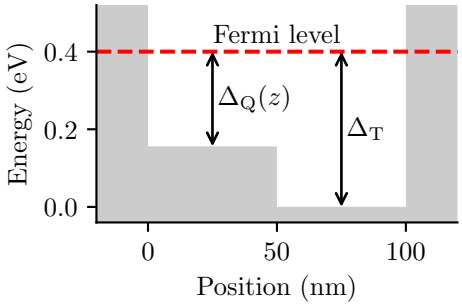

Fig. 5.7 The quantities Δ_T and Δ_Q are defined for a constant Fermi level. The dependence of Δ_Q on the InAlAs content z is made explicit.

well reproduce almost exactly the experimentally observed energies.

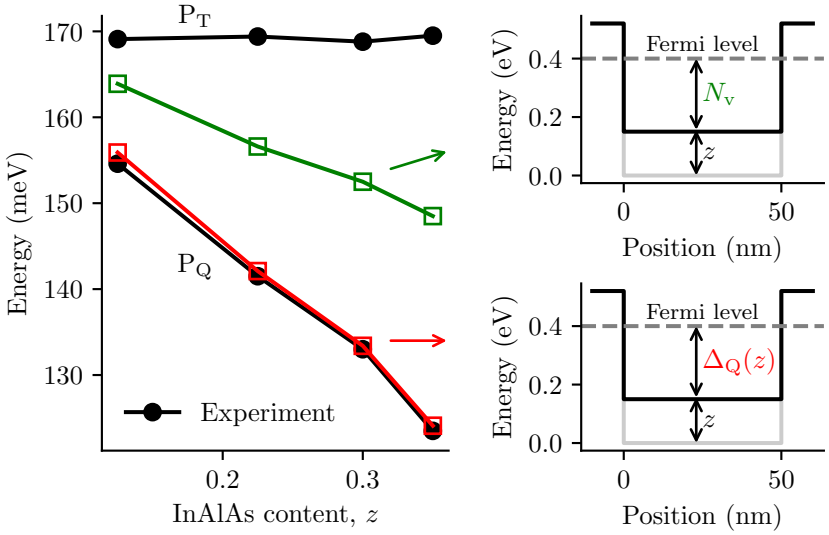

Fig. 5.8 In black, the experimental P_T and P_Q energies are plotted as a function of the InAlAs content in the step. In red, the Berreman modes of a 50 nm quaternary well, calculated for the same Δ_Q as the step well structure, as sketched on the bottom right, are plotted for varying z. In green, the Berreman modes of a 50 nm quaternary well, calculated using the electronic density of the step well structure as sketched in the upper right, are plotted for varying z.

The step well structures consist of two material layers with different effective masses. Therefore, it interesting to ask if the two collective modes of the step well can be described classically by considering a separate plasma energy for each side of the well.[2] This corresponds to describing the step well with separate 50 nm quantum wells with the same

[2]Recall that the Berreman mode of a wide quantum well can be described classically, considering only the Drude model and a thin film geometry, in which case the mode is resonant at the plasma energy.

electronic density for each side of the step.

The green curve of Fig. 5.8 demonstrates that it is not possible to describe the modes of the step well in this way. The green curve shows the Berreman mode energies of a 50 nm quaternary well calculated using the values of N_v extracted from the experiment as the quaternary content is varied. The curve is shifted to significantly higher energy with respect to the experimental P_Q modes (black).

As already observed, the experimental modes can be reproduced when Δ_Q is fixed in the 50 nm quaternary well (red). However, fixing Δ_Q requires a different electronic density than that of the full step structure, which is nonphysical. We conclude that a quantum description is necessary to model the collective modes.

5.3.3 Static Charge Effects on Step Potential

When the electronic charge distribution is not identical to the charge distribution of the donor ions, an electrostatic potential arises (see Section 1.2.2.1). In the step well structures, which are nominally uniformly doped, the electronic charge density is greater on the deeper side of the well. Consequently, static charge effects are significant.

In Fig. 5.9a, the step potential for an InAlAs fraction of $z = 0.60$ is plotted in gray, neglecting charge effects. The potential found as as the self-consistent solution to the coupled Schrödinger and Poisson equations is plotted in black. The self-consistent solution was calculated with nextnano using an 8-band $\mathbf{k} \cdot \mathbf{p}$ model for the effective mass and considering a volume electron density of $N_v = 1.75 \times 10^{19}\,\mathrm{cm}^{-3}$. The charge effects result in a significant lowering of the step height from 0.312 eV to 0.207 eV.

In the experimental studies reported above, the InAlAs fraction was extracted from simulations in which charge effects were neglected. When neglecting charge effects, the InAlAs fraction must be underestimated to have the correct Δ_Q to correctly reproduce the energy of the lower energy step well mode.

In Fig. 5.9b, the InAlAs fraction z extracted from modeling of the experimental spectra is compared with the nominal value of z (or the value of z determined by HAADF-STEM, indicated by empty markers), considering (red) and neglecting (blue) charge effects. When charge effects are neglected, the extracted value of z diverges away from the nominal value towards smaller values with increasing z. When charge effects are taken into account, the value of z extracted from the modeling of the experiment and the nominal value do not diverge, and instead offset by a small but constant amount.

The divergence between the nominal and extracted value of z with increasing z when charge effects are neglected implies that charge effects are increasingly important as the step height is increased. This is because the distribution of electronic charge becomes increasingly non-uniform as the step height is increased.

5.3.4 Microscopic Description of Step Potential Modes

In this section, the microscopic properties of the collective modes of the step well are investigated. We begin by more closely examining the calculated absorption spectra of the step well as a function of the step height. In the color plot of Fig. 5.10, the absorptivity of a 100 nm step well, calculated for an 18° angle of incidence and for a fixed Fermi level of 0.4 eV, is plotted on a logarithmic scale as a function of the InAlAs content in the quaternary side of the well.

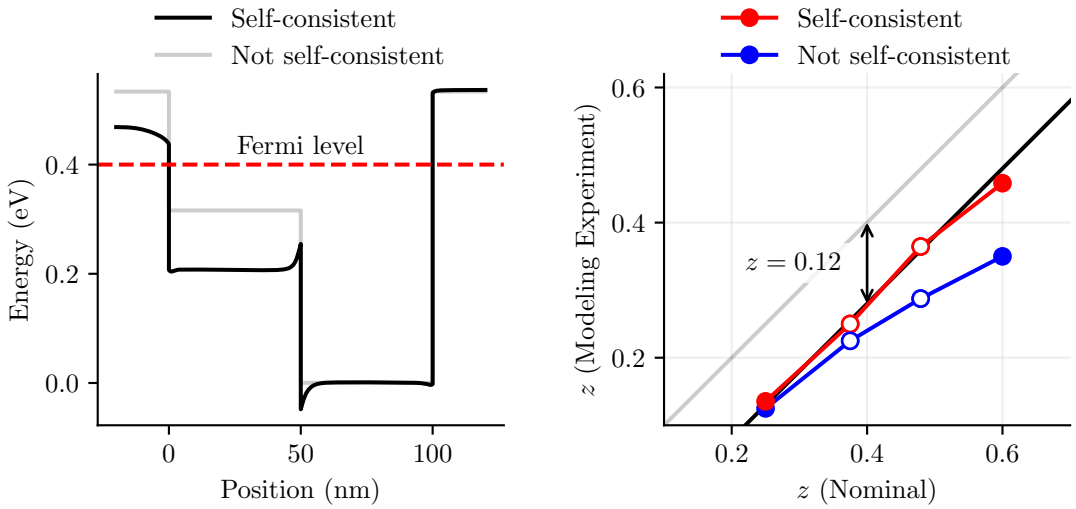

Fig. 5.9 (a) The step potential calculated self-consistently as the solution to the coupled Schrödinger and Poisson equations (black) is compared with the potential determined only by the conduction band offsets of the materials (gray). An InAlAs content of $z = 0.60$ and a volume charge density of $N_v = 1.75 \times 10^{19}\,\mathrm{cm}^{-3}$ were used in the calculation. (b) The InAlAs content z extracted from modeling of the experimental results is compared with the nominal value of z, or where indicated with empty markers, the value of z determined by HAADF-STEM.

The logarithmic scale permits three branches of modes to be identified in the color plot. The highest energy branch, marked with three blue dots, is nearly constant in energy as a function of z, and is identified as the $\mathrm{P_T}$ mode observed in the experiments of the previous sections. The mode is labeled as $\mathrm{P_T^{(1)}}$ on the color plot for reasons which will become clear. The lowest energy branch, marked with three red dots, redshifts with increasing z. This mode corresponds to the $\mathrm{P_Q}$ mode observed in the experiments, and is denoted $\mathrm{P_Q^{(1)}}$ on the color plot. A third branch of modes is observed between the two already identified branches. This mode, which is always approximately 24 meV above the $\mathrm{P_Q^{(1)}}$ mode, is labeled $\mathrm{P_Q^{(3)}}$. Due to its small oscillator strength, this mode was not observed in the experiments.

The InAlAs content, z, is varied from zero to 0.5 on the horizontal axis of the color plot. At $z = 0$, the step height is zero, and the structure is that of the 100 nm InGaAs/InAlAs quantum well sketched in Panel (b). The energies of the $j = 1$, 3, and 5 longitudinal modes of the 100 nm InGaAs/InAlAs quantum well are indicated on the left edge of the color plot in magenta. As $z \to 0$, the modes of the step well converge to the modes of the 100 nm well, as they must.

On the right side of the color plot where $z = 0.5$, the energies of the $j = 1$, 3, and 5 longitudinal modes of the 50 nm quaternary well sketched in Panel (c), with $z = 0.5$ and with a Fermi level set by $\Delta_Q = 0.14\,\mathrm{eV}$, are indicated. Likewise, the $j = 1$ (Berreman) mode of the 50 nm InGaAs/InAlAs quantum well sketched in Panel (d) is also indicated on the right edge of the color plot, in blue.

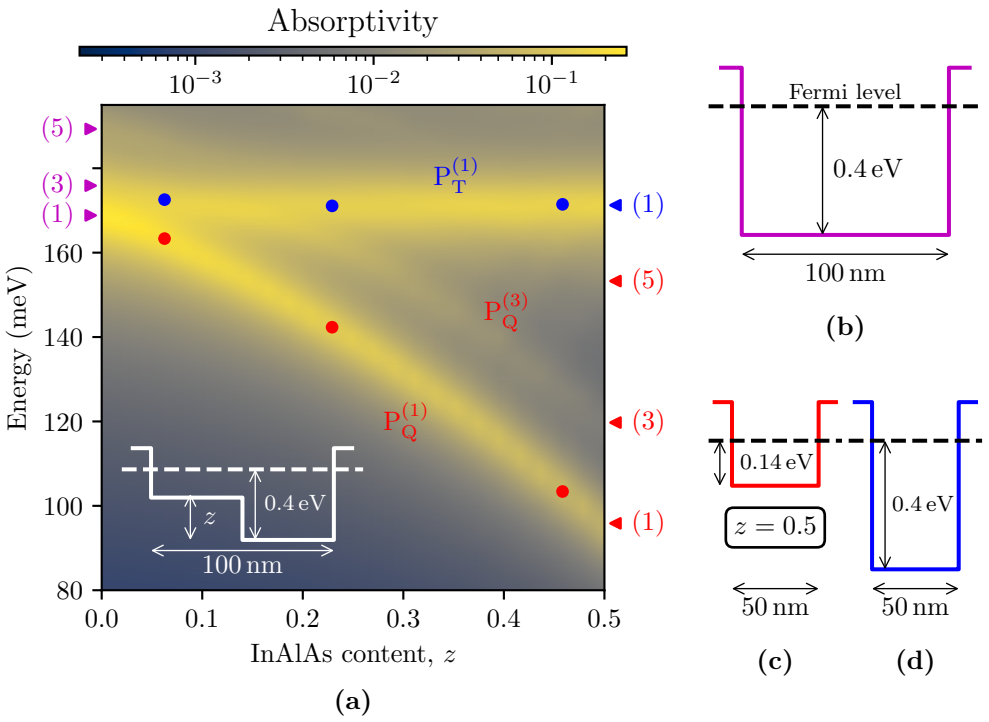

Fig. 5.10 (a) The calculated absorptivity of a 100 nm step well with a Fermi level of 0.4 eV (sketched in white) is plotted with a log scale color map as a function of the InAlAs content in the quaternary side of the well for an 18° angle of incidence. The magenta annotations on the left side of the color plot correspond to the modes of the 100 nm InGaAs/InAlAs quantum well sketched in (b). The red and blue annotations on the right side of the color plot correspond to the modes of the 50 nm $(InGaAs)_{0.5}(InAlAs)_{0.5}$/InAlAs quantum well sketched in (c), and the first mode of the 50 nm InGaAs/InAlAs quantum well sketched in (d). The microcurrents of the modes indicated with dots on the color map are plotted in Fig. 5.11.

The $P_Q^{(1)}$ and $P_Q^{(3)}$ modes of the step well converge to the $j = 1$ and $j = 3$ modes (red annotations) of the 50 nm quaternary well (Panel (c)), as the z content of the step approaches 0.5. The $P_T^{(1)}$ mode of the step well converges to the $j = 1$ mode of the 50 nm InGaAs/InAlAs well (Panel (d)). This suggests that the $P_Q^{(1)}$ and $P_Q^{(3)}$ modes and the $P_T^{(1)}$ mode are well localized, respectively, to the quaternary and ternary sides of the step well, and are thus spatially separated.

As the step height is decreased, the $P_Q^{(3)}$ mode blueshifts until it merges into the $P_T^{(1)}$ mode at approximately $z = 0.23$. The single mode at $z = 0.23$ results from the merging of two modes localized on different sides of the well, and is therefore delocalized across the entire step well. This interpretation is confirmed by the microcurrents which we now consider.

The microcurrents of the two modes of largest oscillator strength for $z = 0.06$, 0.23 and 0.46, corresponding to the modes indicated with blue and red dots on the color plot of Fig. 5.10, are plotted in Fig. 5.11. In Panel (a), the microcurrents of the two modes for $z = 0.06$ are

shown to be delocalized across the entire 100 nm step well, and are similar in form to the $j = 1$ and $j = 3$ modes of a 100 nm quantum well. Notably, the slight perturbation introduced by the small step breaks their symmetry in a similar manner to what was observed for the square quantum well under an applied bias in Fig. 6.1.

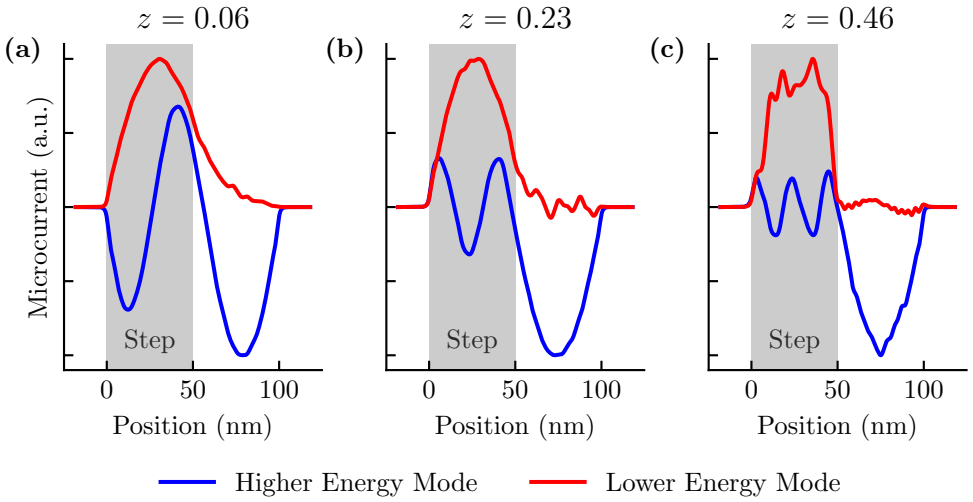

Fig. 5.11 The microcurrents of the modes corresponding to the blue and red dots on the color plot of Fig. 5.10 are plotted. The quaternary, or step, region of the step well is indicated with gray shading.

For $z = 0.23$ and $z = 0.46$, the lower energy mode, for which the red microcurrents are plotted in Panels (b) and (c), corresponds to the $\mathrm{P}_{\mathrm{Q}}^{(1)}$ mode. The microcurrents of this mode are almost completely localized to the quaternary side of the step well. The localization of the microcurrent to the quaternary region is slightly more strict for the larger step height, $z = 0.46$.

The higher energy mode for $z = 0.23$ is the mode at the intersection of the $\mathrm{P}_{\mathrm{Q}}^{(3)}$ and $\mathrm{P}_{\mathrm{T}}^{(1)}$ modes. The microcurrent of this mode (blue curve in Panel (b)) is delocalized across the entire step structure. It has the form of a $j = 3$ mode over the quaternary side of the step well and the form of a $j = 1$ mode over the ternary side of the step well, indicating that it results from a *hybridization* [52, 108, 143] of spatially separated modes.

A similar phenomenon is observed for the microcurrent of the higher energy mode at $z = 0.46$ (blue curve in Panel (c)). The microcurrent has the form of a $j = 5$ mode over the quaternary region of the structure and a $j = 1$ mode over the ternary region of the structure. The mode results from the hybridization of the $j = 5$ mode of the quaternary side and the $j = 1$ mode of the ternary side of the step well structure.

The hybridization picture can also describe the form of the microcurrent of the higher energy mode for $z = 0.06$ (blue curve in Panel (a)). This mode was described above as a $j = 3$-like mode of a perturbed 100 nm square well. A closer look at the microcurrent reveals that there is a node at approximately the center step of the well. As a result, this mode can be interpreted as resulting from the hybridization of a dark $j = 2$ mode from the quaternary side with a bright $j = 1$ mode from the ternary side of the step well.

The spatial distribution of the microcurrents for the $z = 0.23$ and $z = 0.46$ cases confirms

that the modes of the step well are well described as arising from separate 50 nm quaternary and ternary square quantum wells. This description must become increasingly inaccurate as $z \to 0$. This is seen in the decreasing localization of the microcurrent of the lower energy mode (red curve) in Fig. 5.11 as z is decreased from 0.46 to 0.06. To better quantify the influence of the step height on the spatial extent of the modes, the effective lengths L_{eff} of the first two modes of largest oscillator strength are plotted in Fig. 5.12.

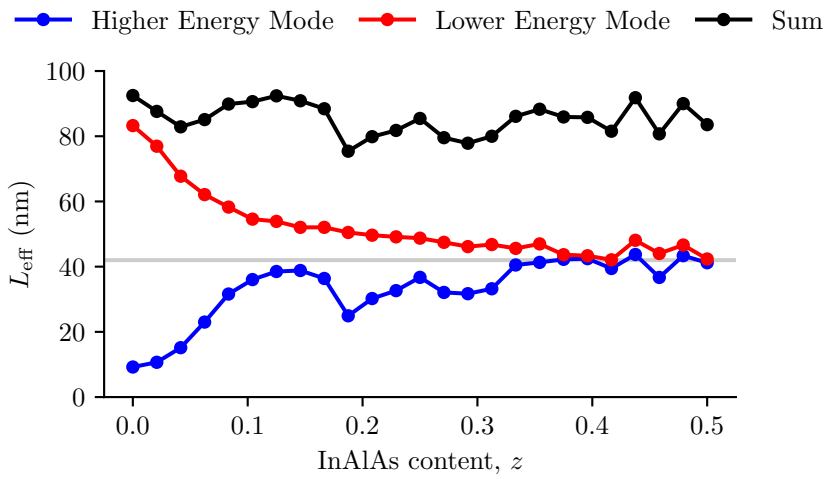

Fig. 5.12 The effective length of the first two modes of largest oscillator strength for a 100 nm step well structure with Fermi level of 0.4 eV are plotted as a function of the InAlAs content in the step side of the well. The effective length of both modes approaches 42 nm, indicated with grey line, as z is increased.

For $z = 0$, the higher energy mode is the $j = 3$ mode of a 100 nm square well and the lower energy mode is the $j = 1$ mode of a 100 nm square well. As z is increased, the effective length of the lower energy mode rapidly decreases while that of the higher energy mode rapidly increases. For both modes, the effective length approaches 42 nm for large z. Already, for z slightly larger than 0.1, the two modes have comparable effective lengths close to 50 nm. The smallest z of the step wells experimentally investigated in Section 5.3.2 was extracted as 0.15, which explains why the two separate well model so accurately described the results.

5.4 Conclusion

In this chapter, the microscopic model introduced in Chapter 4 was exploited to study ways in which the static electronic potential can be designed to engineer the collective electronic response. Three studies were presented in which the collective response was engineered with dramatic effect.

In the study of the tunnel-coupled quantum well structure, the coupling between transitions which normally do not couple was engineered. In the studies of a quantum well under an applied electric field and the step well, breaking of the square well symmetry was demonstrated to be a key element for engineering a novel collective response. Remarkably, in the

structure with the applied electric field, it was demonstrated that normally dark plasmonic modes could be made bright.

The practicality of collective mode engineering was demonstrated with the experimental study of step well structures. The hybridization of spatially separated plasmons was demonstrated to occur when the modes are of the same energy. This feature can be used to tailor the spatial extent of the collective mode polarization. An enticing future study could be to investigate the spatial hybridization of the plasmon modes with other matter polarizations external to the semiconductor sample, introduced close to the surface.

Chapter 6

Berreman Mode Photodetectors

In this chapter, photodetector devices are investigated in which the Berreman mode of a heavily doped quantum well is used as the photoabsorber. The first observation of photocurrent from a Berreman mode excitation is reported. The study is interesting from a fundamental point of view because of the collective nature of the Berreman mode excitation.

Photodetection involves both the absorption of incident photons and the transport of photoexcited carriers. In most commonly studied photodetectors, the absorption of a photon coincides with the transition of an electron between two single particle states. The subsequent transport problem is well defined as the state of the excited carrier is known. This is the case for the well-known unipolar intersubband Quantum Well Infrared Photodetector (QWIP) [33, 71, 97, 111, 114] and Quantum Cascade Detector (QCD) [14, 47, 58]. As an example, the bound-to-continuum transition typically employed in a QWIP is sketched in Fig. 6.1a. An electron is excited from its initial bound state E_0 to a quasi-bound state in the continuum just above the barrier. With the application of an electric field, the electron can be collected.

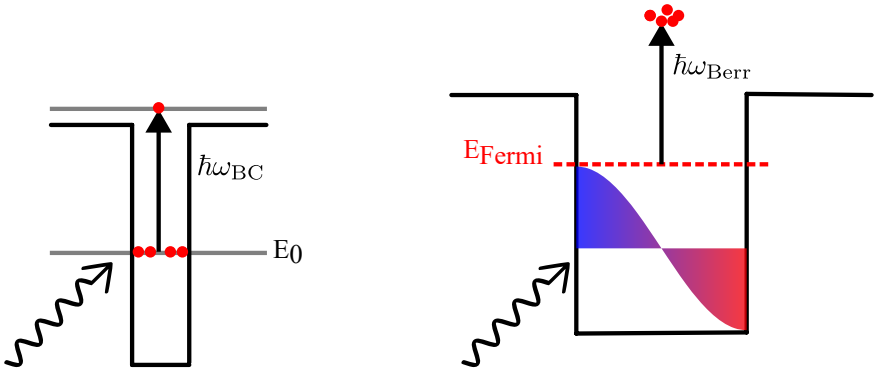

(a) A *single particle* transition.

(b) A *collective* excitation.

Fig. 6.1 The typical bound-to-continuum transition scheme employed in a QWIP is sketched in (a). A photon of energy $\hbar\omega_{BC}$ excites an electron initially in the bound states E_0. For the collective excitation sketched in (b), while the excitation energy $\hbar\omega_{Berr}$ is known, it is not obvious at which energy the population of excited carriers lies after the excitation. In the sketch, the energy of the excited carrier population has been assumed to lie at $E_{Fermi} + \hbar\omega_{Berr}$.

Because the Berreman mode is a collective excitation, the absorption of a photon by the mode cannot be indicated on a band diagram as a transition between single particle electronic states. The collective nature of the excitation was made explicit in the quantum mechanical description of Chapter 4, where the mode was demonstrated to arise from the dipole-dipole coupling of all the allowed single particle transitions.

It is possible to indicate on a band diagram the population of out-of-equilibrium electrons, or *hot carriers*, which result from the decay of the collective excitation. However, the energy distribution of the hot carrier population is not easily known. This is a serious problem for designing a photodetector.

In Fig. 6.1b, hot carriers resulting from the excitation of a Berreman mode are sketched at the energy of the excitation *above the Fermi level*. It is one of the goals of our study to investigate if this physical pictures accurately describes the Berreman mode photodetection phenomenon. More generally, we are motivated to understand how a collective bosonic excitation scatters into a single-particle fermionic current.

6.1 Background: Plasmonic Photodetectors

The use of a collective excitation as the absorption mechanism in a photodetector is not a new concept: these type of detectors are usually called plasmonic photodetectors. They have been extensively studied in the short-wave infrared spectral range [21, 48, 49, 51, 67, 90], and always exploit *surface* plasmon resonances.

It is important to distinguish between two types of plasmonic photodetectors [38]: those in which the metal itself constitutes the absorber, and those in which the metal provides an electromagnetic enhancement for another absorber [95, 96, 112, 122]. (In both cases, the metal is understood to support a plasmon resonance). Here, we are concerned only with the first type.

A figure from one of the pioneering works [67] in which this concept was introduced is reproduced in Fig. 6.2, and provides a clear illustration of the concept underlying these type of detectors. In this work, gold nanoantennas supporting localized surface plasmon resonances were used to concentrate and absorb the incident light. Surface plasmons are resonantly excited upon illumination, and decay into energetic hot-carriers, electrons which are out of equilibrium with the electron bath. Some of the hot carriers are injected over a Schottky barrier which forms at the interface between the Au and semiconductor surface on which the antennas were fabricated, resulting in a photocurrent. The detector thus operates as an internal emission Schottky photodiode, but for which the strong absorption characteristics of the plasmon mode are exploited.

The theoretical description of an internal emission plasmon photodetector requires the understanding of the hot carrier generation process, as well as a model for the internal photoemission process in which the hot carriers are collected. The generation of the hot-carriers is understood to result from Landau damping of the plasmonic excitation [65, 73] and occurs on the femtosecond time scale [17].

Perhaps the simplest and most commonly used description of the internal emission process is given by the Fowler law, derived under the assumption that photoexcited hot carriers have an isotropic momentum distribution, and that only the subset of hot carriers which have sufficient momentum and energy in the correct direction are collected [44, 111]. Later, a fuller

Fig. 6.2 A gold nanoantenna which supports a localized surface plasmon resonance is used as an optical detector. The gold nanoantennas are fabricated on Si, and the metal-semiconductor interface is exploited to realize an internal emission photodetector in which hot carriers resulting from the decay of the plasmon resonance are collected over the Schottky barrier, ϕ_{B}, giving rise to a photocurrent. Figure reproduced from [67].

description of the photoemission process was introduced by Spicer [123, 124] who described the phenomenon in three steps: photoexcitation of electrons (the hot carrier distribution), the motion of electrons through the crystal (transport), and finally the escape of the electrons over a barrier (collection).

The detailed description of these processes is beyond the scope of this section. A concise review of the hot carrier physics involved in plasmon-based hot electron photodetection can be found in [72], and a more comprehensive review on plasmon-induced hot carrier science and technology can be found in [17].

We conclude this section by highlighting the novelty of the present work. In the experiments which follow, we demonstrate the first plasmonic photodetector using a Berreman mode as the collective excitation. To the best of our knowledge, our experiment is the first in which a volume plasmon, rather than a surface plasmon, is used as the absorber in a plasmonic photodetector. Furthermore, our demonstration is the first in which the plasmonic photodetector concept is implemented in the long wavelength infrared.

The most important aspect of the work, however, is that we provide the first demonstration of a plasmonic photodetector in a mature III-V semiconductor platform. Consequently, all of the tools of quantum band structure engineering can be employed to aide in the investigation of the fundamental physics behind the phenomenon.

6.2 Description of Experiment

6.2.1 Samples

In this chapter, two InGaAs/AlInAs samples which host Berreman modes are investigated as photodetectors. In both samples, a highly doped ($\sim 2 \times 10^{19}\,\mathrm{cm}^{-3}$) InGaAs layer which supports a Berreman mode is grown between two AlInAs barrier layers. Less doped ($\sim 2 \times 10^{18}\,\mathrm{cm}^{-3}$) InGaAs layers are grown on either side of the structure so that the devices can be ohmically contacted.

Sample V0386 was designed with a 84.4 nm AlInAs lower barrier, a 100 nm heavily doped InGaAs layer, and a 30 nm AlInAs upper barrier. The layers were grown via MOCVD in the order described, on an InP substrate (see the growth sheet on Page 202). The growth was performed by the team of Grégoire Beaudoin, Konstantinos Pantzas, and Isabelle Sagnes at the Centre de Nanosciences et Nanotechnologies (C2N) in Palaiseau, France.

Because of the large electronic densities in the structure ($N_\mathrm{v} = 2 \times 10^{19}\,\mathrm{cm}^{-3}$), static charge effects must be considered to properly calculate the band structure and describe the device operation. In Fig. 6.3, the band structure calculated as the self-consistent solution to the coupled Schrödinger-Poisson equations in the constant effective mass approximation is plotted.

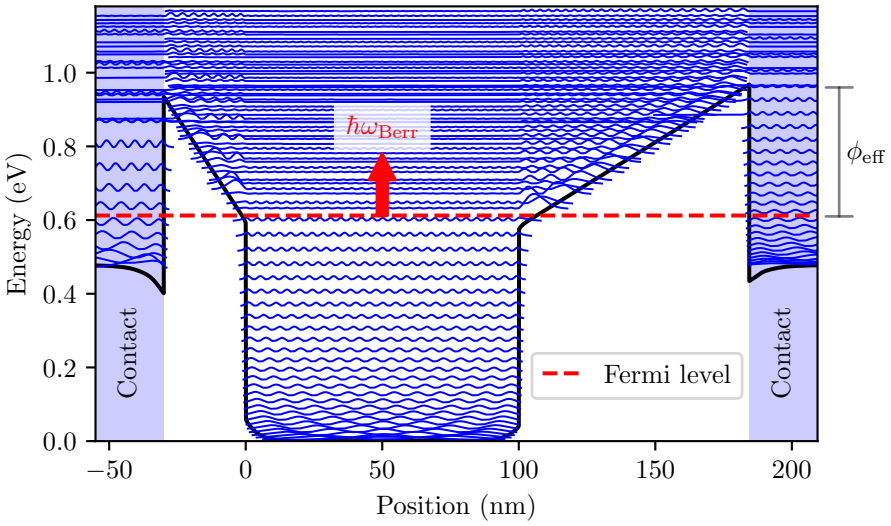

Fig. 6.3 Single-band Schrödinger-Poisson solution for the band structure of the nominal V0386 sample calculated with nextnano for $N_\mathrm{v} = 2 \times 10^{19}\,\mathrm{cm}^{-3}$.

Because the Fermi level must be constant across the structure at equilibrium, the less-doped contact regions and barriers on either side of the main InGaAs well bend upwards. Consequently, the effective potential barrier ϕ_eff that an electron at the Fermi level must overcome to travel to a contact region is set by the energy difference between the barrier edge and the Fermi level in the contacts.

If the plasmonic excitation decays into a population of electrons at an energy $\hbar\omega_\mathrm{Berr}$ above the Fermi level (sketched with the red arrow in the figure), it is evident that a bias will need to be applied to the device to collect the electrons (observe a photocurrent).

In the above band structure calculation, we have settled for a solution calculated in the single band, constant effective mass approximation simply because it is difficult to find a converging self-consistent solution considering the coupling between 8 bands for such a wide and heavily doped quantum well as the one we study here. Because nonparabolicity is significant in InGaAs, the resulting band structure should not be relied on for quantitative predictions. It does, however, describe the correct qualitative picture.

Sample G0662 was designed to be symmetric: 50 nm AlInAs barrier layers were grown before and after a 200 nm InGaAs layer.[1] A large electronic density was added to a 180 nm thick region centered in the 200 nm InGaAs layer, so that 10 nm not-intentionally-doped InGaAs layers lie between the heavily doped region and the barriers. These not-intentionally-doped layers are included in order to limit the unintentional incorporation of dopants into the AlInAs barrier regions, a problem which arose in the study of the V0386 sample. The sample was grown via molecular beam epitaxy (MBE) on an InP substrate (see the growth sheet on Page 206) by Lianhe Li, Edmund Linfield, and Giles Davies at the University of Leeds.

We note here that results from the study of additional plasmon detector samples are reported in Appendices B and C.

6.2.2 Photovoltage Measurements

The V0386 and G0662 samples are processed into circular mesa devices 100 µm in diameter. To couple light into the devices at the angles for which the maximum absorptivity occurs, facets are mechanically polished onto the InP substrate (sketched in green in Fig. 6.4).

In the photodetection experiments, light from a Globar source inside a Fourier Transform Interferometer (FTIR) is focused with a 2" germanium F1 lens through a ZnSe window and through the polished facet onto the detector mesa. The devices are mounted onto a copper cold finger inside a continuous flow cryostat and are cooled with liquid helium to a temperature of 7 K.

Two types of measurements are performed with the set-up sketched in Fig. 6.4: (1) the total photodetected signal is measured as a function of the potential across the device, and (2) spectra of the photodetected signal are measured for a fixed potential.

In practice, the devices are biased with an applied current, I_{app} using a Keithley 2450 SourceMeter. In what follows, the resulting DC voltage V_{meas} is often referred to as the bias voltage, with the understanding that it is the current which is sourced.

The devices behave as photoconductors, so that their conductivity changes upon illumination. Because the current is fixed, it is a photo*voltage* signal that is measured upon illumination. In the discussion of the photoresponse of the devices, we often refer to photo*current* generation. This is not inaccurate. It is a choice of the experiment to measure the photovoltage for a fixed current, instead of the photocurrent for a fixed bias.[2]

[1] The wider 200 nm InGaAs heavily doped layer for the Berreman mode of the G0662 sample was chosen because the structure was designed to be inserted into a double metal optical cavity to study polariton modes (see Chapter 7). Increasing the ratio of the well width to the total structure thickness maximizes the overlap between the cavity mode and the Berreman mode excitation (see Section 7.1).

[2] The choice to source the current (I_{app}) rather than apply a voltage bias was made so that the SR560 *voltage* pre-amplifier could be used in the experiment. One might be tempted to apply a bias voltage and replace the SR560 voltage pre-amplifier in Fig. 6.4 with a transimpedance amplifier. However, the transimpedance amplifier amplifies a current signal, and since a voltage source has a low impedance, one would find that some

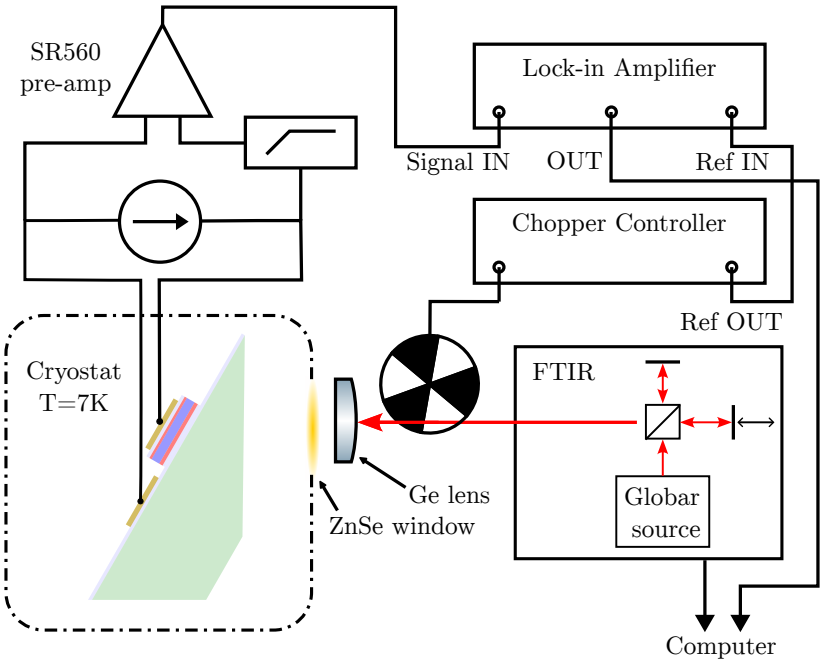

Fig. 6.4 The experiment for the photovoltage detection is sketched for the lock-in detection technique.

The incident light is modulated at 165 Hz using a mechanical chopper. The time-varying voltage response to the modulated light is amplified using a Stanford Research Instruments SR560 pre-amplifier. Built-in low-pass and high-pass filters from the SR560 pre-amplifier are employed: the high-pass filter cuts the DC bias, whereas the low-pass filter helps to limit the amplification of any high-frequency noise.

For the first type of measurement described above, the mirrors of the FTIR are fixed, and the magnitude and phase of the photovoltage signal is read from the lock-in amplifier as a function of the DC bias V_{meas}. Even using a relatively long (1 s) time constant for the lock-in measurement,[3] the signal and phase can still vary quite a bit. Rather than increasing the lock-in time-constant, the signal and phase are sampled over a period of time and averaged. The standard deviation of each set is calculated as a first indication of the level of noise present in the signal.

While the amplitude of the signal measured from the lock-in amplifier is strictly positive and phase-independent, changes in the phase with the bias can provide information regarding the direction of the current flow. The phase reported by the lock-in amplifier is the phase difference between the signal and reference oscillator: $\theta = \theta_{\text{sig}} - \theta_{\text{ref}}$. In Fig. 6.5, a sinusoidal

of the photocurrent goes to the voltage source instead of the transimpedance amplifier. While a commercial transimpedance amplifier designed with the correct circuitry to correctly measure the photocurrent with an applied voltage bias was available for the following experiments, the applied voltage had to be manually changed via a screw, and could not be controlled via a computer, as required to record continuous curves of the signal as a function of the potential across the device.

[3]The time-constant of the lock-in amplifier sets the low-pass filter bandwidth. Recall that the ideal lock-in output is a DC signal obtained by filtering the AC components from the product of the input signal and a reference oscillator.

Reference signal is plotted in black and an example of a possible photovoltage signal is plotted in red (Signal 1). Without loss of generality, Signal 1 is plotted exactly in-phase with the reference signal, so that the phase displayed by the lock-in would be zero. A second signal is plotted in blue (Signal 2) to represent the case when the polarity of the photovoltage of Signal 1 has flipped (corresponding to a change in the direction of the photocurrent). The lock-in reports the same signal magnitude for Signals 1 and 2; it is the π-phase shift which indicates that the two signals correspond to a photovoltage response of opposite polarity.

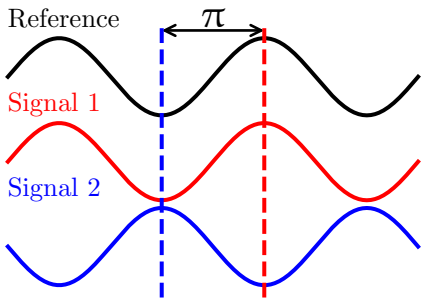

Fig. 6.5 A change in the direction of the photovoltage corresponds to a 180° phase shift in the the phase reported on the lock-in amplifier.

To measure photovoltage spectra using the lock-in technique, the FTIR is operated in step-scan mode. In this mode, the mirror (or the path length) of an arm of the interferometer is fixed for a brief period of time, during which the photovoltage is measured with the lock-in detection technique. The path length of the interferometer arm is then slightly adjusted and another photovoltage measurement is recorded. The process is repeated until an interferogram is recorded, which is then Fourier Transformed to reveal the spectral information of the photovoltage signal.

Photovoltage spectra may also be recorded without the use of a chopper or lock-in detection technique by using the FTIR in rapid-scan mode. In this mode, the path length of one arm of the Michelson interferometer is continuously and periodically modified. Consequently, many interferograms can be recorded at a much faster rate than in step-scan mode. However, because the photovoltage response of the devices in the present study is quite noisy, a very large number of scans (≈ 30000) are required to obtain a reasonable interferogram.

For acquiring the photovoltage spectra, the step-scan technique is generally preferred since a lock-in technique is ideal for extracting a signal from a noisy background. However, a drawback with the step-scan/lock-in technique, is that the interferogram is only recorded once. Therefore, any spike of noise during the rather long scan time completely ruins the photovoltage spectrum. In the photovoltage experiments for the V0386 devices, random spikes of noise plagued the step-scan measurements, and thus long rapid-scan measurements were preferred. For the study of the G0662 devices, the lock-in technique proved more stable and was preferred.

6.3 First Observation of Berreman Mode Photocurrent

In this section, the experimental results are reported for devices fabricated from the V0386 sample. The first observation of photocurrent from the excitaton of a Berreman mode is reported. The section is organized as follows: first, the fabrication of the devices is described; second, the devices are electrically characterized; third, the thermal activation energy is extracted through electrical measurements, and finally, the photodetection measurements are reported.

We begin by presenting in Fig. 6.6 the absorption spectrum of the Berreman mode of the V0386 sample, determined from room temperature transmission measurements at Brewster's angle. The plasmon resonance is centered at 168.7 meV and has a quality factor of Q = 20.0. From the resonance energy, the electronic density of the 100 nm InGaAs layer is determined to be $N_v = 2 \times 10^{19}\,\mathrm{cm}^{-3}$.

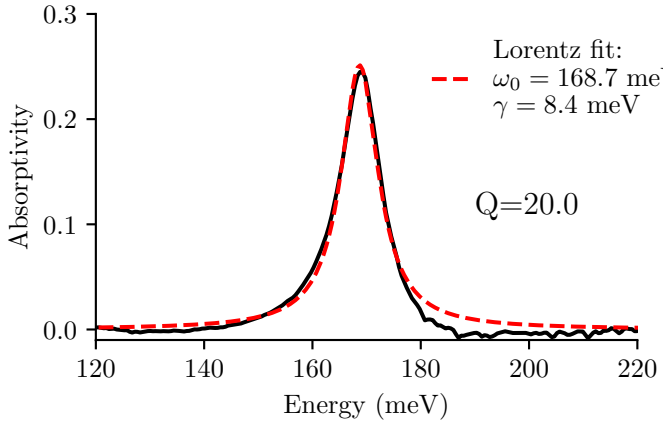

Fig. 6.6 The absorption spectrum of the V0386 sample determined from transmission measurements at Brewster's angle is plotted with a Lorentzian fit (dashed line).

6.3.1 Device Processing

Due to the highly doped nature of the 100 nm layer which hosts the Berreman mode, it may be electrically contacted itself. Three different processing schemes are employed to realize two-terminal 100 µm diameter mesa devices for three different contact schemes, as illustrated in Fig. 6.7. This allows for the role of the barrier regions on either side of the highly doped middle layer to be studied independently. The 'Top-Bottom' scheme of Fig. 6.7a and the 'Top-Middle' scheme of Fig. 6.7b are realized via a single wet etch step with a $H_2O_2/H_3PO_4/H_2O$ solution, in which the etch is carefully stopped midway though the layer to be contacted. The 'Middle-Bottom' configuration is achieved by defining mesas during two consecutive wet etch steps. This process permits the electromagnetic boundary conditions of the heavily doped thin layer to remain the same as the other two configuration, while allowing for the heavily doped middle layer to be contacted in plane. After the definition of the mesas, a 5 nm layer of Ti and a 150 nm layer of Au are deposited on the sample surface and the devices are electrically contacted by gold wirebonds.

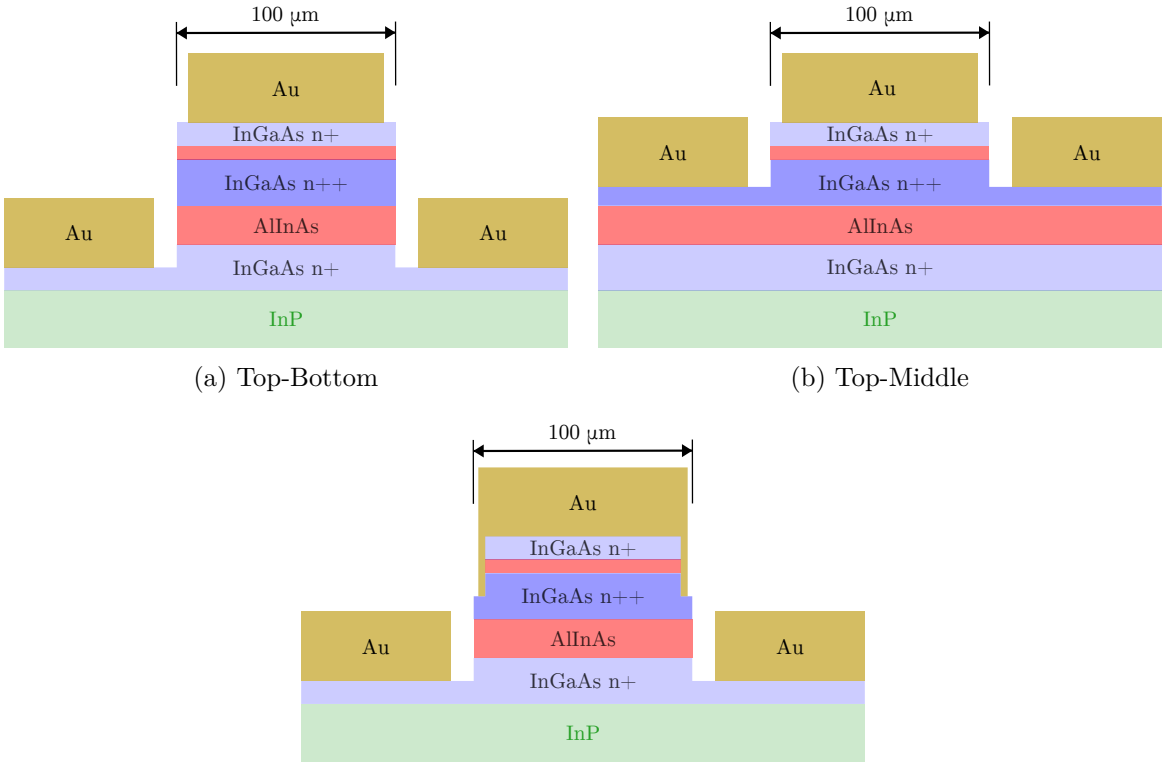

(a) Top-Bottom

(b) Top-Middle

(c) Middle-Bottom

Fig. 6.7 Three different contact schemes are illustrated.

6.3.2 Electrical Characterization

Current-voltage (I-V) curves of V0386 devices for each of the three contact schemes described above were measured at T=7 K using a Keithley Model 2450 SourceMeter, and are shown in Fig. 6.8. A positive voltage lowers the energy of the second contact specified. Thus, for the Top-Bottom device under a positive applied bias, electrons move from the top contact to the bottom contact.

The Top-Middle I-V curve is perfectly linear, and has a resistance of less than 5 Ω even at a temperature of 7 K. The 30 nm AlInAs barrier separating the top and middle contact layers must be conductive, which suggests that dopant impurities were unintentionally incorporated into this layer during the growth. This layer is grown immediately after the highly doped middle layer which supports the Berreman mode. To achieve a high electronic density in the middle layer, the MOCVD process is pushed to an extreme, and it is difficult to abruptly stop the incorporation of dopants in the barrier layer grown immediately afterwards.

To approximate the effect of dopants in the top 30 nm barrier, the band structure shown in Fig. 6.9 was calculated assuming an electronic density of 2×10^{18} cm^{-3} in the 30 nm AlInAs barrier. Under these conditions, the barrier is essentially transparent to the electrons.

Because the top 30 nm barrier is conductive, the Top-Bottom and Middle-Bottom I-V curves are nearly superimposed. The curves are highly asymmetric. Near zero bias, the differential resistance is nearly infinite. The differential resistance undergoes a dramatic

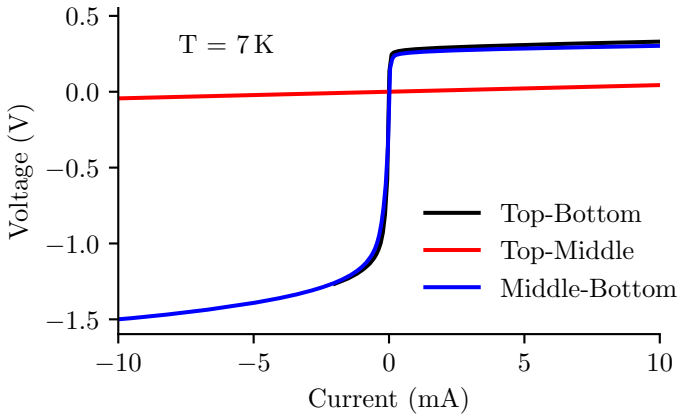

Fig. 6.8 Current-voltage curves for 100 µm diameter V0386 mesas measured with the devices mounted on a cold finger at T=7 K are plotted. The devices are exposed to the room temperature background radiation.

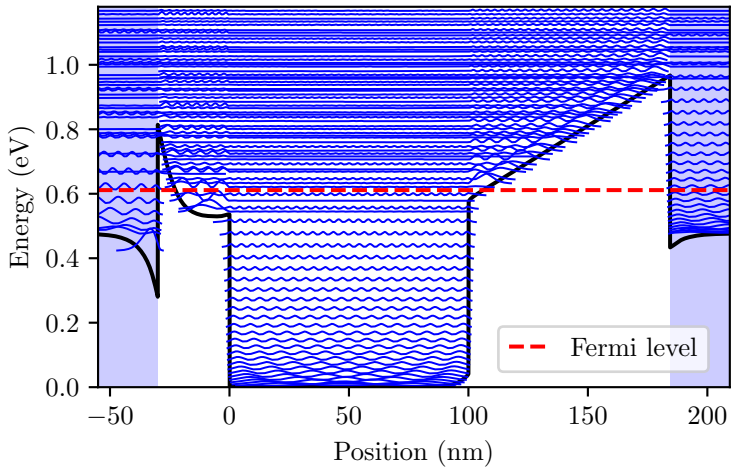

Fig. 6.9 The band structure for sample V0386, calculated assuming an electronic density of 2×10^{18} cm^{-3} in the top 30 nm AlInAs barrier, is plotted. The band structure was calculated self-consistently for a constant effective mass using nextnano.

drop for a much smaller positive bias than negative bias.

The asymmetry can be explained considering a simple thermionic emission model, sketched in Fig. 6.10 for the Middle-Bottom device. The model assumes that the energy difference between the maximum of an adjacent barrier potential, E_{barr}, and the Fermi level in a given doped layer determines the magnitude of current for a given bias. We call this quantity the thermal activation energy E_{act}. It is an effective barrier height for an electron to escape from a degenerately doped region.

In the absence of an applied bias, the conduction band of the top contact region bends upward so that a constant Fermi level is maintained across the structure. Neglecting tunneling, the thermal activation energy is the same for electrons in the middle layer or the bottom

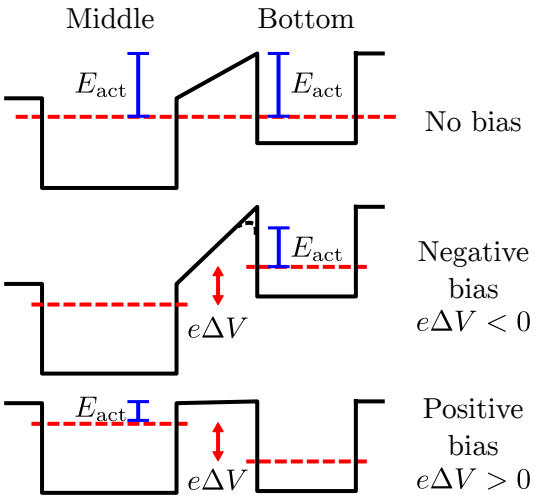

Fig. 6.10 A band structure diagram is sketched for the Middle-Bottom device for three bias conditions. The Fermi level (or quasi-Fermi level) is indicated as a dotted red line. The thermal activation energy E_{act} is sketched in blue.

contact.

Under negative bias, the thermal activation energy for electrons in the bottom contact is hardly changed, apart from an effective lowering of the barrier height when tunneling is considered. On the contrary, for a positive bias, the thermal activation energy is greatly reduced. This explains why the differential resistance, which is near infinite for both positive and negative biases close to zero, undergoes a dramatic drop for a smaller magnitude of positive bias than negative bias.

This simple model relates the asymmetry of the I-V curve to the fundamental asymmetry of the Middle-Bottom structure, which is the relative proximity of the Fermi level to the barrier edge in either layer. The model is, of course, overly simplified.

6.3.3 Extraction of Thermal Activation Energy

In this section, we attempt to extract from a series of temperature dependent I-V curve measurements in the dark the thermal activation energy required for an electron to move from the highly doped middle layer over the bottom barrier. Two different models for the dark current are considered which lead to similar values for the activation energy.

In the first model, we consider that the interface between the highly doped middle layer and the adjacent barrier can be treated as a Schottky junction, with the degenerately-doped middle layer fulfilling the role of the metal, and the AlInAs barrier layer fulfilling the traditional role of the semiconductor. The activation energy is equivalent to the Schottky barrier height, ϕ_{B}. From the well-known expression describing the current-voltage characteristics of a Schottky diode [74, 83, 111] operating in reverse bias, the current J_{dark} is found to be proportional to:

$$J_{\mathrm{dark}} \propto (kT)^2 \exp\left(\frac{-E_{\mathrm{act}}}{kT}\right) \tag{6.1}$$

The second model we consider is the so-called 3D carrier drift model [114]. It is frequently used to describe the dark current characteristics of quantum well infrared photodetectors

(QWIPs). These detectors consist of repeating periods of thin, doped quantum wells with one occupied subband sandwiched between much wider barriers. In the 3D carrier drift model, the dark current density is written:

$$J_{\text{dark}} = eN_{\text{3D}}v(E) \tag{6.2}$$

In this equation, N_{3D} is the 3D electron density *above* the barriers, and $v(E)$ is the electric field-dependent electron drift velocity.

The key step in the model is the evaluation of N_{3D}. Under the assumption that $E_{\text{act}} = E_{\text{barr}} - E_{\text{F}} \gg kT$, than N_{3D} may be calculated by replacing the Fermi-Dirac function $f(E)$ with the Boltzmann distribution $\exp(-(E - E_{\text{F}})/kT)$ in considering the overlap with the density of states in the conduction band $\rho_{\text{c}}(E)$:

$$\begin{aligned} N_{\text{3D}} &= \int_{E_{\text{barr}}}^{\infty} \rho_{\text{c}}(E) f(E)\, \mathrm{d}E \\ &= \int_{E_{\text{barr}}}^{\infty} \rho_{\text{c}}(E) \exp\left(\frac{-(E - E_{\text{F}})}{kT}\right) \mathrm{d}E \\ &= \frac{1}{4}\left(\frac{2m_{\text{b}}^{*}kT}{\pi\hbar^2}\right)^{\frac{3}{2}} \exp\left(\frac{-E_{\text{act}}}{kT}\right) \end{aligned} \tag{6.3}$$

It is important to note that N_{3D} is calculated for the system at equilibrium, without an applied bias. Consequently, the model is only expected to be valid for small applied voltages.

Under the assumption that the electron mobility and saturation velocity are temperature independent, then from Eq. (6.2), it holds that:

$$J_{\text{dark}} \propto (kT)^{\frac{3}{2}} \exp\left(\frac{-E_{\text{act}}}{kT}\right) \tag{6.4}$$

Equations (6.1) and (6.4) differ only by the power of kT in front of the exponential.

The activation energy E_{act} is experimentally extracted by measuring I-V curves as a function of temperature in the dark. For these measurements, the device is placed inside a metal cryoshield which is kept as closely as possible to the same temperature as the copper cold finger, in order that the device is in thermal equilibrium with the background radiation to which it is exposed. Current-voltage curves of the V0386 Top-Bottom device measured as a function of temperature are plotted in Fig. 6.11a for positive voltages. As expected, the resistance of the device decreases with increasing temperature.

To extract the activation energy, Eqs. (6.1) and (6.4) are fit to the current as a function of temperature curve for a fixed bias. In Fig. 6.11b, the measured current I is plotted as a function of the temperature T for a fixed bias of 5 mV. Equations (6.1) and (6.4) are fit to the I(T) curve over a temperature ranging from 170 K to 300 K. The proportionality constant α is introduced. Over the temperature range indicated, both models fit the I(T) curve well and are nearly superimposed. From the Schottky diode model (blue) E_{act} is extracted as 165 meV, while for the 3D carrier drift model, the activation energy is extracted as 176 meV.

These values are significantly smaller than the value of the effective barrier potential $\phi_{\text{eff}} = 350$ meV determined from the calculation of the V0386 band structure, shown in Fig. 6.3. While the definition of ϕ_{eff} neglects tunneling through triangular AlInAs barriers (see Fig. 6.3), it is unlikely that tunneling alone can explain the discrepancy between the

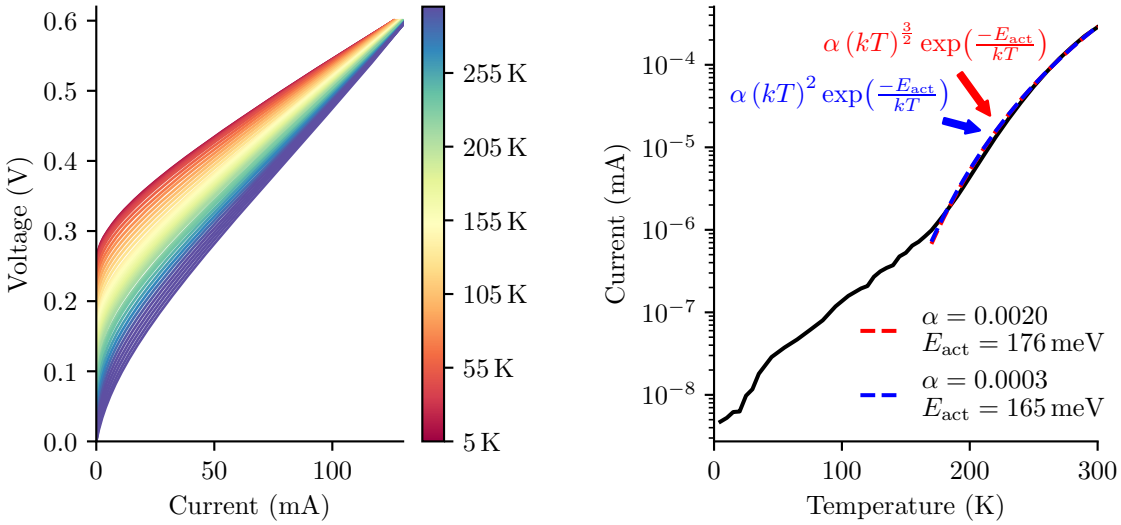

(a) $I - V$ curves for $V > 0$

(b) $I(T)$ for $V = 5\,\text{mV}$

Fig. 6.11 The activation energy E_{act} is extracted from fits of the current as a function of temperature for a small fixed voltage for the V0386 Top-Bottom device. Assuming a complete electrical short between the top and middle doped regions, $V = 5\,\text{mV}$ corresponds to an electric field of $0.571\,\text{kV cm}^{-1}$ between the middle and bottom doped layers.

experimentally extracted value of E_{act} and ϕ_{eff}. The values extracted for E_{act} are more inline with the difference between the barrier height (520 meV) and the Fermi level (370 meV) in the highly doped middle layer, if the band bending effect is neglected. This discussion highlights the significant uncertainty in the band structure modeling of our devices, due to the large electronic densities involved and uncertainties in the material growth.

6.3.4 Photovoltage Measurements

Photovoltage measurements for the V0386 Top-Bottom and Middle-Bottom devices were recorded for light incident at 30° inside the semiconductor, close to the critical coupling angle at which incident radiation is totally absorbed. The light was coupled into the semiconductor from free space at normal incidence across a facet polished at an angle of 30° with respect to the sample plane.

In the upper panels of Fig. 6.12, photovoltage spectra measured at T=7 K in rapid-scan mode are shown for each device for positive V_{meas}. The spectra have not been treated to account for the shape of the blackbody light source.

A resonant feature is observed at the energy of the Berreman mode. For positive biases, the potential energy of the bottom contact is lowered. The resonant feature arises then from electrons which traverse the 84.4 nm barrier separating the middle and bottom contact layers. No photovoltage features were observed for negative biases, most likely due to the electrically shorted 30 nm barrier.

For comparison, experimental absorption spectra determined from Brewster's angle trans-

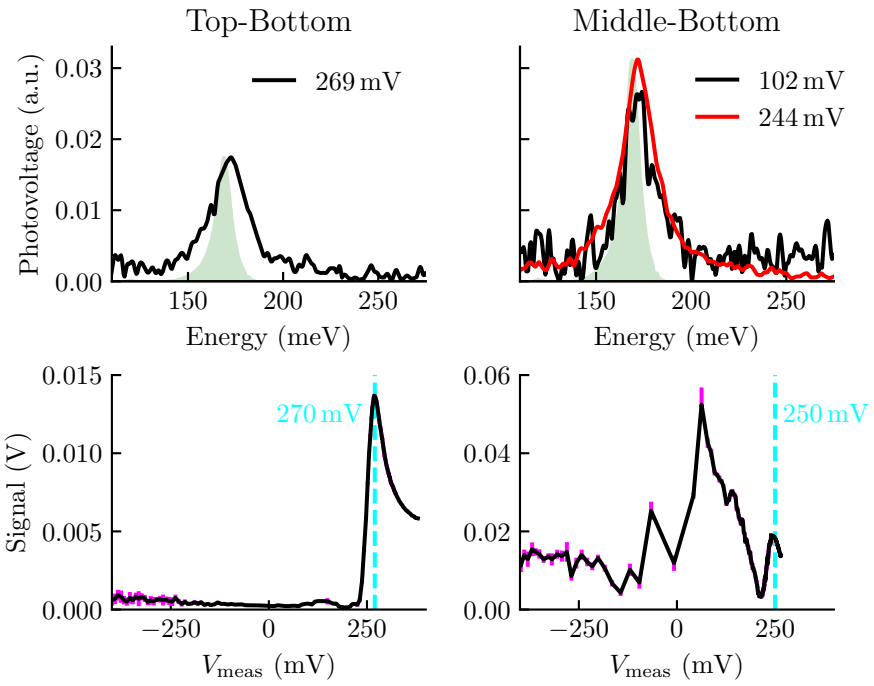

Fig. 6.12 Experimental photovoltage results measured at a temperature of 7 K are presented for devices fabricated from sample V0386. The green shaded spectra are absorption measurements at Brewster's angle, normalized here to the photovoltage spectra.

mission measurements are plotted in shaded green normalized to the maximum of the photovoltage spectra. The resonances of the photovoltage spectra, measured at a 30° angle, have a larger linewidth than the absorption resonance, measured at an 18° angle. This is explained by the radiative broadening effect described in Section 2.2.1, in which the radiative decay rate increases as a function of angle and reaches values larger than the nonradiative decay rate.

The photovoltage resonance, centered at 172 meV, is blueshifted from the absorption resonance, centered at 168.5 meV in the spectrum measured at 18°. This effect can be attributed to the dispersion of the Berreman mode with the in-plane wavevector (which varies with angle), described in Section 2.3.1. A similar blueshift was observed in the absorption measurements of Fig. 2.9.

We conclude that the observed photocurrent lineshape follows closely the form expected for the absorption. This suggests that the transport of the photoexcited carriers is not dependent on the energy of the excited carriers over the bandwidth that the absorption resonance is observed.

In the bottom panels, the photovoltage signal measured on the lock-in as a function of the bias is plotted. Errorbars indicating the standard deviation of the lock-in signal over a sampling time of 10 seconds for a fixed time constant are plotted in magenta. For the Top-Bottom device, the signal is negligible other than a slight bump around 150 mV until it peaks dramatically for a bias of 270 mV, after which it decays more slowly. For the Middle-

Bottom device, the signal increases from zero bias, reaching a noisy first maximum for a bias of 60 mV, and a second less-noisy maximum for a bias of 250 mV.

Note that the y-axis of the lock-in signal differs by a factor of 4 between the panels for the Top-Bottom and Middle-Bottom devices. Thus, the peak at 250 mV observed in the Middle-Bottom lock-in signal curve is similar in form, magnitude, and noise to that observed in the Top-Bottom curve for a bias of 270 mV.

The relative amplitudes of the peaks in the Middle-Bottom photovoltage spectra do not correspond to the relative signal amplitudes in the the lock-in signal as a function of bias curve. This suggests that some of the signal contributing to the first peak around 60 mV does not originate from a resonant plasmonic feature.

For both the V0386 Top-Bottom and Middle-Bottom devices, the bias at which the photovoltage signal reaches a smooth peak corresponds to the voltage at which the differential resistances of the I-V curve undergoes a dramatic drop. In Fig. 6.13, the differential resistance of the V0386 Top-Bottom and Middle-Bottom I-V curves (shown already in Fig. 6.8) is plotted on a logarithmic scale. The differential resistance drops by nearly four orders of magnitude at the voltages for which the photovoltage signals peak (250 mV for the Middle-Bottom device and 270 mV for the Top-Bottom device).

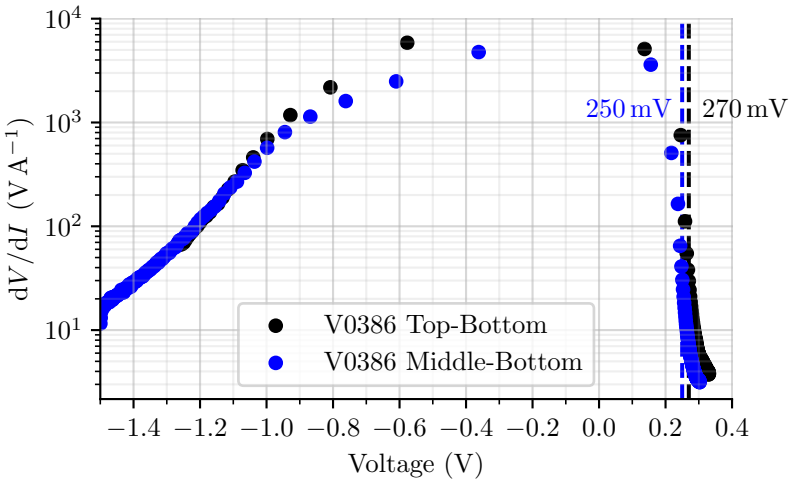

Fig. 6.13 The differential resistance of the V0386 Top-Bottom and Middle-Bottom I-V curves from Fig. 6.8 is plotted as a function of the bias voltage. The vertical lines plotted at 250 meV and 270 meV indicate the bias values for which the photocurrent signal of the respecitve device reached a maximum in Fig. 6.12.

The correspondence between the voltage at which a peak-like feature is observed in the signal as a function of bias curve, and the voltage at which a strong drop in the differential resistance is observed, has been repeatedly observed across many different samples, including for the G0662 sample studied later in this chapter and the samples studied in Appendices B and C. A physical description linking the two observations remains to be established. It is clear, however, that the plasmonic photocurrent signal is strongest in the region where the I-V curves are strongly nonlinear.

6.3.5 Photovoltage Spectra as Function of Angle

In this section, photovoltage spectra measured with the FTIR/blackbody source at various angles of incidence for the V0386 Top-Bottom devices are investigated. Due to the radiative broadening effect described in Section 2.2.1, the linewidth of the Berreman mode absorption resonance increases with the angle of incidence. We exploit this effect to investigate how changes in the absorption spectrum are manifested in the photovoltage spectra.

Let us assume that the photovoltage spectra can be described as:

$$V_{\text{photo}}(\omega,\theta) = \alpha(\omega,\theta) \times F_{\text{trans}}(\omega) \tag{6.5}$$

where $\alpha(\omega,\theta)$ is the absorptivity spectrum, and $F_{\text{trans}}(\omega)$ is an energy-dependent function describing the electronic transport. By comparing $V_{\text{photo}}(\omega,\theta)$ with $\alpha(\omega,\theta)$, the form of the function $F_{\text{trans}}(\omega)$ can be extracted. The form of F_{trans} should provide information on the population distribution of hot carriers after the decay of the collective excitation.

As the angle of incidence is increased, and the linewidth of $\alpha(\omega,\theta)$ is broadened, the spectral range over which the transport function $F_{\text{trans}}(\omega)$ can be studied is expanded. With this, more insight can be gained into the physics of the photodection process.

As an example, if hot carriers are excited to the energy of the collective excitation above the Fermi level, than we should expect to observe an asymmetric broadening of the linewidth like that sketched in Fig. 6.14 due to a low energy cut-off set by the difference between the barrier height and the Fermi level.

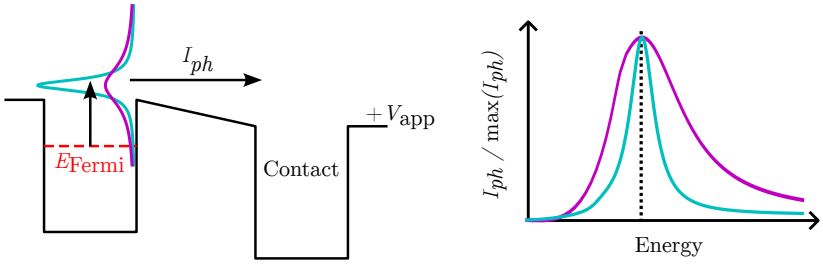

Fig. 6.14 The plasmonic excitation is sketched for light incident at a low angle (cyan) and for light incident at a high angle (magenta) for which the radiative broadening effect is significant. The hypothesized shape of the resulting photocurrent spectra are sketched.

Experimental photocurrent spectra for the Top-Bottom contact scheme of sample V0386 are presented in Fig. 6.15. The spectra were measured at T=7 K for a 270 mV potential between the top and bottom contacts. The spectrum recorded at 30° was measured from a device polished with a 30° facet, while the other spectra were measured with light incident at various angles on a device with a 70.5° facet. The spectra have been treated to consider the emission shape of the blackbody light source, then smoothed and normalized to one at their maximum.

A clear broadening of the photocurrent spectra is observed as the angle is increased from 30° to 58° and then to 67°. For the photocurrent spectrum measured at 77°, a relatively narrow peak resides on top of an otherwise broadened background. The energy at which the photocurrent peaks at 30° is slightly shifted from that of the other spectra. This origin of

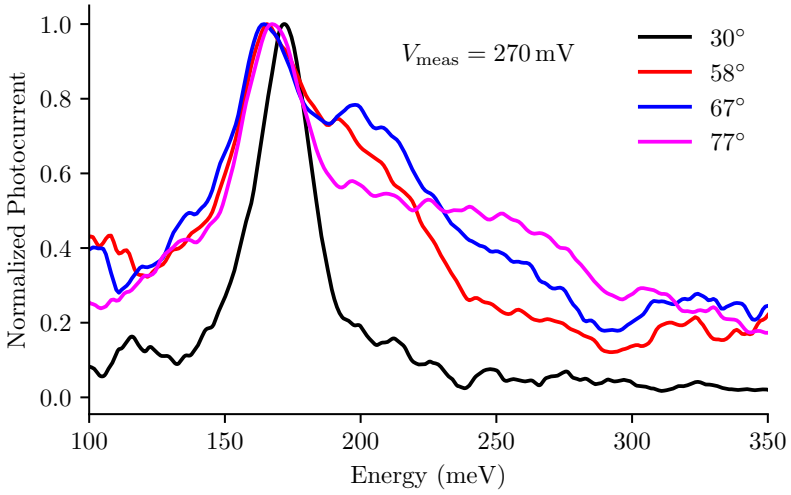

Fig. 6.15 Experimental photocurrent spectra measured at T=7 K for a 270 mV potential between the top and bottom contacts are plotted for various angles.

this effect is uncertain, and may be due to the fact that the 30° spectrum was measured for a different device than the other spectra.

As the incidence angle increases from 58° to 77°, the low energy side of the spectral feature does not broaden, in contrast to the high energy side. The study is complicated by the small responsivity of the device and the large quantity of noise present. Nonetheless, the data provides initial evidence for the validity of the model sketched in Fig. 6.14.

6.4 Three-Terminal Berreman Mode Photodetector

In this section, experimental results are reported for photodetector devices fabricated from the MBE-grown G0662 sample, described in Section 6.2.1. The sample was processed into three-terminal devices in which the top contact, bottom contact, and highly doped middle layer could be independently contacted. The three terminal design permits the potential drop across any two of the three contact layers to be set independently of the third and permits the isolated study of the top and bottom barriers in the same device.

One motivation for the study of the MBE-grown G0662 sample was to compare similar devices grown via alternative techniques, as the high doping level pushes the growth processes to their limits. A series of samples similar to the G0662 sample, grown with MOCVD, were also investigated. The results of these studies are reported in Appendix C and confirm all of the essential observations which we now recount for the G0662 sample.

The section is organized as follows: first, the fabrication of the devices is described; second, the devices are electrically characterized; third, FTIR photodetection measurements with a blackbody source are reported; and lastly, photodetection measurements with a tunable quantum cascade laser (QCL) are reported.

The absorption spectrum of the Berreman mode of the G0662 sample, determined from room temperature transmission measurements at Brewster's angle, is presented in Fig. 6.16. The plasmon resonance is centered at 156 meV and has a quality factor of Q = 15.5. From

the plasmon resonance, the electronic density of the 200 nm InGaAs layer is determined as $N_v = 1.6 \times 10^{19}\,\mathrm{cm}^{-3}$.

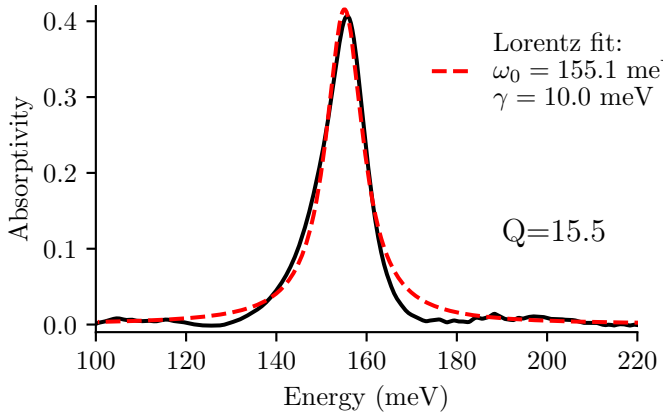

Fig. 6.16 The absorption spectrum at room temperature of the G0662 sample determined from transmission measurements at Brewster's angle is plotted.

The quality factor of the resonance is less than the value of 20.0 observed for the Berreman resonance of the MOCVD grown V0386 sample at Brewster's angle. However, the radiative broadening effect is more significant for the Berreman mode of the G0662 sample because of the wider 200 nm well. This is because the radiative emission rate, defined in Eq. (2.3), is proportional to the surfacic electron density, $N_v \cdot L$, where L is the well width.

6.4.1 Three-Terminal Device Processing

A side-profile sketch and a top-view optical image of the final G0662 three-terminal device are shown in Fig. 6.17. The devices are fabricated into mesa structures of 100 µm diameter.

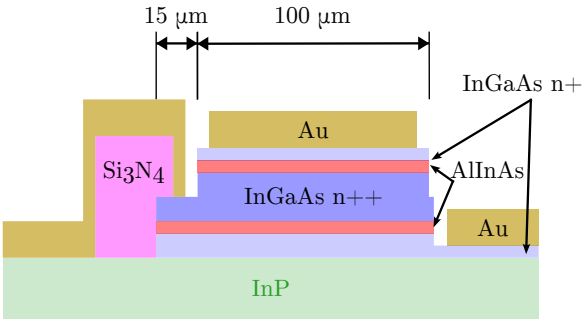

(a) Side-profile sketch of three-terminal G0662 device

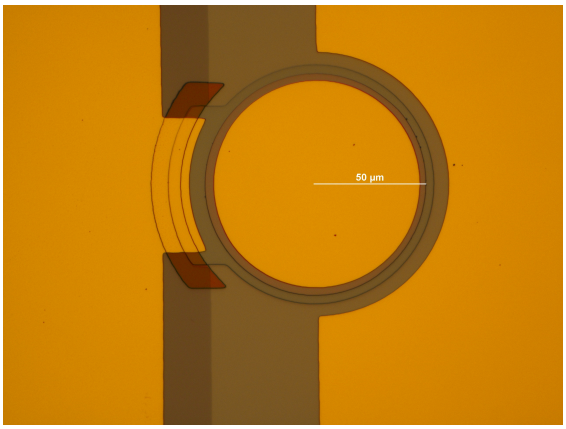

(b) 50× optical image of device

Fig. 6.17 A side-profile sketch and an optical image taken after fabrication of the G0662 three-terminal device are shown.

To achieve the final structure shown, three successive optical lithography and wet etch steps with an H_3PO_4:H_2O_2:H_2O solution are performed. The first and second wet etches are carefully calibrated to stop in the center of the middle highly doped layer and the center of the bottom contact. The third wet etch is selective against the semi-insulating Fe-doped InP substrate. Following the definition of the semiconductor plateaus, Si_3N_4 is deposited on the entirety of the sample surface via plasma-enhanced chemical vapor deposition (PECVD). Note that the deposition is conformal and not directional. A mask of resist is fabricated with optical lithography and reactive ion etching (RIE) is used to vertically etch the exposed Si_3N_4. A final lithography step is performed to define the areas where Ti/Au contacts are deposited. The metal deposition is followed by a lift-off step, after which the microfabrication of the devices is complete. The devices are electrically connected with gold wire bonds.

6.4.2 Electrical Characterization

In the left panel of Fig. 6.18a, current-voltage curves measured at room temperature for various contact schemes of the G0662 three terminal device are plotted. The voltage biases are described with respect to the top contact.

There are two sets of similar curves. The green and purple curves correspond to I-V measurements between the top and bottom contacts. The green curve was measured with the middle contact left floating. The purple curve was measured with the top contact and middle contact electrically shorted. The two curves are nearly identical, especially for negative voltages where they are essentially superimposed. This implies that the nonlinear shape of the curves is determined by the transport of electrons over the lower barrier.

The cyan and brown dashed curves were measured between the top contact and middle layer. The cyan curve was measured with the bottom contact left floating, whereas the brown curve was measured with the top and bottom contacts electrically shorted. The two curves are essentially superimposed on one another. This implies that essentially no current flows over the lower barrier. The differential resistance of the lower barrier is thus orders of magnitude greater than the differential resistance of the upper barrier. This is sketched in the inset of the left panel of the figure.

In the right panel of Fig. 6.18a, I-V curves measured at T=10 K between the top and bottom contacts, for which the middle layer was held to a fixed potential with respect to the top contact, are plotted. It is observed that the entire curve shifts upwards or downwards in voltage by a magnitude close to that of the bias on the middle contact.

This behavior is explained by considering that the majority of the voltage drop between the top and bottom contacts occurs across the bottom barrier, consistent with the picture that the bottom barrier gives rise to a larger differential resistance than the top barrier.

In the upper band diagram of Fig. 6.18b, this scenario is sketched for a positive bias between the top and bottom contacts. The potential offset between the middle and bottom contacts is intentionally drawn to be much greater than that between the top and middle contacts.

If the voltage drop between the middle and bottom contacts determines the current flow, then for the same current flow to be maintained in the device when a positive bias is applied between the top contact and middle layer, a larger bias is required between the top and bottom contacts to maintain the voltage drop between the middle and bottom contacts. This is sketched in the lower band diagram of Fig. 6.18b. While not sketched, a similar

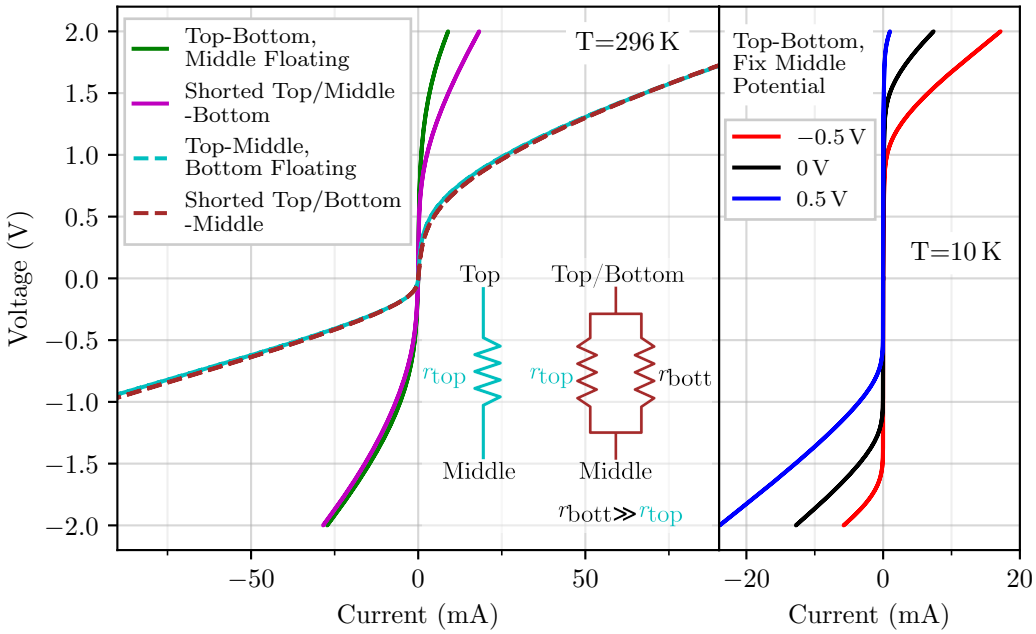

(a) In the left panel, room temperature I-V curves are plotted for various contact schemes. The voltage reported is with respect to the first contact (or shorted contacts) mentioned in the legend entry prior to the dash. Circuit diagrams are sketched in the inset for the Top-Middle curves for the case when the bottom contact is floating (cyan), and for the case when the Top and Bottom are shorted (brown). The differential resistance is represented by r. In the right panel, I-V curves measured between the top and bottom contacts at 10 K are plotted for fixed potentials on the middle contact.

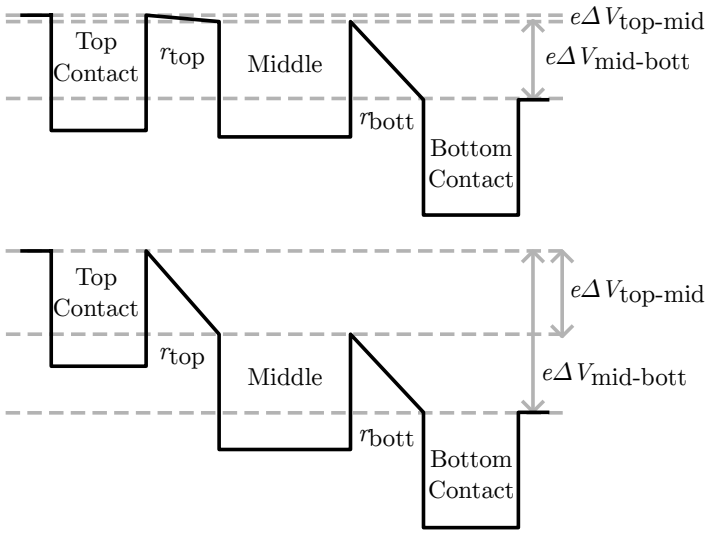

(b) Band diagrams are sketched for a positive bias applied between the top and bottom contacts. In the upper band diagram, the middle contact is left floating. In the lower band diagram, the middle contact is fixed to a positive bias with respect to the top contact.

Fig. 6.18 I-V curves measured for the G0662 three-terminal device are shown in the upper panel. In the lower panel, band diagrams are sketched.

argument holds for the case of a negative potential between the top and bottom contacts. For such a case, a positive bias between the top and middle layer increases the potential drop between the middle and bottom contacts. This explains why current begins to flow for a negative Top-Bottom potential for a smaller voltage magnitude when the middle layer is positively biased with respect to the top contact.

While the above results already demonstrate that the upper and lower barriers contribute quite differently to the transport in the device, the three-terminal device permits each barrier to be studied independently. In Fig. 6.19, two I-V curves measured at T=11 K, one between the top and middle contacts, and the other between the bottom and middle contacts, are plotted. To permit easy comparison, both curves have been plotted so that a negative voltage corresponds to an increased potential energy of the highly doped middle layer, for which case electrons are favored to flow from the middle layer over the respective barrier toward the contact. In the bottom panel of the same Fig. 6.19, the differential resistance for the two curves is plotted as a function of the voltage.

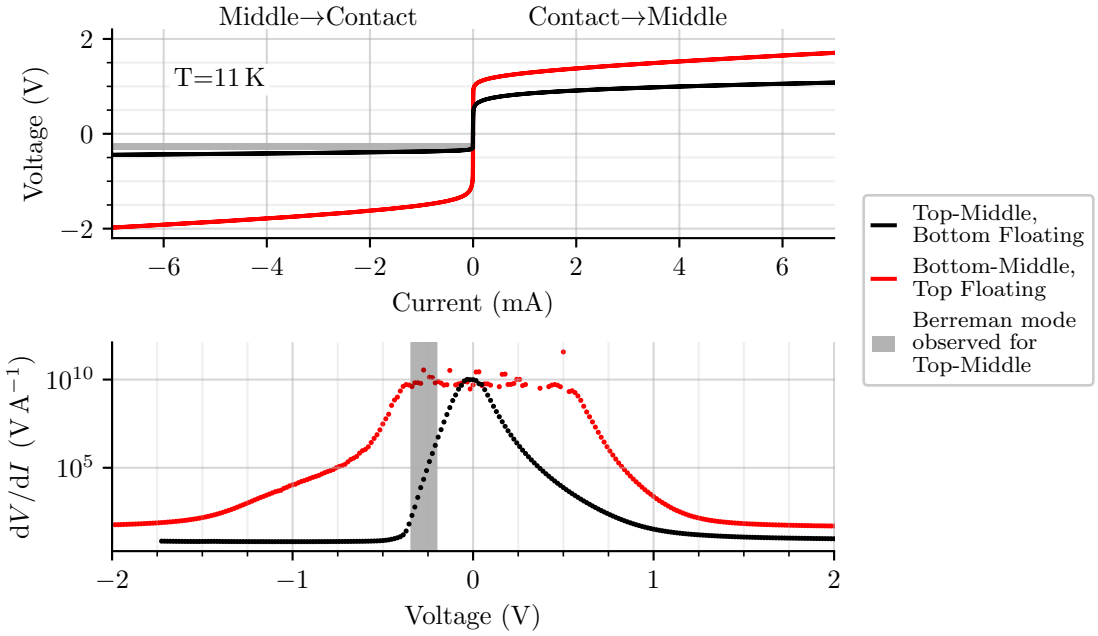

Fig. 6.19 In the upper panel, I-V curves measured at T=11 K for two contact configurations chosen to isolate the top or bottom barrier are plotted. The differential resistance is plotted in the lower panel with a logarithmic y-axis. In both panels, the voltage range over which the Berreman mode is observed in Fig. 6.20 for a bias between the middle layer and shorted top/bottom layers, is shaded.

The voltage range over which the differential resistance is near infinite is much larger for the Bottom-Middle I-V curve than for the Top-Middle I-V curve, both for positive and negative biases. Even for biases for which the differential resistance of the Bottom-Middle I-V curve does decrease, it remains orders of magnitude greater than the differential resistance of the Top-Middle I-V curve. This confirms the interpretations offered above for the results presented in Fig. 6.18: the bottom barrier is much more resistive than the top barrier.

The origin of the asymmetric electrical response of the device, which should nominally be symmetric, must be a consequence of the growth process, and is attributed to the incorporation of dopants in the layers grown immediately following the highly doped middle layer. The same explanation was provided to account for the completely conductive top barrier of the MOCVD-grown V0386 sample.

6.4.3 Photovoltage Measurements

The critical coupling angle for the Berreman mode of the 200 nm highly doped layer of the G0662 sample is close to 20°. To couple light into the devices with this angle of incidence inside the semiconductor, the devices were polished with 20° facets.

Photocurrent from the Berreman mode was only observed for a negative bias on the middle layer with respect to the top contact, in which case photoexcited electrons in the middle layer are collected over the less resistive top barrier. No Berreman mode photocurrent was observed over the more resistive bottom barrier, which suggests that the thermal activation energy for transport in this direction is large compared with the energy of the collective excitation. The much larger magnitude of negative voltage required before the differential resistance drops in the Bottom-Middle I-V curve of Fig. 6.19 as compared with the Top-Middle curve supports this interpretation.

An identical photoresponse was observed in experiments for a bias between the top and middle layers, and for a bias between shorted top/bottom layers and the middle layer. The differential resistance of the bottom barrier is so large compared with that of the top barrier that all the photocurrent moves toward the upper contact over the top barrier, and the bottom contact is essentially electrically floating.

A series of photovoltage spectra measured as a function of the voltage on the middle layer with respect to shorted top/bottom layers, are presented in Fig. 6.20. The spectra were recorded at T=9 K under illumination with *p*-polarized light. The spectra are plotted in Panel (a) on a logarithmic y-scale, with the polarity of the photovoltage indicated. In Panel (b), the spectra are normalized between zero and one and offset for clarity. In either panel, the spectra have not been corrected for the shape of the blackbody source, shown at top of Panel (b). The 156 meV energy of the Berreman mode resonance determined from the Brewster's angle transmission measurement of Fig. 6.16 is indicated with a vertical line.

A resonant photocurrent feature is observed at the energy of the Berreman mode only for negative biases less than −200 mV. In all of the spectra, for both positive and negative biases, there are broad features with widths on the order of 100 meV observed at energies greater than the Berreman mode. In a separate series of photovoltage spectra measured for *s*-polarized light (not shown here), the broad features were also observed. To the contrary, the resonant Berreman mode feature does not appear in the *s*-polarized photovoltage spectra, as expected. The amplitude of the Berreman mode feature increases with respect to that of the broad feature as the magnitude of the negative bias is increased.

The Berreman mode resonance is observed at 162.5 meV in the photovoltage spectrum measured at 20°. This energy is blueshifted with respect to the 155.6 meV centerline measured for the Brewster's angle measurement at 18°. This effect is highlighted in Fig. 6.21. A similar shift was observed between the Brewster's angle spectrum and the photovoltage measurements reported in Fig. 6.12 for the V0386 sample, and was attributed to the dispersion of the Berreman mode with the in-plane vector. Here, the shift is more dramatic due to

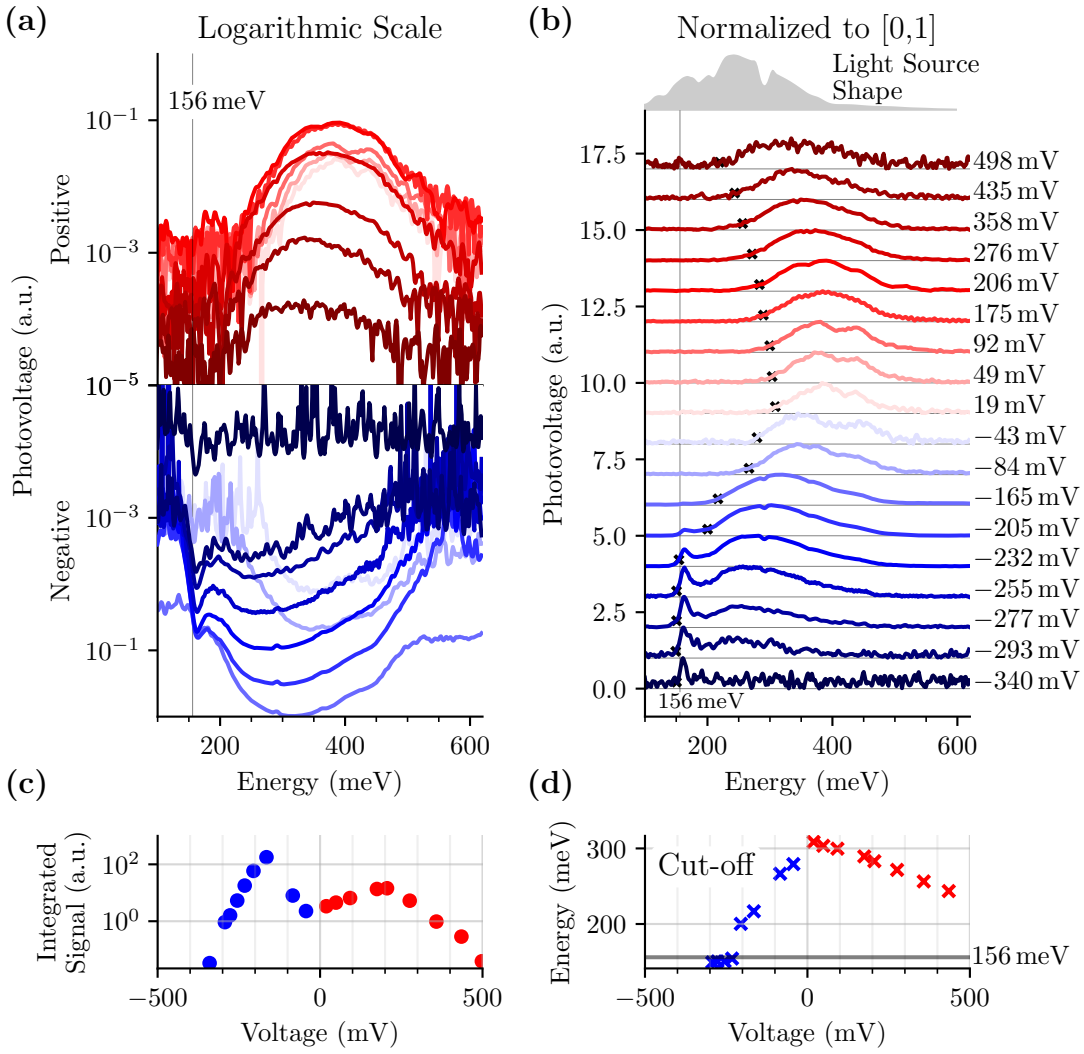

Fig. 6.20 Photovoltage spectra measured at T=9 K between the middle and shorted top/bottom contacts of the G0662 three-terminal device are plotted in Panel (a) on a logarithmic y-scale, and plotted in Panel (b) normalized and offset for clarity. The correspondence between the line color and the voltage bias indicated in Panel (b) holds for Panel (a). In Panel (c), the integrated photovoltage signal for the spectra in Panel (a) is plotted on a logarithmic scale as a function of the voltage potential. In Panel (d), the cut-off energy, calculated as the energy at which the photovoltage is 20 % of the maximum value in the spectrum, is plotted as a function of the voltage.

the increased radiative decay rate associated with the higher surfacic density of the 200 nm quantum well, and because the two measurements are recorded close to the critical coupling angle.

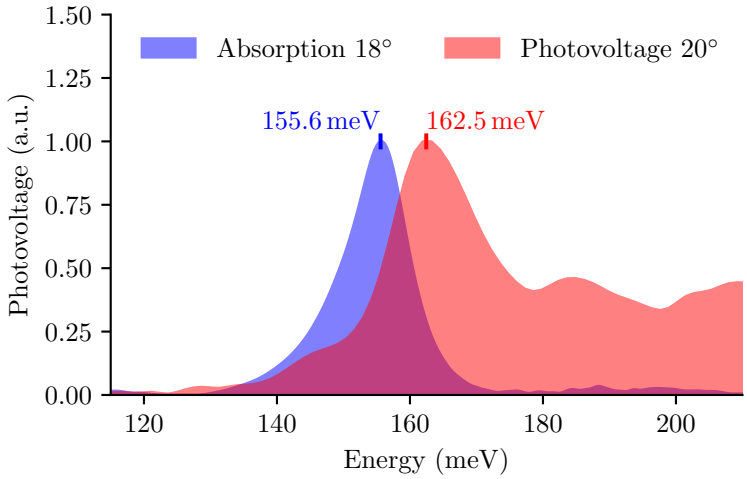

Fig. 6.21 The absorption spectrum of the G0662 sample determined from transmission measurements at Brewster's angle is compared with a photovoltage spectrum measured at T=9 K for a bias of −277 mV on the the middle contact with respect to shorted top/bottom contacts of the G0662 three-terminal device.

The bias range over which the Berreman mode is observed is shaded in Fig. 6.19. The photocurrent from the Berreman mode is observed over the negative voltage range for which the Top-Middle I-V curve flattens and current begins to flow. The voltage range over which the Berreman mode photocurrent is observed thus coincides with the voltage range over which a rapid drop in the differential resistance occurs (see lower panel of Fig. 6.19). The same observation was made for the V0386 sample and the studies reported in Appendix C.

We attribute the high energy features observed in the spectra of Fig. 6.20 to photocurrent arising from nonresonant single particle excitations (free carrier absorption) of the electron gas in the contact and in the middle layer.[4,5] The photoemission of carriers excited via free carrier absorption from a heavily doped layer over a neighboring barrier region has been purposefully exploited in numerous studies to realize all-semiconductor internal emission photodetectors [83, 102].

The broad high energy features shift toward lower energy as the magnitude of the bias voltage is increased. To quantify this effect, the energy at which the photovoltage is 20 % of the spectrum maximum is plotted as a function of the bias voltage in Panel (d). As the magnitude of the bias is increased, the 20 % cut-off energy redshifts.

A similar effect was reported in a study of an internal emission infrared photodetector based on free carrier absorption [83]. The detector studied showed a broadband photore-

[4]It is open question why similar features were not observed in the V0386 photovoltage spectra.

[5]Similar features are not observed in QWIP or QCD structures grown with the same materials, and with similarly doped contacts. However, QWIP and QCD structures are microns thick, whereas the G0662 structure is only 500 nm thick. This sets a completely different length scale over which photoexcited carriers must drift without scattering before collection.

sponse and had a cut-off energy that redshifted with increasing bias. The cut-off energy was demonstrated to be equal to the thermal activation energy (barrier height minus Fermi level) for electrons in the degenerately doped layer. Under an applied bias, the barrier height, and thus the thermal activation energy, are reduced, resulting in the redshift of the cut-off energy.

For the spectra of Fig. 6.20, equating the cut-off energy to the thermal activation energy leads to a qualitative explanation for why the redshift of the cut-off energy with bias shown in Panel (d) is more severe for negative biases. We consider again a simple model for the activation energies like that first introduced in Section 6.3.2 to qualitatively explain the asymmetry of the V0386 Middle-Bottom I-V curve.

The model is sketched again in Fig. 6.22 for the top and middle layers. The activation energies are now indicated with vertical arrows, to indicate the lowest energy excitations for which the photoemission of electrons can take place. We recall that because the electronic density in the middle layer is greater, the conduction band of the top contact region bends upward in the absence of an applied bias.

At zero bias, the cut-off energy for electrons in the top or middle layers is the same, neglecting tunneling. This behavior is observed in the experiment. In Panel (d) of Fig. 6.20, the cut-off energy as a function of the bias voltage converges to the same value as zero bias is approached from both sides.

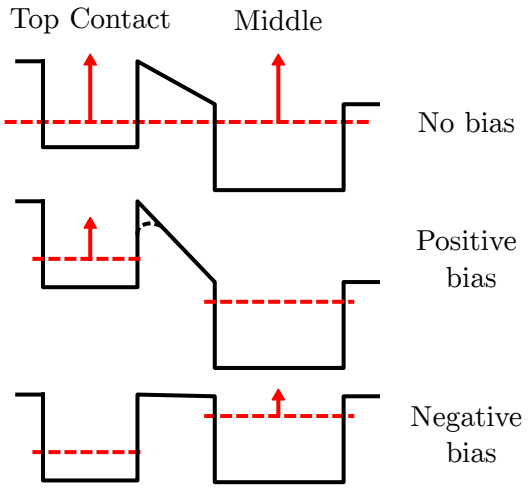

Fig. 6.22 The band structure diagram is sketched for the Top-Middle device for three bias conditions. The Fermi level is indicated as a dotted red line. The photodetection cut-off energy is sketched with arrows intend to represent the photoemission process. The lowering of the effective barrier separating the top contact and middle layer due to a tunneling effect is sketched with a dotted black line.

For a positive bias, the conduction band of the middle layer moves to lower energy with respect to the top contact. Apart from a small tunneling effect, the effective barrier height, or activation energy, for electrons in the top contact is unchanged. On the contrary, for a negative bias, for which the potential energy of the middle layer increases, the difference between the effective barrier height and the Fermi level in the middle layer is greatly reduced.

The model of Fig. 6.22 also explains the asymmetry of the G0662 Top-Middle I-V curve, shown in Fig. 6.19, in which the differential resistance decreases more quickly for decreasing

negative biases than for increasing positive biases. Of note, there is a striking similarity between the Top-Middle differential resistance as a function of voltage curve of Fig. 6.19 and the photovoltage cut-off as a function of voltage curve in Panel (d) of Fig. 6.20. The proposed model links both of these observations to the asymmetric change with bias polarity in the activation energy electrons must surmount to contribute to transport.

In Panel (c) of Fig. 6.20, the integrated photovoltage signal from each spectrum is plotted on a logarithmic scale as a function of the bias voltage. The maximum of the integrated signal reaches a value approximately 10 times larger for the negative bias than for positive bias. Evidently, the photoemission process is more efficient for electrons excited from the middle layer over the barrier toward the top contact than the reverse process.

The Berreman mode feature only appears in the photovoltage spectra for biases of sufficient magnitude that the broad high energy feature redshifts enough to overlap with the Berreman mode energy. From this, it can be inferred that the origin of the cut-off energy is the same for electrons photoemitted due to the excitation of the collective mode, and electrons photoemitted due to single particle excitations. This is a first indication that the collective mode decays into electrons at the energy of the collective mode *above the Fermi level*.

6.4.4 Photovoltage Spectra as Function of Angle

In the left panel of Fig. 6.23, photovoltage spectra from the G0662 three-terminal device for a $-276\,\mathrm{mV}$ potential on the middle layer with respect to shorted top/bottom contacts are plotted for various angles of incidence, offset for clarity. The photovoltage spectra measured between 17° and 36° were measured from a device with a 20° facet. The photovoltage spectra between 40° and 58° were measured from a device with a 45° facet. The spectra have been multiplied by a factor to account for the different reflection amplitudes of the incident radiation on the facet face depending on the angle of incidence, but have otherwise not been normalized.

A broad feature from 150 meV to 400 meV is observed in the spectra at all angles with a nearly constant shape. On the contrary, the resonant Berreman mode feature, observed at 163 meV at 17°, broadens dramatically with increasing angle up to at least 58°, where it can no longer be resolved.

In the right panel of the figure, the same spectra are plotted on top of each other, normalized to one. The spectra broaden asymmetrically only on the higher energy side. Additionally, the center line of the resonance shifts towards higher energy with increasing angle, which can be attributed to the dispersion of the Berreman mode with the in-plane wavevector. Analysis of the linewidth broadening and the shift in resonance energy is complicated by the fact that the resonance lies on a steep background feature

6.4.5 Photovoltage Response to Tunable-QCL Source

In this section, the response of the three-terminal G0662 device, contacted in the Top-Middle configuration, is studied under illumination by a tunable laser source. The use of a laser source has multiple advantages. First, the photoresponse can be studied specifically at the Berreman mode energy as a function of the voltage potential. Second, because the intensity of the laser emission is orders of magnitude greater than that of the blackbody, the signal-to-noise ratio of the photovoltage response is massively improved. Third, the power of the

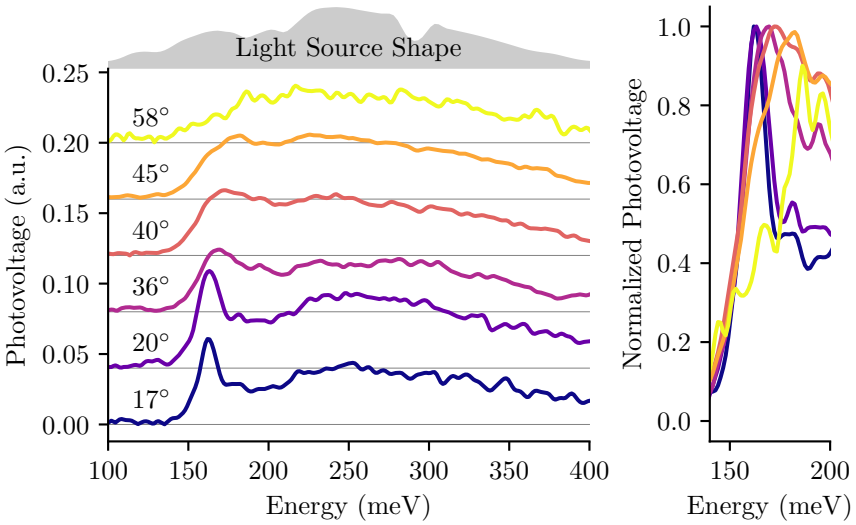

Fig. 6.23 Photovoltage spectra measured at T=10 K between the middle and shorted top/bottom contacts of the G0662 three-terminal device are plotted for varying angle of incidence, for a bias of −276 mV on the middle layer. On the left, the spectra are plotted without normalization and are offset for clarity. On the right, the spectra are normalized to one and plotted over a reduced energy range.

laser is easy to quantify, and thus permits an easy determination of the responsivity of the devices under study.

A commercial MIRcat system packaged with two QCLs, continuously tunable from 7.4 µm to 11.29 µm, is employed as the laser source. The MIRcat uses an external cavity to tune the emission line over the gain bandwidth of each QCL. Multiple QCLs with different gain curves enable a wider tuning range. The calibration of the emitted optical power of the MIRcat source is described in Appendix D.

The experiment to characterize the photoresponse of the devices remains the same as illustrated in Section 6.2.2, except the FTIR and chopper are replaced with the MIRcat laser source, set to emit pulses of 960 ns duration at a rate of 100 kHz. The detector device is cooled to T=7 K. The photovoltage is measured after amplification via a lock-in amplifier, which receives a 100 kHz reference signal from the emitting MIRcat laser.

In Fig. 6.24, the responsivity of the G0662 device is plotted as a function of the voltage (top panel) and as a function of the applied current (middle panel) under laser illumination at energies of 124 meV, 139.9 meV, and 167.5 meV. In the bottom panel, the current-voltage curves of the device under illumination at each laser energy are plotted, and are found to be exactly superimposed.

As was the case in the FTIR experiments, the current is sourced with the Keithley Model 2450 SourceMeter, and the photoresponse is measured by detection of the voltage change upon illumination. The current source range determines the maximum value of the current which can be sourced, but also in effect determines the the minimum interval (or step) which can be accurately sourced. In Fig. 6.24, the current source range was fixed to 100 uA. Consequently, the instrument cannot source the vary small values of current required to

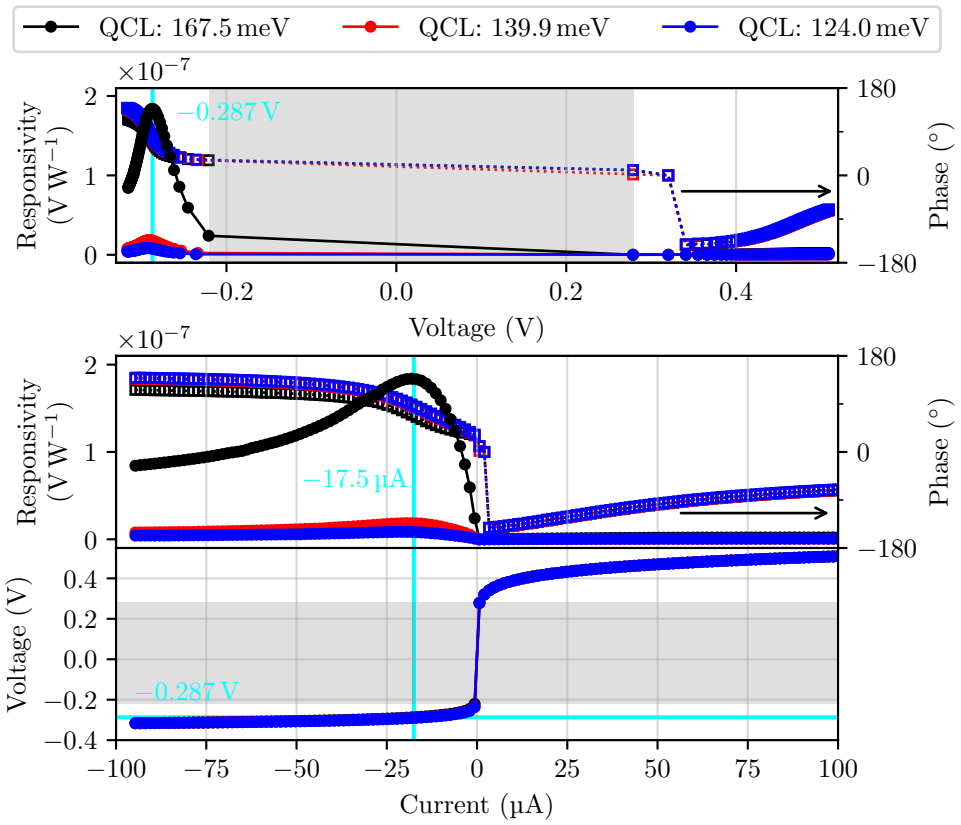

Fig. 6.24 The responsivity measured at T =7 K of the G0662 three-terminal device is plotted on the left y-axis as a function of the bias voltage (current) between the top and middle layers in the upper (middle panel) for three laser excitation energies. The phase is plotted on the right y-axis. In the bottom panel, I-V curves measured under illumination at the three energies are plotted. The voltage range over which no data points are measured is shaded in gray.

measure data over the extremely high differential resistance region of the I-V curve. The shaded regions in the figure indicate the voltage range over which no data was collected. While it is possible to change the current source range in order to source very small current values, an offset was observed in the photovoltage each time the source range was changed. To avoid these artifacts, the source range was fixed for the entirety of the scan.

For all three laser energies, the peak responsivity of the detector is observed for a bias of −0.287 V. For this bias, the responsivity at 167.5 meV is 10 and 20 times larger than that measured at 139.9 meV and 124.0 meV, respectively. This is the expected behavior as the energy of the laser is tuned away from the Berreman mode resonance.

For all three laser energies, the peak responsivity measured at −0.287 V is approximately two orders of magnitude larger than the peak responsivity measured for a positive bias. This is similar to what was observed for the blackbody FTIR measurements for the same device where the signal integrated over the whole spectrum was found to reach a maximum over negative biases orders of magnitude larger than that reached for positive biases.

The curve of the responsivity as a function of the voltage shows a similar form to the curve of the lock-in signal as a function of bias measured for the V0386 Top-Bottom device shown in Fig. 6.12. We recall that for the V0386 device, only the Berreman mode feature was observed in the spectra, and thus the lock-in signal as a function of bias curve can be interpreted as *signal from the Berreman mode* as a function of bias, which allows for a direct comparison with the G0662 responsivity curve measured under resonant illumination at the Berreman mode energy. In both cases, the photoresponse peaks for a bias of a magnitude of a few hundred millivolts, and then begins to decline. In both cases, the bias for which the responsivity peaks corresponds closely with the voltage at which the I-V curve flattens and the differential resistance undergoes a dramatic drop.

In the middle panel of Fig. 6.24, the responsivity dramatically increases with the magnitude of the negative current, *starting from zero.* As a function of the voltage, the responsivity is essentially zero until the negative bias reaches a magnitude greater than $-0.2\,\mathrm{V}$. The near infinite differential resistance over the range from $0\,\mathrm{V}$ to $-0.2\,\mathrm{V}$ links these two behaviors.

A clear 180° phase shift in the photovoltage signal is observed as the polarity of the current is inverted around zero. The same 180° phase shift is observed as a function of the voltage in the first data points recorded on either side of zero. As the magnitude of the current is increased, the phase shifts continuously upward for both polarities, accumulating nearly 90° by the point at which the magnitude of the current reaches $100\,\mu\mathrm{A}$. The origin of this shift is unknown, but for positive and negative currents of equivalent magnitude, the photovoltage signal is consistently 180° out-of-phase.

In Fig. 6.25, photovoltage responsivity spectra of the three-terminal G0662 device are shown for various biases between the top contact and middle layer. The shape of the spectra are similar, with the responsivity consistently peaking around 160 meV. This energy is blueshifted from the Berreman mode resonance observed in the Brewster's angle transmission measurement at 156 meV. This is consistent with the behavior observed in the photovoltage spectra recorded with the FTIR, presented in Fig. 6.20.

6.5 Electroluminescence from V0386 Devices

In this section, it is demonstrated that the same V0386 device which functions as a photodetector can also function as an electroluminescent source. The experimental set-up for the electroluminescence experiments is sketched in Fig. 6.26. In the sketch, the devices are shown inside a cryostat at a temperature of 7 K, but the experiments may also be conducted at room temperature, as will soon be shown.

The plasmonic Berreman mode is electrically excited by 1 µs square voltage pulses repeating at a frequency of 100 kHz (10 % duty cycle). A reference signal passed from the signal generator to the lock-in amplifier permits a lock-in detection technique to be employed. The light emitted from the excited Berreman mode passes through the polished 30° facet of the device and is collimated by a 2" f/1 Ge lens into the FTIR. An MCT detector placed at the exit of the FTIR is used to detect the emitted radiation. The signal from the MCT is amplified 100× before detection by the lock-in amplifier. To get the spectral dependence of the emission signal, an interferogram is recorded using the FTIR in step-scan mode and then Fourier transformed into a spectrum of the emitted radiation. The spectrum is then corrected to account for the frequency-dependent response of the MCT detector.

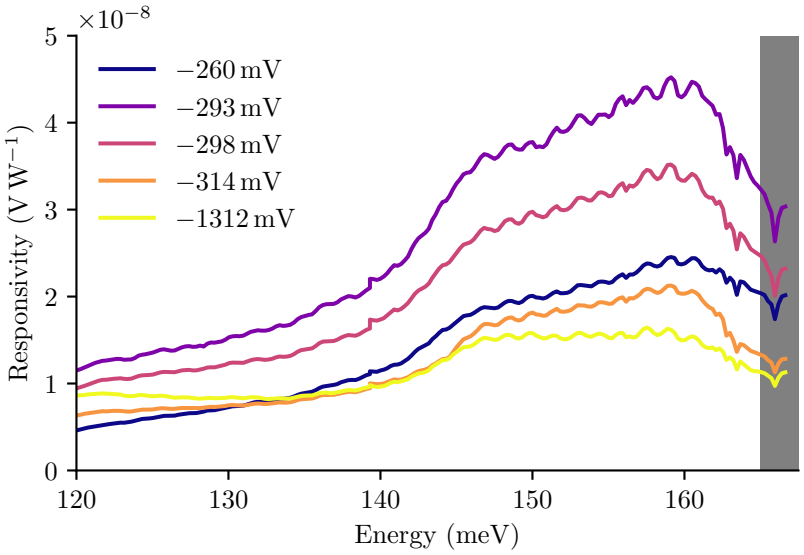

Fig. 6.25 The measured responsivity at T=7 K of the G0662 three-terminal device for voltages between the top and middle layers is plotted as a function of the laser energy. The energy range over which it is difficult to calibrate the optical power emitted from the MIRcat, due to a rapid decrease in the emitted power, is shaded. For the calibration, see Fig. D.1.

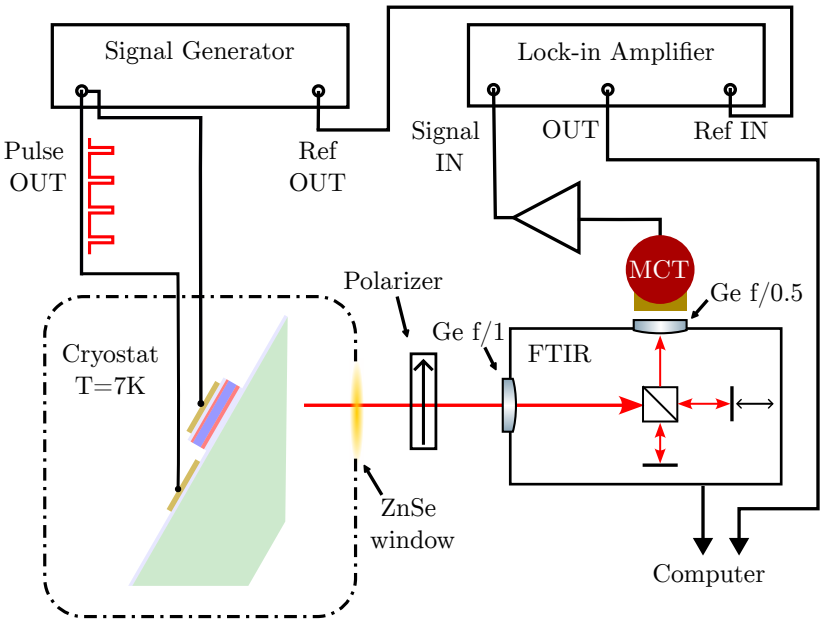

Fig. 6.26 The set-up for the electroluminescence experiment.

In the left panel of Fig. 6.27, current-voltage curves measured for a 10 % duty cycle are plotted at T=300 K and 7 K for the V0386 Top-Bottom sample in black. Also in the left panel, the luminescence signal measured on the lock-in amplifier is plotted in red and blue as a function of the current, the red (blue) indicating a negative (positive) polarity of the voltage pulse. At T=300 K, for either polarity, the luminescence curve is superlinear. However, at T=7 K, the luminescence curve becomes linear for negative polarity pulses. The linearity of the luminescence curve for negative polarity pulses is highlighted in the figure with a linear fit plotted in gray. The linear relationship between the injected current and the photon emission suggests that the collective mode is resonantly excited [70].

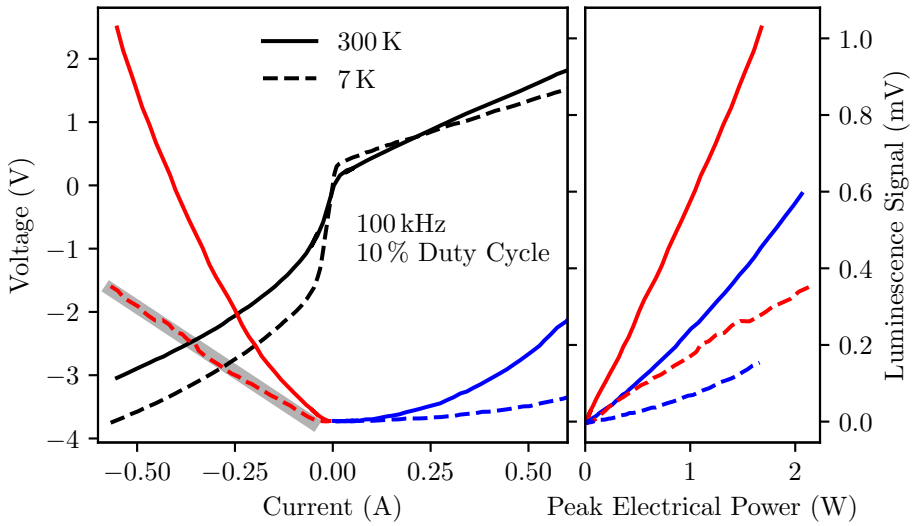

Fig. 6.27 The electrical characteristics (black curves, left y-axis) and the luminescence signal (red and blue curves, right y-axis) as a function of the injected current (left panel) or injected electrical power (right panel) are plotted for the V0386 Top-Bottom device at T=300 K (solid lines) and T=7 K (dotted lines). The red and blue colors indicate the polarity of the pulse. A linear fit is plotted as a shadowing grey line.

In the right panel of Fig. 6.27, the luminescence signal is plotted as a function of the peak injected electrical power (current × voltage during pulse) at T=7 K and 300 K for negative (red) and positive (blue) polarity pulses. At both T=7 K and 300 K, the luminescence signal is greater for negative polarity pulses for a given electrical power injected. Under the application of a negative bias voltage, electrons excite the Berreman mode in the heavily doped middle layer by traversing the lower 84.4 nm barrier from the bottom contact. The fact that the 30 nm upper barrier between the top contact and the middle layer is essentially shorted, as described in the proceeding sections, likely explains why so little luminescence is observed for positive polarity pulses.

In the thermal emission model presented in Section 2.4.1, the temperature rise ΔT of the electron gas is simply proportional to the electrical power injected, and thus the excitation does not depend on the polarity of the applied pulses. The observation that the luminescence signal does depend strongly on the direction of the electron flow suggests a resonant excitation

mechanism.

Electroluminescence spectra of the V0386 Top-Bottom sample measured at T=300 K are shown in Fig. 6.28. Emission spectra are plotted for positive and negative pulse polarities corresponding to an identical peak electrical power injected W_{PP} = 0.92 W. The plasmon mode is present in both spectra, however, the magnitude of the emission from the plasmon mode is much larger for the negative polarity pulse. In both cases, there is a broad background contribution to the emission spectrum. By subtracting the emission spectrum measured for positive polarity from that measured for negative polarity,[6] the Lorentzian shaped spectra plotted in the right panel of Fig. 6.28 is found. A Lorentzian fit is plotted with a thick grey line.

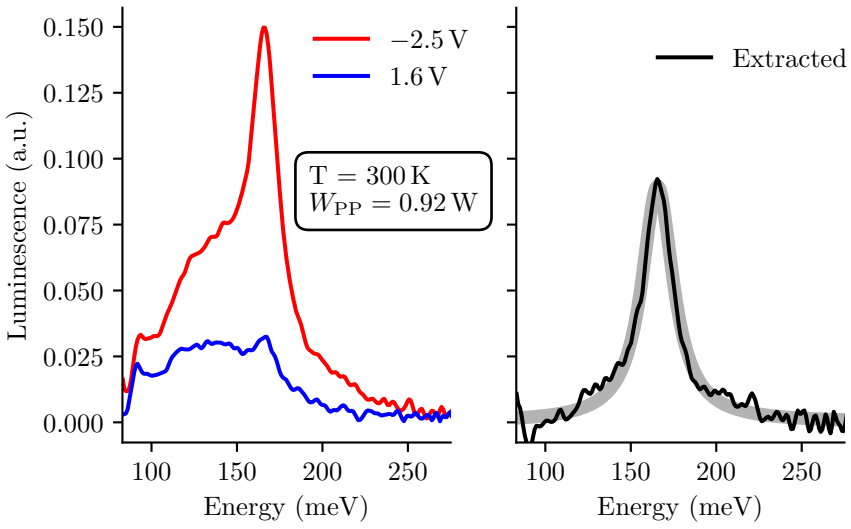

Fig. 6.28 Electroluminescence spectra measured at 300 K for positive (blue) and negative (red) polarity pulses corresponding to an identical peak electrical power injected W_{PP} are plotted in the left panel. In the right panel, a Lorentzian lineshape is extracted (black) and fit (grey) as described in the text.

Electroluminescence spectra measured at T=7 K are shown in the left panel of Fig. 6.29, for positive and negative pulse polarities corresponding to an identical peak electrical power injected W_{PP} of 1.62 W. The amplitude of the plasmon resonance with respect to the background contribution is significantly decreased with respect to the emission spectrum at T=300 K, suggesting that some of the emission from the Berreman mode at T=300 K was thermal. Emission from the plasmon resonance is only present in the spectrum for the negative polarity pulses.

In the right panel of Fig. 6.29, polarized electroluminescence spectra measured from a different V0386 Top-Bottom mesa for a heat sink temperature also at T=7 K are plotted. The background contribution to the emission spectrum is greatly reduced. While this could be due to the smaller injected electrical power, it may also be due to variations between the different devices.

It is compelling from a fundamental point of view to have a single device in which both

[6]Prior to the substraction, the positive polarity spectrum is first multiplied by a factor of order 1.

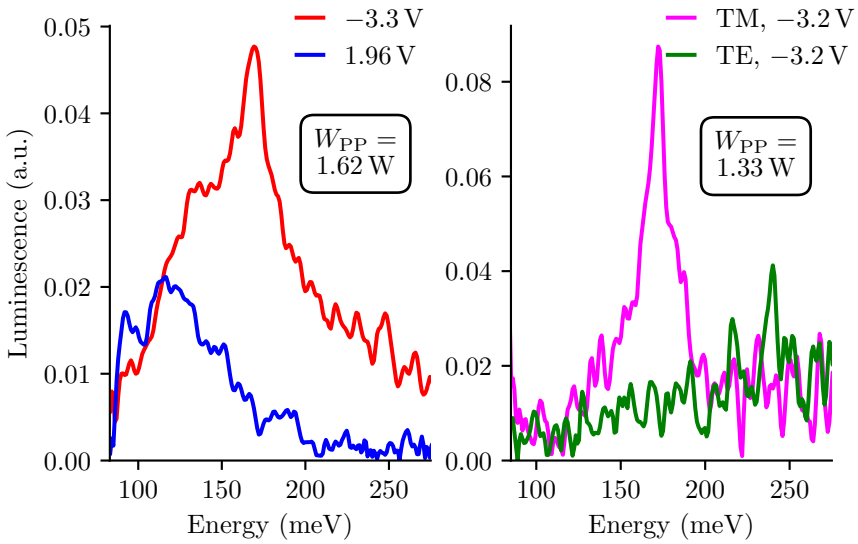

Fig. 6.29 Electroluminescence spectra measured for a heat sink temperature of T=7 K are plotted. The spectra in the left panel are measured for positive (blue) and negative (red) polarity pulses which correspond to an identical peak electrical power injected W_{PP}. In the right panel, polarized emission spectra from another mesa are plotted.

the emission and photodetection problems may be studied. In the resonant injection scheme, the collective mode is excited by a resonant electron-plasmon scattering process, in which the kinetic energy of single particle electrons is transferred to the collective mode [70]. A microscopic theory is still missing to describe this phenomenon, as is a microscopic theory to describe the photodetection process from the Berreman mode. In both cases, it is the transfer of energy between a single-particle excitation and a many-body excitation which is at the core of the problem.

6.6 Conclusion

A resonant Berreman mode feature was observed in the photovoltage spectra of the V0386 and G0662 devices. For both samples, the mode was observed for only one bias polarity. For the V0386 sample, this is because the upper barrier was completely conductive. For the G0662 sample, the potential height of the lower barrier is most likely too large for photoexcited electrons from the Berreman mode to surpass.

For the V0386 and G0662 devices, and the additional Berreman mode detectors studied in Appendices B and C, the Berreman mode photovoltage feature was always observed near the voltage at which the differential resistance of the I-V curve sharply drops. This observation is most simply explained by linking the activation energy with a cut-off energy for the photodetection process. An applied bias has the same lowering effect on both quantities.

In the study of the of the G0662 sample, unexpected features were observed at energies above the Berreman mode resonance. These features were attributed to the photoemission

of single particle electrons excited via free carrier absorption. Similar features were observed in the study of the MOCVD grown samples of Appendix C. It remains a mystery why such features were not observed in the photovoltage spectra of sample V0386, or sample V0385 studied in Appendix B.

The efficiency for which the collective excitation is converted into photocurrent appears to be very low. The photovoltage features attributed to free carrier absorption are of much greater amplitude than the Berreman mode features, despite the fact that the absorptivity from free carrier absorption is orders of magnitude smaller than the absorptivity of the collective mode, which is unity at the critical coupling angle.

Finally, we have demonstrated that a collective mode can be resonantly excited and utilized as a photodetector in the same device. This highlights the potential for heavily doped quantum wells as an intriguing platform to study the interaction between collective excitations and electronic current.

Chapter 7

Plasmonic Detectors Operating in the Ultrastrong Coupling Regime

In this chapter, photocurrent from the excitation of coupled light-matter modes, the well-known cavity polaritons, is studied. The Berreman mode photodetector structures investigated in the previous chapter are put inside an optical microcavity. The Berreman mode couples *ultra*strongly to the cavity mode, resulting in two polariton modes at energies significantly detuned from that of the bare resonance.

Three are three principle motivations for the study. First, the microcavities act as a spectral filter for incident free space radiation. Incident light is reflected unless it excites a mode of the cavity. Consequently, the large photocurrent features observed above the Berreman mode energy in the study of the Berreman mode detectors should not be observed when the structure is placed inside a cavity.

Second, by varying the cavity parameters, the energy of the polaritonic excitation can be tuned. By measuring the photoresponse as a function of the polariton energy, the internal photoemission model can be investigated, and perhaps reveal a cut-off energy.

Third, the study is motivated by the same reasons put forth in the introduction of the previous chapter: to understand the physics behind the generation of photocurrent from a mode with an excitation energy which is renormalized by the Coulomb interaction from that of the single particle electrons which constitute it. The interaction of the matter excitation with the cavity mode is just one more dipolar oscillator coupled to the system. The fundamental question remains: after the normal mode of the system is excited, at which energy are the carriers left which participate in the transport?

The chapter begins with a brief quantum description of the polaritons. This is followed by a description of the microcavity resonators used and the fabrication of the photodetector devices. Finally, experimental results are presented.

7.1 Polariton Modes

In Chapter 4, the *matter* Hamiltonian (Eq. (4.25)) describing the single particle intersubband excitations of a quantum well and their mutual Coulomb interaction was diagonalized for the case of many occupied subbands. The diagonalized Hamiltonian (Eq. (4.35)) is written in terms of raising $P_n^\dagger$ and lowering P_n operators for the collective excitations of frequency

Ω_n.

We now consider the full Hamiltonian Eq. (4.21), including the radiation and light-matter interaction terms, which were not considered in Chapter 4. With the matter part already diagonalized, this Hamiltonian takes the form [34]:

$$H = E_c\left(a^\dagger a + \frac{1}{2}\right) + \sum_n \hbar\Omega_n P_n^\dagger P_n + \mathrm{i}\sum_n \frac{\hbar\omega_{\mathrm{p}_n}}{2}\sqrt{F\frac{\omega_\mathrm{c}}{\Omega_n}}\left(a^\dagger - a\right)\left(P_n^\dagger - P_n\right) \tag{7.1}$$

where the operators $a^\dagger$ and a describe the creation and annihilation of a photon in the mode $E_\mathrm{c} = \hbar\omega_\mathrm{c}$, ω_{p_n} is an effective plasma frequency associated with the Ω_n mode, and F describes the spatial overlap between the matter polarization and the photon mode.

In the experimental studies which follow, we will consider a 200 nm InGaAs/AlInAs heavily doped quantum well in which all of the oscillator strength is coupled into a single bright mode: the Berreman mode. We drop the sum over n, and consider only a single collective excitation at the energy $E_\mathrm{Berr} = \hbar\Omega_1$.

The exact diagonalization of the Hamiltonian, including the antiresonant terms $a^\dagger P^\dagger$ and aP, results in the following eigenvalue equation [34, 131]:

$$\left(E^2 - E_\mathrm{Berr}^2\right)\left(E^2 - E_\mathrm{c}^2\right) = E_\mathrm{R}^2 E_\mathrm{c}^2 \tag{7.2}$$

where the Rabi energy $E_\mathrm{R} = \hbar\Omega_P\sqrt{F}$ has been introduced. This equation admits two positive solutions for each cavity mode energy E_c. The higher energy and lower energy solutions are continuous functions of E_c, and are referred to as the upper and lower polariton branches. The solutions are found as:

$$E_\mathrm{UP/LP}^2 = \frac{1}{2}\left(E_\mathrm{c}^2 + E_\mathrm{Berr}^2 \pm \sqrt{\left(E_\mathrm{c}^2 - E_\mathrm{Berr}^2\right)^2 + 4E_\mathrm{R}^2 E_\mathrm{c}^2}\right) \tag{7.3}$$

The solutions are the oscillation frequencies of the coupled light-matter modes, called polaritons. These modes are observed under the condition that the light-matter coupling, quantified by E_R, is sufficiently strong as compared with the damping rate in the system [37].

Equation (7.3) defines the dispersion of the polariton modes. The dispersion is plotted in Fig. 7.1 for the case of the G0662 sample inserted into a microcavity, in which case $E_\mathrm{Berr} = \hbar\Omega_P = 156\,\mathrm{meV}$ and $F = 0.444$. Here, F is taken as the ratio of the quantum well width to the ratio of the total thickness of the sample, which defines the cavity height. For these parameters, $E_\mathrm{R} = 104\,\mathrm{meV}$.

As the cavity mode energy is increasingly detuned from the Berreman mode towards higher energies, the upper polariton branch approaches the energy of the bare cavity mode. Similarly, when the cavity mode energy is increasingly detuned towards lower energies, the lower polariton branch approaches the bare cavity energy.

Between the upper and lower polariton modes, there is an energy region with no solutions, indicating a photonic gap in which no light is admitted into the microcavities. The appearance of the photonic gap is a hallmark of the ultrastrong coupling (USC) regime, and is only found when the antiresonant terms in Eq. (7.1) are considered [34, 63, 131]. The width of the gap is found as:

$$E_\mathrm{g} = E_\mathrm{Berr}\left(1 - \sqrt{1 - \left(\frac{E_\mathrm{R}}{E_\mathrm{Berr}}\right)^2}\right) \tag{7.4}$$

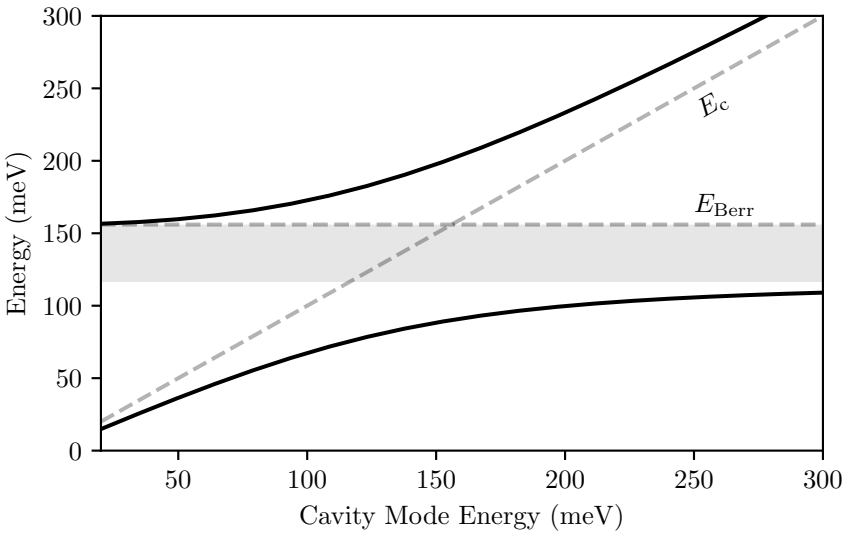

Fig. 7.1 The upper and lower polariton modes from Eq. (7.3) are plotted in black for the G0662 sample.

The relative weight of the photonic or matter components which constitute a polariton mode can be described by Hopfield coefficients [59, 135]. In the regime where the upper polariton approaches the cavity mode energy, the matter component becomes increasingly small, and the polariton mode becomes increasingly photon-like.

In the experimental study which follows, we attempt to observe photocurrent from the upper polariton mode. It is an interesting question what influence the ratio of matter component to photonic component has on the generation of photocurrent. Even if the photocurrent generation is reduced as the relative weight of the matter component is reduced, it remains possible that the increased energy of the electrons which decay from the mode might be advantageous for their collection.

7.2 Metal-Dielectric-Metal Microcavities

The Berreman mode is coupled to the fundamental photonic mode of metal-dielectric-metal microcavities like those sketched in Fig. 7.2a. The upper gold and dielectric layers of a metal-dielectric-metal structure are patterned on a sub-wavelength scale to realize a periodic motif of stripes of width s, realizing a metamaterial. Each stripe supports a resonant photonic mode. The periodicity of the stripes determines the efficiency with which free space radiation is coupled into the dielectric region of sub-wavelength thickness h in each stripe [133].

Let z be the direction perpendicular to the metallic plane, and x be the direction perpendicular to the stripes, as shown in Fig. 7.2a. We consider p-polarized (TM) incident waves such that the electric field lies in the $x-z$ plane. The modes excited under such illumination consist almost exclusively of a strongly confined z-polarized electric field E_z within each stripe and are therefore ideal for coupling with the Berreman mode, which only interacts with the z-polarized electric field.

The E_z profile for the fundamental mode excited in each stripe is plotted in Fig. 7.2b,

where the blue and red colors indicate the amplitude of positive and negative fields. The E_z field is confined between the upper gold layer and the bottom gold plane, and is found to be constant with z, like a TM_0 guided mode between two metallic plates.

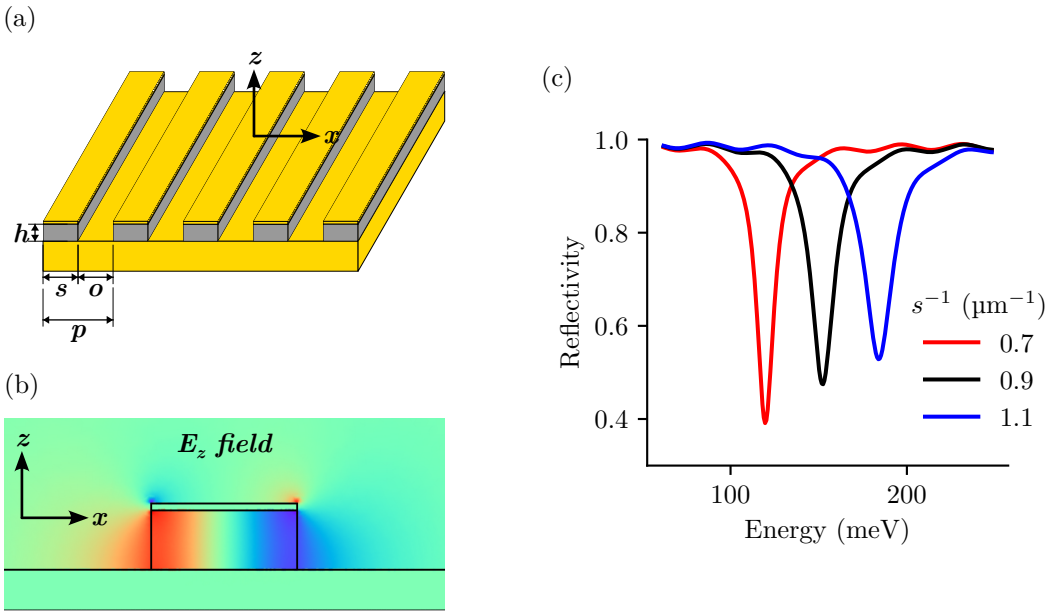

Fig. 7.2 (a) The geometry of the stripe resonators is defined, with the dielectric height h, stripe width s, and pitch o indicated. (b) The E_z field of the fundamental resonator mode excited by light at normal incidence polarized perpendicular to the stripes with photon energy $E = 152\,\text{meV}$ is plotted for $h = 450\,\text{nm}$, $s = 1.1\,\mu\text{m}$, and $o = 3\,\mu\text{m}$. (c) Simulated reflectivity spectra for resonators of varying s are plotted, for $h = 450\,\text{nm}$ and $o = 3\,\mu\text{m}$.

The x-dependence of E_z for the fundamental cavity mode is that of a standing wave pattern, for which a single node is observed near the center of the stripe. More generally, the E_z field of the K^{th} mode is written [133]:

$$E_z(x) = E_z \cos\left(\frac{\pi K}{s} x\right) \tag{7.5}$$

In Fig. 7.2c, reflectivity spectra calculated with a finite element solver (COMSOL) are plotted for three simulations for which s is varied. The energy of the cavity mode resonance is found to be linearly proportional to s^{-1}. More generally, the energy of the K^{th}-order mode can be written as [132]:

$$E_K = hc\frac{K}{2n_{\text{eff}}}\frac{1}{s} \tag{7.6}$$

where an effective modal index has been introduced as n_{eff}. For the remainder of the chapter, we shall only concern ourselves with the fundamental $K = 1$ mode, and refer to it unambiguously as the cavity mode. Then, by fabricating structures of various stripe width s, the cavity mode resonance can be tuned.

The contrast of the cavity mode, defined as one minus the reflectivity minimum, depends on the geometry of the resonators, notably the dielectric height h and the stripe separation

o. Similarly, the contrast of the polariton resonances observed when a matter excitation is coupled to the cavity mode, is determined by these parameters.

In the experiments which follow, we aim to observe photocurrent from the upper polariton of the coupled Berreman mode-micocavity mode system. To this end, the geometry of the microcavities is optimized to maximize the contrast of the upper polariton mode.

The microcavites are fabricated around the same G0662 structure as studied in the previous chapter. The height h of the cavities is fixed by the semiconductor growth to a value of 450 nm. This leaves the pitch o as the only free parameter to optimize.

The optimal value of o for which the contrast of the upper polariton is maximized between 150 meV and 200 meV is determined from finite element simulations to be 3 µm. Simulated reflectivity spectra for stripe cavities containing the G0662 structure for this value of o and for varying s are plotted in Fig. 7.3. A value of 9.8 meV is used for the nonradiative linewidth γ_{NR} of the Berreman mode in the simulations.

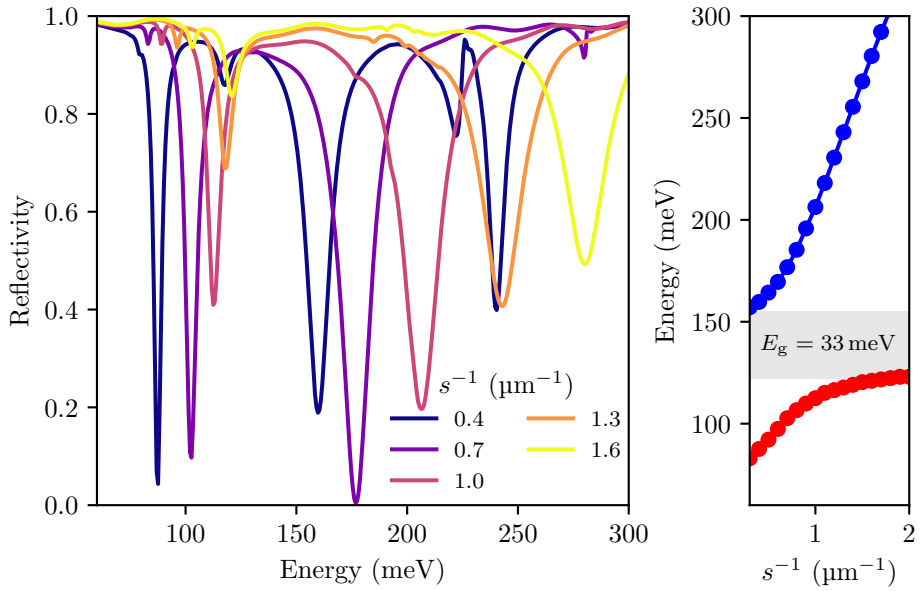

Fig. 7.3 Simulated reflectivity spectra and the extracted polariton dispersion are plotted for stripe cavities containing the G0662 structure for various stripe width s, for height $h = 450$ nm and separation $o = 3$ µm. The photonic gap separating the upper (blue) and lower (red) polariton branches is shaded in gray on the dispersion plot.

The dispersion of the polariton modes is plotted in the right panel of Fig. 7.3. A photonic gap E_g of about 33 meV separates the two polariton branches, indicating that the system is in the ultrastrong coupling regime. From the width of the gap, the Rabi energy E_R is extracted according to Eq. (7.4) as approximately 96 meV, or 62 % of the matter excitation energy, corresponding to an overlap factor of $F = 0.38$. This value of F is slightly lower than that calculated as the ratio of the quantum well width to h. This is because in the finite element simulations, the nonuniform field distribution is considered.

7.3 Device Fabrication

7.3.1 Device Overview

To observe photocurrent from the polariton modes, the microcavity devices must be electrically contacted. Furthermore, a three-terminal device is desired, for which independent electrical connections can be made to the top contact layer, the highly doped middle layer, and the bottom contact layer, as was done for the G0662 three-terminal device described in the previous chapter.

The fabrication of devices meeting these criteria constituted a considerable challenge and had not previously been realized in the Quantum Devices team. The procedure developed to realize these devices is detailed in the following section.

An optical image of the final device is shown in Fig. 7.4. Two of the contacts are established with air bridges, while the third contact is simply the gold ground plane.

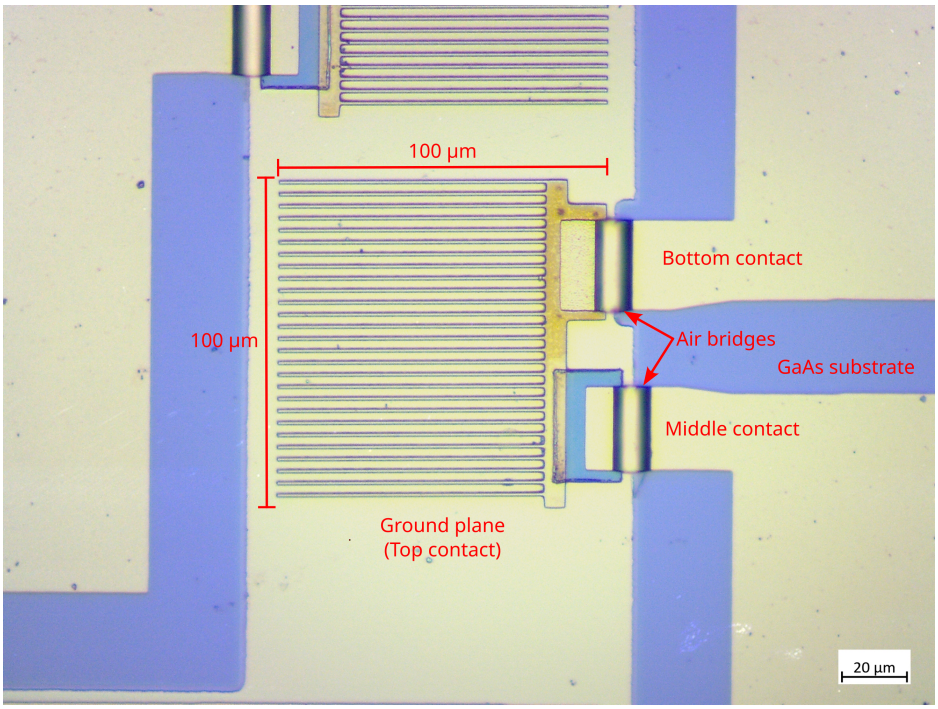

Fig. 7.4 A G0696 microcavity resonator device after fabrication

As will be detailed, the InGaAs/AlInAs heterostructure is flipped during the device fabrication due to a wafer bonding step. To keep the naming convention consistent with the mesa devices, references to the top and bottom contacts are still made with respect to the order of the semiconductor growth, and do not correspond to the relative position of the layers with respect to the gold ground plane of the final device. Thus, in the image, the bottom contact is made by contacting the top gold layer of the resonators.

The microcavity detector devices studied in this chapter were fabricated from sample G0696, grown to be an identical copy of the G0662 sample studied in the previous chapter. The sample was grown via MBE by Lianhe Li, Giles Davies, and Edmund Linfield at the University of Leeds. The growth sheet can be found on Page 206.

7.3.2 Fabrication Procedure

Wafer bonding and Substrate Removal A thin Ti adhesion layer followed by a few hundred nanometers of Au are deposited on the surfaces of the GaInAs/AlInAs semiconductor epitaxial wafer and a semi-insulating GaAs host wafer. After the metal deposition, the metallic sides of the wafers are brought into contact. The application of heat and pressure lead to the bonding of the Au layers.[1] After the wafer bonding, the sample is placed into concentrated HCl to selectively remove the InP substrate on which the semiconductor growth initially took place.

Definition of Metallic Resonators The stripe pattern, the region connecting the stripes, and a region destined to be contacted are defined via electron beam lithography. A bilayer resist, consisting of a PMGI bottom layer and a PMMA top layer, is used to ease the lift-off process. The PMMA layer is patterned with electron beam lithography[2] and then selectively developed in a 1:3 MIBK:isopropanol solution. Where the PMMA has been removed, the PMGI layer is exposed to MF319 developer. The developer removes the PMGI layer in the exposed regions and undercuts beneath the PMMA pattern. The result is shown in Fig. 7.5a. After the bilayer resist has been developed, 5 nm of Ti, 150 nm of Au, and 40 nm of Ni are deposited on the sample surface. The Ni layer is deposited to protect the gold during the later ICP etch step. The lift-off is achieved with DMSO heated to 50 °C.

Si_3N_4 Hard Masking of Eventual Middle Contact Area A 200 nm layer of Si_3N_4 is deposited on the entire sample surface. An optical lithograpy step is used to define a rectangular resist region which will later become the middle contact. The resist region serves as a mask during the subsequent reactive ion etching (RIE) step, where the Si_3N_4 layer is removed from the sample surface apart from the resist-protected region. Upon removal of the resist, a rectangular Si_3N_4 region is left behind to serve as a hard mask for the subsequent ICP etch step. The Si_3N_4 hard mask is shown in Fig. 7.5b.

ICP Etch An inductively coupled plasma (ICP) etch of the exposed GaInAs/AlInAs semiconductor layers is performed[3] to realize vertical sidewalls. The ICP etch removes some, if not all, of the Ni layer deposited on top of the resonator devices. The ICP etch should be carefully stopped just as the gold ground plane becomes visible. The careful stopping of the ICP etch is the largest source of non-reproducibility during the entire device fabrication, if not the entire ICP step itself. Further refinement of the ICP recipe is still needed to achieve ideal results.

Removal of Si_3N_4 Hard Mask and Wet Etch to Middle Layer Following the ICP step, the Si_3N_4 hard mask is removed with RIE, leaving behind the exposed semiconductor layers. The image of Fig. 7.5c shows the sample at this stage of the fabrication.

An optical lithography step is used to define a windows wherein only the already exposed semiconductor area is left uncovered by resist, as seen in Fig. 7.5d. The resist protects the stripe resonators from being etched from the side. One dimension of the

[1] Nathalie Isac performed the wafer bonding step at the Centre de Nanosciences et Nanotechnologies (C2N).
[2] Thomas Bonazzi performed the electron beam lithography step of the fabrication.
[3] Thomas Bonazzi calibrated and performed the ICP etch step of the fabrication.

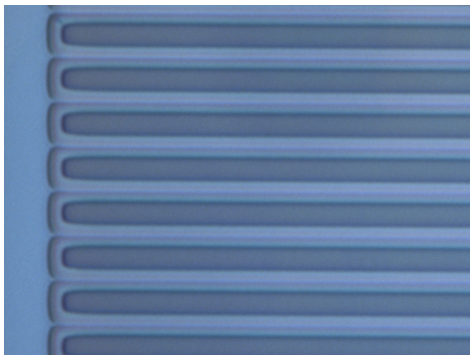

(a) Bilayer resist for metal deposition

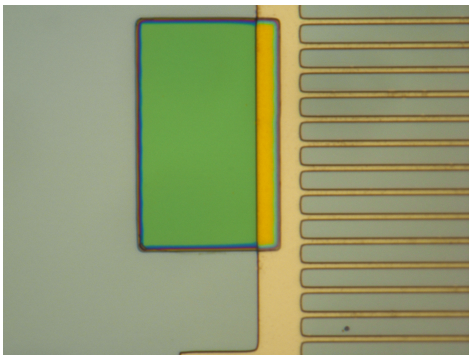

(b) Si_3N_4 hard mask

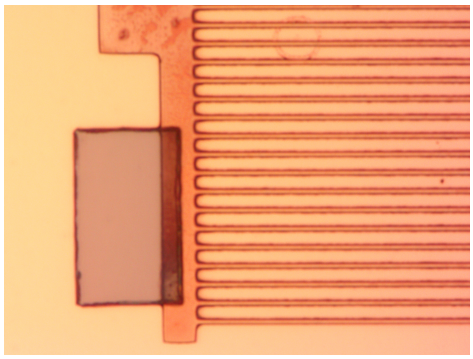

(c) After ICP and hard mask removal

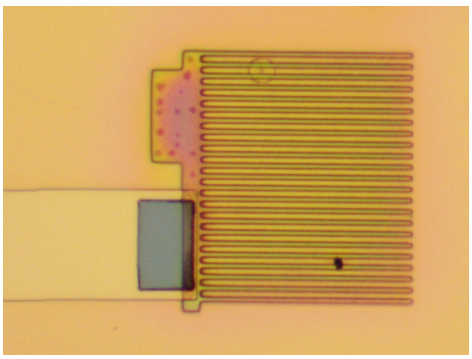

(d) Wet etch window for middle contact

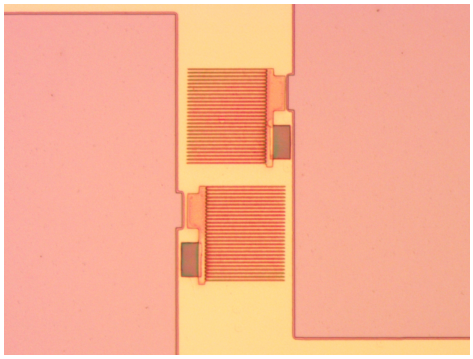

(e) After etch of Au ground plane

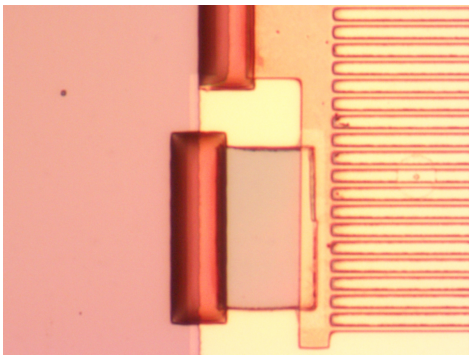

(f) Hard baked pillows for bridges

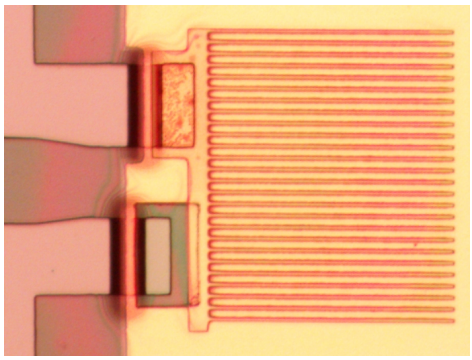

(g) Definition of metal deposition areas

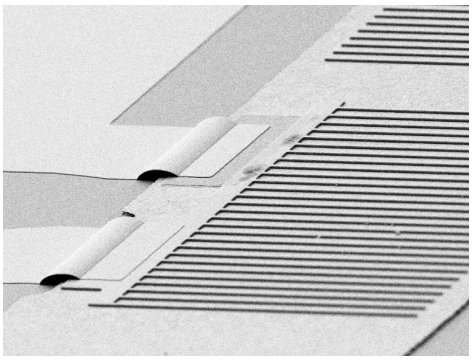

(h) SEM image of final device

Fig. 7.5 Images taken at various steps of the device fabrication are presented. The SEM image of (h) was taken by Thomas Bonazzi.

window is extended over the metal ground plane which is impervious to the etchant solution. This permits profilemeter measurements to be performed to confirm the depth of the wet etch. An $H_2O_2/H_3PO_4/H_2O$ solution is used to etch approximately 200 nm of the exposed InGaAs/AlInAs layers until the center of the highly doped middle layer is reached.

Removal of Ti/Au Ground Plane to Expose GaAs Host Wafer In order to realize contact pads which are electrically insulated from the device ground plane, the Ti/Au ground plane must be removed from the areas where the future contact pads will be deposited. Note that the so-called *semi*-insulating GaAs host wafer is, in fact, very insulating, such that the contact pads deposited directly on it remain electrically separated.

An optical lithography step defines the area where the gold will be removed. The exposed gold is then selectively removed from the underlying Ti layer by a KI/I_2 solution ($KI{:}I_2{:}H_2O$ = 4 g:1 g:40 mL). The image of Fig. 7.5e shows the sample just after the gold wet etch. The remaining thin ($\approx$ 5 nm) layer of Ti is then removed via RIE with SF_6 gas. The resist protecting the remainder of the sample is then removed. At this point, the GaAs host substrate is now exposed over the areas where the metallic contacts will be deposited.

Support Pillow for Contact Bridges The two contact pads to be deposited on the GaAs host substrate must be electrically connected, separately, to the upper metallic surface of the resonator and to the exposed semiconductor middle contact. To avoid electrical shorts, these connections are achieved with air bridges. A pillow of hard baked resist serves as the support for the bridge structures during the metal deposition step.

The resist pillow is defined by optical lithography, using S1818 positive photoresist. After development, the resist is hard baked. The hard bake serves two purposes. When heated above its softening temperature, the resist reflows, so that its edges become rounded, necessary to create a smooth surface for the metal deposition. Second, the hard bake induces thermal cross-linking which renders the resist stable against usual resist developers. This is important since a subsequent optical lithography step is necessary to define the area over which metal will be deposited. The hard baked pillow is shown in Fig. 7.5f.

Deposition of Metallic Contacts A negative photoresist is used to define the areas of the metal deposition, as shown in Fig. 7.5g. Due to the hard bake, the support pillow for the air bridges is not developed during this lithography step. A 5 nm layer of Ti and 150 nm layer of gold are deposited. The lift-off is performed with SVC-14 Photoresist Stripper heated to 80 °C. At the stage, the microfabrication of the devices is complete. An SEM image of a final device is shown in Fig. 7.5h. The devices are ready to be mounted, at which point, electrical connections can be established via wirebonds.

7.4 Experimental Study

7.4.1 Reflectivity Measurements

Reflectivity spectra of G0696 resonator devices were measured at room temperature using a Bruker HYPERION FTIR microscope.[4] The microscope allows for the selection of a microscopic area of the sample surface over which reflectivity spectra can be measured. For the G0696 devices, spectra were measured over a 50 µm×50 µm region of each 100 µm×100 µm resonator device. The reflectivity spectra of G0696 devices of various stripe width are plotted in Fig. 7.6.

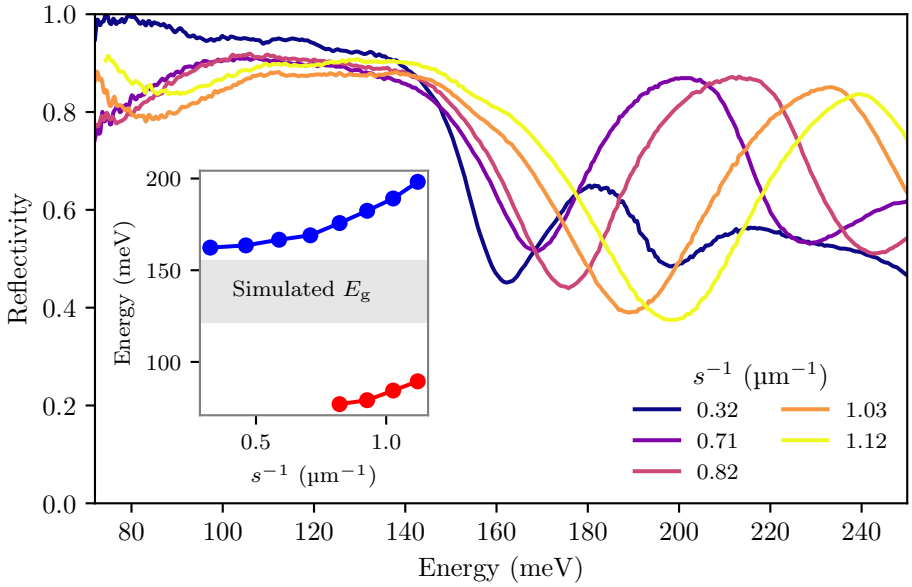

Fig. 7.6 Reflectivity spectra measured at room temperature for G0696 devices of various stripe width s are plotted. In the inset, the experimental energies of the upper and lower polariton resonances are plotted as a function of s^{-1}. The photonic gap extracted from finite element simulations is plotted.

For the smallest value of s^{-1}, the upper polariton resonance is at 162 meV, close to the energy of the bare Berreman mode. As s^{-1} is increased, the upper polariton resonance blueshifts towards increasingly high energies. Minima in the reflectivity spectra corresponding to the lower polariton mode are distinguishable at energies of 90 meV or less for the spectra shown with the three largest values of s^{-1}. For the other values of s^{-1}, the lower polariton redshifts to energies below the cut-off of the MCT detector used in the experiment. The contrast of the lower polariton is significantly reduced from that of the upper polariton, a consequence of the choice of the stripe separation length, o.

The dispersion of the upper and lower polariton modes is plotted in the inset of Fig. 7.6. A photonic gap is clearly present, indicating that the ultrastrong coupling regime has been

[4]These measurements were performed with the aid of Baptiste Fix at the Optics and Associated Techniques Department (DOTA) of ONERA.

reached. However, without reflectivity spectra for larger values of s^{-1}, the asymptote which sets the upper bound for the lower polariton branch cannot be determined, and thus the Rabi energy is not extracted from the experimental dispersion. The photonic gap from the finite element simulations of Fig. 7.3 is plotted on the inset for comparison.

In the simulated spectra of Fig. 7.3, the contrast of the upper polariton mode approaches unity when the mode is resonant near 175 meV, and then declines as the mode is blueshifted, though it still remains near 85 % when the upper polariton is at 200 meV. In the experimental spectra, the contrast is found to continually increase as the polariton mode is blueshifted, reaching of maximum of just over 60 % for the spectrum measured from the device with the largest value of s^{-1}.

The FWHM of the experimental upper polariton resonances is about 23 % of the mode energy; for the simulated spectra, the FWHM of the upper polariton modes between 160 meV and 200 meV is about 9.5 % of the mode energy. The larger linewidths observed in the experiment explain the discrepancy in the contrast between the simulation and experiment. The broader experimental linewidths are likely due to imperfections in the definition of the stripe resonators during the ICP etch step. SEM images showed that the sidewalls of the resonators were not smooth.

7.4.2 Electrical Characterization

Before proceeding, it is noted that the results presented in this section are from the study of devices fabricated separately from those for which the optical spectra were reported in the previous section. An electrical short due to a fabrication issue prevented the study of the electrical properties of those devices. The optical characterization of the devices studied in this section has not yet been performed, but it is expected to yield similar results as those described in the previous section.

For all contact schemes, the G0696 resonator devices were much less resistive near zero bias than the G0662 mesa devices studied in the previous chapter. Current-voltage curves for the Top-Middle contact scheme are plotted in Fig. 7.7a for resonator devices of various stripe widths and for the G0662 mesa device studied in the previous chapter. Under a negative bias of the same magnitude at which plasmonic photocurrent could be observed from the G0662 mesa device (around −200 mV), an orders of magnitude larger current density is observed for the resonator devices.

In Fig. 7.7b, current-voltage curves for the Top-Middle and Bottom-Middle contact configurations of the same s=2.86 µm G0696 device are plotted. Contrary to the case for the G0662 mesa device, in which the bottom barrier was found to be much more resistive than the top barrier (see Fig. 6.19), for the s=2.86 µm G0696 device, the I-V curves for the two contact configurations are rather similiar, with the Top-Middle configuration actually being slightly more resistive near zero bias than the Bottom-Middle configuration.

The reason for the reduced resistivity of the resonator devices, and specifically, the huge reduction in the differential resistance around zero bias as compared with the G0662 mesa device, is not known.[5] Interestingly, the differential resistance around zero bias for the Top-Middle configuration shown in Fig. 7.7a is reduced almost systematically as the stripe width is reduced. It is possible that a contaminating layer is deposited on the sidewalls of the

[5]To rule out the influence of the wafer bonding step, mesa structures were fabricated on a wafer bonded sample, and were found to have the same electrical properties as mesas fabricated directly on the InP substrate.

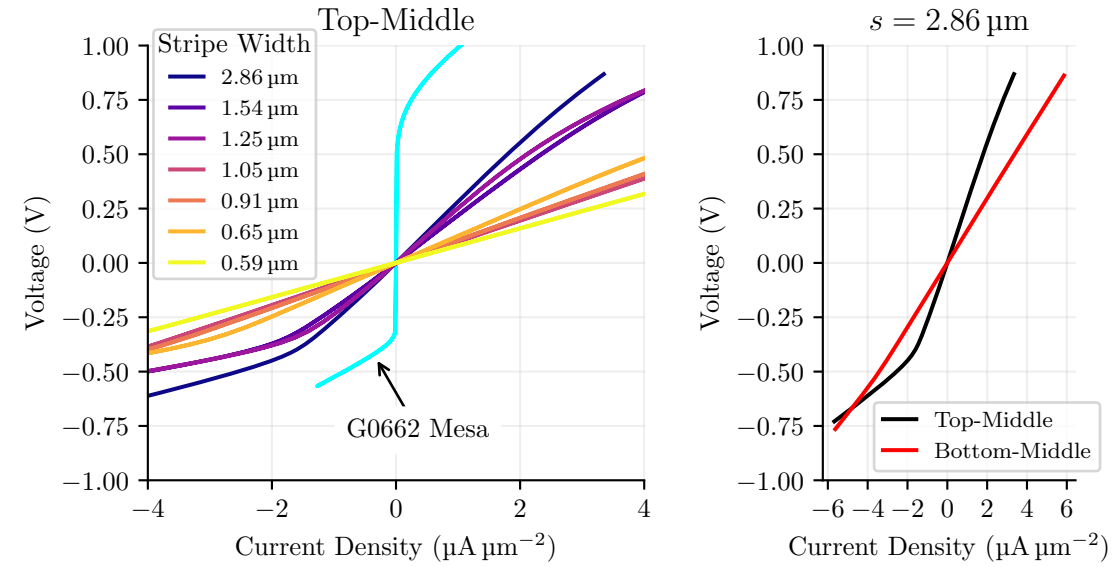

(a) (b)

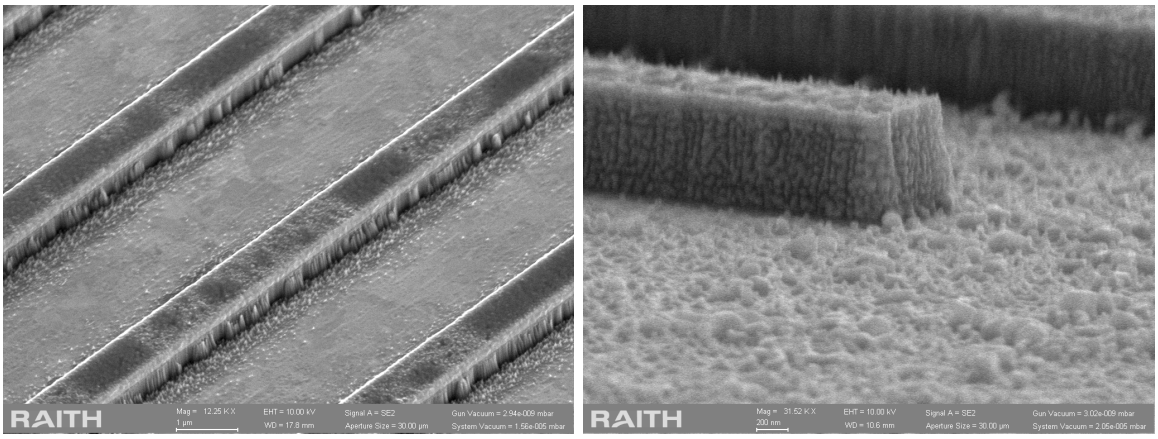

(c) (d)

Fig. 7.7 (a) I-V curves measured at T=10 K between top contact and middle layer for various devices. The differential resistance of the 100 µm diameter G0662 circular mesa around zero bias is much greater than that of any of the G0696 resonator devices. (b) I-V curves measured at T=10 K for different contact schemes of same G0696 s=2.86 µm device. The resistance of the Bottom-Middle curve is even less than that of the Top-Middle configuration. (c) SEM image of G0696 sidewalls (12.25 k× magnification). Unknown features are found to mar the resonator sidewalls. (d) SEM image of V0760 sidewalls (31.52 k× magnification). A layer of unknown origin covers the sidewalls. The SEM images were taken by Thomas Bonazzi.

resonators during the ICP etch step which provides an additional current pathway. The relative contribution of current passing through a sidewall path to the total current would be expected to increase as the resonator width is reduced.

An SEM image of the G0696 sidewalls immediately after the ICP step is shown in Fig. 7.7c, where unknown features can be observed. Another SEM image is presented in Fig. 7.7d, in which an unknown material is seen coating the sidewalls of a similar sample (V0760), fabricated in the same manner.

7.4.3 Photoresponsivity Measurements

For the same experiment described in Section 6.2.2, using the internal blackbody of the FTIR as the light source, and employing a lock-in detection technique, no photoresponse could be detected above the noise level from the resonator devices at T=10 K for any contact configuration under any voltage bias. For this reason, the photoresponse of the devices was studied under laser illumination from the tunable MIRcat multi-QCL system, introduced in the previous chapter and characterized in Appendix D.

Unfortunately, the largest energy to which the MIRcat laser could be tuned was 167.5 meV. The investigation was thus limited to excitation energies far below the region in which the upper polariton resonances are expected for the devices. Nonetheless, in what follows, we present indirect evidence that the resonator devices show a resonant photoresponse at the energy of the upper polariton mode.

We begin by comparing the photoresponse of the G0696 resonator device with the largest stripe width, s=2.86 µm, to that of the G0662 100 µm diameter mesa. For this stripe width, corresponding to a value of $s^{-1} = 0.35\,\mu\text{m}^{-1}$, the upper polariton mode is expected at 159 meV, only slightly blueshifted from the bare resonance of the Berreman mode. Therefore, a photoresponse similar to the mesa device is expected.

In the lower panel of Fig. 7.8, the responsivity of the G0696 s=2.86 µm device is plotted as a function of the voltage bias on the middle layer with respect to the top contact, for three different laser energies. The responsivity of the same device is also plotted for a bias between the bottom contact and the middle layer for a single laser energy. The responsivity is determined from the photovoltage signal measured with a lock-in amplifier. For each measurement, a clear 180° shift of the phase of the photovoltage signal was observed on the lock-in for a negative value of the voltage, indicating a reversal in the photocurrent direction. The responsivity curves plotted in Fig. 7.8 have been multiplied by −1 for voltages greater than that at which the phase shift is observed.

The responsivity curve for the Top-Middle contact configuration of the G0696 s=2.86 µm device exhibits a relatively sharp peak at a negative bias of a few hundred millivolts for all three laser excitation energies, similar to what was observed for the G0662 mesa device in Fig. 6.24. As the laser is tuned from 167.5 meV to 139.9 meV and then to 124.0 meV, the peak responsivity drops by a factor of 6, and then 20, with respect to the responsivity measured with the laser fixed to 167.5 meV. This is the expected behavior as the laser is tuned away from the upper polariton, estimated to be at 159 meV, and is also similar to the behavior observed for the responsivity of G0662 mesa as the laser was redshifted away from the Berreman mode resonance.

The peak responsivity and the bias at which it occurs differ between the G0662 mesa device and the G0696 s=2.86 µm device for the same Top-Middle contact configuration.

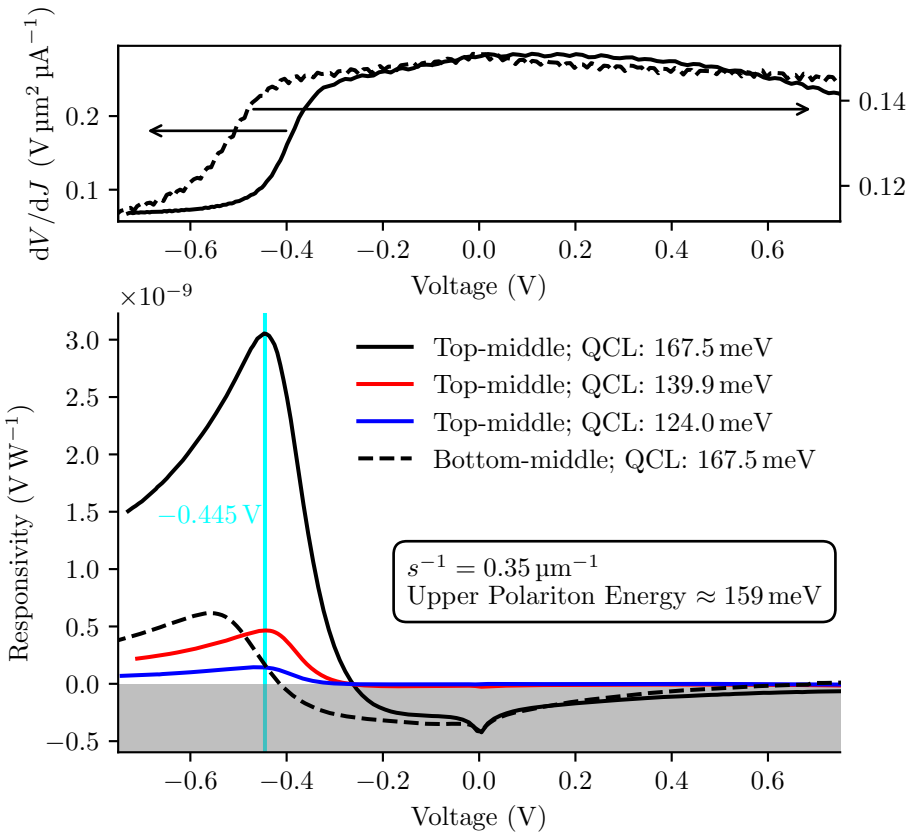

Fig. 7.8 In the upper panel, the differential resistance, calculated as the derivative of the voltage with respect to the current density, is plotted for the G0696 s=2.86 µm device, for the Top-Middle contact scheme (solid lines, left axis) and the Bottom-Middle contact scheme (dotted line, right axis). These curves are the derivatives of the I-V curves plotted in Fig. 7.7b. In the lower panel, responsivity curves for the G0696 s=2.86 µm resonator device, determined from photovoltage measurements recorded at T=7 K, are plotted for the Top-Middle contact scheme for various laser excitation energies, and for the Bottom-Middle contact scheme for a single excitation energy. The responsivity is plotted as a negative quantity over the voltage range for which the photocurrent direction is opposite.

The peak responsivity observed for the G0662 mesa device ($1.8 \times 10^{-7}\,\mathrm{V\,W^{-1}}$) is nearly two orders of magnitude greater than of the G0696 s=2.86 µm device ($3 \times 10^{-9}\,\mathrm{V\,W^{-1}}$) under illumination by the laser tuned to 167.5 meV. This is consistent with the fact that no photoresponse could be detected from the resonator devices under illumination with the blackbody of the FTIR.

For the G0662 mesa device, the peak responsivity was reached for a bias of −0.287 V, whereas for the G0696 s=2.86 µm device, the peak occurs for a bias of −0.445 mV. One of the important findings of the previous chapter, observed for the G0662 mesa device, is that the responsivity peaks near the voltage at which the differential resistance rapidly drops. This correspondence is observed for both the Top-Middle and Bottom-Middle contact schemes of the G0696 s=2.86 µm device in Fig. 7.8, where the differential resistance is plotted in the upper panel on the same voltage axis over which the responsivity is plotted in the lower panel. This suggests that the difference in the bias at which the responsivity peaks for the G0662 mesa device and the G0696 s=2.86 µm device can be attributed to the different electrical characteristics of the devices.

For the same 167.5 meV laser energy, the peak responsivity of the Top-Middle contact configuration is nearly five times greater than the peak responsivity observed for the Bottom-Middle contact scheme. For the G0662 mesa device, the peak responsivity of the Top-Middle contact configuration was 40 times greater than that observed for the Bottom-Middle contact scheme. For the G0696 s=2.86 µm device, the I-V curves for the Top-Middle and Bottom-Middle configurations are more similar (Fig. 7.7b) than they were for the G0662 mesas (Fig. 6.19). This explains why the relative difference in responsivity between the contact configurations is reduced.

The upper polaritons of the various G0696 device cannot be directly excited since they lie at energies above the tuning range of the MIRcat. Instead, we fix the energy of the laser to 167.5 meV and measure the responsivity of the detectors as the upper polariton mode is tuned away from the laser and to increasingly large energy. In practice, this corresponds to measuring the responsivity of various devices for decreasing stripe width s, or for increasing value of s^{-1}.

In the upper left panel of Fig. 7.9, the responsivity is plotted as a function of the bias voltage for G0696 devices of different stripe width contacted in the Top-Middle configuration under illumination by the laser at 167.5 meV. The responsivity of each device reaches a maximum between −0.4 V and −0.6 V. The peak responsivity is found to systematically decline as the the value of s^{-1} (and the energy of the upper polariton mode) is increased.

If the photocurrent response of the devices mirrors the optical absorption, so that resonances in the photocurrent occur at the energies of the upper polariton mode, then the responsivity of the devices should decrease as the upper polariton mode is blueshifted away from the fixed energy of the laser. This is exactly the behavior observed in Fig. 7.9.

A particular interest of this study was to look for a modification of the voltage at which the responsivity peaks, as the energy of the upper polariton is modified. If the internal photoemission model describes the photocurrent generation process, then for a cut-off energy fixed by the conduction band potential, an increase in the energy of the excited polariton mode should result in a reduction of the bias voltage at which the peak responsivity is observed.

The bias voltage at which the peak responsivity is observed in the upper left panel of Fig. 7.9 does not follow a monotonic trend with s^{-1}. Instead, the bias voltage at which

the peak responsivity is observed for a given device correlates with the voltage at which the differential resistance of the I-V curve undergoes a decline, as shown in the bottom left panel of Fig. 7.9. We are unable to conclude from our data that the polariton energy modifies the voltage for which the peak responsivity is observed.

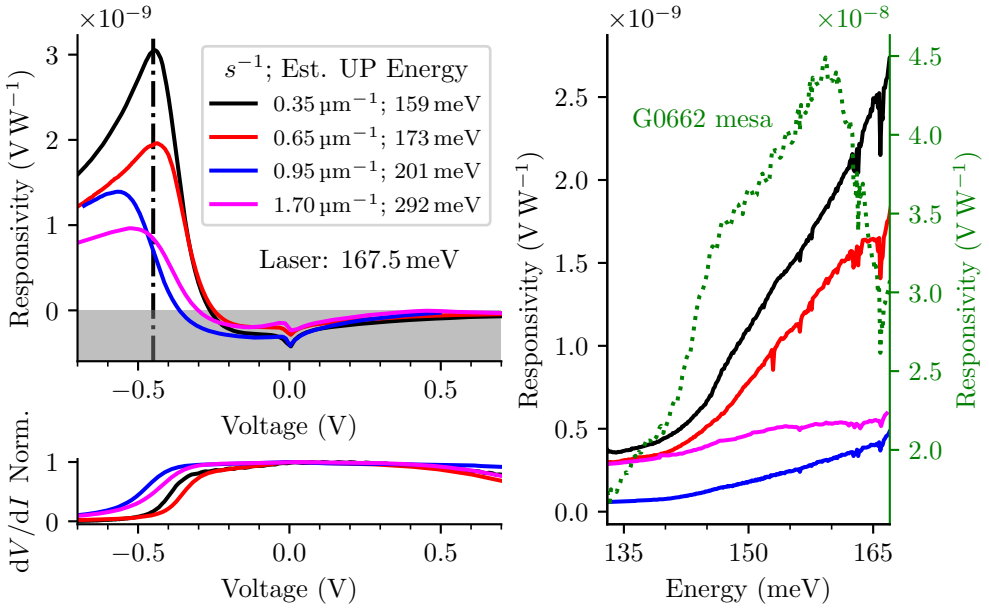

Fig. 7.9 In the upper left panel, photovoltage responsivity curves are plotted for resonators of varying stripe width s under illumination by the laser at 167.5 meV. The estimated energy of the upper polariton (UP) mode is indicated in the legend. In the lower left panel, the differential resistance, normalized between zero and one, is plotted for the same devices. Responsivity spectra are plotted in the right panel for the same devices, biased at −450 mV (indicated by dashed vertical line in upper left panel). The responsivity measured for the G0662 mesa device for a voltage of −287 mV is plotted on the right y-axis. All devices are contacted in the Top-Middle configuration.

In the right panel of Fig. 7.9, photovoltage responsivity spectra measured at a bias of −450 mV are plotted for the same devices studied in the left panels. The photovoltage spectrum of the G0662 mesa measured under a bias of −287 mV, corresponding to its peak responsivity, is plotted on the right y-axis for comparison. As already stated, the responsivity of the mesa device is far superior to the resonator devices.

Whereas the responsivity peak of the G0662 mesa device can be observed at 159 meV, the peak responsivities of the polariton devices lie beyond the cut-off of the MIRcat laser. It is noteworthy that the upper polariton for the $s^{-1} = 0.35\,\mu\text{m}^{-1}$ device appears to lie beyond the 167.5 meV cut-off, since the resonance for the upper polariton of a device with $s^{-1} = 0.32\,\mu\text{m}^{-1}$, fabricated from the same sample, was observed at 160 meV in the reflectivity spectra of Fig. 7.6.

For increasing value of s^{-1}, the responsivity spectra of the polariton devices have a smaller slope for a given energy. Additionally, excluding the spectra from the $s^{-1} = 0.95\,\mu\text{m}^{-1}$

device, the amplitude of the responsivity spectra are systematically reduced as the value of s^{-1} is increased. The $s^{-1} = 0.95\,\mu m^{-1}$ device only fails to follow this trend because the peak responsivity for this device occurs at a smaller bias voltage than the other spectra. The dashed vertical black line in the upper left panel of the figure indicates the voltage at which the polariton device responsivity spectra were measured. It is evident that if the responsivity spectra were measured for a slightly smaller voltage, the trend in the decrease of the spectral amplitude with increasing value of s^{-1} would be monotonic.

The reduction in amplitude and slope of the responsivity spectra with increasing value of s^{-1} is exactly the behavior expected if the responsivity spectra are measured on the low energy tail of a resonance which is blueshifting with increasing value of s^{-1}. The results presented here thus constitute the first preliminary evidence of the detection of resonant photocurrent features originating from polaritons in the ultrastrong coupling regime.

7.5 Conclusion

For the first time, metal-dielectric-metal microcavities with three contact terminals were fabricated. While the ICP etch procedure still requires some improvement, this is a significant step which introduces a new degree of electrical control to be exploited in future studies of microcavity polariton devices.

Optically, the devices were demonstrated to work in the ultrastrong coupling regime. Electrically, the devices were much less resistive than expected and more investigation is required to determine the underlying cause. Photocurrent was detected under laser illumination, and the first evidence of photocurrent features from polaritons in the ultrastrong coupling regime was presented.

It is hoped that with the availability of a laser tunable beyond 167 meV, the resonant nature of the photocurrent response of the upper polariton in the ultrastrong coupling regime can be more firmly established for the devices already fabricated. In future devices, the polariton dispersion could be shifted to lower energies by reducing the electronic density of the Berreman mode layer, or by switching to another material system with a heavier effective mass in the well layer, such as GaAs/AlGaAs. With a better understanding of the Berreman mode detection phenomenon, more responsive devices can be fabricated, thus alleviating the laser constraint altogether.

Conclusion

In this work, we have used the many degrees of freedom available in a semiconductor platform to manipulate and control the optical properties of collective electronic excitations.

We demonstrated that plasmonic modes can be studied in a single material semiconductor platform simply by introducing a high density of dopant impurities to a subwavelength layer. The plasmonic modes supported by the highly doped layer, above and below the light line, were characterized with optical measurements and thermal emission experiments. It was shown that under certain conditions, the modes act as perfect absorbers, and as a consequence of Kirchhoff's law, also act as perfect thermal emitters. This demonstrates perhaps the most favorable property of the collective excitations, their extremely strong interaction with light.

One of the unifying themes throughout this work is the coupling of oscillators, or various matter polarizations. In Chapter 3, the polarization of plasma oscillations was coupled to the polarization of the longitudinal phonons. The quantum model introduced for the collective modes in Chapter 4 is, at its core, a description of how polarizations associated with single particle transitions couple to give rise to collective modes. It was from this description that we established the form of the dispersion for the collective modes in a square well potential and directly linked it to the size confinement of the single particle electronic states.

The understanding of the microscopic origin of the collective modes conferred by the quantum model, that they arise from the coupling of polarizations from single particle transitions, immediately leads to the exciting perspective that new collective coherences can be engineered in the system. This is where the semiconductor platform becomes most appealing, as the full technological toolbox of band structure engineering is available to engineer the single particle electronic states, and consequently, the polarizations associated with the single particle transitions. The difficulty of engineering the collective modes, however, is that they represent an *emergent* phenomenon. It is difficult to know, apart from a physicist's intuition, how the design of the single particle band structure will influence the collective excitations.

One of the most basic intuitions in physics is that new properties arise when symmetries are broken. It was with this principle that we successfully demonstrated for the first time that collective modes can be engineered. With this demonstration, we have extended the domain of quantum plasmonics from merely *describing* the effect of quantum confinement on the collective optical response of the electron gas, to the *use* of confinement as a tool to manipulate that response.

One of the most exciting aspects of this work is that it constitutes some first steps towards achieving active plasmonic optoelectronic devices in the mid- and far-infrared. The successful implementation of these devices will require an understanding of how collective excitations

interact with single particle electronic current. Our demonstration that the excitation of the Berreman mode can give rise to a photocurrent is a step in this direction. Moreover, we have demonstrated that the fundamental problem can be studied from two directions in the same device. In one direction, that of photodection, energy is transferred from the collective mode to excited single particle electrons. In the other direction, that of luminescence, we demonstrated that the plasmon mode can be resonantly excited by a transfer of energy from single particle electrons to a collective excitation. The semiconductor platform is ideal for this fundamental study, for, as we have now demonstrated, it permits both the single particle states and collective excitations to be engineered.

An important perspective of this work is an extension of one of the principal themes, the coupling of various oscillators. In this regard, it will be interesting to study hybrid system in which electronic polarizations outside the semiconductor are coupled with the plasmonic modes of the thin highly doped layer in the semiconductor. The plasmonic mode below the light line is particularly well-suited for this venture, as its electric field extends into space beyond the semiconductor surface.

We conclude by remarking that the study of confinement on the collective excitations of the electron gas has been fundamentally enabled by the technological progress of nanotechnology, including, most notably for the present study, the development of well-controlled semiconductor growth methods. It is unlikely that the authors who originally described plasma oscillations in bulk metals could have envisioned that the phenomenon could, one day, not only be studied, but readily manipulated, in the quantum confined regime.

Appendices

Appendix A

Longitudinal Solutions to the Wave Equation

Traveling wave solutions to Maxwell's equations are solutions of the wave equation. To arrive at the wave equation, we combine the two curl equations of Maxwell's set given by:

$$\boldsymbol{\nabla} \times \mathbf{E} = -\frac{\partial \mathbf{B}}{\partial t} \tag{A.1}$$

$$\boldsymbol{\nabla} \times \mathbf{H} = \mathbf{J}_{\text{ext}} + \frac{\partial \mathbf{D}}{\partial t} \tag{A.2}$$

For static $\mathbf{J}_{\text{ext}}$, the wave equation is written:

$$\boldsymbol{\nabla} \times \boldsymbol{\nabla} \times \mathbf{E} = -\mu_0 \frac{\partial^2 \mathbf{D}}{\partial t^2} \tag{A.3}$$

Assuming time harmonic solutions for the fields, the wave equation may be written:

$$\mathbf{q}\left(\mathbf{q} \cdot \mathbf{E}\right) - q^2 \mathbf{E} = -\varepsilon_{\text{r}}\left(\omega\right) \frac{\omega^2}{c^2} \mathbf{E} \tag{A.4}$$

where the speed of light has been introduced as $c = \left(\epsilon_0 \mu_0\right)^{-\frac{1}{2}}$. For transverse waves ($\mathbf{q} \perp \mathbf{E}$), the solutions to the wave equations are those satisfying:

$$q^2 \mathbf{E} = \varepsilon_{\text{r}}\left(\omega\right) \frac{\omega^2}{c^2} \mathbf{E} \tag{A.5}$$

This expression determines the dispersion relation for transverse waves:

$$\omega^2 = \frac{c^2 q^2}{\varepsilon_{\text{r}}(\omega)} \tag{A.6}$$

For longitudinal waves ($\mathbf{q} \parallel \mathbf{E}$), the left side of Eq. (A.4) goes to zero, and nontrivial solutions are only found for:

$$\varepsilon_{\text{r}}\left(\omega\right) = 0 \tag{A.7}$$

Note that one can already see from Gauss's law that the dielectric function must go to zero for the medium to support a longitudinal wave [149] in the absence of external charge. In neutral media, Gauss's law states that the divergence of the displacement field is zero:

$$\boldsymbol{\nabla} \cdot \mathbf{D} = \mathbf{q} \cdot \mathbf{D} = 0 \tag{A.8}$$

For a spatially homogeneous dielectric function, we find:

$$\varepsilon\,(\mathbf{q}\cdot\mathbf{E_0}) = 0 \tag{A.9}$$

This equation is satisfied automatically for transverse waves, but requires $\varepsilon \to 0$ for longitudinal waves.

Since $\varepsilon = 0$ is a necessary condition for longitudinal waves, then these waves have no displacement field accompanying them, since $\mathbf{D} = \varepsilon\mathbf{E} = 0$.[1] From this fact, we may easily demonstrate that a longitudinal electronic wave can only exist in a medium with a nonzero polarization density. From the definition of the displacement given in Eq. (1.2), for $\mathbf{D} = 0$ it holds that

$$\mathbf{P} = -\epsilon_0\mathbf{E} \tag{A.10}$$

While it may seem obvious that a nonzero polarization density is necessary to support a longitudinal wave, note that it contrasts strongly with the case for transverse waves, which of course appear in vacuum in the absence of any charge.

Longitudinal waves cannot couple with light (transverse radiation) in an *infinite* medium. For this reason, to study longitudinal waves in a plasma, a beam of accelerated electrons is used to excite the mode, since such a beam may be described as a longitudinal wave.

[1] In the case of transverse waves in the absence of damping, at the resonance frequency ω_0 it may be said that no electric field accompanies the wave since $\mathbf{E} = \frac{\mathbf{D}}{\varepsilon}$ and $\varepsilon(\omega_0) \to \infty$ at ω_0.

Appendix B

Photovoltaic Berreman Mode Photodetector

The strong influence of static charge effects on the device band structure was not fully appreciated at the outset of our study of the Berreman mode photodetectors. In the following, the experimental results of a study in which an attempt was made to engineer the continuum of electronic states above the barrier in order to engineer the transport of photoexcited electrons are reported. The sample studied was designed without the consideration of static charge effects. Consequently, the effect of the quantum engineering is not realized as intended.

B.1 Engineering of the Continuum States

If static charge effects are neglected, the electronic potential for sample V0386, introduced in Section 6.2.1, is that of a square 100 nm InGaAs/AlInAs quantum well with a barrier height of 0.52 eV. For an electronic density of $N_v = 2 \times 10^{19}\,\mathrm{cm}^{-3}$ in the well, the Fermi level lies 110 meV below the AlInAs barrier edge. Electrons excited to an energy $\hbar\omega_{\mathrm{Berr}} = 169\,\mathrm{meV}$ above the Fermi level should therefore be freed from the quantum well.

To collect the electrons excited above the barrier edge, a bias would need to be applied. However, due to the small energy difference between the barrier edges of the quantum well and the Fermi level (a small activation energy), a large dark current would result from the application of even a small bias. To avoid this issue, a sample was designed to operate in photovoltaic mode. Sample V0385 was designed with the same dimensions as sample V0386, described in the text, except a series of five tunnel-coupled quantum wells were introduced in the 84.4 nm barrier region (see Page 201 for the growth sheet).

The series of tunnel-coupled quantum wells realizes a Bragg reflector for the electronic wavefunctions over an energy range just above the barrier edge [20, 118]. This is shown in the left panel of Fig. B.1, where a forbidden band can be observed above the barrier to the right of the 100 nm well. As sketched with the gray arrow, over a given energy band, excited electrons should undergo preferential transport in the direction opposite the Bragg reflector. This concept was experimentally demonstrated in [121].

The V0385 sample was designed for the band structure plotted in the left panel of Fig. B.1. However, when static charge effects are considered, the band structure appears like that plotted in the left panel of Fig. B.1. The electronic potential is strongly modified due to

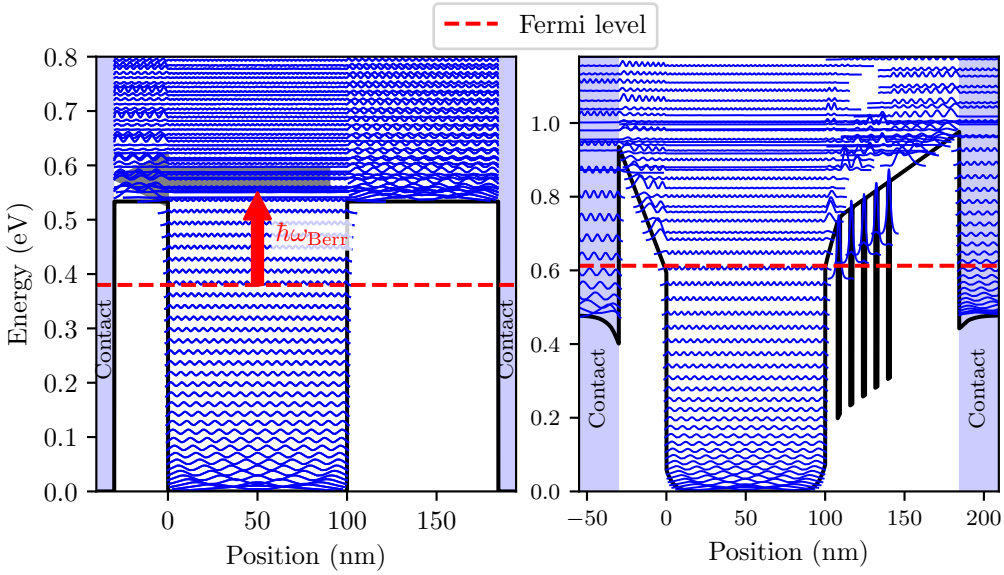

Fig. B.1 The band structure of sample V0385 is plotted on the left neglecting static charge effects, and on the right, as the self-consistent solution to the Schrödinger and Poisson equations. The band structure on the left is calculated considering nonparabolicity using the $\mathbf{k} \cdot \mathbf{p}$ method for 8 coupled bands, whereas the band structure on the right is calculated for a constant effective mass (single band approximation). The band structures were calculated with nextnano.

the nonuniform distribution of electronic densities across the structure. The first forbidden band of the Bragg reflector lies below the maximum barrier height that an electron must overcome to reach a contact, and thus losses its intended purpose.

B.2 Experimental Results

The V0385 sample was processed into devices of three different contact schemes as described in Section 6.3.1. This permits the upper 30 nm AlInAs barrier and the lower 84.4 nm electron Bragg reflector region to be studied independently.

Current-voltage (I-V) curves, measured for the V0385 devices at T=7 K for each of the three contact schemes, are shown in Fig. B.2. The voltages are applied to the second contact, with respect to the first contact, of the device name. As was the case for the V0386 sample studied in the main text, the Top-Middle I-V curve is completely linear and has a resistance of less than 5 Ω, indicating that dopants were unintentionally incorporated into the upper 30 nm AlInAs layer during the growth. The Top-Bottom and Middle-Bottom I-V curves are quite similar, as expected due to the very small ohmic resistance between the top and middle layers.

The V0386 Top-Bottom I-V curve is plotted on the right y-axis for comparison. Despite the fact that the only intentional difference in the growth of the V0385 and V0386 samples was the introduction of the series of tunnel-coupled quantum wells in the 84.4 nm barrier region of the V0385 sample, the Top-Bottom I-V curves are dramatically different between the

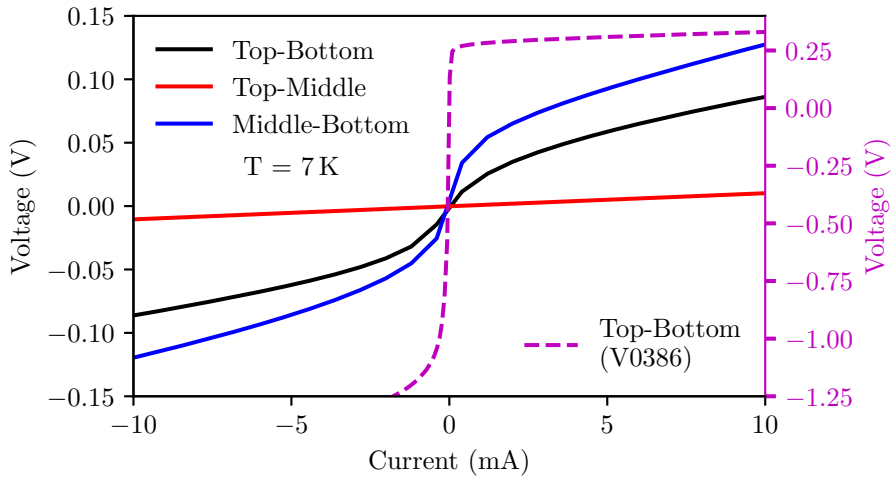

Fig. B.2 Current-voltage curves for 100 µm diameter V0385 mesas devices of various contact schemes measured at T=7 K are plotted on the left y-axis. The current-voltage curve for the V0386 Top-Bottom device measured at T=7 K is plotted on the right y-axis for comparison.

two samples. The V0386 Top-Bottom I-V curve shows a near infinite differential resistance from −1 V to 0.25 V, while for a bias of less than 100 mV, the differential resistance of the V0385 Top-Bottom I-V curve is just a few ohms. Both the Top-Bottom and Middle-Bottom I-V curves for the V0385 sample are quite symmetric with respect to the voltage, whereas the Top-Bottom I-V curve of the V0386 sample is strongly asymmetric.

It is not expected from the band structure modeling of the nominal V0385 and V0386 samples that the inclusion of the tunnel-coupled wells should so dramatically reduce the resistance of the device.

The photovoltage measurements for the V0385 Top-Bottom and Middle-Bottom devices are presented in Fig. B.3. For these measurements, the devices were polished with 30° facets and aligned with light normally incident to the facet to realize a 30° angle of incidence inside the semiconductor.

In the upper panels, photovoltage spectra measured in rapid-scan mode are shown for each device for various biases V_{meas}. For both contact schemes, a resonant photovoltage feature is observed at the energy of the Berreman mode for zero and positive bias (on the bottom contact). For comparison, experimental absorption spectra determined from transmission measurements at Brewster's angle are plotted in shaded green, normalized to the maximum photovoltage in each panel. The photovoltage spectra have not been treated to account for the shape of the blackbody light source.

As interpreted similarly in the main text for the V0386 photocurrent spectra, the larger linewidth of the photovoltage resonance compared with the absorption resonance is explained accounting for the difference in radiative lifetime (which contributes to the linewidth) of the plasmon mode due to the different angle of incidence at which the measurements were made.

In the lower panels, the magnitude and phase of the photovoltage signal measured on the lock-in are plotted as a function of the bias voltage V_{meas}.

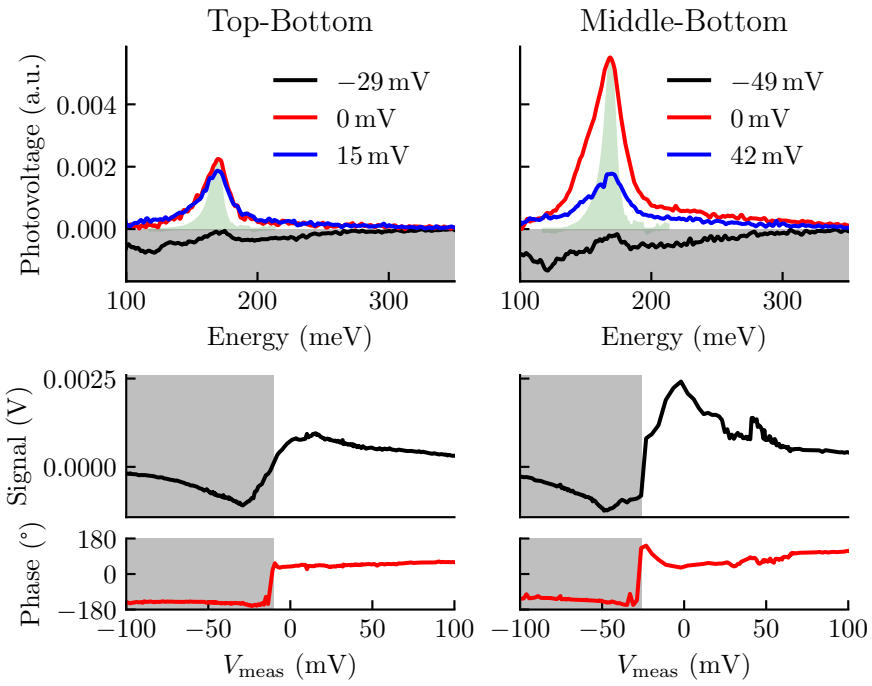

Fig. B.3 Experimental photovoltage results measured at a temperature of 7 K are presented for V0385 devices. The shaded green spectra are absorption measurements at Brewster's angle, normalized to the maximum of the photovoltage spectra. As described in the text, the negative polarity of the photovoltage spectra shown in black has been assigned. The negative polarity of the total photovoltage signal in the middle panels has also been assigned according to the analysis of the π-phase shift observed in the phase.

The phase is measured over a period of 2π, but with periodic boundary conditions, meaning, for example, that a phase of −181° will be mapped to 179°. This behavior is observed for the phase of the Top-Bottom and Middle-Bottom devices at biases of −10 mV and −30 mV, respectively. For both devices, the total phase shift is ≈ 180°, indicating a reversal of the photocurrent. The lock-in signal, measured as a strictly positive quantity, has been assigned a negative polarity for the biases below that at which the phase shift occurs. Likewise, the photovoltage spectra measured for biases of −29 mV and −49 mV are assigned a negative polarity. The area under these spectra correspond to photocurrent moving in the opposite direction with respect to that of the spectra measured at zero and positive biases.

We determine that for zero and positive bias, photoexcited electrons from the plasmon mode are collected at the bottom contact, and thus move over the Bragg reflector region of the structure, contrary to expectation and the intended design of the device. For negative bias, the direction of the photocurrent is reversed, and photoexcited electrons move towards the top or middle. The magnitude of the negative polarity photocurrent under negative bias is reduced near the energy of the Berreman mode. This is explained considering that the photocurrent contribution from the Berreman mode continues to move towards the lower contact, canceling some of the photocurrent moving in the opposite direction.

The photocurrent measured from the Top-Bottom and Middle-Bottom devices is essentially identical, both in spectral form as a function of applied bias, and in terms of the signal and phase as a function of the bias. This further confirms the conclusion from the electrical measurements that the top barrier is electrically shorted.

The primary observation from this study is that the plasmonic photocurrent moves over the Bragg reflector region of the sample towards the lower contact, in contrast to expectation, even for a small negative bias. Because the upper 30 nm barrier is doped, the only barrier over which electrons can be photoexcited and captured is the 84.4 nm region with the tunnel-coupled quantum wells. That photocurrent is collected from this pathway suggests that the devices operate similarly to internal emission Schottky photodiodes.

We conclude by noting that the V0385 devices are thus far the the only Berreman mode photodetectors for which a resonant plasmonic feature has been observed without an applied bias. In all the other samples studied, the bias for which the plasmonic photocurrent is observed corresponds with the voltage at which the differential resistance undergoes a dramatic decline. Of note, the V0385 samples are the only devices studied in which the differential resistance is already small close to zero bias.

Appendix C

MOCVD-Grown Berreman Mode Photodetectors

As described in the main text, a series of samples similar to the MBE-grown G0662 sample were grown with MOCVD. Results from the investigation of these samples are reported here.

Samples V0580, V0581, and V0582 were designed to be symmetric around a central 200 nm highly doped InGaAs layer. On both sides of the central layer is a 10 nm not-intentionally-doped InGaAs layer, a 100 nm AlInAs barrier, and a 100 nm InGaAs layer nominally doped with an electronic density of $N_v = 1 \times 10^{18}\,\mathrm{cm}^{-3}$ to serve as a contact. The 10 nm intrinsic InGaAs layers were included in the design of the structure in order to limit the unintentional incorporation of dopants in the AlInAs layer grown subsequent to the highly doped InGaAs layer, an effect observed for the V0386 sample studied in the main text, and the V0385 sample studied in Appendix B.

The three structures differ only in the electronic density added to the central 200 nm layer. The electronic density was varied in order to study the photodetection effect as a function of the Berreman mode excitation energy. The actual electronic densities realized in the growth of the samples do not differ much between the structures, as will be evident. The growth sheets of the samples can be found on Pages 203 to 205.

C.1 Optical and Electrical Characterization of Devices

Electronic densities of the 200 nm InGaAs layers were determined by modeling the experimental Brewster's angle transmission spectra shown in the top panel of Fig. C.1.[1] From the simulations plotted in the figure with dashed lines, electronic densities of $1.81 \times 10^{18}\,\mathrm{cm}^{-3}$, $1.61 \times 10^{18}\,\mathrm{cm}^{-3}$, and $1.32 \times 10^{18}\,\mathrm{cm}^{-3}$ were determined for the V0580, V0581, and V0582 samples, respectively.

All three samples were processed into 100 nm diameter circular mesas for the Top-Bottom contact scheme described in Section 6.3.1. Devices of the Top-Middle contact scheme were realized for the V0581 sample.

Current-voltage curves measured at T=7 K for the four types of devices are shown in the middle panel of Fig. C.1. Electrons move from the top contact toward the bottom contact

[1] These measurements were performed by Tereasa Stefanini during her Masters Internship under my guidance.

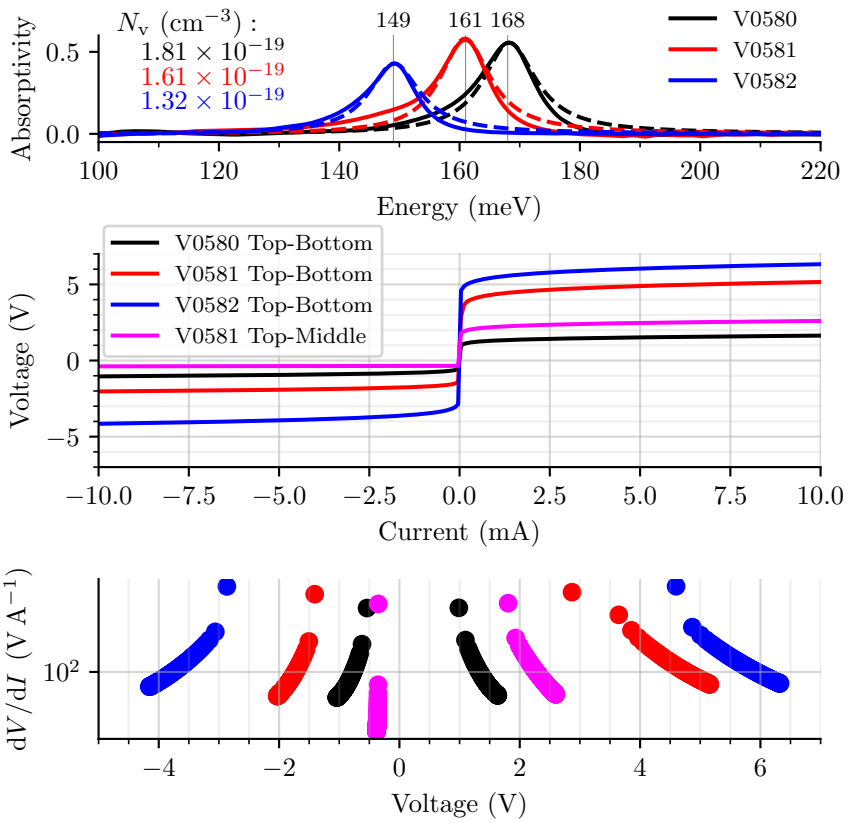

Fig. C.1 Absorption spectra extracted from transmission measurements at Brewster's angle are presented in the upper panel with solid lines. Simulated spectra, from which the electronic densities of the 200 nm highly doped layers are extracted, are plotted in dashed lines. In the middle panel, the voltage response is plotted as a function of the current sourced. In the lower panel, the differential resistance is plotted as a function of the voltage.

(or middle layer) under a positive bias.

All of the I-V curves exhibit near infinite differential resistance around zero bias. For the Top-Bottom devices, there is an inverse relationship between the magnitude of voltage at which the differential resistance drops (associated with a flattening of the I-V curve), and the electronic density of the highly doped 200 nm layer. For example, the differential resistance of the most-doped V0580 sample undergoes a dramatic decline for a positive bias of ≈ 1 V, whereas the differential resistance of the least-doped V0582 sample does not significantly decline until until a bias of approximately ≈ 4.5 V.

Despite the perfect symmetry of the nominal structures, none of the I-V curves are symmetric with respect to the voltage. For each of the curves, the differential resistance undergoes a rapid decline over a range of negative voltages of smaller magnitude than it does for positive voltages. We infer that the upper barrier is slightly less resistive than the lower barrier. This can be attributed to residual doping from the growth of the highly doped 200 nm layer. Note that the severity of this effect, compared with the V0385 and V0386

samples, has been hugely reduced by the inclusion of the 10 nm not-intentionally-doped InGaAs layers.

The I-V curve for the V0581 Top-Middle device, which is an asymmetric structure, is highly asymmetric around zero voltage. The I-V curve flattens (the differential resistance drops) for a negative voltage of smaller magnitude than it does for positive voltage. This implies that the activation energy for electronic transport from the middle layer to the top contact under a bias of similar magnitude is less than the activation energy for transport from the top contact to the middle layer. A similar behavior was observed for the V0386 Middle-Bottom device, and qualitatively explained in the model sketched in Fig. 6.10.

C.2 Photocurrent Measurements

The photoresponse of the Top-Bottom V0580, V0581, and V0582 devices, and the V0581 Top-Middle device was characterized using the experimental set-up described in Section 6.2.2. A 20° facet was polished onto each device. The devices were aligned for light normally incident on the facet for a 20° angle of incidence inside the InP substrate. The photovoltage spectra for these devices were recorded with the FTIR in step-scan mode, with the light mechanically chopped at 160 Hz, a bandpass of 10 Hz-3 kHz selected on the SR560 pre-amplifier, and a 300 ms time constant used on the lock-in amplifier.

A Berreman mode photovoltage resonance was only observed for the Top-Bottom device fabricated from the V0580 sample and for the V0581 Top-Middle device. The results from the study of these two devices are presented in the subsequent sections.

C.2.1 V0580 Top-Bottom

In the left panel of Fig. C.2, raw (strictly positive) photovoltage spectra for the V0580 Top-Bottom device are plotted for various biases between the top and bottom contacts.[2] The spectra were recorded without a polarizer and have not been modified to take into account the shape of the blackbody source which is shown in the upper-left of the figure.

For both positive and negative biases, a resonant feature is observed at 168 meV, the same energy at which the Berreman mode is observed in the Brewster's angle absorption measurements. Though not shown here, the feature was confirmed to only be present for excitation with p-polarized light. It is thus attributed to the Berreman mode.

In all of the spectra, there are additional broad features at energies above the Berreman mode. These features were observed for both p- and s-polarized light. At zero bias, a particularly intense feature centered at 400 meV is observed. If the shape of the blackbody source is considered, the relative responsivity of the device over the energy range of the broad high energy features is even more significant.

The spectra measured at biases of 9 mV, 60 mV, and 88 mV touch zero twice at about 200 meV and 300 meV. This is indicative of a current reversal phenomenon. Over nearly the same energy range, a dip is observed in the spectra measured at biases of 129 mV and 206 mV. The feature observed between 200 meV and 300 meV in the 9 mV, 60 mV, and 88 mV spectra is inferred to correspond to photocurrent moving in the opposite direction of

[2] As described in Section 6.2.2, the current is being sourced, and the bias voltage is the potential difference measured between the two contacts.

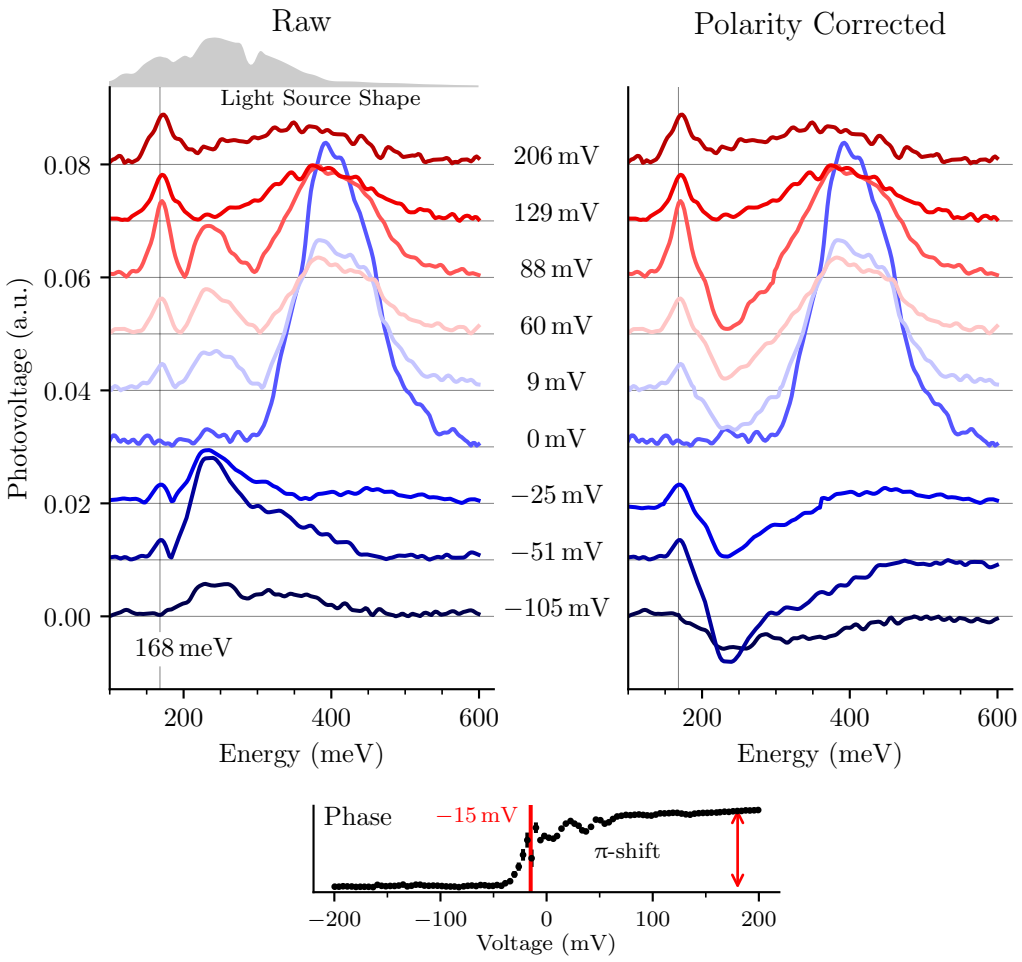

Fig. C.2 In the left panel, raw photovoltage spectra from the V0580 Top-Bottom device are plotted for various potentials between the top and bottom contacts, offset for clarity. The photovoltage spectra have not been treated for the shape of the blackbody source, plotted at the top of the figure. In the right panel, the photovoltage spectra are replotted with some regions assigned a negative polarity, as discussed in the text. At the bottom of the figure, the phase of the total photovoltage signal is plotted as a function of the bias.

the photocurrent observed at the Berreman mode energy. In the right panel of Fig. C.2, the spectra are plotted with the inferred polarity for each region bordered by zero crossings.

At the bottom of the figure, the phase of the total photovoltage signal measured on the lock-in is plotted as a function of the bias. A π-phase shift is observed around $-15\,\mathrm{mV}$. Because the total lock-in signal should be equivalent to the area under the spectrum, this implies that the mathematical area of the spectra shifts sign around $-15\,\mathrm{mV}$. This determines that the sign of the area under the spectrum measured for $0\,\mathrm{mV}$ bias must be the same as the sign of the area under the spectra measured for positive bias. Likewise, it implies that the largest amplitude features of the spectra measured for negative bias must be assigned to the opposite polarity.

Once the polarity of the photovoltage features has been assigned, we are left with the conclusion that the photovoltage from the plasmon mode is always of positive polarity. Then, the plasmonic photocurrent is only detected for electrons photoexcited over the botom 100 nm AlInAs barrier toward the bottom contact. This is consistent with the V0385 and V0386 experiments.

We attribute the broad features at energies above the Berreman mode to the photoemission of electrons excited via free carrier absorption in the highly doped layers, similar to what is described beginning on Page 138. It remains a challenge, however, to explain the physical origin of the current reversal.

No Berreman mode resonance was observed in the photovoltage spectra (not shown) of the V0581 Top-Bottom or V0582 Top-Bottom devices, up to biases of 1 V and 2 V, respectively. However, broad high energy features were observed in the photovoltage spectra of these devices, and were found to behave similarly as a function of bias as the broad features observed in the V0580 Top-Bottom photovoltage spectra.

As highlighted in the main text, there is a correspondence between the bias at which a rapid drop in the differential resistance occurs, and the bias for which the Berreman mode photovoltage can be detected. The differential resistance of the V0581 Top-Bottom and V0582 Top-Bottom devices dramatically drops for biases of magnitude no smaller than 1 V and 4 V respectively, as shown in Fig. C.1. For biases this large, the photovoltage signal was not stable enough to record spectra. This could explain why the Berreman mode feature was not observed for these devices.

C.2.2 V0581 Top-Middle

We now consider the photoresponse of the V0581 Top-Middle device, presented in Fig. C.3. In the left panel, the photovoltage spectra from the V0581 Top-Middle device are plotted without normalization for various biases between the top and middle contacts. The spectra have not been modified to take into account the shape of the blackbody source, shown in the upper right of the figure.

None of the spectra in the series go to zero as a function of the photon energy, and therefore, all of the photocurrent of a given spectrum moves in the same direction, regardless of the photon energy. Spectra measured for positive biases on the middle layer correspond to photocurrent moving from the top contact to the middle layer. Spectra measured for negative biases on the middle layer correspond to photocurrent moving from the middle layer to the top contact. For both polarities, the amplitude of the spectra decreases as the magnitude of the bias goes to zero. In the right panel of the figure, the same spectra are

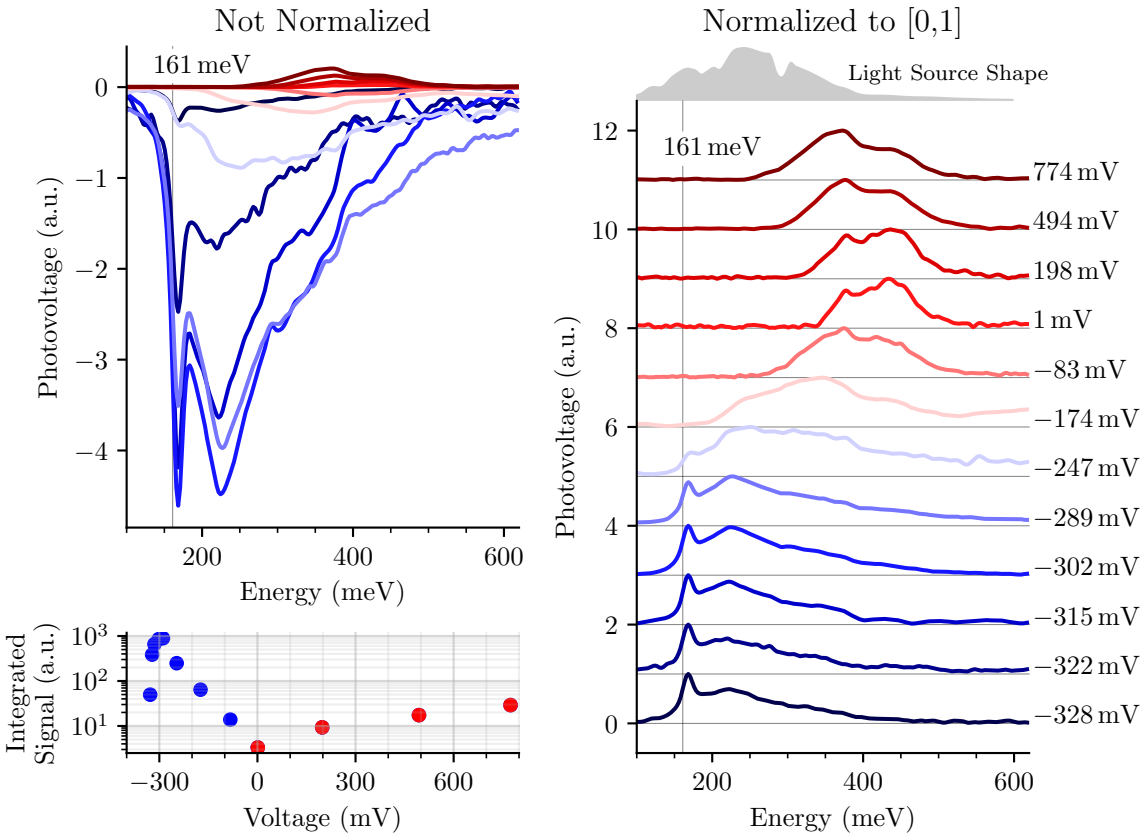

Fig. C.3 In the left panel, photovoltage spectra measured at various biases are plotted without normalization or correction for the shape of the blackbody source. The pairing between the line color and the bias voltage is established in the right panel of the figure, where the same spectra are normalized between zero and one and offset for clarity. In the left panel, spectra measured for negative biases are plotted as negative photovoltage signals.

shown normalized between between zero and one, and offset for clarity.

All of the essential features observed in the V0581 Top-Middle spectra, which are pointed out below, were already observed for the G0662 Top-Middle photovoltage spectra shown in Fig. 6.20. The reader is thus referred to Section 6.4.3 for a more in-depth discussion of the physical phenomena.

The Berreman mode resonance is observed for negative biases of increasing magnitude beginning around −250 mV. This bias corresponds to the voltage at which the differential resistance of the I-V curve begins to decline dramatically.

The Berreman mode resonance is observed in the photovoltage spectra at 168 meV, blueshifted from the 161 meV resonance observed in the Brewster's angle absorption spectrum. In the main text, this was attributed to the dispersion of the mode with in-plane wavevector and the fact that the two measurements are recorded for different angles of incidence.

Broad high energy features are observed at energies above the Berreman mode energy.

The features redshift as the magnitude of the bias voltage is increased. The redshift of the low energy edge of the broad features is more significant for negative biases than positive biases of similar magnitude.

The Berreman mode resonance is only observed for biases for which the broad feature is redshifted to low enough energy to overlap with the Berreman mode. This suggests a common reference energy, above which the Berreman mode decays into hot carriers, and from which single electrons transition, assuming that the broad features are due to free carrier absorption.

The amplitudes of the spectra change dramatically with the applied bias, an effect clearly evident in the set of spectra which have not been normalized. This observation is quantified in the bottom left panel of the Fig. C.3, where the total integrated signal from each spectrum is plotted as a function of the bias voltage on a logarithmic y-axis. The maximum integrated photovoltage signal for a negative voltage is two orders of magnitude larger than the maximum integrated photovoltage signal for a positive voltage.

The negative polarity integrated photovoltage signal peaks for a bias of approximately $-300\,\mathrm{mV}$, which corresponds closely to the voltage at which the differential resistance drops dramatically in the I-V curve. For a positive bias, the differential resistance does not undergo a dramatic decrease until around $2\,\mathrm{V}$. This likely explains why a peak in the integrated photovoltage signal is not observed for a positive bias.

C.2.3 Device Comparison

We conclude this appendix by comparing the responsivity of the V0580 Top-Bottom device to that of the V0581 Top-Middle device. In the upper panel of Fig. C.4, a photovoltage spectrum is plotted for each device, measured at the bias condition for which the amplitude of the Berreman mode feature was maximized. The V0580 Top-Middle spectrum measured at a bias of $88\,\mathrm{mV}$ must be multiplied by a factor of 300 in order for the photovoltage response at the Berreman mode energy to be comparable to that of the V0581 Top-Middle spectrum.

In the lower panel of the same figure, the same spectra are plotted as photocurrent, determined by dividing each photovoltage spectrum by the differential resistance at the bias at which it was recorded. The responsivity of the V0581 Top-Middle device in current per incident power is $100\times$ better than the V0580 Top-Bottom device.

While the two devices were processed from two different growths, this is some evidence that directly contacting the middle highly doped layer is favorable for the observation of the plasmonic photocurrent. This can be justified on account of the fact that a smaller bias is required to achieve the same potential difference between the middle layer and one of the contacts when the middle layer is contacted directly than if bias is applied across the entire structure between the top and bottom contacts.

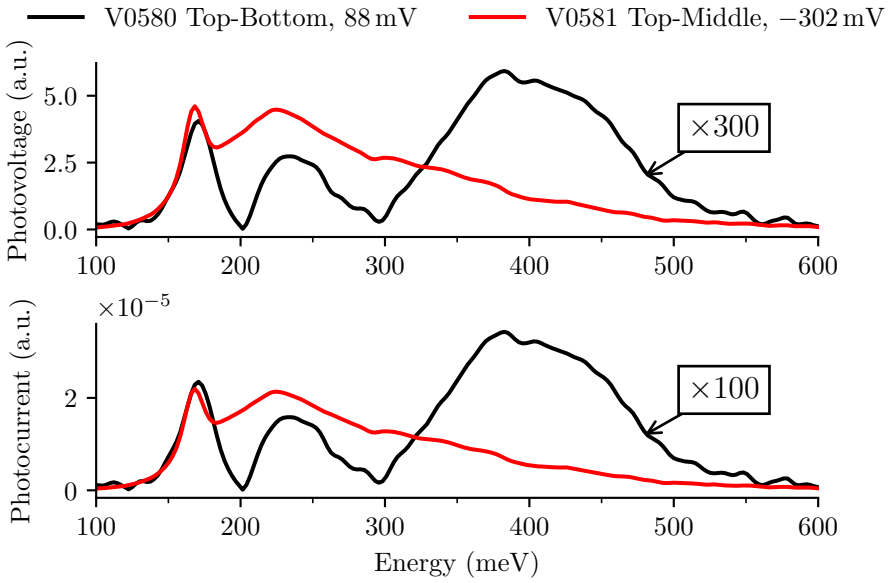

Fig. C.4 In the upper panel, photovoltage spectra from a V0580 Top-Bottom and V0581 Top-Middle devices are compared, after the V0580 Top-Bottom spectrum has been multiplied by 300. In the lower panel, the photovoltage spectra from the upper panel are converted into photocurrent spectra, and the V0580 Top-Bottom spectrum is plotted after multiplication by 100.

Appendix D

Calibration of MIRcat Emission

The MIRcat laser is a one box multi-quantum cascade laser (QCL) system, in which the emission wavelength can be continuously tuned with an external cavity. The MIRcat used in the experiments described in the text had two QCL modules installed: QCL1 could scan from 7.4 µm to 9.35 µm; QCL2 could scan from 8.6 µm to 11.29 µm.

The optical power emitted by either laser varies as a function of the wavelength, peaking close to the center of the tuning range, and rapidly dropping towards the edge. Consequently, to compare the response of photodetectors at different wavelengths (e.g. as in a spectrum), it is necessary to calibrate the emission spectrum of the MIRcat. The calibration of the wavelength-dependent optical power emitted by the MIRcat is shown in Fig. D.1.

In the experiments described in the text, the MIRcat laser is always operated in pulsed mode and set to emit pulses of 960 ns duration at a repetition rate of 100 kHz (9.6 % duty cycle). QCL1 is always sourced with a current of 825 mA, and QCL2 is always sourced with a current of 1200 mA.

To calibrate the MIRcat, its emission is detected via an MCT detector placed into the identical optical set-up as used in the experiment, in which a 1" F1 ZnSe lens focuses the light onto the detector. However, in order not to damage the MCT or saturate its photoresponse, a series of optical densities is placed in the beam path prior to the MCT detector. It is an assumption of the calibration that the transmission of the optical densities is not wavelength dependent.

The optical signal detected by the MCT is plotted as a dotted blue curve in Fig. D.1. The oscillations superimposed on the curve are likely due to a Fabry-Perot effect, perhaps due to the thin window of the MCT packaging. The oscillations are smoothed to obtain the continuous blue curve. The detected emission must be corrected for the relative response of the MCT. For this, the blue curve is divided by the red curve to obtain the shape of the black curve. Finally, the absolute optical power emitted at a fixed wavelength of 9.16 µm (dashed vertical green line) is measured with a power meter, which permits the absolute scaling of the black calibrated QCL emission curve.

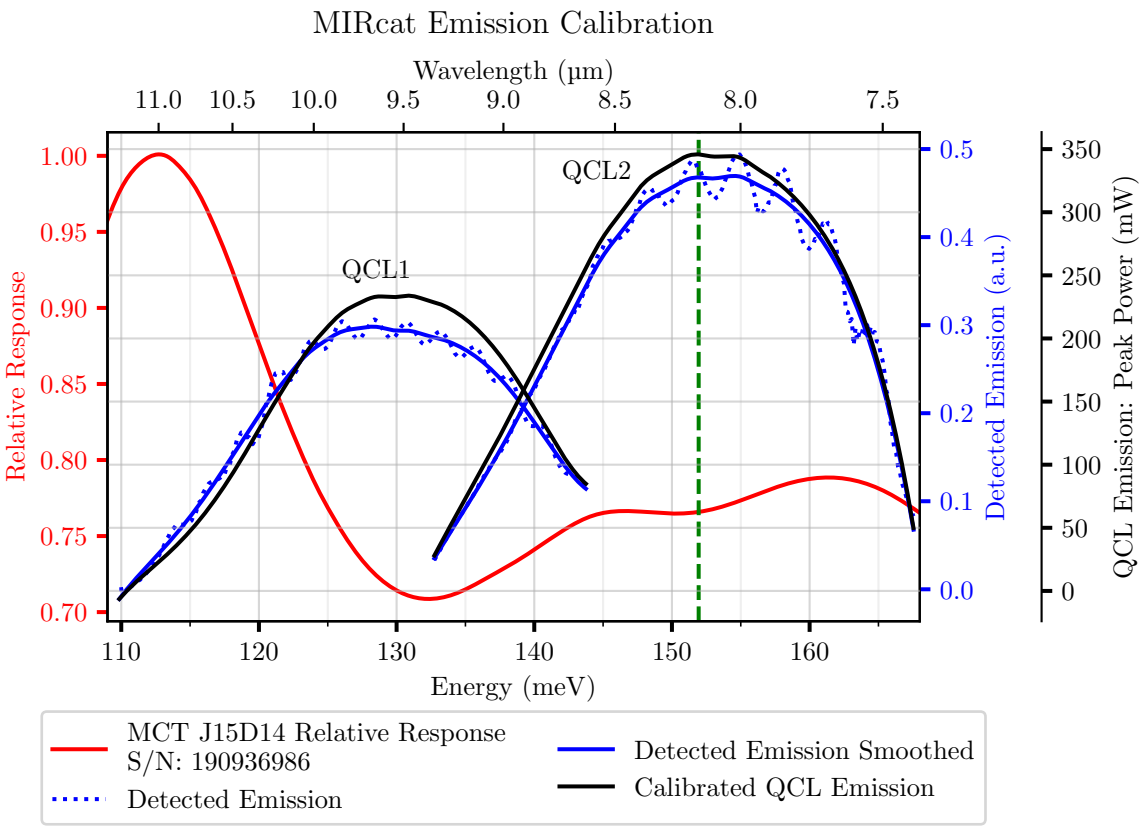

Fig. D.1 Calibration of the emitted optical power of the MIRcat laser as a function of wavelength for 960 ns pulses repeated at 100 kHz, for currents of 825 mA and 1200 mA injected into QCL1 and QCL2, respectively.

Appendix E

Growth Sheets

InP1716

Description	Doping (Nominal)	Desired Thickness (nm)
InGaAs : Si	$1 \times 10^{18}\ \mathrm{cm}^{-3}$	20.0
InGaAs : Si	$2 \times 10^{17}\ \mathrm{cm}^{-3}$	80.0
InGaAs		30.0
AlInAs		10.0
InGaAs		30.0
InGaAs : Si	$2 \times 10^{19}\ \mathrm{cm}^{-3}$	150.0
InGaAs		70.0
InGaAs : Si	$1 \times 10^{18}\ \mathrm{cm}^{-3}$	300.0
Buffer		
InP : Fe		

V0211

Description	Doping (Nominal)	Desired Thickness (nm)
InGaAs		100.0
InGaAs : Si	$2 \times 10^{19}\ \mathrm{cm}^{-3}$	150.0
InGaAs		100.0
Buffer		
InP : Fe		

V0296

Description	Doping (Nominal)	Desired Thickness (nm)	
InGaAs		50.0	
AlInAs		10.0	Repeat 30x
InGaAs		45.0	
AlInAs		10.0	
InGaAs		100.0	
Buffer			
InP: Fe			

V0300

Description	Doping (Nominal)	Desired Thickness (nm)	
InGaAs		50.0	
AlInAs		10.0	Repeat 30x
InGaAs : Si	$2 \times 10^{17}\ \mathrm{cm}^{-3}$	45.0	
AlInAs		10.0	
InGaAs		100.0	
Buffer			
InP: Fe			

V0301

Description	Doping (Nominal)	Desired Thickness (nm)	
InGaAs		50.0	
AlInAs		10.0	Repeat 50x
InGaAs : Si	$1 \times 10^{17}\ \mathrm{cm}^{-3}$	35.0	
AlInAs		10.0	
InGaAs		100.0	
Buffer			
InP: Fe			

V0388

Description	Doping (Nominal)	Desired Thickness (nm)	
InGaAs		20.0	
AlInAs		10.0	
InGaAs : Si	$2 \times 10^{18}\ \mathrm{cm}^{-3}$	50.0	
AlInAs		1.0	Repeat 25x
InGaAs : Si	$2 \times 10^{18}\ \mathrm{cm}^{-3}$	1.0	
AlInAs		10.0	
InGaAs		100.0	
InP: Fe			

V0389

Description	Doping (Nominal)	Desired Thickness (nm)	
InGaAs		20.0	
AlInAs		10.0	
InGaAs : Si	$2 \times 10^{19}\,\mathrm{cm}^{-3}$	50.0	
AlInAs		1.0	Repeat 25x
InGaAs : Si	$2 \times 10^{19}\mathrm{cm}^{-3}$	1.0	
AlInAs		10.0	
InGaAs		100.0	
InP: Fe			

V0588

Description	Doping (Nominal)	Desired Thickness (nm)
InGaAs		50.0
AlInAs		30.0
$(InGaAs)_{0.75}(AlInAs)_{0.25}$: Si	$2 \times 10^{19}\ cm^{-3}$	50.0
InGaAs : Si	$2 \times 10^{19}\ cm^{-3}$	50.0
AlInAs		10.0
InGaAs		100.0
Buffer		
InP: Fe		

V0589

Description	Doping (Nominal)	Desired Thickness (nm)
InGaAs		50.0
AlInAs		30.0
$(InGaAs)_{0.60}(AlInAs)_{0.40}$: Si	$2 \times 10^{19}\ \mathrm{cm}^{-3}$	50.0
InGaAs : Si	$2 \times 10^{19}\ \mathrm{cm}^{-3}$	50.0
AlInAs		10.0
InGaAs		100.0
Buffer		
InP: Fe		

V0390

Description	Doping (Nominal)	Desired Thickness (nm)
InGaAs		20.0
AlInAs		10.0
$(InGaAs)_{0.50}(AlInAs)_{0.50}$: Si	$2 \times 10^{19}\ \mathrm{cm}^{-3}$	50.0
InGaAs : Si	$2 \times 10^{19}\ \mathrm{cm}^{-3}$	50.0
AlInAs		10.0
InGaAs		100.0
Buffer		
InP: Fe		

V0590

Description	Doping (Nominal)	Desired Thickness (nm)
InGaAs		50.0
AlInAs		30.0
$(InGaAs)_{0.40}(AlInAs)_{0.60}$: Si	$2 \times 10^{19}\ \mathrm{cm}^{-3}$	50.0
InGaAs : Si	$2 \times 10^{19}\ \mathrm{cm}^{-3}$	50.0
AlInAs		10.0
InGaAs		100.0
Buffer		
InP: Fe		

V0385

Description	Doping (Nominal)	Desired Thickness (nm)	
InGaAs : Si	$2 \times 10^{18}\ \mathrm{cm}^{-3}$	50.0	
AlInAs		30.0	
InGaAs : Si	$2 \times 10^{19}\ \mathrm{cm}^{-3}$	100.0	
AlInAs		7.9	
InGaAs		1.4	Repeat 5x
AlInAs		7.9	
AlInAs		30.0	
InGaAs : Si	$2 \times 10^{18}\ \mathrm{cm}^{-3}$	100.0	
InP: Fe			

V0386

Description	Doping (Nominal)	Desired Thickness (nm)
InGaAs : Si	$2 \times 10^{18}\ \mathrm{cm}^{-3}$	50.0
AlInAs		30.0
InGaAs : Si	$2 \times 10^{19}\ \mathrm{cm}^{-3}$	100.0
AlInAs		84.4
InGaAs : Si	$2 \times 10^{18}\ \mathrm{cm}^{-3}$	100.0
InP: Fe		

V0580

Description	Doping (Nominal)	Desired Thickness (nm)
InGaAs : Si	$1 \times 10^{18}\ \mathrm{cm}^{-3}$	100.0
AlInAs		100.0
InGaAs		10.0
InGaAs : Si	$2 \times 10^{19}\ \mathrm{cm}^{-3}$	200.0
InGaAs		10.0
AlInAs		100.0
InGaAs : Si	$1 \times 10^{18}\ \mathrm{cm}^{-3}$	100.0
Buffer		
InP: Fe		

V0581

Description	Doping (Nominal)	Desired Thickness (nm)
InGaAs : Si	$1 \times 10^{18}\ \mathrm{cm}^{-3}$	100.0
AlInAs		100.0
InGaAs		10.0
InGaAs : Si	$1 \times 10^{19}\ \mathrm{cm}^{-3}$	200.0
InGaAs		10.0
AlInAs		100.0
InGaAs : Si	$1 \times 10^{18}\ \mathrm{cm}^{-3}$	100.0
Buffer		
InP: Fe		

V0582

Description	Doping (Nominal)	Desired Thickness (nm)
InGaAs : Si	$1 \times 10^{18}\ \mathrm{cm}^{-3}$	100.0
AlInAs		100.0
InGaAs		10.0
InGaAs : Si	$5 \times 10^{18}\ \mathrm{cm}^{-3}$	200.0
InGaAs		10.0
AlInAs		100.0
InGaAs : Si	$1 \times 10^{18}\ \mathrm{cm}^{-3}$	100.0
Buffer		
InP: Fe		

G0662/G0696

Description	Doping (Nominal)	Desired Thickness (nm)
InGaAs : Si	$2 \times 10^{18}\ \mathrm{cm}^{-3}$	50.0
AlInAs		50.0
InGaAs		10.0
InGaAs : Si	$2 \times 10^{19}\ \mathrm{cm}^{-3}$	180.0
InGaAs		10.0
AlInAs		50.0
InGaAs : Si	$2 \times 10^{18}\ \mathrm{cm}^{-3}$	100.0
InP: Fe		

Appendix F

Résumé en français

Chapitre 1

Dans la gamme spectrale de l'infrarouge, la réponse optique des couches semiconductrices d'épaisseur inférieure à la longueur d'onde est déterminée microscopiquement par les vibrations du réseau cristallin (les phonons) et, dans le cas où le semiconducteur est fortement dopé, par la pulsation de plasma du gaz d'électrons.

Dans les matériaux massifs, les résonances optiques ont généralement lieu aux pôles de la fonction diélectrique, tandis qu'elles se produisent aux zéros de la fonction diélectrique dans le cas des couches sub-longueur d'onde soumises à une lumière polarisée p incidente à des angles obliques. Ce phénomène est appelé l'effet Berreman. La nature résonante de l'effet est classiquement expliquée en considérant que la lumière induit une polarisation uniforme dans la couche mince, faisant apparaitre sur les côtés opposés de la couche des densités surfaciques de charge positive et négative, formant un dipôle macroscopique.

Il faut préciser que, pour les couches minces décrites par une fonction diélectrique isotrope, les résonances sont observées aux pôles *et* aux zéros de la fonction diélectrique dans les spectres expérimentaux. La composante du champ électrique de la lumière parallèle au plan de couche excite les résonances aux pôles de la fonction diélectrique, alors que la composante perpendiculaire du champ électrique excite les résonances aux zéros à cause de l'effet Berreman. De ce fait, on observe dans les spectres polarisés p des couches minces semiconductrices, mesurés en incidence oblique, des pics aux fréquences des phonons transverses (les pôles de la fonction diélectrique) et aux fréquences des phonons longitudinaux (les zéros de la fonction diélectrique).

La réponse optique des électrons d'une couche dopée d'une épaisseur suffisante pour que les électrons ne soient pas confinés quantiquement est décrite par la fonction diélectrique isotrope de Drude. La fonction de Drude peut être décrite comme ayant un pôle à fréquence nulle et un zéro à la fréquence qu'on définit comme la fréquence plasma. Par conséquent, les spectres polarisés p d'un gaz d'électrons libres dans une couche fine ont un seul pic de résonance, qui est excité par la composante perpendiculaire du champs électrique de la lumière incidente. Cette résonance est associée à une excitation collective du gaz d'électrons, appelé un plasmon.

Dans des couches suffisamment fines, le gaz d'électrons est confiné. Il a un spectre d'excitation discret et sa réponse optique diffère de celle d'un gaz d'électrons libres. Pour

décrire la réponse optique du gaz d'électrons confinés, un modèle semi-classique pour la fonction diélectrique est introduit. Dans ce model, toutes les contributions à la polarisation originant des électrons qui participent aux différentes transitions optiques sont additionnées. En pratique, la population d'électrons qui participe à chaque transition optique est calculée, puis la réponse optique de celle-ci est décrite comme un oscillateur classique de la forme forme Drude-Lorentz. Pour trouver la fonction diélectrique finale, toutes les fonctions de type Drude-Lorentz, dont chacune décrit les électrons qui participent à une transition spécifique, sont additionnées.

De même que pour un gaz d'électrons libres, les résonances optiques sont aussi observées aux zéros de la fonction diélectrique pour un gaz d'électrons confinés quantiquement. Dans le cas où le confinement donne lieu à un spectre d'états confinés très rapprochés en fréquences, toutes les fréquences de transition sont petites, et la fonction diélectrique calculée s'approche de celle du modèle de Drude. Quand le gaz d'électrons est de plus en plus confiné, le zero de la fonction diélectrique, et donc, la résonance du plasmon, se décalent vers le bleu. Dans le cas où le gaz d'électrons est confiné à tel point que seulement quelques niveaux sont occupés, plusieurs résonances peuvent être observées dans le spectre optique. En effet, les zéros de la fonction diélectrique deviennent alors bien séparés en fréquence.

Pour mettre en lumière l'origine physique de l'observation de résonances aux zéros de la fonction diélectriques dans les couches minces, un modèle semi-classique est introduit. Une équation du mouvement est alors écrite pour chaque population d'électrons participant à une transition donnée. Des termes sont introduits pour prendre en compte les forces coulombiennes sur cette population. Ces forces proviennent des charges surfaciques issues du déplacement de cette population d'électrons induit par le rayonnement incident, ainsi que par les autres transitions électroniques. Cette dernière contribution couple toutes les équations du mouvement, donnant lieu à un système d'oscillateurs couplés. Il est démontré que les solutions de ce système sont exactement les zéros de la fonction diélectrique.

Chapitre 2

Il est expérimentalement démontré que le mode de Berreman peut être observé dans l'infrarouge dans une structure composé d'un seul type de semiconducteur si une haute densité de dopants est introduite dans une couche sub-longueur d'onde. En trouvant les fonctions d'onde qui sont simultanément des solutions aux equation de Schrödinger et de Poisson, il est démontré que le champ électrostatique des donneurs ionisés est suffisamment fort pour confiner les électrons dans la couche sub-longueur d'onde.

Les propriétés optiques du gaz d'électrons dans une couche sub-longueur d'onde d'InGaAs fortement dopée n sont étudiées par spectroscopie à transformée de Fourier. Comme il se couple directement à la lumière de l'espace libre, le mode de Berreman est observé dans des mesures de transmission à des angles d'incidence faible jusqu'à l'angle de réflexion totale interne. Un autre mode, existant sous la ligne de lumière de l'espace libre, qualifié de type epsilon-near-zero (ENZ), est aussi observé expérimentalement pour des angles internes plus élevés en utilisant un biseau pour coupler la lumière à l'intérieur et hors du semi-conducteur.

Le mode de Berreman est étudié dans une autre configuration où une couche d'or, agissant comme un miroir, est déposée sur la surface du semi-conducteur proche de la couche fortement dopée. Dans cette configuration, l'absorptivité du mode de Berreman peut être

directement déterminée comme 1 - réflectivité, car la couche fortement dopée ne partage plus d'interface avec l'espace libre. Le mode de Berreman peut être expérimentalement étudié jusqu'à la ligne de la lumière du semi-conducteur, au-delà de celle de l'espace libre.

Dans la dernière partie du chapitre, des expériences d'émission thermique sont rapportées. Dans ces expériences, la température du gaz d'électrons est modulée grâce à l'effet Joule en injectant un courant pulsé dans le plan de la couche dopée. L'émission thermique, qui prend la forme de l'émission d'un corps noir (loi de Planck) multipliée par l'émissivité (égale à l'absorptivité selon la loi de Kirchhoff), est donc aussi modulée, permettant aux plasmons d'être observés grâce à une détection synchrone. L'émission thermique du mode de Berreman et du mode non-radiatif ENZ est étudiée en utilisant des dispositifs avec et sans couche d'or adjacente à la couche fortement dopée. Nous démontrons que la dispersion et le couplage à la lumière des deux modes sont différents.

Chapitre 3

Le couplage entre plasmons et phonons optiques longitudinaux est étudié. La dépendance de la fréquence plasma de la densité électronique dans les semi-conducteurs dopés est exploitée afin de mettre en résonance la fréquence plasma avec la bande Reststrahlen.

Une fonction diélectrique est introduite pour décrire la réponse optique des semi-conducteurs dopés dans la bande Reststrahlen. Elle consiste en une somme des termes décrivant les phonons, et un terme de Drude, décrivant le gaz d'électrons libres. Les termes décrivant la réponse des phonons prennent la forme d'oscillateurs de Lorentz avec des pôles aux fréquences des phonons optiques transverses et des zéros aux fréquences des phonons longitudinaux. Les modes couplés plasmon-phonon se trouvent aux zéros de la fonction diélectrique totale. Grâce à l'effet Berreman, ces modes peuvent être directement observés dans les couche sub-longueur d'onde.

Les résultats des expériences réalisées sur trois échantillons sont rapportés. Les échantillons sont composés d'une répétition de couches fines d'InGaAs et d'AlInAs, épitaxiés sur un substrat InP. Deux des échantillons sont identiques, à l'exception de la densité d'électrons dans les couches d'InGaAs: dans le premier l'InGaAs est non intentionnellement dopé, tandis que le deuxième échantillon est dopé de sorte que la fréquence de plasma est proche de celle des phonons optiques. Pour ces échantillons, l'épaisseur des couches d'InGaAs a été choisie suffisamment épaisse pour que les électrons puissent être considérés comme libres. Pour le troisième échantillon, l'épaisseur des couches dopées d'InGaAs a été choisi suffisamment fine pour confiner les électrons, donnant ainsi lieu à des transitions intrabandes.

Dans les spectres polarisés p de l'échantillon non-dopé, nous observons les résonances de phonons optiques transverses et longitudinaux des couches InGaAs et AlInAs. Comme attendu, seulement les phonons transverses sont observés dans les spectres polarisés s. Dans les spectres des échantillons dopés, l'une des résonances de phonons optiques longitudinaux d'InGaAs n'apparait plus, alors qu'une nouvelle résonance apparaît à une énergie plus haute. Ces nouvelles résonances correspondent aux modes couplés plasmon-phonon.

Chapitre 4

Un modèle quantique microscopique est introduit pour décrire les excitations électroniques collectives d'un gaz d'électrons confinés. Les excitations collectives sont construites à partir de la base de toutes les transitions électroniques optiquement actives, ce qui implique que le confinement quantique est naturellement considéré dans le modèle. Les modes collectifs sont calculés à travers la diagonalisation d'un Hamiltonien qui contient deux termes, l'un décrivant des transitions électroniques optiquement actives et l'autre leur couplage Coulombien.

L'écriture du Hamiltonien dans la représentation de Power, Zienau, et Woolley permet au terme de couplage d'apparaître sous la forme du carré de l'opérateur de polarisation. Dans le modèle, la dépendance spatiale de la polarisation microscopique de la matière est décrite comme une fonction des états électroniques stationnaires des électrons uniques. Ainsi, le modèle décrit naturellement la non-localité des excitations collectives.

Le modèle est appliqué pour décrire analytiquement les modes longitudinaux collectifs observés dans un puits quantique large fortement dopé. Il est démontré que chaque mode collectif dans un puits carré se produit grâce au couplage des transitions électroniques de même symétrie spatiale.

Des expressions analytiques sont dérivées pour la dispersion quantifiée des modes longitudinaux collectifs comme une fonction du vecteur d'onde dans la direction du confinement. Nous démontrons que, en l'absence de confinement, la formule de Lindhard, pour les modes de plasma d'un gaz d'électrons libres, peut être retrouvée. En considérant le confinement des états électroniques, nous démontrons que notre modèle analytique décrit bien les modes collectifs expérimentalement observés dans un puits quantique large (100 nm) fortement dopé de InGaAs/AlInAs.

Chapitre 5

Le modèle quantique microscopique, introduit dans le chapitre précédent, est exploité afin de concevoir des nouveaux modes collectifs électroniques en utilisant le potentiel électronique de confinement comme un degré de liberté. Les modes collectifs de trois potentiels électroniques différents, choisis pour avoir une symétrie différente de celle d'un puits carré, sont étudiés.

En premier, les modes collectifs sont calculés pour une hétérostructure constituée de puits quantiques couplés par effet tunnel. Nous observons que dans cette structure les transitions normalement interdites par la symétrie d'un puits carré, sont permises. L'ingénierie des états électroniques permet donc de modifier profondément les excitations collectives et en conséquence le spectre d'absorptivité par rapport à celui d'un puits carré de la même épaisseur.

Dans une deuxième étude théorique, les modes plasmoniques d'un gaz d'électrons confinés dans un potentiel quasi-triangulaire, réalisé par l'application d'un champs électrique à un puits carré, sont étudiés. Du fait de la rupture de la symétrie miroir, de nouveaux modes plasmoniques, qui n'interagissent normalement pas avec la lumière (appelés noirs), apparaissent dans le spectre d'absorptivité.

Le dernier potentiel étudié est celui d'une marche. Les modes de plasmons confinés dans ce potentiel sont étudiés théoriquement et expérimentalement. Les structures sont réalisées expérimentalement en utilisant la croissance d'un alliage quaternaire dans la région de la marche. En changeant la concentration du quaternaire, la hauteur de la marche est variée.

Sur l'ensemble des spectres expérimentaux obtenus sur des échantillons avec des hauteurs différentes de la marche, deux modes de plasmon sont observés. Le mode à plus haute énergie est peu affecté par l'augmentation de la hauteur de la marche, alors que le mode à plus basse énergie se décale vers le rouge. Ces résultats sont expliqués par des calculs qui démontrent que le mode à plus haute énergie est localisé dans la région la plus profonde du potentiel, tandis que le mode à plus basse énergie est localisé dans la région quaternaire de la marche. Plus exactement, il est démontré théoriquement qu'il existe une dispersion des modes plasmoniques qui peuvent être excités de chaque côté de la structure, et que des modes provenant des côtés opposés, lorsqu'ils sont en résonance, peuvent être couplés pour former des modes hybridisés.

Chapitre 6

Des photodetecteurs sont étudiés dans lesquels le mode de Berreman d'un puits fortement dopé est utilisé comme photoabsorbeur. La première observation de photocourant généré par l'excitation d'un mode de Berreman est rapportée.

La chapitre commence par un résumé des motivations de l'étude, dont la principale est d'étudier comment une excitation bosonique multi-corps peut générer un courant électronique. Nous établissons un lien entre notre étude et des résultats précédents de photodetecteurs plasmoniques à électrons chauds, qui utilisent un plasmon de surface pour l'absorption. Dans ces études, il est indiqué que l'excitation plasmonique se désintègre en une population de porteurs hors-équilibre et chauds qui sont ensuite collectés.

Les études expérimentales de deux échantillons différents sont rapportées. Ces échantillons contiennent chacun un puits épais central fortement dopé flanqué de chaque côté par une barrière et une couche de contact dopée. La fabrication des dispositifs et les expériences faites pour les caractériser sont décrites. Pour chaque échantillon, des mesures de spectres optiques, de caractérisation électrique, et de photoréponse sont réalisées. Pour une tension proche de zéro, les courbes de courant-tension de chaque dispositif présentent une grande résistance différentielle. Il est démontré que les photodetecteurs atteignent leur responsivité maximale au voltage où la résistance différentielle décroît rapidement. À ce voltage, les spectres de photovoltage ressemblent aux spectres d'absorptivité du mode de Berreman, au moins autour de sa fréquence d'excitation. Des caractéristiques supplémentaires sont observées dans les spectres de photovoltage de l'un des échantillons à des énergies supérieures au mode de Berreman, et sont associées à de l'absorption par porteurs libres. Les caractéristiques courant-tension et la photoréponse des dispositifs sont expliquées par un simple modèle d'émission thermionique, dans lequel l'énergie d'activation est liée à la hauteur effective de la barrière que les électrons doivent surmonter afin d'être collectés. Les résultats de l'étude de la photoréponse de l'un des deux dispositifs sous éclairage d'une source laser à cascade quantique accordable sont également rapportés.

Dans la dernière partie du chapitre, il est démontré expérimentalement que le même dispositif à mode de Berreman qui fonctionne comme un photodétecteur peut aussi fonctionner comme un émetteur électroluminescent. Ces expériences montrent que le mode plasmon peut être excité par un courant continu par le biais d'un processus de diffusion résonante électron-plasmon.

Chapitre 7

Le photocourant issu de l'excitation de polaritons est étudié. Ces derniers sont des modes couplés matière-lumière observés quand le mode de Berreman est couplé à un mode de microcavité. En ajustant les paramètres de la cavité, l'énergie des éxcitations de polaritons peut être modifiée, ce qui permet d'étudier le photocourant en fonction de l'énergie d'excitation collective.

La chapitre commence par la description quantique des modes polaritons. Les microcavités métal-diélectrique-métal auxquelles le mode de Berrman est couplé sont décrites. Les spectres de réflectivité des modes de polariton sont calculés pour des cavités d'épaisseur variable. La procédure pour la fabrication des dispositifs à microcavité double-métal avec trois contacts électriques est décrite en détail. Les images de chaque étape de la fabrication sont présentées.

Les résultats de la caractérisation expérimentale des dispositifs sont présentés en trois parties. Tout d'abord, les spectres de réflectivité des dispositifs à résonateur unique dont la largeur de la cavité varie, mesurés à l'aide d'un microscope à spectromètre infrarouge à transformée de Fourier, sont rapportés. En accord avec les spectres simulés, un décalage vers le bleu du polariton supérieur est observé lorsque la largeur de la cavité est réduite. Une bande spectrale de réflectivité parfaite est observée entre les modes de polariton supérieur et inférieur, ce qui indique que les dispositifs fonctionnent dans le régime de couplage ultra-fort.

Les courbes courant-tension des dispositifs à différentes énergies de mode de cavité sont ensuite rapportées. Les courbes, bien qu'elles ne soient pas linéaires, montrent une résistance différentielle très réduite proche du voltage nul par rapport à celles obtenues avec un dispositif simple de type mésa, fabriqué à partir du même échantillon. Cela indique la présence de courants parasites induits par des défauts de fabrication.

Dans la dernière section du chapitre, des mesures de photoresponsivité des dispositifs de résonateur sous illumination par un laser à cascade quantique accordable sont rapportées. Malheureusement, le laser à cascade quantique n'a pu être accordé qu'un peu au-delà de l'énergie d'excitation du mode de Berreman non couplé, ce qui a empêché l'observation directe du photocourant provenant des modes de polaritons supérieurs. Avec cette contrainte, deux études sont présentées qui fournissent la première preuve de l'observation d'un photocourant provenant de modes polaritons dans le régime de couplage ultra-fort: premièrement, la responsivité d'un dispositif à résonateur avec un mode de polariton supérieur à une énergie proche de la coupure du laser est étudiée. Lorsque le laser est accordé à des énergies plus faibles, la responsivité des dispositifs diminue. Dans la seconde étude, le laser est fixée à une énergie proche de celle du mode de Berreman non couplé, et des dispositifs de résonateur à énergie de cavité variable sont étudiés. Lorsque l'énergie du mode de polariton supérieur est augmentée, la responsivité des dispositifs diminue, ce qui est conforme aux attentes si le photocourant provient du mode de polariton supérieur.

Bibliography

[1] Sadao Adachi 1985. "GaAs, AlAs, and AlGaAs: Material parameters for use in research and device applications". *Journal of Applied Physics* **58**(3), p. R1–R29. Cited page 25

[2] K. Alavi, R. Aggarwal & S. Groves 1980. "Interband magnetoabsorption of $In_{0.53}Ga_{0.47}As$". *Physical Review B* **21**(3), p. 1311–1315. Cited page 7

[3] S. J. Allen, D. C. Tsui & B. Vinter 1993. "On the absorption of infrared radiation by electrons in semiconductor inversion layers". *Solid State Communications* **88**(11), p. 939–942. Cited page x

[4] Filippo Alpeggiani & Lucio Claudio Andreani 2014. "Semiclassical theory of multisubband plasmons: Nonlocal electrodynamics and radiative effects". *Physical Review B* **90**(11), p. 115 311. Cited pages 12 and 41

[5] L. N. Alyabyeva, E. S. Zhukova, M. A. Belkin & B. P. Gorshunov 2017. "Dielectric properties of semi-insulating Fe-doped InP in the terahertz spectral region". *Scientific Reports* **7**(1), p. 7360. Cited page 60

[6] Tsuneya Ando, Alan B. Fowler & Frank Stern 1982. "Electronic properties of two-dimensional systems". *Reviews of Modern Physics* **54**(2), p. 437–672. Cited pages ix, 11, 17, 18, and 20

[7] David L. Andrews, Garth A. Jones, A. Salam & R. Guy Woolley 2018. "Perspective: Quantum Hamiltonians for optical interactions". *The Journal of Chemical Physics* **148**(4), p. 040 901. Cited page 83

[8] B Askenazi, A Vasanelli, A Delteil, Y Todorov, L C Andreani, G Beaudoin, I Sagnes & C Sirtori 2014. "Ultra-strong light–matter coupling for designer Reststrahlen band". *New Journal of Physics* **16**(4), p. 043 029. Cited pages x, 3, 8, 15, 27, and 95

[9] Gerald Bastard 1988. *Wave mechanics applied to semiconductor heterostructures*. Monographies de physique (Les Editions de Physique ; Halsted Press, Les Ulis Cedex, France : New York, N.Y). ISBN 978-0-470-21708-5 978-2-86883-092-0. Cited page 6

[10] R. J. Becker, P. F. Luehrmann & D. W. Langer 1985. "Raman scattering from phonon-plasmon modes in $Ga_{1-x}Al_xAs$". *Applied Physics Letters* **47**(5), p. 513–515. Cited pages 58 and 59

[11] D. W. Berreman 1963. "Infrared Absorption at Longitudinal Optic Frequency in Cubic Crystal Films". *Physical Review* **130**(6), p. 2193–2198. Cited pages 1 and 2

[12] Dwight W. Berreman & F. C. Unterwald 1968. "Adjusting Poles and Zeros of Dielectric Dispersion to Fit Reststrahlen of $PrCl_3$ and $LaCl_3$". *Physical Review* **174**(3), p. 791–799. Cited page 26

[13] A Bichri, J Lafait & H Welsch 1993. "Visible and infrared optical properties of Ag/SiO_2 multilayers: radiative virtual modes and coupling effects". *Journal of Physics: Condensed Matter* **5**(40), p. 7361–7374. Cited page 27

[14] Azzurra Bigioli, Giovanni Armaroli, Angela Vasanelli, Djamal Gacemi, Yanko Todorov, Daniele Palaferri, Lianhe Li, A. Giles Davies, Edmund H. Linfield & Carlo Sirtori 2020. "Long-wavelength infrared photovoltaic heterodyne receivers using patch-antenna quantum cascade detectors". *Applied Physics Letters* **116**(16), p. 161 101. Cited page 115

[15] Stefan Birner, Tobias Zibold, Till Andlauer, Tillmann Kubis, Matthias Sabathil, Alex Trellakis & Peter Vogl 2007. "nextnano: General Purpose 3-D Simulations". *IEEE Transactions on Electron Devices* **54**(9), p. 2137–2142. Conference Name: IEEE Transactions on Electron Devices. Cited pages 8, 9, and 30

[16] J. S. Blakemore 1982. "Semiconducting and other major properties of gallium arsenide". *Journal of Applied Physics* **53**(10), p. R123–R181. Cited page 25

[17] Mark L. Brongersma, Naomi J. Halas & Peter Nordlander 2015. "Plasmon-induced hot carrier science and technology". *Nature Nanotechnology* **10**(1), p. 25–34. Cited pages 116 and 117

[18] Salvatore Campione, Igal Brener & Francois Marquier 2015. "Theory of epsilon-near-zero modes in ultrathin films". *Physical Review B* **91**(12), p. 121 408. Cited pages 41, 42, and 45

[19] Salvatore Campione, Iltai Kim, Domenico de Ceglia, Gordon A. Keeler & Ting S. Luk 2016. "Experimental verification of epsilon-near-zero plasmon polariton modes in degenerately doped semiconductor nanolayers". *Optics Express* **24**(16), p. 18 782. Cited pages 27 and 45

[20] Federico Capasso, Carlo Sirtori, Jerome Faist, Deborah L. Sivco, Sung-Nee G. Chu & Alfred Y. Cho 1992. "Observation of an electronic bound state above a potential well". *Nature* **358**(6387), p. 565–567. Cited page 173

[21] Hamidreza Chalabi, David Schoen & Mark L. Brongersma 2014. "Hot-Electron Photodetection with a Plasmonic Nanostripe Antenna". *Nano Letters* **14**(3), p. 1374–1380. Cited page 116

[22] W. P. Chen, Y. J. Chen & E. Burstein 1976. "The interface EM modes of a "surface quantized" plasma layer on a semiconductor surface". *Surface Science* **58**(1), p. 263–265. Cited page 18

[23] A.Y. Cho & J.R. Arthur 1975. "Molecular beam epitaxy". *Progress in Solid State Chemistry* **10**, p. 157–191. Cited page ix

[24] Cristiano Ciuti, Gérald Bastard & Iacopo Carusotto 2005. "Quantum vacuum properties of the intersubband cavity polariton field". *Physical Review B* **72**(11), p. 115 303. Cited page 79

[25] Claude Cohen-Tannoudji, Jacques Dupont-Roc & Gilbert Grynberg 2001. *Photons et atomes: introduction à l'électrodynamique quantique*. Savoirs actuels Physique (EDP Sciences [u.a.], Les Ulis). ISBN 978-2-222-03966-2 978-2-86883-535-2. Cited page 84

[26] Claude Cohen-Tannoudji, Jacques Dupont-Roc, Gilbert Grynberg & Claude Cohen-Tannoudji 2004. *Photons and atoms: introduction to quantum electrodynamics*. Physics textbook (Wiley-VCH, Weinheim). ISBN 978-0-471-18433-1. Cited page 83

[27] F. Compagnone, A. Di Carlo & P. Lugli 2002. "Electron–optical-phonon interaction in the $In_{1-x}Ga_xAs/In_{1-y}Al_yAs$ superlattice". *Physical Review B* **65**(12), p. 125 314. Cited pages 26, 58, and 66

[28] Sébastien Cosme 2019. *Emetteurs infrarouges superradiants*. Thèse de doctorat Sorbonne Paris Cité. Cited page 30

[29] K. Craig, B. Galdrikian, J. N. Heyman, A. G. Markelz, J. B. Williams, M. S. Sherwin, K. Campman, P. F. Hopkins & A. C. Gossard 1996. "Undressing a Collective Intersubband Excitation in a Quantum Well". *Physical Review Letters* **76**(13), p. 2382–2385. Cited page 61

[30] M. Creuzburg & H. Raether 1964. "Comparison of energy losses of electrons with optical properties of KCl and KBr". *Solid State Communications* **2**(11), p. 345–347. Cited page 20

[31] Baptiste Dailly 2018. *Properties Optiques de Plasmons Superradiants*. Thèse de doctorat Université Paris Diderot - Paris 7. Cited pages 36 and 38

[32] F. Javier García de Abajo 2012. "Plasmons go quantum". *Nature* **483**(7390), p. 417–418. Cited page ix

[33] Alexandre Delga 2020. "Quantum cascade detectors: A review". Dans "Mid-infrared Optoelectronics", (Elsevier). ISBN 978-0-08-102709-7 p. 337–377. URL `http://dx.doi.org/10.1016/B978-0-08-102709-7.00008-5`. Cited page 115

[34] A. Delteil, A. Vasanelli, Y. Todorov, C. Feuillet Palma, M. Renaudat St-Jean, G. Beaudoin, I. Sagnes & C. Sirtori 2012. "Charge-Induced Coherence between Intersubband Plasmons in a Quantum Structure". *Physical Review Letters* **109**(24), p. 246 808. Cited pages x, 16, 17, and 150

[35] A. Delteil, A. Vasanelli, Y. Todorov, B. Paulillo, G. Biasiol, L. Sorba & C. Sirtori 2013. "Gate controlled coupling of intersubband plasmons". *Applied Physics Letters* **102**(3), p. 031 102. Cited page 19

[36] Aymeric Delteil 2012. *Exaltation multicorps du couplage lumière-matière*. These de doctorat Paris 7. URL https://www.theses.fr/2012PA077214. Cited page 21

[37] Dimitri Dini, Rüdeger Köhler, Alessandro Tredicucci, Giorgio Biasiol & Lucia Sorba 2003. "Microcavity Polariton Splitting of Intersubband Transitions". *Physical Review Letters* **90**(11), p. 116 401. Cited page 150

[38] Alexander Dorodnyy, Yannick Salamin, Ping Ma, Jelena Vukajlovic Plestina, Nolan Lassaline, Dmitry Mikulik, Pablo Romero-Gomez, Anna Fontcuberta i Morral & Juerg Leuthold 2018. "Plasmonic Photodetectors". *IEEE Journal of Selected Topics in Quantum Electronics* **24**(6), p. 1–13. Cited page 116

[39] Adam D. Dunkelberger, Daniel C. Ratchford, Andrea B. Grafton, Vanessa M. Breslin, Elizabeth S. Ryland, D. Scott Katzer, Kenan P. Fears, R. Joseph Weiblen, Igor Vurgaftman, Alexander J. Giles *et al.* 2020. "Ultrafast Active Tuning of the Berreman Mode". *ACS Photonics* **7**(1), p. 279–287. Cited page 27

[40] Jerome Faist, Federico Capasso, Deborah L. Sivco, Carlo Sirtori, Albert L. Hutchinson & Alfred Y. Cho 1994. "Quantum Cascade Laser". *Science* **264**(5158), p. 553–556. Cited page ix

[41] Richard A. Ferrell 1958. "Predicted Radiation of Plasma Oscillations in Metal Films". *Physical Review* **111**(5), p. 1214–1222. Cited pages ix and 3

[42] Jamie M. Fitzgerald, Prineha Narang, Richard V. Craster, Stefan A. Maier & Vincenzo Giannini 2016. "Quantum Plasmonics". *Proceedings of the IEEE* **104**(12), p. 2307–2322. Cited page ix

[43] P. Forn-Díaz, L. Lamata, E. Rico, J. Kono & E. Solano 2019. "Ultrastrong coupling regimes of light-matter interaction". *Reviews of Modern Physics* **91**(2), p. 025 005. Cited page 58

[44] R. H. Fowler 1931. "The Analysis of Photoelectric Sensitivity Curves for Clean Metals at Various Temperatures". *Physical Review* **38**(1), p. 45–56. Cited page 116

[45] Mark Fox 2001. *Optical properties of solids*. Oxford master series in condensed matter physics (Oxford University Press, Oxford ; New York). ISBN 978-0-19-850613-3 978-0-19-850612-6. Cited pages 11, 16, and 33

[46] G Frucci, S Huppert, A Vasanelli, B Dailly, Y Todorov, G Beaudoin, I Sagnes & C Sirtori 2017. "Cooperative Lamb shift and superradiance in an optoelectronic device". *New Journal of Physics* **19**(4), p. 043 006. Cited page 41

[47] L. Gendron, M. Carras, A. Huynh, V. Ortiz, C. Koeniguer & V. Berger 2004. "Quantum cascade photodetector". *Applied Physics Letters* **85**(14), p. 2824–2826. Cited pages ix and 115

[48] Jacek Gosciniak, Fatih B. Atar, Brian Corbett & Mahmoud Rasras 2019. "Plasmonic Schottky photodetector with metal stripe embedded into semiconductor

and with a CMOS-compatible titanium nitride". *Scientific Reports* **9**(1). Cited page 116

[49] Ilya Goykhman, Boris Desiatov, Jacob Khurgin, Joseph Shappir & Uriel Levy 2012. "Waveguide based compact silicon Schottky photodetector with enhanced responsivity in the telecom spectral band". *Optics Express* **20**(27), p. 28 594. Cited page 116

[50] S. Graf, H. Sigg, K. Köhler & W. Bächtold 2000. "Direct Observation of Depolarization Shift of the Intersubband Resonance". *Physical Review Letters* **84**(12), p. 2686–2689. Cited page x

[51] Meir Grajower, Boris Desiatov, Noa Mazurski, Joseph Shappir, Jacob B. Khurgin & Uriel Levy 2017. "Optimization and Experimental Demonstration of Plasmonic Enhanced Internal Photoemission Silicon Schottky Detectors in the Mid-IR". *ACS Photonics* **4**(4), p. 1015–1020. Cited page 116

[52] Naomi J. Halas, Surbhi Lal, Wei-Shun Chang, Stephan Link & Peter Nordlander 2011. "Plasmons in Strongly Coupled Metallic Nanostructures". *Chemical Reviews* **111**(6), p. 3913–3961. Cited page 112

[53] W. P. Halperin 1986. "Quantum size effects in metal particles". *Reviews of Modern Physics* **58**(3), p. 533–606. Cited page ix

[54] B. Harbecke, B. Heinz & P. Grosse 1985. "Optical properties of thin films and the Berreman effect". *Applied Physics A Solids and Surfaces* **38**(4), p. 263–267. Cited page 20

[55] P. Harrison 2009. *Quantum wells, wires and dots: theoretical and computational physics* (Wiley, West Sussex, England ; Hoboken, NJ) 3rd ed édition. ISBN 978-0-470-77098-6 978-0-470-77097-9. Cited page 8

[56] D. A. Hart & N. L. Oleson 1969. "Experimental Study of Tonks-Dattner Resonances in Rare-Gas Plasmas". *Journal of Applied Physics* **40**(11), p. 4541–4553. Cited page 94

[57] Manfred Helm 1999. "Chapter 1 The Basic Physics of Intersubband Transitions". Dans "Semiconductors and Semimetals", tome 62 (Elsevier). ISBN 978-0-12-752171-8 p. 1–99. URL http://dx.doi.org/10.1016/S0080-8784(08)60304-X. Cited pages 8, 10, 12, and 18

[58] Johannes Hillbrand, Léonard Matthieu Krüger, Sandro Dal Cin, Hedwig Knötig, Jonas Heidrich, Aaron Maxwell Andrews, Gottfried Strasser, Ursula Keller & Benedikt Schwarz 2021. "High-speed quantum cascade detector characterized with a mid-infrared femtosecond oscillator". *Optics Express* **29**(4), p. 5774. Cited page 115

[59] J. J. Hopfield 1958. "Theory of the Contribution of Excitons to the Complex Dielectric Constant of Crystals". *Physical Review* **112**(5), p. 1555–1567. Cited pages 79 and 151

[60] S. Huppert, A. Vasanelli, G. Pegolotti, Y. Todorov & C. Sirtori 2016. "Strong and ultrastrong coupling with free-space radiation". *Physical Review B* **94**(15), p. 155 418. Cited pages 34, 35, 41, 42, 55, and 87

[61] J. Ibáñez, Enver Tarhan, A. K. Ramdas, S. Hernández, R. Cuscó, L. Artús, M. R. Melloch & M. Hopkinson 2004. "Direct observation of LO phonon-plasmon coupled modes in the infrared transmission spectra of n-GaAs and $n-In_xGa_{1-x}As$ epilayers". *Physical Review B* **69**(7), p. 075 314. Cited page 59

[62] M. Ilegems & G. L. Pearson 1970. "Infrared Reflection Spectra of $Ga_{1-x}Al_xAs$ Mixed Crystals". *Physical Review B* **1**(4), p. 1576–1582. Cited pages 25 and 26

[63] P. Jouy, A. Vasanelli, Y. Todorov, A. Delteil, G. Biasiol, L. Sorba & C. Sirtori 2011. "Transition from strong to ultrastrong coupling regime in mid-infrared metal-dielectric-metal cavities". *Applied Physics Letters* **98**(23), p. 231 114. Cited page 150

[64] A. Kamgar, P. Kneschaurek, G. Dorda & J. F. Koch 1974. "Resonance Spectroscopy of Electronic Levels in a Surface Accumulation Layer". *Physical Review Letters* **32**(22), p. 1251–1254. Cited page ix

[65] Jacob B. Khurgin 2019. "Hot carriers generated by plasmons: where are they generated and where do they go from there?" *Faraday Discussions* **214**, p. 35–58. Cited page 116

[66] O. K. Kim & W. G. Spitzer 1979. "Study of plasmon—LO-phonon coupling in Te-doped $Ga_{1-x}Al_xAs$". *Physical Review B* **20**(8), p. 3258–3266. Cited page 59

[67] M. W. Knight, H. Sobhani, P. Nordlander & N. J. Halas 2011. "Photodetection with Active Optical Antennas". *Science* **332**(6030), p. 702–704. Cited pages 116 and 117

[68] E. Kretschmann & H. Raether 1968. "Notizen: Radiative Decay of Non Radiative Surface Plasmons Excited by Light". *Zeitschrift für Naturforschung A* **23**(12), p. 2135–2136. Cited page 43

[69] T. Laurent, Y. Todorov, A. Vasanelli, A. Delteil, C. Sirtori, I. Sagnes & G. Beaudoin 2015. "Superradiant Emission from a Collective Excitation in a Semiconductor". *Physical Review Letters* **115**(18), p. 187 402. Cited pages 34 and 35

[70] Thibault Laurent, Yanko Todorov, Angela Vasanelli, Isabelle Sagnes, Grégoire Beaudoin & Carlo Sirtori 2015. "Electrical excitation of superradiant intersubband plasmons". *Applied Physics Letters* **107**(24), p. 241 112. Cited pages 47, 49, 145, and 147

[71] B. F. Levine 1993. "Quantum-well infrared photodetectors". *Journal of Applied Physics* **74**(8), p. R1–R81. Cited pages ix and 115

[72] Wei Li & Jason G. Valentine 2017. "Harvesting the loss: surface plasmon-based hot electron photodetection". *Nanophotonics* **6**(1), p. 177–191. Cited page 117

[73] Xiaoguang Li, Di Xiao & Zhenyu Zhang 2013. "Landau damping of quantum plasmons in metal nanostructures". *New Journal of Physics* **15**(2), p. 023 011. Cited page 116

[74] T. L. Lin & J. Maserjian 1990. "Novel SiGeSi heterojunction internal photoemission long-wavelength infrared detectors". *Applied Physics Letters* **57**(14), p. 1422–1424. Cited page 125

[75] I Lindau & P O Nilsson 1971. "Experimental Verification of Optically Excited Longitudinal Plasmons". *Physica Scripta* **3**(2), p. 87–92. Cited page 94

[76] J Lindhard 1954. "On the Properties of a Gas of Charged Particles". *Det Kongelige Danske Videnskabernes Selskab Matematisk-fysiske Meddelelser* **28**(8). Cited pages 93 and 94

[77] D. J. Lockwood, G. Yu, N. L. Rowell & P. J. Poole 2007. "Optical phonons via oblique-incidence infrared spectroscopy and their deformation potentials in $In_{1-x}Ga_xAs$". *Journal of Applied Physics* **101**(11), p. 113 524. Cited page 66

[78] Rodney Loudon 2000. *The quantum theory of light*. Oxford science publications (Oxford University Press, Oxford ; New York) 3rd ed édition. ISBN 978-0-19-850177-0 978-0-19-850176-3. Cited page 83

[79] Gerald D. Mahan 2000. *Many-Particle Physics* (Springer US, Boston, MA). ISBN 978-1-4419-3339-3 978-1-4757-5714-9. URL http://dx.doi.org/10.1007/978-1-4757-5714-9. Cited page 93

[80] Stefan A. Maier 2007. *Plasmonics: Fundamentals and Applications* (Springer US, New York, NY). ISBN 978-0-387-33150-8 978-0-387-37825-1. URL http://dx.doi.org/10.1007/0-387-37825-1. Cited pages 5, 42, and 43

[81] Harold M. Manasevit 1968. "SINGLE-CRYSTAL GALLIUM ARSENIDE ON INSULATING SUBSTRATES". *Applied Physics Letters* **12**(4), p. 156–159. Cited page ix

[82] H.M. Manasevit 1981. "Recollections and reflections of MO-CVD". *Journal of Crystal Growth* **55**(1), p. 1–9. Cited page ix

[83] Mao-Chieh Hsu, Chun-Chi Chen, Chieh-Hsiung Kuan & Shiang-Yu Wang 2003. "Infrared detection utilizing both intersubband and free-carrier absorption in reverse-biased superlattice infrared photodetector". *IEEE Journal of Quantum Electronics* **39**(11), p. 1476–1480. Cited pages 125 and 138

[84] A. J. McAlister & E. A. Stern 1963. "Plasma Resonance Absorption in Thin Metal Films". *Physical Review* **132**(4), p. 1599–1602. Cited pages ix, 1, 2, 4, and 27

[85] W. Patrick McCray 2007. "MBE deserves a place in the history books". *Nature Nanotechnology* **2**(5), p. 259–261. Cited page ix

[86] Jeffrey M. McMahon, Stephen K. Gray & George C. Schatz 2009. "Nonlocal Optical Response of Metal Nanostructures with Arbitrary Shape". *Physical Review Letters* **103**(9), p. 097 403. Cited page ix

[87] A. Mooradian & A. L. McWhorter 1967. "Polarization and Intensity of Raman Scattering from Plasmons and Phonons in Gallium Arsenide". *Physical Review Letters* **19**(15), p. 849–852. Cited page 59

[88] A. Mooradian & G. B. Wright 1966. "Observation of the Interaction of Plasmons with Longitudinal Optical Phonons in GaAs". *Physical Review Letters* **16**(22), p. 999–1001. Cited page 59

[89] D J Mowbray, W Hayes, L L Taylor & S J Bass 1990. "Raman scattering study of the electron-phonon coupling in GaInAs-InP quantum wells". *Semiconductor Science and Technology* **5**(1), p. 83–89. Cited pages 58 and 59

[90] S. Muehlbrandt, A. Melikyan, T. Harter, K. Köhnle, A. Muslija, P. Vincze, S. Wolf, P. Jakobs, Y. Fedoryshyn, W. Freude *et al.* 2016. "Silicon-plasmonic internal-photoemission detector for 40 Gbit/s data reception". *Optica* **3**(7), p. 741. Cited page 116

[91] Shaul Mukamel 2009. *Principles of nonlinear optical spectroscopy.* Numéro 6 dans Oxford series in optical and imaging sciences (Oxford Univ. Press, New York). ISBN 978-0-19-513291-5. Cited page 83

[92] M. Nakayama 1977. "On the strip transmission line spectroscopy of the inter-subband transition of MOS charge layer". *Solid State Communications* **21**(6), p. 587–589. Cited page x

[93] Ward D. Newman, Cristian L. Cortes, Jon Atkinson, Sandipan Pramanik, Raymond G. DeCorby & Zubin Jacob 2015. "Ferrell–Berreman Modes in Plasmonic Epsilon-near-Zero Media". *ACS Photonics* **2**(1), p. 2–7. Cited pages 3, 27, and 67

[94] L. Nordin, O. Dominguez, C. M. Roberts, W. Streyer, K. Feng, Z. Fang, V. A. Podolskiy, A. J. Hoffman & D. Wasserman 2017. "Mid-infrared epsilon-near-zero modes in ultra-thin phononic films". *Applied Physics Letters* **111**(9), p. 091 105. Cited page 27

[95] L. Nordin, A. J. Muhowski & D. Wasserman 2022. "High operating temperature plasmonic infrared detectors". *Applied Physics Letters* **120**(10), p. 101 103. Cited page 116

[96] Leland Nordin, Priyanka Petluru, Abhilasha Kamboj, Aaron J. Muhowski & Daniel Wasserman 2021. "Ultra-thin plasmonic detectors". *Optica* **8**(12), p. 1545. Cited page 116

[97] Daniele Palaferri, Yanko Todorov, Azzurra Bigioli, Alireza Mottaghizadeh, Djamal Gacemi, Allegra Calabrese, Angela Vasanelli, Lianhe Li, A. Giles Davies, Edmund H. Linfield *et al.* 2018. "Room-temperature nine-µm-wavelength

photodetectors and GHz-frequency heterodyne receivers". *Nature* **556**(7699), p. 85–88. Cited page 115

[98] Nikolai Christian Passler, Mathieu Jeannin & Alexander Paarmann 2020. "Layer-resolved absorption of light in arbitrarily anisotropic heterostructures". *Physical Review B* **101**(16), p. 165 425. Cited page 32

[99] Nikolai Christian Passler, I. Razdolski, D. Scott Katzer, D. F. Storm, Joshua D. Caldwell, Martin Wolf & Alexander Paarmann 2019. "Second Harmonic Generation from Phononic Epsilon-Near-Zero Berreman Modes in Ultrathin Polar Crystal Films". *ACS Photonics* **6**(6), p. 1365–1371. Cited page 27

[100] G. Pegolotti, A. Vasanelli, Y. Todorov & C. Sirtori 2014. "Quantum model of coupled intersubband plasmons". *Physical Review B* **90**(3), p. 035 305. Cited pages x, 35, 77, and 87

[101] Giulia Pegolotti 2014. *Quantum engineering of collective states in semiconductor nanostructures*. These de doctorat Paris 7. URL http://www.theses.fr/2014PA077136. Cited pages 11, 21, 86, 87, and 102

[102] A. G. U. Perera, H. X. Yuan & M. H. Francombe 1995. "Homojunction internal photoemission far-infrared detectors: Photoresponse performance analysis". *Journal of Applied Physics* **77**(2), p. 915–924. Cited page 138

[103] A. Pinczuk, Jagdeep Shah, A. C. Gossard & W. Wiegmann 1981. "Light Scattering by Photoexcited Two-Dimensional Electron Plasma in GaAs-(AlGa) As Heterostructures". *Physical Review Letters* **46**(20), p. 1341–1344. Cited page 59

[104] A. Pinczuk & J.M. Worlock 1982. "Light scattering by two-dimensional electron systems in semiconductors". *Surface Science* **113**(1-3), p. 69–84. Cited page 59

[105] David Pines 1956. "Collective Energy Losses in Solids". *Reviews of Modern Physics* **28**(3), p. 184–198. Cited pages ix and 20

[106] David Pines & David Bohm 1952. "A Collective Description of Electron Interactions: II. Collective vs Individual Particle Aspects of the Interactions". *Physical Review* **85**(2), p. 338–353. Cited page ix

[107] Alexander Poddubny, Ivan Iorsh, Pavel Belov & Yuri Kivshar 2013. "Hyperbolic metamaterials". *Nature Photonics* **7**(12), p. 948–957. Cited page 62

[108] E. Prodan, C. Radloff, N. J. Halas & P. Nordlander 2003. "A Hybridization Model for the Plasmon Response of Complex Nanostructures". *Science* **302**(5644), p. 419–422. Cited page 112

[109] Heinz Raether 1980. *Excitation of Plasmons and Interband Transitions by Electrons Springer Tracts in Modern Physics 88*, tome 88 (Springer-Verlag, Berlin/Heidelberg). ISBN 978-3-540-09677-1. URL http://dx.doi.org/10.1007/BFb0045951. Cited page 20

[110] R. H. Ritchie 1957. "Plasma Losses by Fast Electrons in Thin Films". *Physical Review* **106**(5), p. 874–881. Cited page 20

[111] Emmanuel Rosencher & Borge Vinter 2002. *Optoelectronics* (Cambridge University Press) 1 édition. ISBN 978-0-521-77129-0 978-0-521-77813-8 978-0-511-75464-7. URL http://dx.doi.org/10.1017/CBO9780511754647. Cited pages 6, 82, 91, 115, 116, and 125

[112] Yannick Salamin, Ping Ma, Benedikt Baeuerle, Alexandros Emboras, Yuriy Fedoryshyn, Wolfgang Heni, Bojun Cheng, Arne Josten & Juerg Leuthold 2018. "100 GHz Plasmonic Photodetector". *ACS Photonics* **5**(8), p. 3291–3297. Cited page 116

[113] Dror Sarid 1981. "Long-Range Surface-Plasma Waves on Very Thin Metal Films". *Physical Review Letters* **47**(26), p. 1927–1930. Publisher: American Physical Society. Cited page 42

[114] H. Schneider & H. C. Liu 2007. *Quantum well infrared photodetectors: physics and applications*. Numéro 126 dans Springer series in optical sciences (Springer, Berlin ; New York). ISBN 978-3-540-36323-1. OCLC: ocm73108720. Cited pages 115 and 125

[115] Jonathan A. Scholl, Ai Leen Koh & Jennifer A. Dionne 2012. "Quantum plasmon resonances of individual metallic nanoparticles". *Nature* **483**(7390), p. 421–427. Cited page ix

[116] Franz Schwabl 2008. *Advanced quantum mechanics* (Springer, Berlin) 4th ed édition. ISBN 978-3-540-85061-8 978-3-540-85062-5. OCLC: ocn233934756. Cited page 78

[117] Timur Shaykhutdinov, Andreas Furchner, Jörg Rappich & Karsten Hinrichs 2017. "Mid-infrared nanospectroscopy of Berreman mode and epsilon-near-zero local field confinement in thin films". *Optical Materials Express* **7**(10), p. 3706. Cited page 27

[118] Carlo Sirtori, Federico Capasso, Jerome Faist, Deborah L. Sivco, Sung-Nee G. Chu & Alfred Y. Cho 1992. "Quantum wells with localized states at energies above the barrier height: A Fabry–Perot electron filter". *Applied Physics Letters* **61**(8), p. 898–900. Cited page 173

[119] Carlo Sirtori, Federico Capasso, Jérôme Faist & Sandro Scandolo 1994. "Nonparabolicity and a sum rule associated with bound-to-bound and bound-to-continuum intersubband transitions in quantum wells". *Physical Review B* **50**(12), p. 8663–8674. Cited page 7

[120] Carlo Sirtori, Federico Capasso, Deborah L. Sivco, S. N. G. Chu & Alfred Y. Cho 1991. "Observation of large second order susceptibility via intersubband transitions at λ˜10 μm in asymmetric coupled AlInAs/GaInAs quantum wells". *Applied Physics Letters* **59**(18), p. 2302–2304. Cited page 100

[121] Carlo Sirtori, Jerome Faist, Federico Capasso, Deborah L. Sivco & Alfred Y. Cho 1993. "Photocurrent reversal induced by localized continuum resonances in asymmetric quantum semiconductor structures". *Applied Physics Letters* **63**(19), p. 2670–2672. Cited page 173

[122] Ali Sobhani, Adam Lauchner, Sina Najmaei, Ciceron Ayala-Orozco, Fangfang Wen, Jun Lou & Naomi J. Halas 2014. "Enhancing the photocurrent and photoluminescence of single crystal monolayer MoS $_2$ with resonant plasmonic nanoshells". *Applied Physics Letters* **104**(3), p. 031 112. Cited page 116

[123] W. E. Spicer 1958. "Photoemissive, Photoconductive, and Optical Absorption Studies of Alkali-Antimony Compounds". *Physical Review* **112**(1), p. 114–122. Cited page 117

[124] W. E. Spicer 1977. "Negative affinity 3–5 photocathodes: Their physics and technology". *Applied Physics* **12**(2), p. 115–130. Cited page 117

[125] Mark I Stockman, Katrin Kneipp, Sergey I Bozhevolnyi, Soham Saha, Aveek Dutta, Justus Ndukaife, Nathaniel Kinsey, Harsha Reddy, Urcan Guler, Vladimir M Shalaev *et al.* 2018. "Roadmap on plasmonics". *Journal of Optics* **20**(4), p. 043 001. Cited page ix

[126] Thierry Taliercio & Paolo Biagioni 2019. "Semiconductor infrared plasmonics". *Nanophotonics* **8**(6), p. 949–990. Cited page 5

[127] Thierry Taliercio, Vilianne Ntsame Guilengui, Laurent Cerutti, Eric Tournié & Jean-Jacques Greffet 2014. "Brewster "mode" in highly doped semiconductor layers: an all-optical technique to monitor doping concentration". *Optics Express* **22**(20), p. 24 294. Cited pages 27, 29, and 42

[128] M. S. Tame, K. R. McEnery, Ş. K. Özdemir, J. Lee, S. A. Maier & M. S. Kim 2013. "Quantum plasmonics". *Nature Physics* **9**(6), p. 329–340. Cited page ix

[129] I-H. Tan, G. L. Snider, L. D. Chang & E. L. Hu 1990. "A self-consistent solution of Schrödinger–Poisson equations using a nonuniform mesh". *Journal of Applied Physics* **68**(8), p. 4071–4076. Cited page 9

[130] B. Tell & R. J. Martin 1968. "Raman Scattering by Coupled Optical-Phonon-Plasmon Modes in GaAs". *Physical Review* **167**(2), p. 381–386. Cited page 59

[131] Y. Todorov, A. M. Andrews, R. Colombelli, S. De Liberato, C. Ciuti, P. Klang, G. Strasser & C. Sirtori 2010. "Ultrastrong Light-Matter Coupling Regime with Polariton Dots". *Physical Review Letters* **105**(19), p. 196 402. Cited pages 83, 84, and 150

[132] Y. Todorov, A. M. Andrews, I. Sagnes, R. Colombelli, P. Klang, G. Strasser & C. Sirtori 2009. "Strong Light-Matter Coupling in Subwavelength Metal-Dielectric Microcavities at Terahertz Frequencies". *Physical Review Letters* **102**(18), p. 186 402. Cited pages 61 and 152

[133] Y. Todorov, L. Tosetto, J. Teissier, A. M. Andrews, P. Klang, R. Colombelli, I. Sagnes, G. Strasser & C. Sirtori 2010. "Optical properties of metal-dielectric-metal microcavities in the THz frequency range". *Optics Express* **18**(13), p. 13 886. Cited pages 151 and 152

[134] Yanko Todorov 2015. "Dipolar quantum electrodynamics of the two-dimensional electron gas". *Physical Review B* **91**(12), p. 125 409. Cited page 83

[135] Yanko Todorov & Carlo Sirtori 2012. "Intersubband polaritons in the electrical dipole gauge". *Physical Review B* **85**(4), p. 045 304. Cited pages 11, 12, 58, 77, 79, 81, 84, and 151

[136] Alex Trellakis, Tobias Zibold, Till Andlauer, Stefan Birner, R. Kent Smith, Richard Morschl & Peter Vogl 2006. "The 3D nanometer device project nextnano: Concepts, methods, results". *Journal of Computational Electronics* **5**(4), p. 285–289. Cited page 30

[137] C. A. Ullrich & G. Vignale 2001. "Theory of the Linewidth of Intersubband Plasmons in Quantum Wells". *Physical Review Letters* **87**(3), p. 037 402. Cited page 18

[138] Angela Vasanelli, Simon Huppert, Andrew Haky, Thibault Laurent, Yanko Todorov & Carlo Sirtori 2020. "Semiconductor Quantum Plasmonics". *Physical Review Letters* **125**(18), p. 187 401. Cited pages 3, 13, 77, 95, 96, and 97

[139] Angela Vasanelli, Yanko Todorov, Baptiste Dailly, Sébastien Cosme, Djamal Gacemi, Andrew Haky, Isabelle Sagnes & Carlo Sirtori 2020. "Semiconductor quantum plasmons for high frequency thermal emission". *Nanophotonics* **10**(1), p. 607–615. Cited pages 37, 46, and 48

[140] S. Vassant, A. Archambault, F. Marquier, F. Pardo, U. Gennser, A. Cavanna, J. L. Pelouard & J. J. Greffet 2012. "Epsilon-Near-Zero Mode for Active Optoelectronic Devices". *Physical Review Letters* **109**(23), p. 237 401. Cited pages 42 and 45

[141] Simon Vassant, Jean-Paul Hugonin, Francois Marquier & Jean-Jacques Greffet 2012. "Berreman mode and epsilon near zero mode". *Optics Express* **20**(21), p. 23 971. Cited pages 41, 42, 45, and 55

[142] I. Vurgaftman, J. R. Meyer & L. R. Ram-Mohan 2001. "Band parameters for III–V compound semiconductors and their alloys". *Journal of Applied Physics* **89**(11), p. 5815–5875. Cited pages 6, 7, and 104

[143] Hui Wang, Yanpeng Wu, Britt Lassiter, Colleen L. Nehl, Jason H. Hafner, Peter Nordlander & Naomi J. Halas 2006. "Symmetry breaking in individual plasmonic nanoparticles". *Proceedings of the National Academy of Sciences* **103**(29), p. 10 856–10 860. Cited page 112

[144] R. J. Warburton, C. Gauer, A. Wixforth, J. P. Kotthaus, B. Brar & H. Kroemer 1996. "Intersubband resonances in InAs/AlSb quantum wells: Selection rules, matrix elements, and the depolarization field". *Physical Review B* **53**(12), p. 7903–7910. Cited pages 12 and 19

[145] R. J. Warburton, K. Weilhammer, J. P. Kotthaus, M. Thomas & H. Kroemer 1998. "Influence of Collective Effects on the Linewidth of Intersubband Resonance". *Physical Review Letters* **80**(10), p. 2185–2188. Cited page x

[146] L. C. West & S. J. Eglash 1985. "First observation of an extremely large-dipole infrared transition within the conduction band of a GaAs quantum well". *Applied Physics Letters* **46**(12), p. 1156–1158. Cited page ix

[147] J. B. Williams, M. S. Sherwin, K. D. Maranowski & A. C. Gossard 2001. "Dissipation of Intersubband Plasmons in Wide Quantum Wells". *Physical Review Letters* **87**(3), p. 037 401. Cited page 18

[148] Frederick Wooten 2014. *Optical Properties of Solids.* (Elsevier Science, Saint Louis). ISBN 978-1-4832-2076-5. OCLC: 1040269172 URL http://qut.eblib.com.au/patron/FullRecord.aspx?p=1834463. Cited pages 3, 20, and 93

[149] Peter Y Yu & Manuel Cardona 2010. *Fundamentals of semiconductors: physics and materials properties* (Springer, Berlin; New York). ISBN 978-3-642-00709-5 978-3-662-51736-9. Cited pages 5, 7, 24, and 171

[150] T. Yuasa, S. Naritsuka, M. Mannoh, K. Shinozaki, K. Yamanaka, Y. Nomura, M. Mihara & M. Ishii 1985. "Observation of plasmons coupled with optical phonons in n-$Al_xGa_{1-x}As$ by Raman scattering". *Applied Physics Letters* **46**(2), p. 176–178. Cited pages 58 and 59

[151] M. Zal/użny 1991. "Intersubband absorption line broadening in semiconductor quantum wells: Nonparabolicity contribution". *Physical Review B* **43**(5), p. 4511–4514. Cited page x

[152] E. Zielinski, H. Schweizer, K. Streubel, H. Eisele & G. Weimann 1986. "Excitonic transitions and exciton damping processes in InGaAs/InP". *Journal of Applied Physics* **59**(6), p. 2196–2204. Cited page 7

RÉSUMÉ

La plasmonique sur semiconducteurs s'intéresse à l'interaction de la lumière avec un gaz dense d'électrons. Dans ce travail, nous étudions les excitations multi-corps dans des couches minces de semiconducteur, où le déplacement des électrons crée un dipôle optique collectif. Les modes brillants qui en résultent sont des plasmons de volume connus sous le nom de modes de Berreman. Nous démontrons que les propriétés de ces modes peuvent être modifiées en les couplant avec leur environnement (phonons optiques dans le semiconducteur, résonateurs photoniques), ou en manipulant les états électroniques des particules individuelles qui les composent par des potentiels artificiels.
Nous montrons que l'introduction d'une forte densité électronique dans une couche mince d'un matériau semiconducteur unique est suffisante pour observer ces modes collectifs, qui peuvent être exploités pour réaliser des émetteurs thermiques efficaces. Nous observons des résonances couplées plasmon - phonon dans des expériences de spectroscopie lorsque la fréquence de plasma est proche de celle des phonons optiques. Ce couplage donne lieu à une modification de la bande Reststrahlen du semiconducteur.
Pour des couches suffisamment fines, la réponse collective du gaz d'électrons est modifiée en raison du confinement quantique. Un modèle microscopique quantique est introduit dans lequel la réponse collective est construite à partir du couplage dipolaire des transitions électroniques entre états liés. Avec ce modèle, nous démontrons que le confinement quantique fixe la dispersion des modes plasmoniques dans un potentiel de puits carré. Nous démontrons expérimentalement que de nouveaux modes collectifs peuvent être créés en concevant opportunément le potentiel de confinement du gaz d'électrons.
Dans la dernière partie du travail, les premières observations de photocourant provenant de l'excitation d'un plasmon de volume sont rapportées. Le mécanisme de photodétection est interprété comme résultant de la relaxation de l'excitation collective en une population de porteurs chauds. Pour approfondir cette interprétation, nous étudions des photodétecteurs dans lesquels le mode plasmon est couplé au mode photonique d'une microcavité. Nous rapportons la première preuve de la génération de photocourant à partir de l'excitation de modes couplés lumière-matière en régime de couplage ultra-fort.

MOTS CLÉS

plasmonique, semiconducteur, infrarouge, puits quantiques, polaritons

ABSTRACT

Semiconductor plasmonics is concerned with the interaction of light with a dense electron gas in a semiconductor. In this work, we study many-body excitations in thin films, where the electronic displacement forms a collective optical dipole. The resulting bright modes are volume plasmons known as Berreman modes. We demonstrate that the properties of these modes can be engineered by coupling them with their environment (optical phonons in the semiconductor, photonic resonators), or by manipulating their constituent single-particle electronic states through artificial potentials.
We show that the introduction of a high electronic density to a thin layer in a single semiconductor material is sufficient to observe these collective modes, which can be exploited to realize efficient thermal emitters. We observe coupled plasmon – phonon resonances in spectroscopic measurements when the plasma frequency is close to that of the optical phonons. This coupling results in a modified Reststrahlen band for the semiconductor.
For sufficiently thin layers, the collective response of the electron gas is modified due to the quantum confinement. A quantum microscopic model is introduced in which the collective response is constructed from the dipolar coupling of single particle transitions between bound states. With this model, we demonstrate that quantum confinement fixes the dispersion of plasmonic modes in a square well potential. We experimentally demonstrate that novel collective modes can be engineered by careful design of the confining potential for the electron gas.
In the last part of the work, the first observations of photocurrent from the excitation of a volume plasmon are reported. The photodetection mechanism is interpreted to result from the decay of the collective excitation into a population of hot carriers. To further establish this interpretation, we investigate photodetector devices in which the plasmon mode is coupled to the photonic mode of a microcavity. We report the first evidence of photocurrent generation from the excitation of coupled light-matter modes in the ultrastrong coupling regime.

KEYWORDS

plasmonics, semiconductor, infrared, quantum well, polaritons